1317

ENERGY

ACS SYMPOSIUM SERIES

CATALYSIS BY METAL COMPLEXES & NANOMATERIALS

FUNDAMENTALS & APPLICATIONS

ZHOU

ACS Publications

Catalysis by Metal Complexes and Nanomaterials: Fundamentals and Applications

ACS SYMPOSIUM SERIES **1317**

Catalysis by Metal Complexes and Nanomaterials: Fundamentals and Applications

Meng Zhou, Editor
Lawrence Technological University
Southfield, Michigan, United States

American Chemical Society, Washington, DC

Library of Congress Cataloging-in-Publication Data

Names: Zhou, Meng (Chemistry professor), editor.
Title: Catalysis by metal complexes and nanomaterials : fundamentals and applications / Meng Zhou, editor, Lawrence Technological University, Southfield, Michigan, United States.
Description: Washington, DC : American Chemical Society, [2019] | Series: ACS symposium series; 1317 | Includes bibliographical references and index.
Identifiers: LCCN 2019022641 (print) | LCCN 2019022642 (ebook) | ISBN 9780841234376 (hardback) | ISBN 9780841234369 (ebook other)
Subjects: LCSH: Catalysis. | Transition metal catalysts. | Nanostructured materials.
Classification: LCC QD505 .C3826 2019 (print) | LCC QD505 (ebook) | DDC 541/.395--dc23
LC record available at https://lccn.loc.gov/2019022641
LC ebook record available at https://lccn.loc.gov/2019022642

The paper used in this publication meets the minimum requirements of American National Standard for Information Sciences—Permanence of Paper for Printed Library Materials, ANSI Z39.48n1984.

PRINTED IN THE UNITED STATES OF AMERICA

Foreword

The purpose of the series is to publish timely, comprehensive books developed from the ACS sponsored symposia based on current scientific research. Occasionally, books are developed from symposia sponsored by other organizations when the topic is of keen interest to the chemistry audience.

Before a book proposal is accepted, the proposed table of contents is reviewed for appropriate and comprehensive coverage and for interest to the audience. Some papers may be excluded to better focus the book; others may be added to provide comprehensiveness. When appropriate, overview or introductory chapters are added. Drafts of chapters are peer-reviewed prior to final acceptance or rejection.

As a rule, only original research papers and original review papers are included in the volumes. Verbatim reproductions of previous published papers are not accepted.

ACS Books Department

Contents

Preface

Catalysis, primarily a kinetic phenomenon, occurs when a catalyst forges a new reaction pathway that is unavailable to an uncatalyzed reaction. The catalytic reaction outruns the competing reactions and is therefore more efficient and selective. Important applications of catalysis include the synthesis of pharmaceutically active ingredients, production of petrochemicals and nitrogen fertilizers, degradation of pollutants, CO_2 reduction, chemical sensing, and the development of renewable energy. But what are the structures of catalysts? How do they work, and how are they developed? Answers vary depending on whom you ask and their specific field of study.

Catalysis is truly an interdisciplinary field to which chemists, biologists, physicists, and engineers have made seminal contributions. This book aims to address the notably diverse topic of transition-metal catalysis in a single volume. The first half of the book is dedicated to the discrete and atomically precise metal complexes for homogeneous catalysis. Bimetallic, organometallic, and coordination complexes of early, late, and post-transition metals are described. Catalytic hydrogenation, oxidation, and coupling reactions are presented. The second half of the book focuses on three distinct types of nanomaterials: (1) zero–valent metallic nanoparticles, (2) titanium dioxide semiconductors, and (3) the porous coordination polymer known as the metal–organic framework. The chapters illustrate how deeply catalysis is influenced by other disciplines (e.g., coordination chemistry, bioinorganic chemistry, organometallic chemistry, computational chemistry, organic synthesis, photochemistry, materials science, environmental chemistry, green chemistry, and renewable energy). Advancements in these areas fuel the rapid growth of catalysis science.

This book allows readers to reach a high-level of understanding in catalysis by learning from the perspectives of active practitioners. Unlike a textbook that provides a systematic, comprehensive, and historical education on the general topics of catalysis, this book offers critical case studies on select topics. Substantial emphasis is placed on the structural and fundamental properties that dictate catalyst performance, enabling readers to quickly understand and apply knowledge from cutting-edge studies and applications detailed within. This book can be utilized as a handbook, a textbook or textbook supplement, or a reference to guide future work.

This book was co-written by chemists and engineers from the United States and Canada. I first learned about the coauthor's work at the 2017 Central Regional Meeting of the American Chemical Society, held in Dearborn, Michigan, and the 2018 New Faculty Workshop co-sponsored by Cottrell Scholars Collaborative and the American Chemical Society, held in Denver, Colorado. During the Dearborn meeting, I organized the symposium "Catalysis by Metal Complexes and Nanomaterials", the purpose of which was to bridge the knowledge gap between catalysis scientists from distinct fields and inspire interdisciplinary research. This book is the culmination of the knowledge and spirit of the symposium.

I thank Amanda Koenig and David Andrews from the publications division of the American Chemical Society for technical assistance and Ferman Chavez, Richard Finke, Robert Crabtree, Alan Goldman, Xinrui Zhou, and Danielle Hanson for helpful discussions.

Cover Credit: Scanning Electron Microscope Image of the Seed Inside The MOF Crystals. Photographers: Dr. Paolo Falcaro and Dr. Dario Buso. Photo under CC-BY license

Meng Zhou

Assistant Professor of Chemistry
Department of Natural Sciences
Lawrence Technological University
21000 West Ten Mile Road
Southfield, Michigan 48075, United States

Chapter 1

Synthesis and Reactivity of Bimetallic Systems Tethered with a 4,5-Diaminoxanthene Linker

Ryan L. Hollingsworth,* Thilini S. Hollingsworth, and Stanislav Groysman

Department of Chemistry, Wayne State University, 5101 Cass Avenue, Detroit, Michigan 48188, United States

***E-mail: rholling@chem.wayne.edu**

Selection of a linker is crucial for the optimal design of bimetallic systems for cooperative reactivity. The xanthene group is a proven bridging unit that has appeared in multiple systems that have displayed metal–metal cooperativity. This chapter focuses on the recent developments in this field, primarily from the Groysman group. Design of xanthene-bridged homo- and hetero-bimetallics will be presented. Several applications of these complexes will be discussed, including cyclotrimerization of terminal alkynes, polymerization of *rac*-lactide, and mimicking the active site of Mo–Cu carbon monoxide dehydrogenase (CODH).

Introduction

There is great current interest in designing dinucleating ligands for transition metals. This interest stems from the ever-growing list of bimetallic and polymetallic centers found in nature that utilize essential small molecules, such as carbon dioxide and dinitrogen, for catalysis. Through the years, many research groups have attempted to replicate the structural and functional metal–metal cooperativity exhibited by these enzymes, in hopes of improving transition metal catalysis. The bridging unit is a crucial element in designing successful dinucleating ligands and is essential for properly spacing the metals, enabling cooperative activation, and catalysis. The xanthene group is an example of an accomplished bridging unit that is easy to synthesize and functionalize.

The xanthene functionality has found its home in many dinucleating scaffolds. Nocera and coworkers and others utilized the xanthene linker in their design of "Pacman" styled complexes featuring porphyrin chelates (Scheme 1a) (*1*–*10*). These complexes range in functionality from electrocatalytic oxygen reduction to water with a dicobalt or di-iron species (*1*, *2*) to catalytic oxidation of dimethyl sulfide to dimethyl sulfoxide, using O_2 as the oxidant with a di-iron system (*3*). In all of these instances, a bridging μ–oxo is observed between the two metals, suggesting that the xanthene linker was paramount in facilitating cooperative catalysis. It is worth noting that Guilard et al., along with Sun and coworkers, have had similar success with "Pacman" systems toward catalytic

reduction of oxygen to water with dicobalt complexes (*6*–*9*) and electrocatalytic water oxidation with a dimanganese species (*10*).

The next successful dinucleating platform featuring the xanthene linker was produced by Limberg and coworkers (*11*–*13*). Employing β-diketiminato chelates (Scheme 1b), Limberg and coworkers were able to catalytically copolymerize CO_2 with epoxides using a dizinc complex (*11*), oxidatively couple 2,4-di-*tert*-butylphenol with a dicopper species (*12*), and cooperatively activate CS_2 in an unprecedented fashion with the same dicopper system (*13*). Similarly, Ma and coworkers. (*14*–*16*), along with Osakada and coworkers (*17*), have had success applying phenoxyiminato chelates in various open chain and macrocyclic ligands for olefin polymerization and copolymerization (Scheme 1c). Specifically, Ma and coworkers catalyzed ethylene polymerization and copolymerization with open chain dititanium and dinickel complexes (*14*, *15*), while Osakada and coworkersutilized a dinickel, double-decker-style macrocycle for their catalysis (*17*). Another example of employing phenoxyiminato chelating agents comes from Hirotsu and coworkers, who synthesized macrocyclic dimanganese complexes for catalytic asymmetric oxidation reactions of sulfide (Scheme 1d) (*18*, *19*). These subtle variations in ligand scaffolding highlight the versatility of the xanthene group.

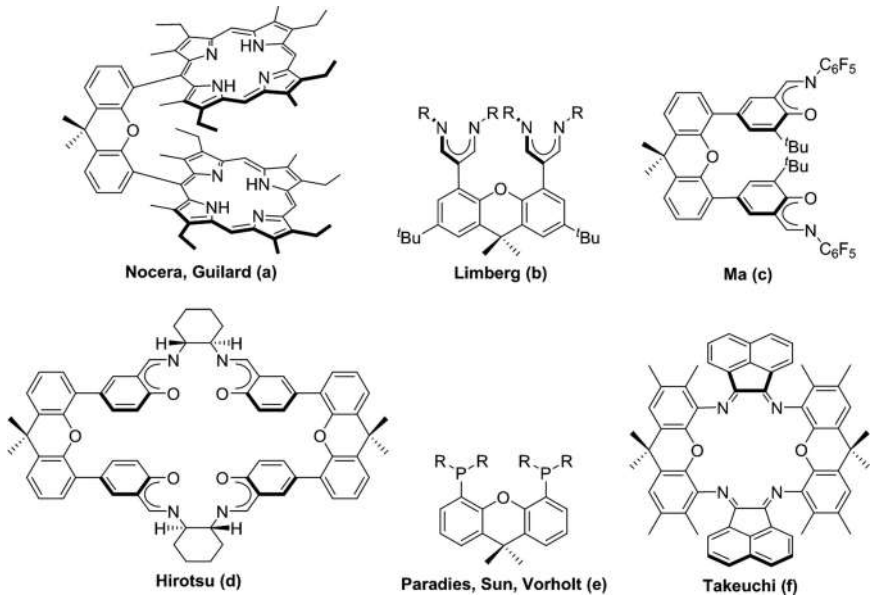

Scheme 1. Selected examples of successful dinucleating ligands that feature the xanthene linker: (a) "Pacman" systems (1–10), (b) Limberg's β-diketiminato system (11–13), (c) Ma's phenoxyiminato system (14–16), (d) Hirotsu's macrocyclic phenoxyiminato system (18, 19), (e) "xantphos" systems (20–22), (f) Takeuchi's "double-decker" diimine system (23, 24).

Two more chelating groups of interest that involve the xanthene linker are phosphines (*20*–*22*) and diimines (Scheme 1e and 1f) (*23*–*25*). Referred to as "xantphos," the Paradies (*20*), Sun (*21*), and Vorholt (*22*) groups have demonstrated the usefulness of the xanthene group in bimetallic cooperativity utilizing phosphine chelates. Their use ranges from digold-catalyzed hydroamidation (*20*) to cross-coupling enynones with diazo compounds utilizing a digold system (*21*), to tandem-catalyzed hydroaminomethylation with a dirhodium complex (*22*). With regard to diimine chelates,

Takeuchi and coworkers (*23*, *24*), along with Chen and coworkers (*25*), have synthesized dipalladium complexes toward ethylene polymerization. The list of xanthene-based dinucleating ligands with assorted chelating units capable of initiating metal–metal cooperativity is quite extensive (*26*–*33*).

The Groysman group is investigating the design and cooperative reactivity of bimetallic complexes in small molecule activation and catalysis (*34*–*43*). Recently, Groysman and coworkers have advanced the potential of the xanthene linker for bimetallic cooperativity through various avenues (*34*–*38*). Their primary source of xanthene for ligand synthesis is 4,5-diaminoxanthene, leading to nitrogen-based ligands. The group has synthesized bis(iminopyridine) dicopper and dinickel complexes toward small molecule activation and alkyne cyclotrimerization, respectively (*34*, *35*), a macrocyclic cobalt carbonyl complex featuring two bis(iminopyridine) chelates (*36*), a bis(phenoxyimine) dizinc system capable of lactide polymerization (*37*), and a hetero-dinuclear molybdenum–copper model of Mo–Cu carbon monoxide dehydrogenase (CODH) (*38*). This chapter will focus on the work from the Groysman lab and their efforts toward design and synthesis of homo- and hetero-bimetallic systems capable of cooperative reactivity.

Synthesis of Bis(iminopyridine) Dicopper Complexes

Groysman and coworkers' interest in cooperative activation of small molecules first led them to explore a ligand featuring two iminopyridine chelating units for binding late, electron-rich, first-row transition metals, such as copper and nickel (*34*, *35*). It is worth noting that typical synthesis of the dinucleating ligands mentioned in this chapter involved preparation of xanthene-4,5-diamine according to a previously described procedure (*44*), followed by subsequent condensation with an aldehyde incorporating the appropriate chelating functionality.

The bis(iminopyridine) ligand **L¹** was treated with various Cu^{I} precursors. The ensuing complexes exhibited various conformations, based upon the metal precursor and reaction conditions employed (Scheme 2). Treating two equivalents of $[Cu(NCMe)_4](PF_6)$ with one equivalent of **L¹** in weakly coordinating solvents (diethyl ether or CH_2Cl_2) led to the formation of $[Cu_2(L^1)(NCMe)_2](PF_6)_2$ (**1**). In contrast, conducting the same experiment in a stronger coordinating solvent [tetrahydrofuran (THF) or acetonitrile] led to the formation of the bis(homoleptic) $[Cu_2(L^1)_2](PF_6)_2$ (**2**). Analysis of the X-ray structure of **1** demonstrated trigonal Cu^{I} centers separated by a distance of 2.91(1) Å, suggesting a cuprophilic interaction (*45*–*48*).

Conversely, reactions of **L¹** with CuCl and CuBr led to the formation of metallopolymers (Scheme 2). Treating two equivalents of CuBr with one equivalent of **L¹** in CH_2Cl_2 resulted in formation of the polymeric $[Cu_2(L^1)Br_2]_n$ (**3**). A similar reaction with CuCl culminated with the polymer $\{[Cu_3(L^1)_2Cl_2][CuCl_2]\}$ (**4**). X-ray structure analysis revealed that the polymerization is a result of back-to-back antiparallel arrangement of the iminopyridine chelates. Considering these metallopolymers do not qualify as well-defined bimetallic systems, they will not be further discussed in this chapter.

Computational analysis was conducted to further elucidate the presence of cuprophilic interactions within structures **1** and **2**. Inspection of the HOMO-13 (HOMO = Highest Occupied Molecular Orbital) level of **1** (Figure 1) in solid-state and solution-phase optimizations confirmed the presence of a cuprophilic interaction via head-on overlap of both Cu^{I} d_z2 orbitals. This overlap is

consistent with the 2.91(1) Å Cu–Cu distance observed in the crystal structure. The shorter Cu–Cu distance of 2.521 Å observed in the solution-phase optimization advocates a preference for trigonal-planar geometry in the solid state as opposed to the distorted tetrahedral geometry calculated in solution. Conversely, analysis of the HOMO-9 level of **2** displays d_z2 orbitals too distant to overlap, excluding the presence of a cuprophilic interaction [Cu–Cu distance of 4.49(5) Å].

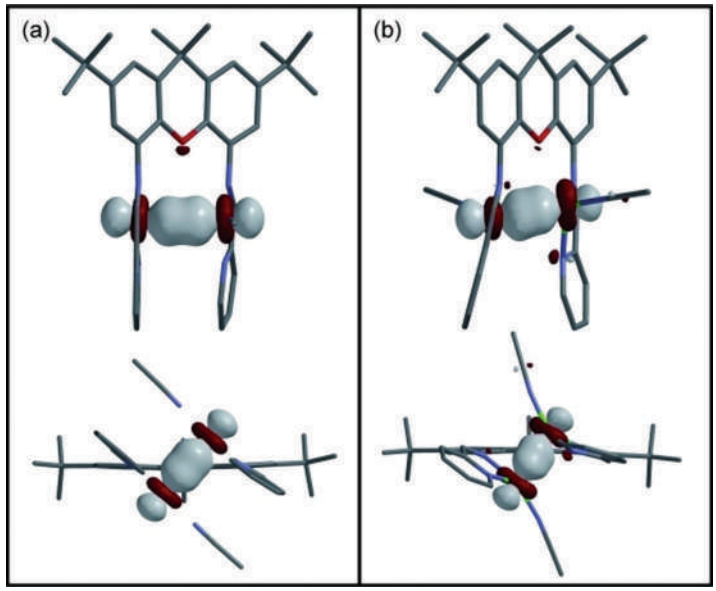

*Figure 1. Frontal and side perspectives of the complex **1** HOMO-13 levels (isosurface value: 0.04) for both (a) solid-state frozen-atom X-ray crystallography coordinates and (b) geometry optimized in an SM8 dichloromethane solvation model, thereby illustrating the trigonal-planar and distorted-tetrahedral geometries, respectively, and effective Cu^I–Cu^I interaction comprising head-on overlap of the d_z2 orbitals from both Cu^I centers [Cu–Cu distance is 2.91(1) Å in (a) and 2.521 Å in (b)]. Reproduced with permission from ref (34). Copyright 2014 John Wiley and Sons.*

After thoroughly investigating potential metal–metal interactions within the bimetallic systems, attention was redirected to reactivity studies. No meaningful reactions were observed for **1** and **2** with adamantyl azide and sulfur. However, exposing **1** to oxygen in CH_2Cl_2 resulted in the formation of at least two species that were determined by X-ray crystallography (Figure 2). Further analysis failed to elucidate the nature of any additional products. The structure of **5** displays a tetranuclear cluster, featuring four Cu^{II} centers adjoined by four ligands. Two of the Cu^{II} centers are pentacoordinate with Cu–O and Cu–Cl bonds, while the other two Cu^{II} centers are pseudooctahedral, displaying weak interactions with the μ_3–Cl. The source of the chloride is most likely dichloromethane. In regard to structure **6**, two ligands bind four Cu^{II} centers, where each Cu is pentacoordinate, consisting of two bridging hydroxides and the iminopyridine chelate.

Synthesis of a Bis(iminopyridine) Dinickel Complex for Alkyne Cyclotrimerization

Having successfully demonstrated some degree of metal–metal interaction with $\mathbf{L^1}$, Groysman and coworkersfocused their attention on utilizing another late, electron-rich, first-row transition metal—nickel (35). Inspiration for this work derived from Uyeda's dinickel system, featuring a

naphthyridine–diimine scaffold, that served as a highly efficient and selective catalyst for the cyclotrimerization of terminal alkynes (*49*). With noted similarities between the two ligand systems, an investigation was conducted to explore the effect of nickel–nickel distance and overall ligand flexibility on cyclotrimerization reactivity.

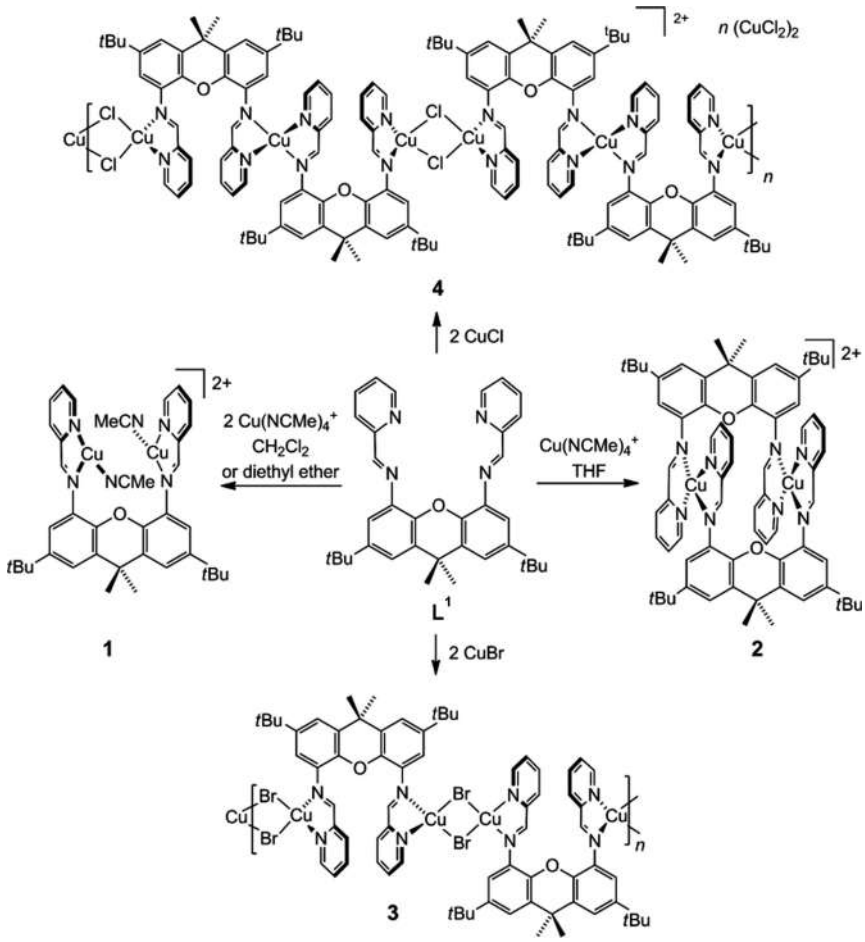

Scheme 2. Formation of dinuclear and polynuclear Cu^{I} complexes with ***L*^{1}**. *Reproduced with permission from ref* (*34*). *Copyright 2014 John Wiley and Sons.*

Initial attempts to synthesize a low-valent dinickel complex with $Ni(COD)_2$ proved fruitless, with H^1 NMR analysis of the reaction mixture suggesting formation of a bis(homoleptic) $Ni_2(L^1)$ species. Striving to overcome bis(homoleptic) formation, attempts shifted to employing a dinickel precursor $Ni_2(COD)_2(DPA)$ (**7**), as reported by Muetterties and coworkers (Scheme 3) (*50*). Treating **7** with one equivalent of **L^{1}** in THF produced the dinuclear $Ni_2(L^1)(DPA)$ (**8**). A one-pot synthesis was later developed, combining two equivalents of $Ni(COD)_2$ with one equivalent of DPA and one equivalent of **L^{1}**. Inspection of the X-ray structure of **8** reveals a Ni–Ni distance of 2.451(1) Å, shorter than the Ni–Ni distance in Uyeda's precatalysts [2.496(1) Å] (*49*). Furthermore, the C–C bond distance of the bridged acetylene was 1.369(4) Å, suggesting significant electron donation from the metal centers to the π* orbitals of the bridged acetylene.

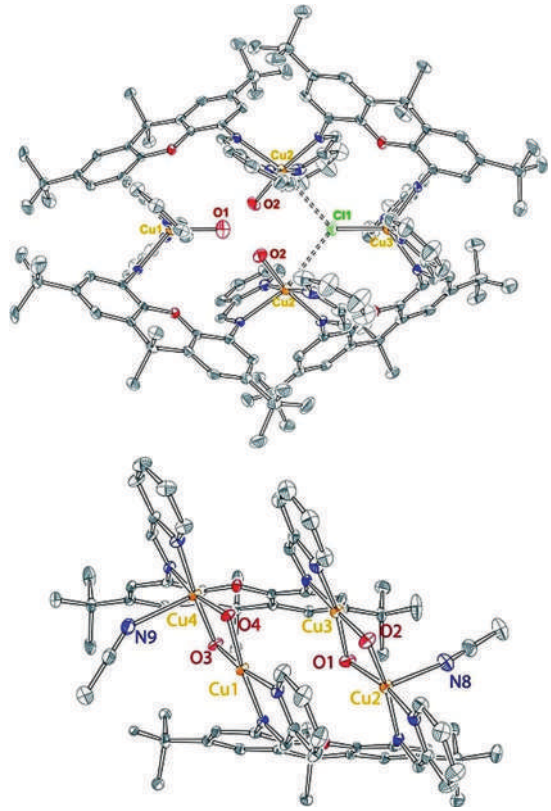

Figure 2. The structure of **5** *(top) and* **6** *(bottom), 30% probability ellipsoids. PF_6 counterions and the crystallization solvent molecules are omitted for clarity. Reproduced with permission from ref* (*34*). *Copyright 2014 John Wiley and Sons.*

Density functional theory (DFT) was used to further interrogate the electronic structure of **8**. Optimization at the B3LYP/6-31G(d) level of theory, with truncated *t*-Bu and Me groups on the ligand and truncated phenyl groups on the bridged acetylene, best characterizes the structure as an open-shell singlet with two Ni^{I} ions antiferromagnetically coupled to both the iminopyridine chelates and the adjacent Ni center. No evidence was found for covalent bonding between the Ni centers.

After examining the electronic structure of the complex, **8** was tested as a catalyst for alkyne cyclotrimerization. Stoichiometric studies with ethyl propiolate as the substrate demonstrated clean conversion to a monoadduct $Ni_2(L^1)(HC{\equiv}CCO_2Et)$ (**9**). Additional equivalents of ethyl propiolate resulted in catalytic turnover to cyclotrimerized products, with reformation of **9**. With this knowledge, catalytic studies were conducted using various catalyst loadings (1 or 5 mol %), solvents (C_6D_6, diethyl ether, THF, acetonitrile), and/or reaction temperatures (room temperature or 50 °C). Interestingly, the results of catalysis were dependent on the terminal alkyne used. For ethyl propiolate and *tert*-butyl propiolate, catalytic cyclotrimerization performed best at 5 mol % catalyst loading, in C_6D_6, at room temperature, with greater than 96% conversion and at least a 3:1 preference for the 1,2,4-isomer versus the 1,3,5-isomer. Similar performance was achieved with phenyl acetylene, but at elevated temperatures. On the other hand, methyl propargyl ether demonstrated a proclivity for cyclooctatetraenes with 1 mol % catalyst loading, regardless of solvent or temperature (a 3:1 preference for cyclooctatetraenes versus cyclotrimerized products at 50 °C in

C_6D_6). However, this inclination was avoided by using a high catalyst loading, eliminating formation of cyclooctatetraenes.

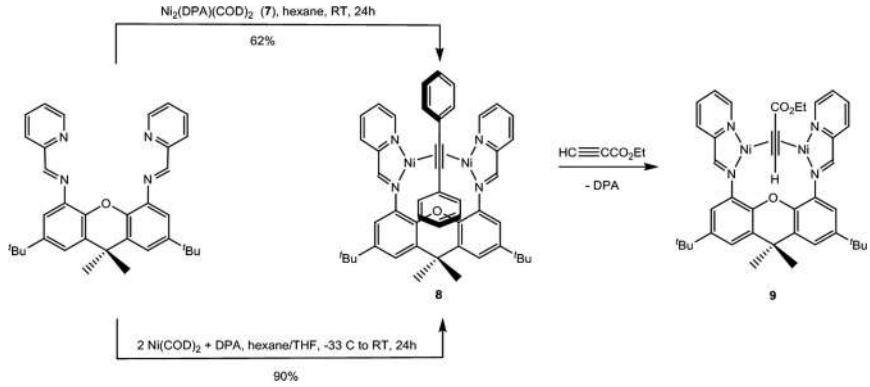

*Scheme 3. Reaction pathways leading to compounds **8** and **9**. Reproduced with permission from ref* (34). *Copyright 2014 John Wiley and Sons.*

To test the presence of metal–metal cooperativity during catalysis, Groysman and coworkers compared the reactivity of their system to Uyeda's (**10**) and two mononuclear iminopyridine systems (**11** and **12**), under identical reaction conditions (Scheme 4). The results of these studies are highlighted in Table 1. It is apparent from the results that mononuclear systems prefer cyclooctatetraene formation, whereas Uyeda's catalyst selectively forms cyclotrimerized products only. Groysman's system appeared to fall in the middle of the selectivity spectrum, producing a small amount of cyclooctatetraenes, while favoring cyclotrimerized products. This suggests a significant degree of cooperativity while lacking the nearly perfect efficiency of Uyeda's catalyst.

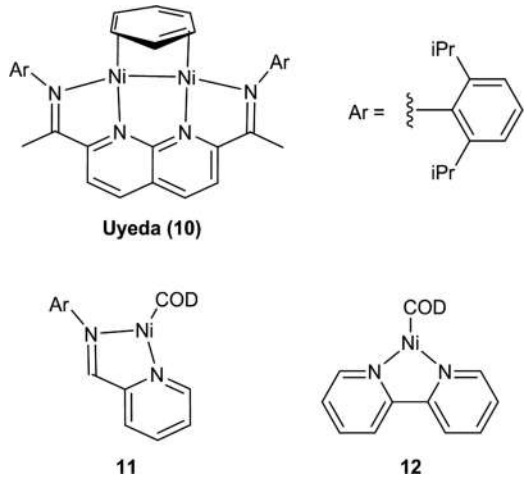

Scheme 4. Structures of precatalysts in Table 1. Reproduced with permission from ref (35). *Copyright 2017 The Royal Society of Chemistry.*

To understand the reaction mechanism for cyclotrimerization, and the observed cyclooctatetraene products, the reaction pathway was mapped for acetylene cyclotrimerization (Figure 3). Two equivalents of acetylene produces a puckered boat complex (**8a**) that quickly rearranges to a metallacyclopentadiene (**8b**), with the adjacent nickel center η^4-coordinated to the metallacycle, in contrast to Uyeda's system that exhibited η^2 coordination by the adjacent nickel

center (*10*). The third equivalent of acetylene inserts into the metallacyclopentadiene, as opposed to [4+2] cycloaddition, resulting in the formation of a metallacycloheptatriene species (**8c**), with the adjacent nickel center η^3-coordinated to the metallacycle. At this point, both iminopyridine chelates are perpendicular to the xanthene backbone, allowing catalysis to occur above the plane of the ligand. This conformation also explains the presence of cyclooctatetraenes, as yet another acetylene molecule can insert to form a metallacyclononatetraene species, eliminating cyclooctatetraene. It is apparent that the increased flexibility in Groysman's system results in decreased selectivity and efficiency when compared to Uyeda's catalyst.

Table 1. Comparison between the Catalytic Reactivity of Complex 8 with the Previously Reported Mononuclear and Dinuclear Compounds[a]. Reproduced with permission from ref (35). Copyright 2017 The Royal Society of Chemistry.

R	*Catalyst*	*% Conversion*	*% Benzenes (1,2,4:1,3,5)*	*% Combined cyclooctatetraenes*
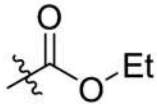	8	46	35 (4:1)	11
	10	100	90 (3:1)	10
	11	33	8 (3:1)	25
	12	32	14 (6:1)	18
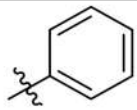	8	64	64 (12:1)	0
	10	100	100 (32:1)	0
	11	53	28 (6:1)	25
	12	40	16 (3:1)	24

[a]Reaction conditions for ethyl propiolate: 22 °C, 11 min, 1 mol % catalyst. Reaction conditions for phenylacetylene: 60 °C, 40 min, 5 mol % catalyst. Structures of the mononuclear precatalysts (other than complex **8**) are given in Scheme 4; their synthesis and reactivity are reported in Pal and Uyeda (*49*).

Reactions of Dicobalt Octacarbonyl with Bis(imino)pyridine Ligands

To overcome the limitations experienced with **L¹**, Groysman and coworkers. sought to synthesize a more rigid system. They envisioned a macrocyclic scaffold, utilizing two bis(imino)pyridine chelating units to link two xanthene moieties together **L²** (Scheme 5). A related

ligand with methyl groups instead of hydrogen on the imine functionalities had been previously reported (*29*). Previous studies by Groysman and coworkers have shown that NNN-pincer ligands struggle to bind low-valent nickel through all three nitrogen (*51*). Thus, their investigation was diverted to other late, electron-rich, first-row transition metals, eventually landing on dicobalt octacarbonyl (*36*). As research into reactivity between $Co_2(CO)_8$ and bis(imino)pyridine chelates is scarce, this provided an opportunity to explore a unique field of coordination chemistry.

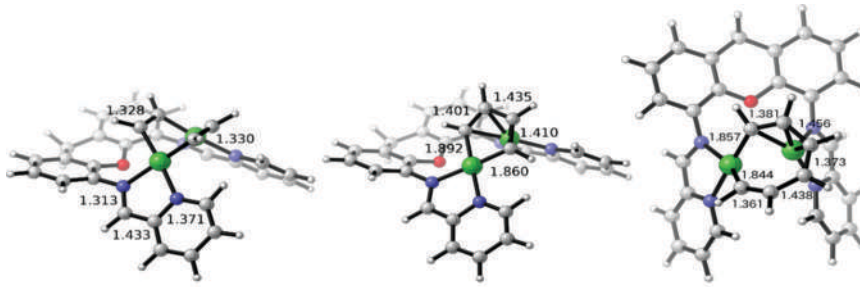

Figure 3. Optimized structures of the dialkyne adduct ***8a*** *(left), the metallacyclopentadiene species* ***8b*** *(center), and the metallacycloheptatriene intermediate* ***8c*** *(right). For the full reaction mechanism, see reference* (*35*). *Reproduced with permission from ref* (*35*). *Copyright 2017 The Royal Society of Chemistry.*

The original intention during investigation was to create a dicobalt complex by treating one equivalent of $Co_2(CO)_8$ with one equivalent of $\mathbf{L^2}$. In contrast to the desired expectation, the reaction formed an interesting tetranuclear system $[Co_2(L^2)(CO)_{10}]$ (**13**). Yield of the tetranuclear species was improved by increasing the equivalents of $Co_2(CO)_8$ utilized from one to two. Intriguingly, **13** crystallizes in two different forms (Figure 4). Both structures exhibit an absence of bridging carbonyls between cobalts, with the internal cobalts bound to the NNN-pincer system, one carbonyl, and an external cobalt, which itself is bound to four carbonyls. The two structures differ in Co–Co distance between both internal cobalts (4.8 versus 5.2 Å), suggesting some degree of flexibility within the rigid "bowl" structure.

Previous studies have shown that the reactions of $Co_2(CO)_8$ depend heavily on the substrate employed, which leads to either partial or full substitution of carbonyl ligands, along with possible cleavage of the Co–Co bond. The formation of the surprising tetranuclear product **13** was postulated to result from the relatively long distance between the NNN-chelates, combined with the rigidity and bulk around them. To evaluate whether the NNN-chelate is a strong enough ligand to completely liberate carbonyl molecules from both cobalts in $Co_2(CO)_8$, an analogous mononucleating ligand, $\mathbf{L^3}$, was synthesized and its subsequent reactivity with $Co_2(CO)_8$ investigated. It is worth noting that synthesis and reactivity of $\mathbf{L^3}$ with nickel was previously reported (*51*).

Treating one equivalent of $Co_2(CO)_8$ with one equivalent of $\mathbf{L^3}$ leads to formation of **14**, which cocrystallized in two different forms in the same unit cell. The two structural isomers differ in the number of bridging carbonyls and Co–Co distance (2.594(1) versus 2.703(1) Å). NMR analysis of **14** reveals a single species in solution, suggesting a preference for one isomer over the other or a rapid conversion between the two isomers. Treating $Co_2(CO)_8$ with two equivalents of $\mathbf{L^3}$, in hopes of splitting the Co–Co bond, leads to the formation of **15**. In contrast to the other cobalt complexes synthesized thus far, **15** is paramagnetic, exhibiting broad proton signals beyond the 20

ppm range. The structure of **15** is similar to previously synthesized complexes by Weighardt and coworkers, where terpyridine heterolytically cleaved the Co–Co bond to form a cationic, NNN-ligated species with a tetracarbonyl cobaltate counterion (*52*). Thus, it was concluded that the NNN-pincer chelate is capable of (heterolytically) splitting $Co_2(CO)_8$ and that the tetranuclear complexes observed is a result of the relatively long distance between the NNN-chelates, combined with the rigidity and bulk around them. Endeavors were made to cleave the Co–Co bonds in **13** and **14**, with the most successful substrate being acetonitrile. Addition of acetonitrile led to the synthesis of **16** and a spectroscopically similar **17**, where the NNN-coordinated cobalts are cationic and pentacoordinate, with two carbonyl ligands along with a tetracarbonyl cobaltate counterion (Scheme 5).

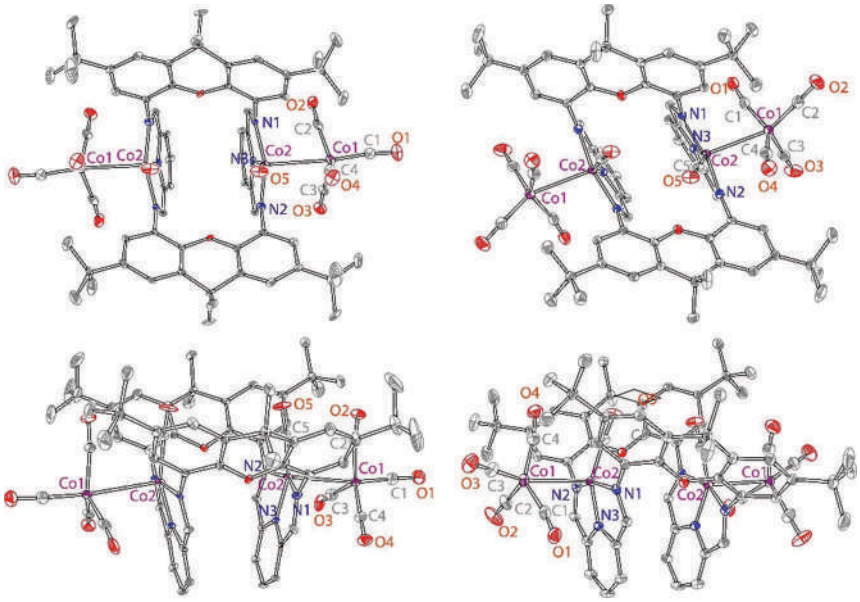

*Figure 4. X-ray crystal structures of **13′** (left – top and bottom) and **13** (right – top and bottom), 50% probability ellipsoids. H-atoms and cocrystallized solvents are omitted for clarity. Reproduced with permission from ref* (*36*). *Copyright 2018 The Royal Society of Chemistry.*

DFT analysis at the B3LYP/6-31G(d) level of theory attempted to explain the electronic nature of the cobalt complexes, as well as elucidate the presence of a Co–Co bond in the different structural isomers of **13** and **14**. Compounds **16** and **17** were best described as low-spin Co^{II} ions antiferromagnetically coupled to an anionic bis(imino)pyridine chelate radical; structure **15** was best described as a high-spin Co^{II} center; and compounds **13** and **14** were best described as Co^{I} ions bound to anionic ligands and external Co^0 moieties. Bridging and unbridging $Co_2(CO)_8$ were studied extensively to determine the presence of Co–Co bonding in the different isomers of **13** and **14**. A source functional analysis of the bond critical points most likely suggested that a Co–Co bond exists in **13**, but not in **14**.

Finally, catalytic studies for cyclotrimerization of ethyl propiolate were conducted for **13**–**17** and compared to $Co_2(CO)_8$, a known alkyne cyclotrimerization catalyst. Reactions were carried out at three different conditions: 40 °C in CD_2Cl_2, 80 °C in C_7D_8, and 70 °C in CD_3CN. Complex **15** demonstrated low reactivity, regardless of reaction conditions. Complexes **13**, **14**, **16**, and **17**

displayed similar reactivity at all reaction conditions, with optimal conditions being 80 °C in C_7D_8. Regardless of the reaction conditions used, $Co_2(CO)_8$ exceeded in efficiency. This lack of reactivity was attributed to increased steric bulk around the metal centers, as well as a lack of available positions for substrate binding. The Groysman group are currently focusing on utilizing these cobalt systems in other catalytic capacities.

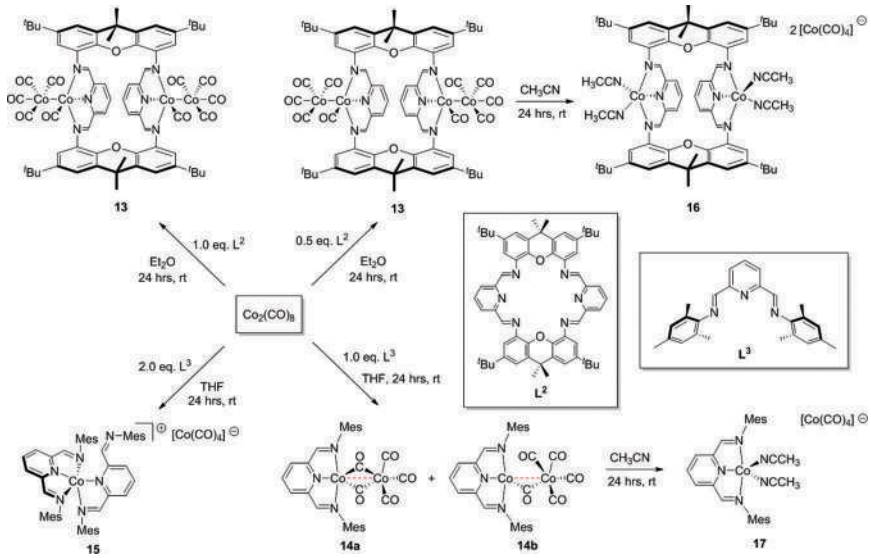

Scheme 5. Reactivity of $\mathbf{L^2}$ *and* $\mathbf{L^3}$ *with* $Co_2(CO)_8$. *Reproduced with permission from ref* (36). *Copyright 2018 The Royal Society of Chemistry.*

Synthesis of Bimetallic Zinc Complexes for Lactide Polymerization

Changing directions, Groysman and coworkers turned to investigate bimetallic cooperativity in lactide polymerization by synthesizing a xanthene-based dizinc complex (37). Since the neutral bis(iminopyridine) chelating units discussed thus far would be ill-suited for the relatively hard dicationic Zn^{II}, they decided to replace the neutral iminopyridine chelating units with monoanionic iminophenolate chelating units (Scheme 6).

Bis(iminophenolate) ligand $\mathbf{L^4}$ produced $\mathbf{L^{4\text{-}syn}}$ and $\mathbf{L^{4\text{-}anti}}$ crystal structures from an analytically and NMR-pure sample of $\mathbf{L^4}$ even though NMR demonstrated a single species in solution, featuring C_{2v} symmetry, with a single peak for both xanthene methyl groups and a single peak for both xanthene *tert*-butyl groups. In $\mathbf{L^{4\text{-}syn}}$, the phenolates are in *syn*-parallel arrangement and the linker appears to be perfectly flat, whereas in the $\mathbf{L^{4\text{-}anti}}$ the phenolates are in the antiparallel arrangement and the linker is slightly puckered, demonstrating the flexible nature of the xanthene linker.

Coordination chemistry of $\mathbf{L^4}$ was first investigated with zinc precursors featuring two bulky alkoxides, $Zn(Cl)(\mu^2\text{–}OR)_2Li(THF)$ (**18**) (OR = di-*tert*-butyl-phenylmethoxide), which formed a mononuclear complex $Zn(L^4)$ (**19**) that was isolated as an H-bond adduct with HOR, $Zn(L^4)\bullet HOR$. The basicity of the zinc-alkoxide precursor or steric bulk of the Zn–OR fragment may have led to the inability of $\mathbf{L^4}$ to function as a dinucleating ligand in this case.

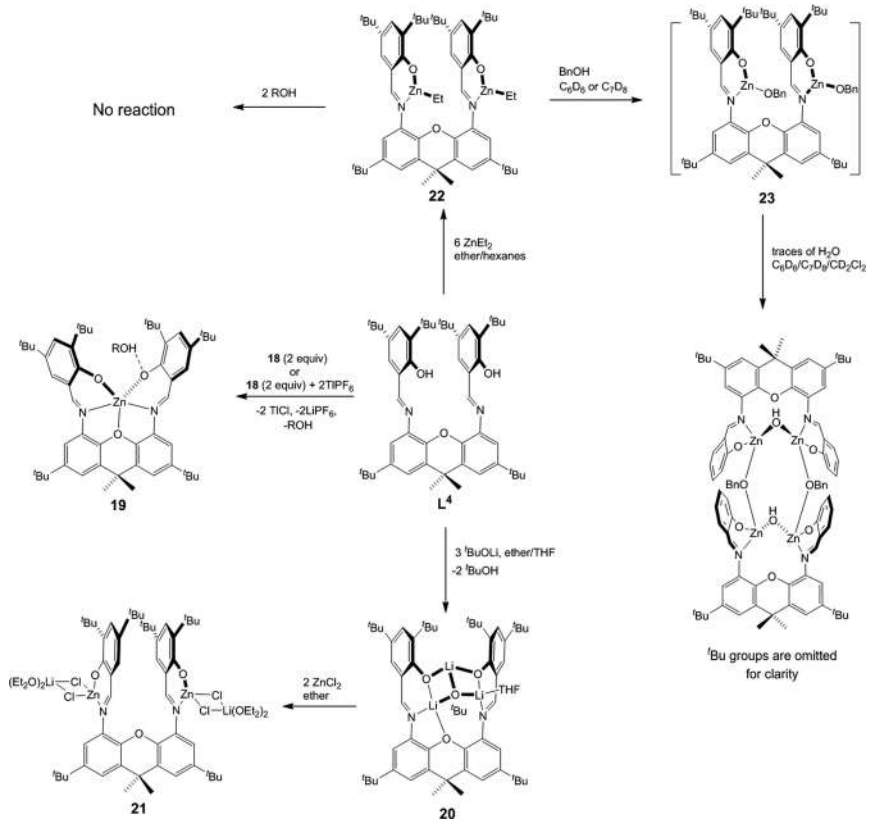

Scheme 6. Coordination chemistry of ***L*****⁴** *with zinc. Complex in square brackets* ***(23)*** *was not characterized by X-ray crystallography, and its structure is proposed based on NMR spectroscopy. Reproduced with permission from ref* (37). *Copyright 2017 The Royal Society of Chemistry.*

The reaction of the lithium salt of **L⁴** (**20**) with zinc chloride led to the formation of the corresponding dinuclear complex $Zn_2(L)(\mu^2\text{–}Cl)_4Li_2(OEt_2)_2$ (**21**) with antiparallel geometry featuring Zn–Zn distance of 6.7 Å. This unfavorable antiparallel arrangement is most likely the result of the steric pressure around each zinc center, due to the intercalated lithium ions. All attempts to remove LiCl to release steric pressure and enable *syn*-geometry resulted in a complex mixture of products from which no zinc-containing products were isolated. In contrast, the protonolysis reaction of **L⁴** with excess diethylzinc led to the formation of the corresponding dinuclear complex $Zn_2(L^4)(Et)_2$ (**22**). NMR studies demonstrate that complex **22** is relatively unstable at low concentrations, decomposing into Zn(L) and $ZnEt_2$, and that this reaction is reversible via the addition of excess $ZnEt_2$.

X-ray structure of $Zn_2(L^4)(Et)_2$ (Figure 5) displays the *syn*-parallel disposition of the two zinc–ethyl units, with a Zn–Zn distance of 4.5 Å. The geometry around the zincs is trigonal planar, and the xanthene linker appears to be perfectly flat. $Zn_2(L^4)(Et_2)$ constitutes a rare structure of an iminophenolate-bound zinc–ethyl in which the zinc center is three-coordinate. One noteworthy feature of this structure is relatively short distance between Zn2 and C1 (methylene bound to Zn_2), 3.46 Å, due to the *syn*-parallel geometry. This relatively short distance may be responsible for the

observed dinuclear–mononuclear equilibrium $Zn_2(L^4)(Et)_2 \rightleftharpoons Zn(L^4) + ZnEt_2$. Zn2–C1 proximity may facilitate Zn–C bond formation, which is achieved by a minimal rotation of one chelate toward the opposite (other) chelate, demonstrating cooperativity between the two units.

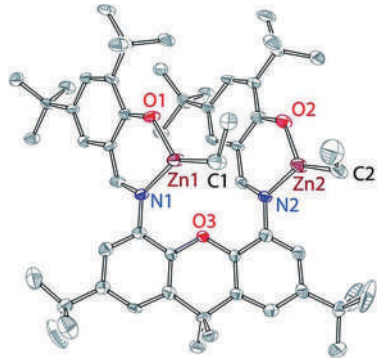

Figure 5. X-ray structure (50% ellipsoids) of **22**. *H-atoms, cocrystallized ether solvent, and an alternative orientation of one of the ethyl groups were omitted for clarity. Reproduced with permission from ref* (*37*). *Copyright 2017 The Royal Society of Chemistry.*

Since previous attempts to obtain $Zn_2(L^4)(OR)_2$ (where OR is a bulky alkoxide OC^tBu_2Ph) were unsuccessful, likely due to the steric bulk of the alkoxide, synthesis of a dinuclear zinc species with benzyloxide was pursued. Treatment of $Zn_2(L^4)(Et)_2$ with benzyl alcohol (BnOH) in deuterated benzene, toluene, or dichloromethane resulted in the formation of $Zn_2(L^4)(OBn)_2$ (**23**).

The synthesis of a mononuclear analogue of $Zn_2(L^4)(Et)_2$ was also attempted. Interestingly, no mononuclear analogue of $Zn_2(L^4)(Et)_2$ could be isolated, since the protonolysis reaction of the mononucleating iminophenol ligand (**L**^{5}) with diethylzinc led to the formation of a bis(homoleptic) complex $Zn(L^5)_2$ (**24**). Since a mononuclear analogue could not be obtained, a direct assessment of the cooperative reactivity in catalysis was not possible. It is noted that the dinucleating ligand enables "cooperative synthesis" of two nearby zinc–iminophenolate–ethyl sites, possibly with the aid of sterics when a mononuclear analogue did not form.

$Zn_2(L^4)(OBn)_2$ served as an efficient catalyst in ring-opening polymerization of *rac*-lactide to afford heterotactically inclined PLA (*37*). Room temperature polymerization was carried out in dichloromethane, which led to the formation of polymers of relatively narrow molecular weight distribution, indicative of well-controlled polymerization under these conditions. Polymerization experiments in toluene, carried out at 70 °C, demonstrated higher activity but led to higher polydispersity index values and diminished heterotacticity.

Synthesis and Reactivity of a Hetero-Bimetallic Molybdenum–Copper Complex To Model Mo–Cu CODH

Groysman and coworkers then embarked on synthesizing a hetero-dinucleating ligand, **L**^{6}, toward replicating the hetero-bimetallic active site found in Mo–Cu CODH. The goal of this project was to understand the origins of hetero-bimetallic cooperativity exhibited by this enzyme (*38*). The hetero-bimetallic system was prepared to target the following features that appeared important for reactivity in the enzyme active site: (1) location of Cu^I near Mo^{VI}, (2) presence of nucleophilic

Mo^{VI}–oxo, and (3) coordinative unsaturation of Cu^{I} in order to bind substrate. The heterodinucleating ligand **L⁶** was designed to feature a hard potentially dianionic catechol for Mo^{VI} binding, with a soft iminopyridine chelate for Cu^{I} binding brought together via the xanthene linker (Scheme 7).

To evaluate the selectivity of the **L⁶** chelates for the designated metals, **L⁶** was first treated with Cu^{I} precursors, $[Cu^{I}(NCMe)_4](PF_6)$ and $[Cu^{I}(NCMe)_4][B(C_6F_5)_4]$, which formed $[Cu^{I}(L^6)](X)$ complexes [X = PF_6 or $B(C_6F_5)_4$] (**25**). X-ray structure of **25** revealed a tridentate coordination of **L⁶** to Cu^{I} via the iminopyridine nitrogen and the secondary (benzylic) nitrogen on the adjacent chelating arm, indicating that Cu^{I} not only demonstrated the anticipated site-selective incorporation to the iminopyridine chelate in **L⁶**, but it also coordinated to the secondary amine to rigidify the overall structure and positions of the catechol unit above copper–iminopyridine. The Cu^{I} in the enzyme active site is coordinatively unsaturated to bind the substrate (CO). Likewise, the Cu^{I} center in **25** is three-coordinate, and thus should also be capable of binding an additional ligand. To validate copper unsaturation in **25**, the compound was treated with a CO analogue, isocyanide CN(2,6-Me_2Ph), which led to the formation of an isocyanide complex $\{Cu^{I}[L^6][CN(2,6\text{-}Me_2Ph)]\}(X)$ (**26**). The coordination of isocyanide to Cu^{I} in **26** was established by NMR and IR spectroscopy.

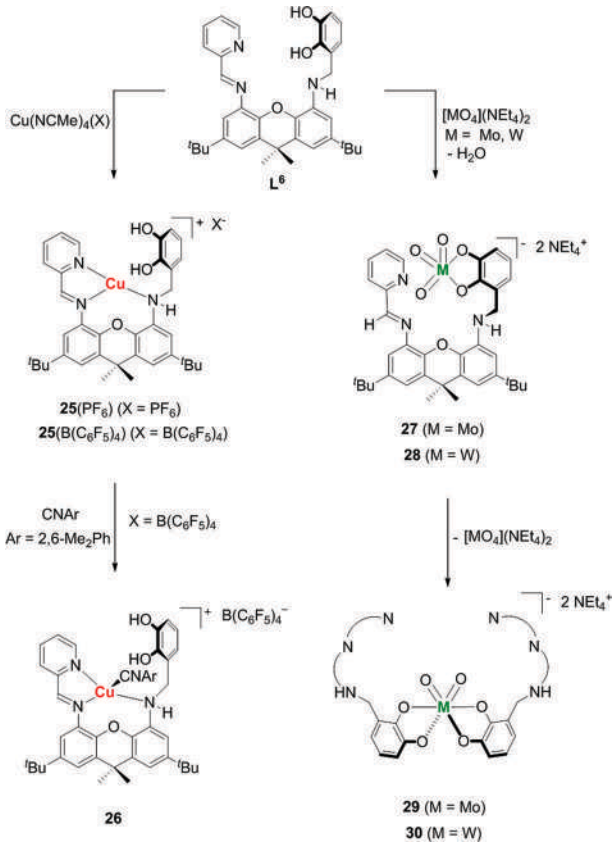

Scheme 7. Reactions of ***L⁶*** *with* Cu^{I} *and* Mo^{VI}/W^{VI} *precursors. Reproduced with permission from ref* (38). *Copyright 2018 The Royal Society of Chemistry.*

Next, the reactivity of **L⁶** with Mo^{VI} and W^{VI} was investigated. Treatment of **L⁶** with $[M^{VI}O_4](NEt_4)_2$ (M = Mo, W) led to the formation of $[M^{VI}(O_3)L^6](NEt_4)_2$ (**27** and **28**). While both $[Cu^{I}(L^6)]^+$ and $[M^{VI}O_3(L^6)]^{2-}$ complexes are stable indefinitely in the solid state, **27** and **28** disproportionated in solution to give $[M^{VI}O_2(L^6)_2](NEt_4)_2$ (**29** and **30**) complexes, with $[M^{VI}O_4]^{2-}$ as the by-product. This reaction is relatively slow in solvents of low polarity (THF) but leads to a significantly faster transformation in more polar solvents (acetonitrile). The X-ray structure of **29** confirmed the expected catecholate coordination to the metal, while the second coordination site, containing three nitrogen, is not bound to the metal. The geometry around the W^{VI} center in **29** is distorted octahedral and features crystallographic C_2 symmetry, giving rise to one distinct W–oxo bond distance and two different W–catecholate bond distances.

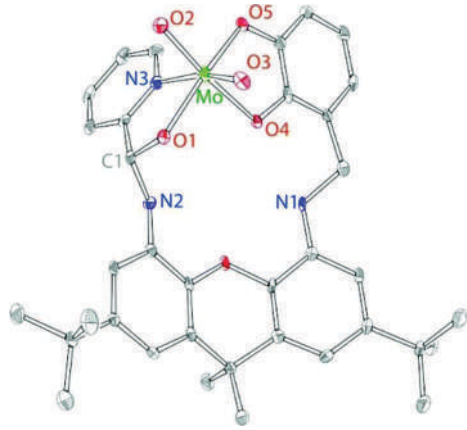

Figure 6. X-ray structure of **32***, 40% probability ellipsoids. NEt_4 was omitted for clarity. Reproduced with permission from ref* (*38*)*. Copyright 2018 The Royal Society of Chemistry.*

After demonstrating the selective coordination chemistry of **L⁶**, the synthesis of hetero-bimetallic complexes were undertaken. Combining the two metals, regardless of sequence, resulted in formation of a highly reactive $[Mo^{VI}O_3Cu^{I}(L^6)](NEt_4)_2$ (**31**), with broad, indecipherable NMR resonances, likely due to the dynamic nature of the species formed. Careful analysis of the reaction mixture by ^1H NMR spectroscopy over several days, shed light on the fate of the transformation. The aromatic region of the reaction mixture revealed the presence of pyridine-2-carboxaldehyde, a compound with broader resonances, and another species that, through recrystallization in CD_2Cl_2 at −30 °C, was elucidated as $[Mo(L^{6\prime})O_2](NEt_4)$ (**32**) (Figure 6). In this structure, the **L⁶** ligand is modified (**L⁶′**), containing a new C–O bond in place of the imine functionality. Further examination of the structure revealed the absence of Cu, while the Mo center appears hexacoordinate. A hypothesized species (**33**) was proposed to explain the broad NMR signals based upon the aforementioned information.

The different reaction products are in a temperature-dependent equilibrium with a mixture of products at room temperature and **32** being the major product at −30 °C. This information, supported by DFT calculations, led Groysman and coworkers to propose a reaction mechanism. Based on the reactions of **L⁶** with Cu^{I} and Mo^{VI}/W^{VI}, the initial formation of a Mo/Cu hetero-dinuclear complex **31** was postulated, accompanied by the formation of water (Scheme 8). The

combination of the two metals in close proximity in this hetero-dinuclear complex activates oxidation reactivity, in which a nucleophilic Mo^{VI}–oxo (part of the $Mo^{VI}O_3$ unit) attacks the electrophilic, nearby positioned Cu^{I}-bound imine that is activated by coordination to Cu^{I}. This results in the formation of a Mo^{VI}–alkoxo and anionic amido, which is protonated by water. The Cu^{I} is then lost, possibly due to amido protonation or the induced flexibility of the NNN-chelate. The immediate hydroxylation product, **32**, exists in the temperature-dependent equilibrium with **33** and pyridine-2-carboxaldehyde.

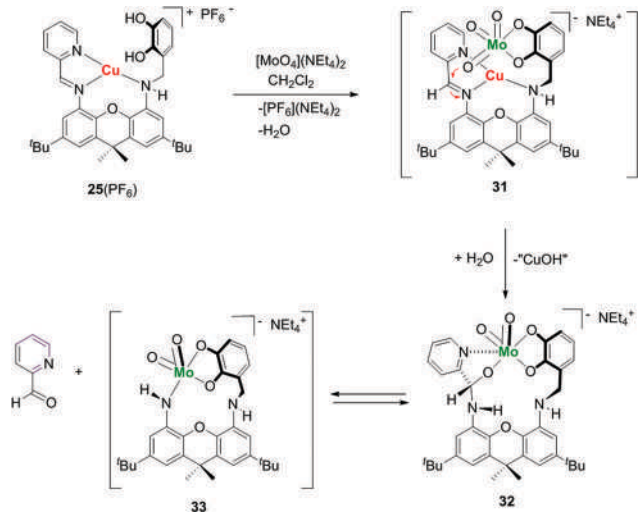

Scheme 8. Possible mechanism for the formation of **32**, *pyridine-2-carboxaldehyde and* **33** *via postulated bimetallic intermediate* **31**. *Reproduced with permission from ref* (38). *Copyright 2018 The Royal Society of Chemistry.*

To evaluate whether there is any evidence of a cooperative bimetallic effect in the aforementioned system, a CD_2Cl_2 solution of **27** was followed by ^{1}H NMR spectroscopy for several days. Slow decomposition of **27** into **29** was observed. In the absence of Cu^{I}, only traces of hydroxylation products are observed in the ^{1}H NMR spectrum.

Summary

The xanthene linker has proven successful in initiating metal–metal cooperativity across a wide variety of dinucleating ligands. Specifically targeting the xanthene-4,5-diamino linker, the Groysman lab has explored the applications of the xanthene group in homo-bimetallic and hetero-bimetallic catalysis and small molecule activation. Using a redox-active bis(iminopyridine) homo-dinucleating system, a dicopper system was prepared, and its reactivity in small molecule activation was investigated. Further expanding on the redox-active bis(iminopyridine) ligand design, they synthesized a dinickel system that displayed cooperative reactivity in catalytic alkyne trimerization. Coordination chemistry and catalytic reactivity of a related homo-dinucleating macrocyclic bis(diiminopyridine) ligand with nickel and cobalt were also investigated. Replacing neutral iminopyridine chelates with monoanionic iminophenolates led to the formation of dianionic homo-dinucleating bis(iminophenolate). Its reactivity in the formation of dizinc complexes and their activity in lactide polymerization were studied. A hetero-dinucleating ligand combining soft

iminopyridine with a hard catecholate site was also synthesized, and its Mo/Cu complexes were investigated as models for the active site of Mo–Cu CODH. Future work from this group will continue to focus on exploiting the benefits of the xanthene unit in bimetallic cooperativity.

References

1. Chang, C. J.; Deng, Y.; Shi, C.; Chang, C. K.; Anson, F. C.; Nocera, D. G. *Chem. Commun.* **2000**, 1355–1356.
2. Chang, C. J.; Loh, Z.-H.; Shi, C.; Anson, F. C.; Nocera, D. G. *J. Am. Chem. Soc.* **2004**, *126*, 10013–10020.
3. Pistorio, B. J.; Chang, C. J.; Nocera, D. G. *J. Am. Chem. Soc.* **2002**, *124*, 7884–7885.
4. Chng, L. L.; Chang, C. J.; Nocera, D. G. *J. Org. Chem.* **2003**, *68*, 4075–4078.
5. Hodgkiss, J. M.; Chang, C. J.; Pistorio, B. J.; Nocera, D. G. *Inorg. Chem.* **2003**, *42*, 8270–8277.
6. Fukuzumi, S.; Okamoto, K.; Gros, C. P.; Guilard, R. *J. Am. Chem. Soc.* **2004**, *126*, 10441–10449.
7. Fukuzumi, S.; Okamoto, K.; Tokuda, Y.; Gros, C. P.; Guilard, R. *J. Am. Chem. Soc.* **2004**, *126*, 17059–17066.
8. Kadish, K. M.; Frémond, L.; Ou, Z.; Shao, J.; Shi, C.; Anson, F. C.; Burdet, F.; Gros, C. P.; Barbe, J.-M.; Guilard, R. *J. Am. Chem. Soc.* **2005**, *127*, 5625–5631.
9. Kadish, K. M.; Frémond, L.; Shen, J.; Chen, P.; Ohkubo, K.; Fukuzumi, S.; Ojaimi, M. E.; Gros, C. P.; Barbe, J.-M.; Guilard, R. *Inorg. Chem.* **2009**, *48*, 2571–2582.
10. Gao, Y.; Liu, J.; Wang, M.; Na, Y.; Akermark, B.; Sun, L. *Tetrahedron* **2007**, *63*, 1967–1994.
11. Pilz, M. F.; Limberg, C.; Lazarov, B. B.; Hultzsch, K. C.; Ziemer, B. *Organometallics* **2007**, *26*, 3668–3676.
12. Haack, P.; Limberg, C.; Ray, K.; Braun, B.; Kuhlmann, U.; Hildebrandt, P.; Herwig, C. *Inorg. Chem.* **2011**, *50*, 2133–2142.
13. Haack, P.; Limberg, C.; Tietz, T.; Metzinger, R. *Chem. Commun.* **2011**, *47*, 6374–6376.
14. Han, S.; Yao, E.; Qin, W.; Zhang, S.; Ma, Y. *Macromolecules* **2012**, *45*, 4054–4059.
15. Chen, Z.; Yao, E.; Wang, J.; Gong, X.; Ma, Y. *Macromolecules* **2016**, *49*, 8848–8854.
16. Chen, Z.; Zhao, X.; Gong, X.; Xu, D.; Ma, Y. *Macromolecules* **2017**, *50*, 6561–6568.
17. Takeuchi, D.; Chiba, Y.; Takano, S.; Osakada, K. *Angew. Chem., Int. Ed.* **2013**, *52*, 12536–12540.
18. Hirotsu, M.; Ohno, N.; Nakajima, T.; Ueno, K. *Chem. Lett.* **2005**, *34*, 848–849.
19. Hirotsu, M.; Ohno, N.; Nakajima, T.; Kushibe, C.; Ueno, K.; Kinoshita, I. *Dalton Trans.* **2010**, *39*, 139–148.
20. Serrano-Becerra, J. M.; Maier, A. F. G.; González-Gallardo, S.; Moos, E.; Kaub, C.; Gaffga, M.; Niedner-Schatteburg, G.; Roesky, P. W.; Breher, F.; Paradies, J. *Eur. J. Org. Chem.* **2014**, 4515–4522.
21. Liu, P.; Sun, J. *Org. Lett.* **2017**, *19*, 3482–3485.
22. Faßbach, T. A.; Sommer, F. O.; Vorholt, A. J. *Adv. Synth. Catal.* **2018**, *360*, 1473–1482.
23. Takano, S.; Takeuchi, D.; Osakada, K.; Akamatsu, N.; Shishido, A. *Angew. Chem., Int. Ed.* **2014**, *53*, 9246–9250.
24. Takano, S.; Takeuchi, D.; Osakada, K. *Chem. Eur. J.* **2015**, *21*, 16209–16218.

25. Wang, R.; Sui, X.; Pang, W.; Chen, C. *ChemCatChem* **2016**, *8*, 434–440.
26. Hanawa, H.; Kii, S.; Maruoka, K. *Adv. Synth. Catal.* **2001**, *343*, 57–60.
27. Wasylenko, D. J.; Ganesamoorthy, C.; Koivisto, B. D.; Berlinguette, C. P. *Eur. J. Inorg. Chem.* **2010**, 3135–3142.
28. Timerbulatova, M. G.; Gatus, M. R. D.; Vuong, K. Q.; Bhadbhade, M.; Algarra, A. G.; Macgregor, S. A.; Messerle, B. A. *Organometallics* **2013**, *32*, 5071–5081.
29. Takano, S.; Takeuchi, Y.; Takeuchi, D.; Osakada, K. *Chem. Lett.* **2014**, *43*, 465–467.
30. Liu, Z.; Gao, Y.; Zhang, M.; Liu, J. *Inorg. Chem. Commun.* **2015**, *55*, 56–59.
31. Rong, C.; Wang, F.; Li, W.; Chen, M. *Organometallics* **2017**, *36*, 4458–4464.
32. Gatus, M. R. D.; Bhadbhade, M.; Messerle, B. A. *Dalton Trans.* **2017**, *46*, 14406–14419.
33. Zhang, L.; Chen, X.; Xiao, X.; Luo, D.; Zheng, Y.; Li, T.; Li, X.; Zhang, A.; Xie, G. *J. Organomet. Chem.* **2018**, *856*, 50–55.
34. Bheemaraju, A.; Beattie, J. W.; Rochford, J.; Groysman, S. *Eur. J. Inorg. Chem.* **2014**, *34*, 5865–5873.
35. Hollingsworth, R. L.; Bheemaraju, A.; Lenca, N.; Lord, R. L.; Groysman, S. *Dalton Trans.* **2017**, *46*, 5605–5616.
36. Hollingsworth, R. L.; Beattie, J. W.; Grass, A.; Groysman, S.; Martin, P.; Lord, R. L. *Dalton Trans.* **2018**, *47*, 15353–15363.
37. Hollingsworth, T. S.; Hollingsworth, R. L.; Rosen, T.; Groysman, S. *RSC Adv.* **2017**, *7*, 41819–41829.
38. Hollingsworth, T. S.; Hollingsworth, R. L.; Lord, R. L.; Groysman, S. *Dalton Trans.* **2018**, *47*, 10017–10024.
39. Bheemaraju, A.; Lord, R. L.; Müller, P.; Groysman, S. *Organometallics* **2012**, *31*, 2120–2123.
40. Bheemaraju, A.; Beattie, J. W.; Lord, R. L.; Martin, P. D.; Groysman, S. *Chem. Commun.* **2012**, *48*, 9595–9597.
41. Bheemaraju, A.; Beattie, J. W.; Tabasan, E. G.; Martin, P. D.; Lord, R. L.; Groysman, S. *Organometallics* **2013**, *32*, 2952–2962.
42. Beattie, J. W.; White, D. S.; Bheemaraju, A.; Martin, P. D.; Groysman, S. *Dalton Trans.* **2014**, *49*, 7979–7986.
43. Beattie, J. W.; SantaLucia, D. J.; White, D. W.; Groysman, S. *Inorg. Chim. Acta* **2017**, *460*, 8–16.
44. Nagamani, A. S.; Norikane, Y.; Tamaoki, N. *J. Org. Chem.* **2005**, *70*, 9304–9313.
45. Davenport, T. C.; Tilley, T. D. *Angew. Chem., Int. Ed.* **2011**, *50*, 12205–12208.
46. Kuganathan, N.; Green, J. C. *Chem. Commun.* **2008**, 2432–2434.
47. Hermann, H. L.; Boche, G.; Schwerdtfeger, P. *Chem. Eur. J.* **2001**, *7*, 533–539.
48. Mehrotra, P. K.; Hoffmann, R. *Inorg. Chem.* **1978**, *17*, 2187–2189.
49. Pal, S.; Uyeda, C. *J. Am. Chem. Soc.* **2015**, *137*, 8042–8045.
50. Day, V. W.; Abdel-Meguid, S. S.; Dabestanti, S.; Thomas, M. G.; Pretzer, W. R.; Muetterties, E. L. *J. Am. Chem. Soc.* **1976**, *98*, 8289–8291.
51. Reed, B. R.; Yousif, M.; Lord, R. L.; McKinnon, M.; Rochford, J.; Groysman, S. *Organometallics* **2017**, *36*, 582–593.
52. England, J.; Bill, E.; Weyhermüller, T.; Neese, F.; Atanasov, M.; Wieghardt, K. *Inorg. Chem.* **2015**, *54*, 12002–12018.

Chapter 2

Gold Catalysis: Fundamentals and Recent Developments

Randall T. Mertens and Samuel G. Awuah*

University of Kentucky, 505 Rose Street, Lexington, Kentucky 40506, United States

***E-mail: awuah@uky.edu**

We present an overview of fundamental organometallic transformations in relation to gold chemistry. The focus of this chapter is to provide comprehensive depth of oxidative addition, transmetalation, reductive elimination, β-hydride elimination, and migratory insertion reactions for the benefit of gold catalysis. Recent advances of these reactions enables intelligent catalyst design and pushes the frontier of homogenous gold catalysis.

Introduction

Gold (Au) has captured the imagination of humanity for years and still does, due to it inertness and unparalleled use in jewelry, currency, decorations, electronics, and even medicine. Over the past two decades tremendous progress has been made to advance Au-catalyzed transformations. However, metallic Au possess inherent chemical and physical properties that limit utility in catalysis including: (1) large relativistic effects, (2) increased ionization energies, and (3) high redox potential. These factors contribute to the sluggish participation of Au in $M^{n/n+2}$ redox processes unlike its Pd counterpart. In an attempt to circumvent the problems outlined to set the stage for practically relevant Au catalysis, several oxidative and redox neutral catalytic reactions have been developed. In addition, intelligently designed catalysts with unique reactivities and activation paradigms have been employed. A plethora of outstanding reviews, chapters, perspectives, and monographs provide deep insights into various aspects of homogenous Au catalysis including activation of unsaturated C–C bonds, ligand effects, synthetic transformation of hydroamination of C–C multiple bonds, propargylic esters, hydroarylation of alkynes, and cross-coupling, to mention a few (*1*–*8*). Within the context of this chapter, our goal is to detail the fundamental steps involved in homogenous Au catalysis, namely: ligand activation/oxidative addition, transmetalation, reductive elimination, and β-hydride elimination. We hope that this knowledge will catapult Au catalyst design in this ever-expanding field.

Structure, Reactivity, and Chemistry of Gold Complexes

The reactivity of Au can be derived partially from the uniqueness of the atoms' properties. The relativistic effects of Au provide the element with characteristics such as higher ionization energies,

electron affinities (discussed later in the chapter), and a very high redox potential (i.e., $Au^{+3} + 2e^- \rightarrow Au^{+1}$ E^o=1.41 V and $Au^{+1} + e^- \rightarrow Au_{(s)}$ E^o=1.69 V) (*9*). All of these properties make the reactivity of Au exceptional. The relativistic effect also contributes to the Lewis acidity of the metal. The relativistic effects lead to contraction of the s- and p-orbitals, which affects the expansion of the outer d- and f-orbitals. This allows for Au coordination to donating ligands such as phosphines or carbenes (*10*). In the case of Au^I complexes, the contracted empty 6s-orbital allows for significant overlap with sigma-donor ligands. Initial design of Au catalysts relied heavily on the classical two coordinate Au^I system (Figure 1) (*11*), which has distinctly shown Lewis acid character by the activation of saturated alkynes/alkenes (*12*). Further exploration has revealed that four-coordinate Au^{III} complexes (Figure 1) (*13*) are also capable of activating unsaturated species evidently displayed in seminal work in the intra-molecular hydroamination of alkynes by Utimoto (*14*, *15*).

In addition to these common coordination or organometallic compounds existing in Au^I and Au^{III} oxidation states, Au has the capability of adopting rare oxidation states such as Au^{II} and Au^V (Figure 1) (*16*, *17*). Au^{II} intermediates have been implicated in homogenous catalysis and biology; however, until recent discoveries, their geometric and electronic structures went unexplored (*18–20*). They are still considered to be less common than the conventional Au^I or Au^{III} derivative (*21*). Au^{II} species are d^9 in character and possess an unpaired electron in an orbital; this contributes to its lability. A few mononuclear Au^{II} complexes have been isolated (*22*, *23*). Other Au^{II} species exist as dinuclear complexes with a Au–Au bond (*23–27*). Still, the lack of compounds did not deter researchers from exploring oxidative addition to Au^{II} complexes, though minimal success has been achieved (*28*). In one specific case, oxidative addition to Au^I produced Au^{II} compounds (*29*). Whereas this report is unique, its application to Au catalysis is limited by the instability of Au^{II} complexes. Despite reports of Au^V compounds (*17*, *30*), no practical use in catalysis exists since their initial discovery. The extremely high oxidation potential of these complexes makes it impractical for catalysis.

In the 1970s early insights into Au^I/Au^{III} alkyl aurates revealed remarkable thermal stability, a feature that remains to be desired in modern catalysis (*31*, *32*). A pentanuclear Au^I mesityl complex has been reported (*33*) and, although this compound has not seen practical utility, insight into stabilizing factors for the Au^I by the mesityl ligand has been obtained. This is important as ligands with similar frameworks have been used in stabilizing Au^I/Au^{III} complexes. In the era of a gold renaissance, this chapter will fill knowledge gaps and drive further research on structure and reactivity of Au complexes in Au-catalyzed organic synthesis.

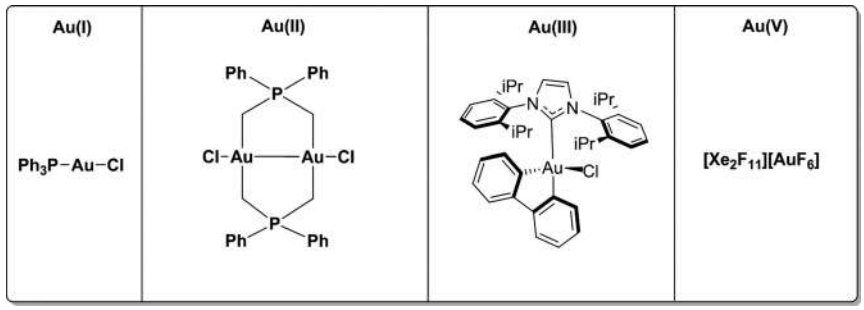

Figure 1. Representative examples of different oxidation states of gold complexes.

Prior insights of the potential for Au catalysis was offered by Kharasch and Isbell in a preliminary communication that outlined the direct introduction of Au into aromatic nucleus leading to arene chlorination using Au salts (*34*, *35*). Early work on Au catalysis featured tetrachloroauric acid ($HAuCl_4$) in the addition of water to an alkyne (Figure 2) (*36*). This reaction was one of the first of its kind to illustrate the catalytic ability of gold and proved superior to mercury catalysts.

Pioneering work by Teles et al. on formal Au-catalyzed acetal formation demonstrated the activation of alkynes for addition of alcohols. Complex stability informed by ligand tuning has the potential to reshape Au catalysis.

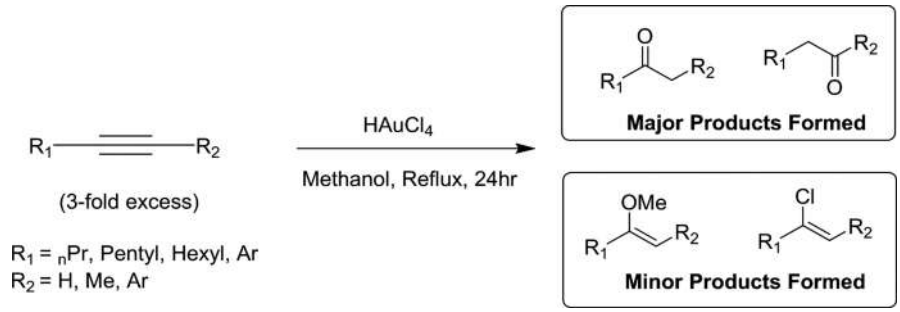

Figure 2. Au-Catalyzed addition of water using a simple, commercially available Au^{III} reagent as catalyst. Disubstituted ketones were obtained as the major products with vinyl chlorides and vinyl ethers being obtained for yields less than 5% (36).

Further insight into the electronic properties of Au elucidate potential problems of gold as a catalyst. When comparing ionization energies of group 11 transition metals, Au has a significantly higher ionization energy than Cu or Ag (Table 1). Higher ionization energies potentially limit key putative steps including oxidative addition in the gold redox cycle. Similarly, the high electron affinity (Table 1) of Au presents the challenge of rapid reduction of the metal complex prior to its catalytic function. These properties limit the utility of Au as a catalyst, pushing researchers to design Au complexes with unique ligand frameworks to circumvent challenges associated with gold in homogeneous catalysis.

Table 1. Reported Experimental Values for the First Two Ionization Energies and Electron Affinities

	Cu	*Ag*	*Au*
Ionization Energies (eV)			
First	7.72638 (*37*)	7.57623 (*38*)	9.22553 (*40*)
Second	20.2924 (*37*)	21.47746 (*39*)	20.20 (*41*)
Electron Affinity (eV)	1.276± 0.010 (*42*)	1.303 ± 0.007 (*42*)	2.3086± 0.0007 (*42*)

Stability and Ligand Tuning

The effects of ligands on different categories of synthetic reactions were highlighted in a comprehensive review by Toste. The crucial role of ligands in impacting reaction yields, diastereoselective, enantioselectivity, regioselectivity, and chemoselectivity cannot be overemphasized (*43*). Our emphasis will be on concepts that affect complex stability.

As previously mentioned, the electron affinity of gold provides a unique ability for its coordination to strong donor ligands toward stabilization. Maintaining gold complex stability during the catalytic process is crucial for the success of any intended synthetic transformation. There are several factors that come into play when establishing what ligand framework to use in catalyst development. Characteristically, a major challenge associated with gold catalysts is premature deactivation owing to reduction (*44*). For a long time, gold was thought to be "catalytically dead" (*45*). Common Au salts and commercially available materials such as $HAuCl_4$, $NaAuCl_4$, and $AuCl_3$ showed promising catalytic ability but were rapidly reduced to elemental gold. Gold catalysis exploded with new innovations at the turn of the 21st century as new researchers claimed stakes in the "gold rush" (*46*). A review paper by Dyker in 2000 highlighted numerous developments by researchers whose contributions have been highlighted in this chapter (*47*). One of the featured works was Hashmi's development of Au^{III}-catalyzed functionalization of phenols (*48*, *49*). Once researchers became acquainted with Au as a potential catalyst, there was a massive surge toward catalyst development. A seemingly trivial yet important place to start is the hard-soft acid base theory (*50*–*52*). This concept as well as other organometallic strategies are well utilized approaches to building ligands that contribute to complex stability. Au^I is a large atom with loosely held electrons, making it polarizable and, as such, classified as a soft Lewis acid. As a result, gold preferentially coordinates strongly with softer Lewis bases and to some nitrogen-containing ligands. A majority of these Au^I complexes with nitrogen ligands exist in the form R_3PAuL with the phosphine ligand (e.g., phosphine ligands (PR_3) and sulfur-based ligands) stabilizing the Au^I complex (*53*). Notably, Au^I complexes bearing nitrogen-donor ligands are rare and tend to occur as imine-type ligands. However, Au^{III} is a relatively harder Lewis acid and has preference toward harder Lewis bases (i.e., nitrogen-containing ligands).

Development of stable gold complexes has been a challenge, but with the use of σ-donor ligands, the electrophilic gold center can be readily stabilized. As previously noted, work done by Teles et al. (*54*) addressed this concern. Their choice of catalyst was a Au^I complex bearing a coordinated phosphine ligand, PR_3 (Figure 3). The proposed catalytic cycle suggests electrophilic attack from the Au–metal center to the unsaturated species, resulting in a dative bond. Throughout the catalytic cycle, the donating ligand is seen present in each step, suggesting that the σ-donation from the phosphine creates a stabilized metal center for the duration of the catalytic cycle.

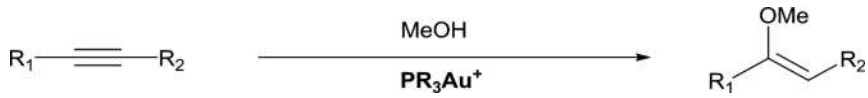

Figure 3. Synthetic scheme illustrating early alkyne hydrofunctionalization using a Au^I–phosphine catalyst (54).

Importantly, appropriate balance of stability and reactivity can affect the efficiency of the catalytic process. As shown in Table 2, different donor ligands used to stabilize the Au center can influence the turnover frequency (TOF) rates of the catalyst.

Table 2. Illustration of TOF's Dependence on Ligand Type

Ligand	$AsPh_3$	PPh_3	$P(4\text{-}F\text{-}C_6H_4)_3$	$P(MeO)_3$	$P(PhO)_3$
Structure	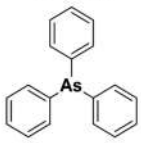	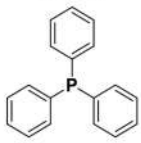	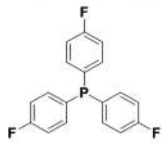	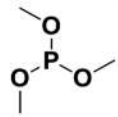	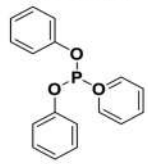
TOF* (h^{-1})	430	610	640	1200	1500

*TOF: A quantitative measurement of the activity catalyst as defined by the number of completed catalytic cycles per specified unit of time.

The importance of the donor ligand is very crucial to the lifetime of the catalyst. Electron-poor donors were seen to be twice as catalytically active; however, at the cost of the catalysts' lifetime. Conversely, electron-rich phosphine ligands, which provide electron density donated into Au's low-lying d-orbitals, stabilized the Au^{I} complex but were less active than other Au^{I} catalysts bearing electron-poor ligands. The ligand $L{=}P(PhO)_3$ was more than twice as active than PPh_3. However, their stability was compromised with a turnover number of 2500 cycles, whereas the ligand PPh_3 was still active after 5000 cycles (*54*). Even slight variance of the electronic properties of the donating ligand proved to be very significant in catalyst development. This work highlighted the impact of ligands on both the stability of Au complexes and their catalytic capability. Recent work by Didier Bourissou details the effect of ligands and geometry on reactivity, as seen in Figure 4 (*55*). The development of this elegant complex is grounded in the fundamental principles of stabilization via strong electron donors. Bidentate ligands stabilize metal centers better than typical monodentate ligands (*56*). Coupling this phenomenon with two heavily σ-donating phosphine ligands creates a metal center that is very electron-rich, allowing for easy stabilization. The importance of this is quite evident as it is one of the first works that shows successful oxidative addition from a Au^{I} to a Au^{III} complex, not a trivial feat over the past decade.

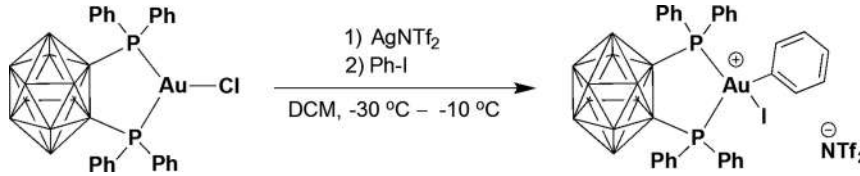

Figure 4. Elucidating the P–Au–P donor system (55). *Electron density from the carborane increases donation from the bidentate P–P ligand system, which results in a stable cationic gold center upon activation via chloride removal. The structure bearing the carborane moiety was originally designed by Jones and coworkers* (57). *Bourissou redesigned the title complex with a* NTf_2 *ligand rather than a Cl ligand* (55).

As described in the seminal work by Hammond and Xu (*58*, *59*), the effect of ligands and ligand design in homogenous Au catalysis can be unpredictable due to premature Au deactivation. This is evidenced in how σ-donating or π-acceptor ligands influence rate of reaction differently. Using the

model catalytic cycle that incorporates three stages: (1) nucleophilic attack and substrate activation, (2) reaction of gold-substrate complex with an electrophile (E^+) with concomitant protodeauration and cationic gold regeneration, and (3) decay of cationic gold, they showed how electronic and steric ligand modifications substantially impact the kinetics of each stage (*60*). This study sets the stage for detailed rational design, taking into account each stage of the catalytic cycle. Notwithstanding, a few examples by Toste in ring expansion of propargyl cyclopropanols (*61*) and hydroamination of allenes (*62*) point to a trend that implicates the effect of electron-rich and electron-deficient ligands on reaction rate (*63–66*).

Highly efficient catalysis of the addition of acids to alkynes was achieved by ligand design with a turnover number up to 99,000 by Zhang and coworkers (*67*). The design attached an amide group to the 3′-position of a 1,1′-biphenyl)-2-ylphosphine framework, allowing a ligand-directed antinucleophilic attack of alkynes (Table 3).

Table 3. Gold-Catalyzed Alkyne Hydration by Ligand-Directed Antinucleophilic Attack

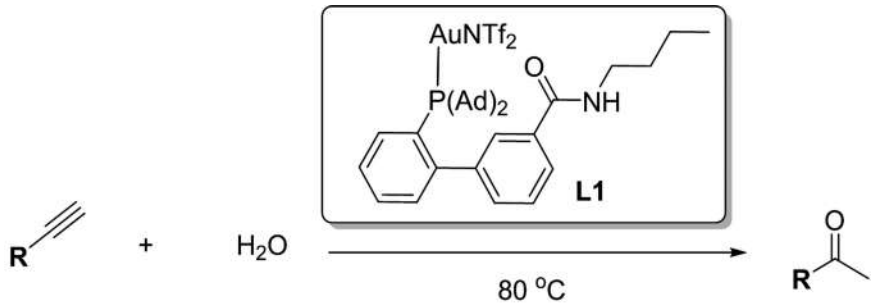

Catalyst	*Yield / Turn Over Number*	
	R = *n*-decyl, [Au] (500 ppm), Toluene (0.25 x *n* R mL), 5h	R = *n*-butyl, [Au] (500 ppm), Methanol (0.25 x *n* mL), 6h
JohnPhosAuNTf$_2$	8%/160	44%/4400
IPrAuNTf$_2$	9%/180	69%/6900
L1	38%/760	100%/10,000

Oxidative Addition

The research on catalysis involves considerable optimization of catalysts and their influence on the various steps of the catalytic cycle. Oxidative addition is a very crucial step, especially in cross-coupling reactions. Given the high ionization energy and redox potential of Au^{III}/Au^{I} cycle, a large energy barrier needs to be overcome in order to transform low-valent Au^{I} to high-valent Au^{III} (*68*). Recent literature shows progress in overcoming this barrier to unleash insightful reactivity useful for Au catalysis. One of the first reports of successful oxidative addition was reported in 1972 by Shiotani and Schmidbaur. They highlighted that it was feasible for Au to undergo such a transformation. Their work showed oxidative addition of methyl iodide to a Au^{I} alkyl complex: $(CH_3)Au(PPh_3)$ (*69*). In this same year, another group used the same Au^{I} alkyl complex for an initial mechanistic study, observing ethane produced from a reaction of the Au^{I} alkyl complex and methyl iodide through an alkyl Au^{III} intermediate (Figure 5) (*70*).

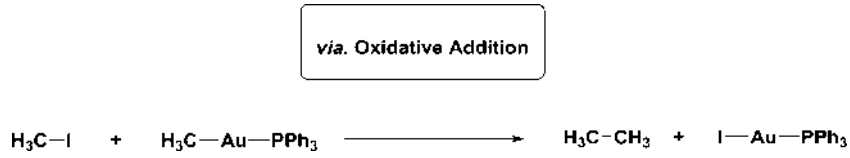

Figure 5. Work elucidating the formation of ethane through oxidative addition to a Au^{I} alkyl complex.

Further work in the 1970s carried out by Tamaki and Kochi as well as Johnson and Puddephatt published several works regarding the synthesis and isolation of Au^{III} alkyl complexes, R_3AuL. These complexes typically had a phosphine ligand (L), and were synthesized with varying routes by oxidative addition to a Au^{I} alkyl precursor (*71*–*75*). Their work offered insight into the mechanism, success, and stability of the oxidative addition process as well as the Au^{III} complexes. Later work tried to advance on this idea by oxidatively adding alkynyl halides to aurate complexes proved to be unsuccessful, yielding only Au^{I} products (*76*). Although previous work had established thermal stability of aurate complexes as well as successful oxidative addition of alkyl halides, a barrier still exists that must be better understood to advance the scope of oxidative addition reactions with Au^{I} complexes. Interestingly, recent developments in density functional theory calculations have been performed to better understand the oxidative addition process.

Investigations into claims that Au could replace palladium in the classical Sonogashira coupling (*77*) were disproved as computational studies revealed that bis-ligated Au^{I} compounds are unreactive toward methyl iodide (*78*), which is further supported by experimental evidence (*79*). Although the study appears disappointing toward the progress of Au catalysis in cross-coupling reactions, the insight was vital to the overall development of Au catalysis.

The majority of Au^{I} catalysts characteristically possess the formulae RAuX, where R can vary between monodentate ligands of all nature to bidentate ligands containing C, N, P, or S coordinating atoms and X is a halide. The use of these atoms enables higher stability because: (1) phosphorus is a softer atom based on hard-soft acid base theory and (2) phosphorus is a third-row element and is a strong σ-donor. Phosphines with generic formulae PR_3, unlike nitrogen, have the ability to coordinate transition metals. In fact, it is accomplished by donating electrons into the sigma antibonding orbitals of the metal with π-symmetry (*19*). Several reports reveal success with oxidative addition to Au^{I}–phosphine complexes (*10*, *73*, *80*). Work in 2014 by Bourissou took advantage of the nature of these phosphine ligands as demonstrated in a Au^{I} complex bearing a naphthyl derivative with phosphine and halogen substituent. Oxidative addition to this Au^{I} complex yielded the corresponding Au^{III} cyclometalated species (*81*).

Other work involving phosphine ligands explored specific reactivity with varying halogenated species. With the use of $(PMe_3)AuX$ as the model Au^{I} precursor it was shown that the nature of aryl halide, ligand, and counterion control the oxidative process (Figure 6) (*82*). Furthermore, the study assessed halide effects on oxidative addition. Au^{I} complexes are d^{10} in nature and typically adopt a linear geometry (*83*). To undergo oxidative addition, the two ligands must undergo strain as Au transitions into the +3 oxidation state. When Au is in the +3 state it is d^{8}, which changes the geometry from linear to square planar. Notably, the choice of the halogen species can lower the overall energy to undergo this change in geometry, indicative of halide dependence. Additionally, there is a decrease in energy required to overcome the activation energy as the halides progress

from a small, low polarizable atom to a heavier, highly polarizable atom (Table 4). The observed characteristic has implications for bond strength, with C(sp^2)–Cl being a stronger bond than C(sp^2)–I.

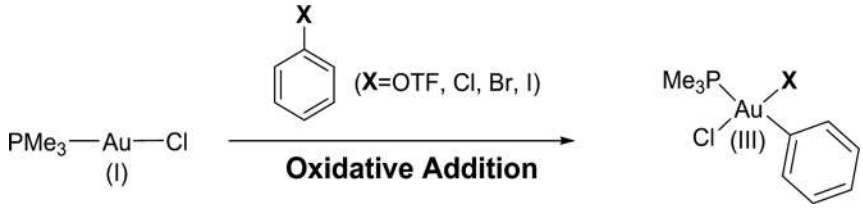

Figure 6. Reaction scheme of the computational studies on the activation barrier of Au^{I} to Au^{III}.

Table 4. Activation Barriers for the Oxidative Addition from Au^{I} to Au^{III}

Au^{I} Substrate	*Phenyl-X*	*$\Delta E^{\ddagger *}$*
$(PMe_3)AuCl$	Ph–OTF	57.4 (*82*)
$(PMe_3)AuCl$	Ph–Cl	40.6 (*82*)
$(PMe_3)AuCl$	Ph–Br	34.9 (*82*)
$(PMe_3)AuCl$	Ph–I	27.7

* Energies are given in units of kcal/mol.

Investigations into the effect of stabilizing ligands on oxidative addition of Ar–I to Au^{I} with the formula RAuCl revealed subtle differences (Figure 7). Comparison of the three R groups PMe_3, $(MeO)_3P$, and N-heterocyclic carbenes (NHC) display activation barrier: 27.7, 29.1, and 28.8 kcal/mol respectively (*82*). Overall, the substrate being oxidatively added plays a vital role in the success of the reaction.

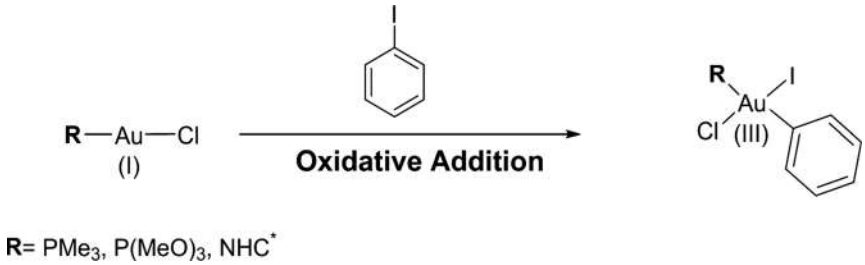

*Figure 7. Synthetic scheme illustrating oxidative addition with varying the R group in the Au^{I} precursor. *NHC = 1,3-bis(phenyl)-1,3-dihydro-2H-imidazol-2-ylidene.*

By using bidentate ligands with short bite angles, a "preorganized" Au^{I} complex was made readily accessible to oxidative addition. These Au^{I} complexes would adopt a tricoordinate geometry, which is rare. In doing so, the substrate would be added to Au^{I} to form the square planar Au^{III} framework. This strategy, although simple, had not been employed in prior work as a vast majority of bidentate ligands formed dinuclear species (Figure 8) (*55*, *84–89*). There is strong preference for Au^{I} species to adopt a linear geometry, rather than other geometries, which can be explained

due to stable aurophilic interactions (*84*, *88*, *90*). These complexes, especially with coordinating phosphine ligands, do exhibit remarkable stability at room temperature (*86–88*) and have provided a foundational framework for researchers to develop oxidative addition protocols (*89*).

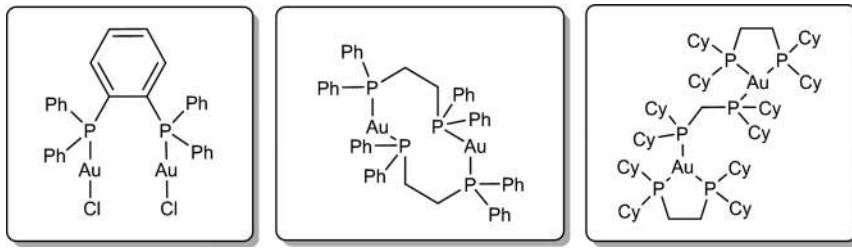

Figure 8. Examples of dinuclear Au^{I} complexes with phosphine ligands.

Importantly, geometry turns on reactivity toward oxidative addition; illustrated well by Bourissou's tricoordinate phosphine carborane Au^{I} and P, N–Au^{I} chelate, even at low/room temperatures (Figure 9) (*55*, *89*, *91*, *92*). This is significant in the development of gold catalysis because the synthetic design opens up a new field for study. With these bidentate chelated Au^{I} complexes successfully synthesized, other platforms could also be employed besides P–P ligands. Possibilities included frameworks such as: N–N, N–P, N–S, S–P bidentate ligands. A more recent publication showing successful oxidative addition to a gold complex bearing N–N bidentate ligand provides evidence of such transformations (*93*). Not only does using a bidentate ligand help stabilize the metal complex itself due to the chelate effect, it also aids in overcoming the energy barrier by helping facilitate the conformational change required to oxidize from the +1 to +3 state, and thus supports the case for how structure affects reactivity.

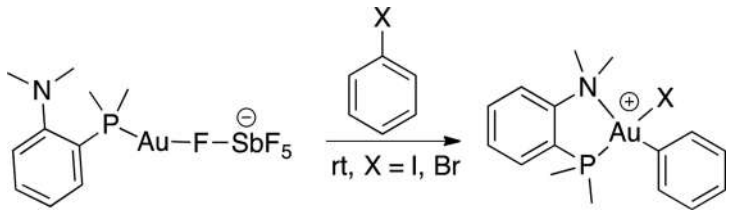

Figure 9. Illustration of pre-P,N-chelated Au^{I} complex and its ability to undergo oxidative addition.

It is important to note that the oxidative addition process is not limited to aryl halides. The use of aryl halides is prevalent in most redox catalytic reactions including C–C, C–N, and cross-coupling reactions. Moreover, recent work by Toste and coworkers expanded the scope of oxidative addition to the addition of strained C–C bond to a Au^{I} center (*13*). The Au^{III} complex was achieved via abstraction of a chlorine ligand using $AgSbF_6$ from a Au^{I}–NHC complex, then oxidatively adding biphenylene, followed by chloride trapping through a salt (Figure 10). The Au^{III} complex is able to perform both selective Diels–Alder additions as well as [2+2] cycloadditions of allenes to α,ß-unsaturated aldehydes (*13*, *91*). Along with Toste, Bourissou also illustrated oxidative addition of biphenylene into a diphosphino carborane Au^{I} complex (*94*). His synthetic methodology was similar in that the Au^{I} complex was activated via chloride abstraction, but with $GaCl_3$ at low temperatures. These discoveries highlight the potential Au has for catalytic transformations. Further work by Hashmi et al. highlighted that Au oxidative addition is not limited to certain ligand systems,

illustrating the capability of Au^{I} to undergo oxidative addition with diazonium salts (*95*). All of these works combine to give researchers a foundation for future integration into catalytic cycles.

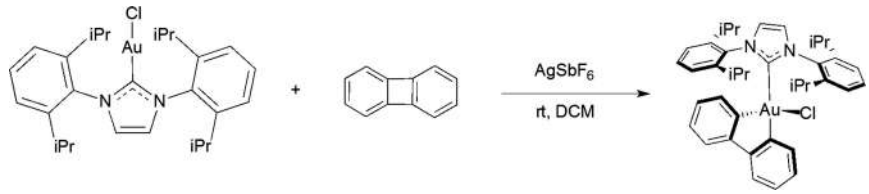

Figure 10. Synthesis of a Au^{III} complex from a Au^{I}–NHC precursor. The title complex was formed by oxidative addition to a C–C bond, an unprecedented transformation at the time.

Reactions involving photoredox catalysis have emerged along with these traditional oxidative reactions. In 2014, Toste explored photoinitiated catalysis by oxidatively adding CF_3I to a Au^{I}–phosphine complex under near UV light (*96*). This work was first of its kind and advanced the scope of Au catalysis as a whole. In another instance, Au was used as a cocatalyst in a photoredox system. Although in the previous case, the Au^{I} complex was photoactivated, this work still highlights the versatility Au has in multiple systems. In this second instance, a photoactivated cocatalyst (Ru) becomes excited upon radiation with visible light. These species then undergo single electron transfer with a diazonium salt to give a radical. The newly formed radical species adds to Au^{I} compound and is eventually oxidized by the previously photoactivated cocatalyst (*97*). This is an unconventional way of achieving oxidative addition from a Au^{I} to Au^{III} complex. In this process, typical Au^{I} compounds used were NHC–Au–Cl complexes or Au^{I}–phosphine complexes PR_3AuX, which have been previously used in oxidative addition evaluations. Optimization was done to see which wavelength gave rise to the highest quantum yields. In the case of this system, a wavelength of 455 nm (blue light) was determined to be the optimal wavelength (*97*).

This system was tested over several different ligand systems to determine if sterics played a role in the success of the oxidative addition. As previously shown in other classical oxidative addition examples, sterics play a pivotal role in reaction progress. If a ligand is sterically demanding, the already high energy barrier to overcome the redox potential is increased further as the conformation change becomes more challenging with bulkier ligands. In this study, the same was true. With the Au^{I} complex having the formula LAuCl, the L group was altered with varying phosphine ligands and NHCs of different sizes (Figure 11).

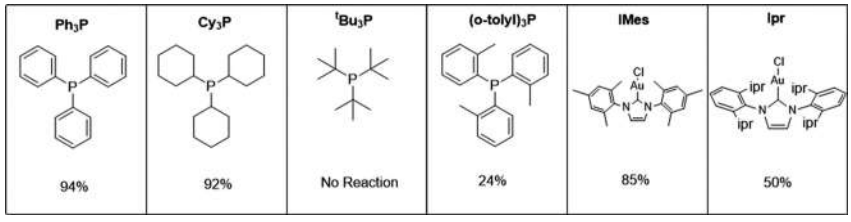

Figure 11. Select ligands (L) showing yield dependence on sterics. Yields are shown below each molecule (*97*).

This study shows that sterics is a driving force in the success of the reaction. Comparing the commonly used NHC ligands, IMes and IPr, the steric demands of the IPr ligand show a 35% decrease in the yield (*97*, *98*). These factors must be taken into consideration in designing new

catalysts and reactions. Many researchers applied the success of this system to various modes of catalysis. In 2014, a dual gold ($Au(PPh_3)Cl$)/photocatalyst (Ru^{II} photoredox catalyst) was used to perform arylative ring expansions (Figure 12). This process shows a unique application of this redox system.

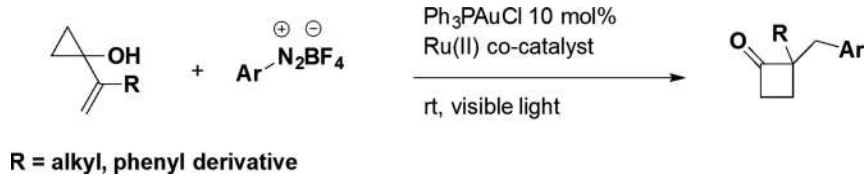

Figure 12. Dual gold/photoredox catalysis of arylative ring expansion (*99*).

Another application involves the arylative cyclization of allenoates (Figure 13) using the same catalytic system as mentioned previously. The difference here is the use of a silver salt to activate the gold complex and using blue LED light for photoactivation (*100*).

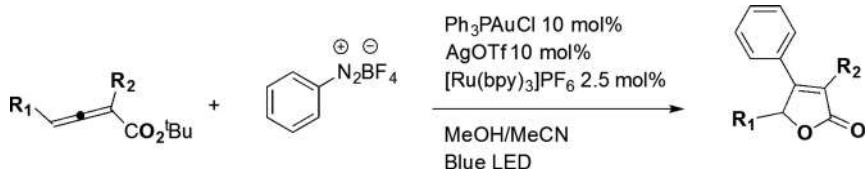

Figure 13. Synthetic scheme illustrating the dual catalyst system in the arylative cyclization of allenoates (*100*).

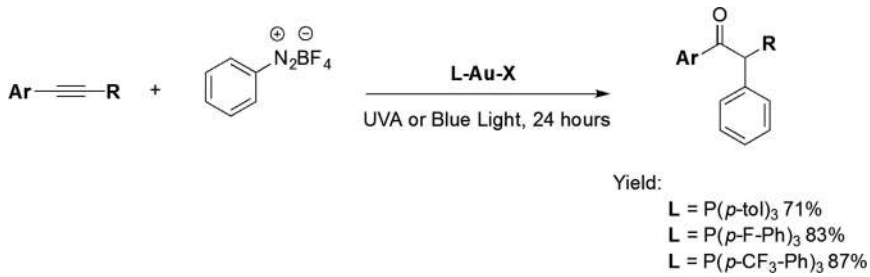

Figure 14. Photoactive catalysis using solely a Au^{I} catalyst. Reactions were performed at room temperature for 24 hours (*101*).

There are other examples in the literature that also use this dual catalyst system to perform catalytic transformations, but further work has demonstrated similar catalytic abilities; yet with just a Au catalyst. Prior work focused on the dual photoredox catalytic system where a second Ru catalyst was activated via light irradiation which facilitated the oxidation addition to Au^{III} during the catalytic cycle. Recent work has shown that the Ru cocatalyst may not be necessary. In this case alkynes are difunctionalized in a homogenous gold catalytic reaction (Figure 14) (*101*). Importantly, the Au^{I} catalyst used bears an extremely strong electron-withdrawing phosphine ligand. In the case of electron-rich ligands, the results were poor (*101*). This shows that regardless of what form of catalysis is employed with Au, there are several underlying factors that determine the success of Au catalysis. These include: (1) the species being oxidatively added, (2) sterics of both the species being added and the ligand attached to gold, and (3) electronics involved with every reactant. Tuning the catalytic

process requires great attention to detail; however, recent advancements show fascinating results in what was a "set-in-stone" field. This brief review reveals the growing possibilities for Au catalysis.

Transmetalation

Transmetalation is a widely used step in cross-coupling reactions. It involves an exchange of ligands between two different metals/metalloids (Figure 15).

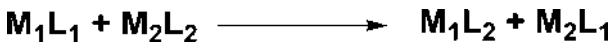

Figure 15. Simplified illustration of the transmetalation step.

Sonogashira, Stille, and Negishi cross-coupling reactions follow an archetypical transmetalation step. For example, Sonogashira cross-coupling reactions feature transmetalation between Cu and Pd metals, the Stille cross-coupling feature transmetalation between Pd and Sn, and the Negishi cross-coupling having a transmetalation step between Pd and Zn (*102–104*). These bimetallic cross-couplings have become increasingly popular and an interesting paradigm employed by Au. Previous reports in the literature have shown that a direct transmetalation step between Au/Pd is possible (*105*, *106*). In the case of Stille and Negishi cross-couplings, replacing the molar equivalent amounts of Sn or Zn with catalytic amounts of Au makes the alternative very attractive. In 2007, a study showed that this was indeed possible. Gold complexes, in the form of sodium salt ($NaAuCl_4$) or AuCl(tht) and $AuCl(PPh_3)$ were used as transmetalating agents in catalytic quantities (Figure 16) (*106*). These reactions were slightly longer than those using Cu as a cocatalyst; however, they were much cleaner in terms of by-products formed (*106*).

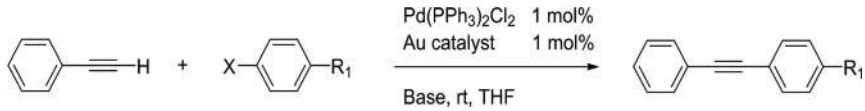

Figure 16. Scheme of Pd-catalyzed Sonogashira-type reaction using a gold cocatalyst instead of a copper cocatalyst.

This cleaner version presents a very attractive alternative to the classic Sonogashira cross-coupling reaction presented in 1975 (*107*). Another common problem that arises when using a Cu cocatalyst is the competitive homocoupling of the alkyne while in solution. High amounts of Cu have shown to be a source of the problem and much research has gone into troubleshooting this unwanted side reaction (*108*). By employing a Au cocatalyst, this problem can be circumvented. The use of Pd/Au-catalyzed reactions has become ever more popular since then (*109–112*). These reactions present atom-efficient conversions. The Pd/Au catalytic cycle resembles that of the Sonogashira cycle (Figure 17), which makes it all the more useful, as the chemistry behind the reaction shares similarity. In addition, the use of Pd/Au in cross-coupling in some cases produces higher yields than traditional cross-coupling reactions (*113*).

The scope of cross-coupling is not limited to just Pd/Au systems. Recent work shows successful gold cocatalyzed reactions featuring transmetalation between Au and Sn in a Stille type cross-coupling reaction (*114*). Conversion of alkynes into olefins is an older strategy using Cu (*115*). Surprisingly, there are very few examples of Pd-catalyzed vinylstannylation reactions (*114*, *116*). The authors report that in the case of the Pd-catalyzed reactions, the double addition products are the main products formed. Their synthesis combines a Au/Pd system to overcome the formation of double addition products, leading to the exclusive formation of mono-addition products as the main

product (*114*). In Figure 18, the Au^{I} cocatalyst uses the innate Lewis acidity to activate the alkyne. This mediates the oxidative addition to the Pd catalyst and enables the cycle to continue.

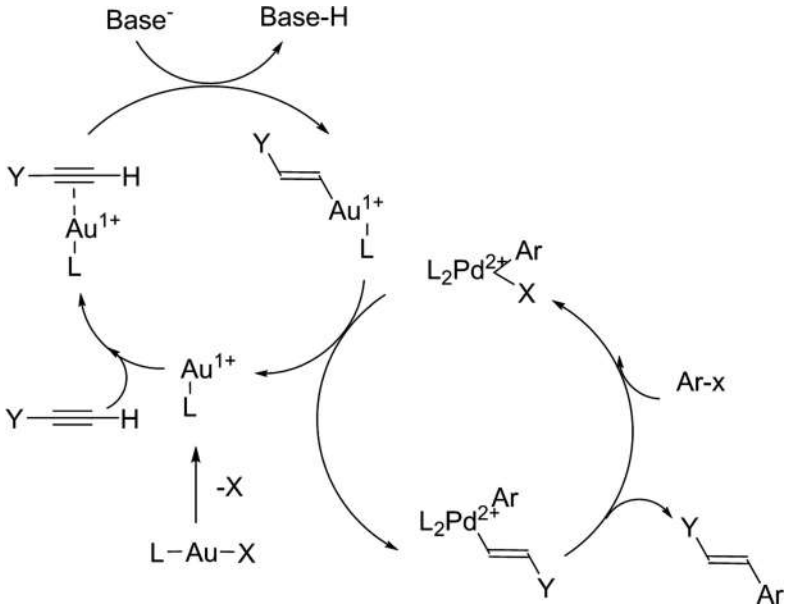

Figure 17. Depicted catalytic cycle of the Au/Pd Sonogashira-type cross-coupling reaction illustrating transmetalation from the organogold intermediate to the Pd complex (*113*).

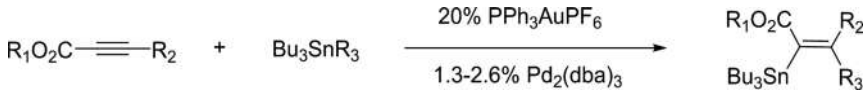

Figure 18. Scheme illustrating the Au/Pd Stille type cross-coupling reaction (*114*).

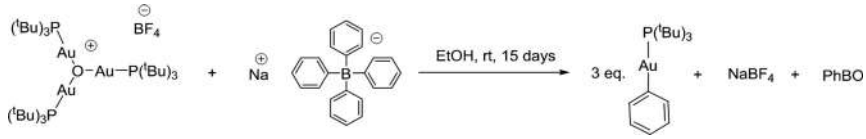

Figure 19. Illustration of the transmetalation between Au/B (*117*).

Other catalytic reactions, such as the Suzuki coupling, use a boronic acid to mediate C–C cross-coupling with a Pd catalyst. This catalytic process uses a transmetalation step between B and Pd. Along with other catalytic processes described thus far, this transformation is not limited to just Pd. Prior work demonstrated that sodium tetraphenylborate ($NaBPh_4$) was capable of mediating phenylation to a Au^{I} complex (Figure 19) (*117*, *118*). Other reports demonstrate that direct C–H arylation of heteroarenes is feasible with proper tuning of the Au catalyst used, a coupling that mirrors that of the Suzuki–Miyaura cross-coupling (*119*, *120*).

Recently, Nevado's group built on this concept and developed a system where a Au^{III} species was able to successfully undergo transmetalation with a boronic acid to form a C–C bond (Figure 20) (*121*, *122*). This work was preceded by Thomas Gray who established the capability of Au^{III} to undergo catalytic mono and diarylation with boronic acid derivatives through a Suzuki-Miyaura coupling (*123*). Other recent developments in this field include work by Bochmann who has further illustrated the capability of Au^{III} hydroxide complexes to undergo transmetalation with boronic acid

derivatives (*124*, *125*). This shows that any "typical" cross-coupling arrangement is not limited to the traditionally known transition metals. Au has found its place in the catalytic world and to much surprise has been a very good alternative to classical catalytic reactions.

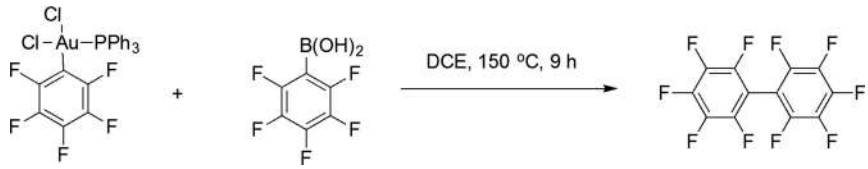

Figure 20. Scheme illustrating the successful transmetalation from a Au^{III} aryl complex to an aryl boronic acid (*126*).

Another important class of transmetalation in Au-catalyzed transformation is the use of other transition metals including rhodium (Rh). Up until now, examples of Pd-associated transition metal catalysis have been discussed. Recent study published the first work featuring successful Rh/Au transmetalation (Figure 21) (*127*). This work established a framework in which a successful transmetalation can be achieved through the use of either electron-poor or electron-rich Au^{I} complexes (*114*). This demonstrates the feasibility to create other metal/Au systems as this particular reaction employed catalytic amounts of organogold intermediates as opposed to previous examples using stoichiometric amounts (*127–130*).

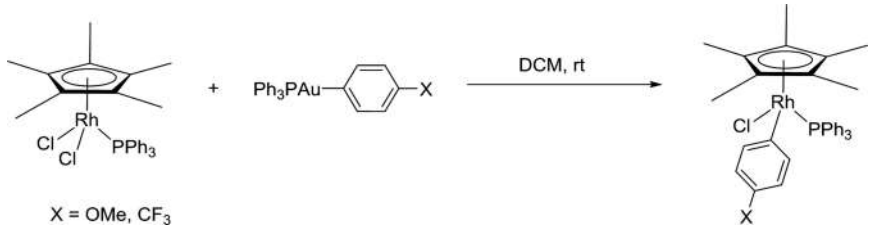

Figure 21. Synthetic scheme illustrating the first transmetalation between Rh and Au (*127*).

Reductive Elimination

Reductive elimination is a common product-releasing step or decomposition mechanism associated with high-valent transition metal compounds including Au^{III} (*131–133*). Analogous d^8 transition metals, like Pt^{IV}, have been investigated and mechanistic insight was reported long before the development of Au catalysis (*134*). Kochi (*135–137*) and Tobias (*138*) revealed in seminal investigations that C–C coupling using alkyl Au^{III} and Vicente demonstrated that unsymmetrical biaryls can be generated via C–C coupling from *cis*-diaryl-Au^{III} with concomitant Au^{I} species as proof of reductive elimination (*139–141*). Other work by Tobias illustrated facile reductive elimination of alkyls (ethane, butane, and octane) from readily synthesized Au^{III} compounds with the generic formula $[L_2AuR_2]X$ (L are commonly used π-acceptors: phosphines, arsines, and stibines) (*142*). Other studies of reductive elimination from Au^{III} revealed that electronics also play a factor in the products formed. From the complex with formula $Me_2AuR(PPh_3)$, when R was an alkenyl, furyl, or aryl group R–Me was observed; however, when R was alkynyl or an electron-withdrawing group, ethane was observed (*143*). Further work done by Schmidbaur illustrated that trialkynyl Au^{III} complexes ($LAu(CCR)_3$) undergo facile reductive elimination unless stabilized by strong electron

donor ligands (*144*). This seminal work provides evidence that electronics of the ligands and R groups attached to Au play a significant role in the mechanism of reductive elimination.

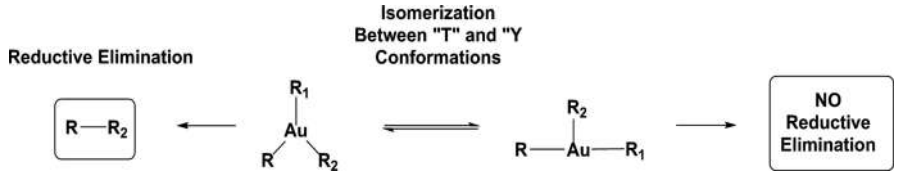

Figure 22. Rendition of the different states observed in the reductive elimination pathway of Au^{III}. (148).

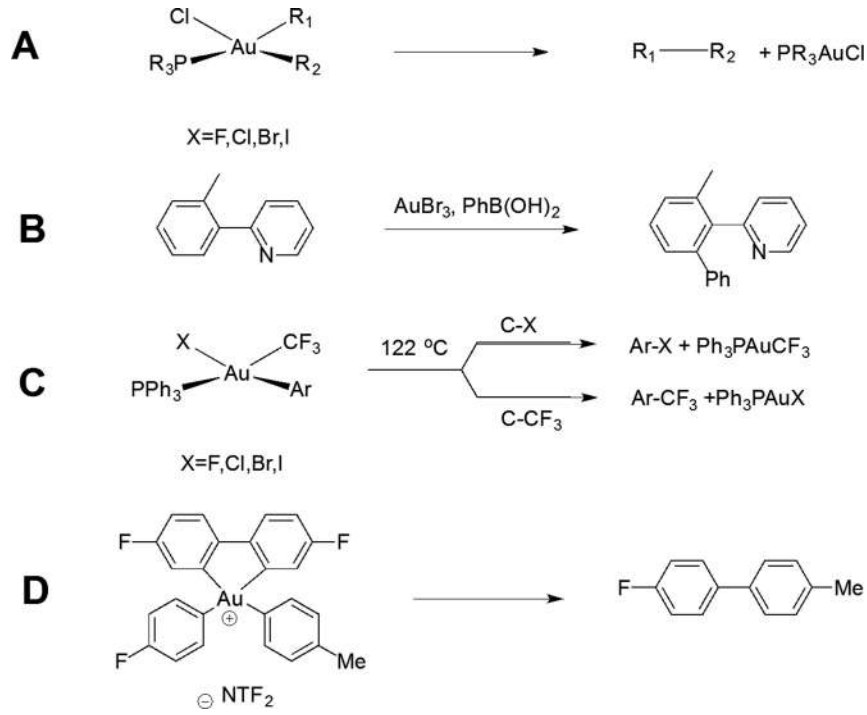

Figure 23. Four recent examples of C–C bond formation via reductive elimination from a Au^{III} complex (93, 126, 146, 150). (a) $C(sp^2)$–$C(sp^2)$ reductive elimination from a neutral Au^{III} to neutral Au^{I} complex. (b) $C(sp^2)$–$C(sp^2)$ reductive elimination via transmetalation of boronic acids. (c) Halide dependent reductive elimination to aryl halides. (d) $C(sp^2)$–$C(sp^2)$ coupling via reductive elimination from a cationic Au^{III} complex.

Toste has since probed the kinetic rates of C–C reductive elimination (*145*). Halide-dependent mechanisms of reductive elimination of Au^{III} have also been recently studied (*146*, *147*). The mechanism by which reductive elimination occurs is not definitely defined. Prior studies did show that when species were oxidatively added there are two possibilities. First, it immediately undergoes reductive elimination and second, isomerization followed by reductive elimination. It has been found that while undergoing these transformations, Au^{III} complexes will adopt one of two conformations, (“T” -shaped or “Y” -shaped conformation) before undergoing reductive elimination (Figure 22) (*148*). These two conformations represent the lowest relative energies. The complex can undergo isomerization between the “T” and “Y” conformation which facilitates the reductive elimination mechanism (*148*). A more recent work published in 2016 illustrates the synthesis and

characterization of such a complex; being a T-shaped pincer complex (*149*). Although this complex was not used in a reductive elimination platform, the isolation of the complex further elucidates stable structural conformations of Au.

The insight gained confirms the ability of Au^{III} species to successfully undergo this catalytic step and proves the catalytic viability of Au. This reductive elimination pathway has been key in the C–C bond formation. As shown in Figure 23, we highlight four examples of C–C bond formation via reductive elimination. These examples will be discussed later in the chapter.

Taking the generic Au^{III} complex with formula R_2PPh_3AuX, reductive elimination to form the products R–R and PPh_3AuX proceeded via first order kinetics (*151*). Furthermore, the study elucidated the rates of reductive elimination when varying the phosphine ligand. Dialkyl Au^{III} complexes were used to evaluate the rate of reductive elimination. Phosphines with higher cone angles (Figure 24): PCy_3 (179°) (*152*), PPh_3 (145°) (*152*), and PMe_3 (118°) (*152*) had a much higher rate of reductive elimination than those without, hinting that relieving strain on the Au^{III} complex is a driving force for reductive elimination (*151*, *153*).

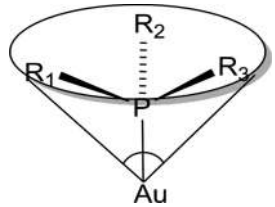

Figure 24. Illustration of the cone angle for varying phosphine ligands. This angle is used as a metric for sterics of symmetrical phosphine ligands (152, 154).

With the fundamental concepts laid out, researchers tried to tackle traditional cross-coupling reactions, but with gold as the catalyst. In 2001 research found that the classical Sonogashira cross-coupling (*155*), could be performed with gold catalysts with slight variation. In this particular coupling, C(sp^2)–C(sp^2) bond formation is achieved through a Sonogashira-type reaction using a terminal alkyne and boronic acid derivative (Figure 25) (*156*). This coupling had previously been carried out with the typical palladium catalyst in the year prior (*157*). Nonetheless, the amount of success gold catalysts would have at the same cross-coupling reactions was not extensively studied (*2*, *158–160*). Toste, again, was not turned away by prior failures. In 2010 and 2014, he published work with newer developments showing successful cross-coupling (C(sp^3)–C(sp^2)) between boronic acid derivatives and alkyl halides, the latter without the use of an oxidant (*161*, *162*). This work has yet again pioneered newer innovations in Au catalysis as more and more examples point to the capability of Au to perform "classical" coupling reactions.

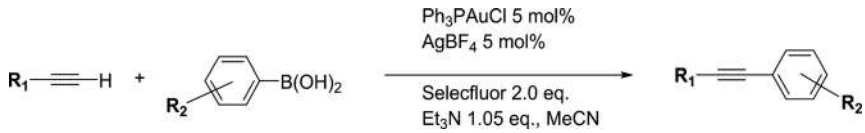

Figure 25. Illustration of Au-catalyzed Sonogashira-type C(sp^2)–C(sp^2) cross-coupling. Temperature varied with different R groups. Selectfluor is 1-chloromethyl-4-fluoro-1,4 diazoniabicyclo[2.2.2]octane bis(tetrafluoroborate), used as an oxidizing agent for Au^I to Au^{III} (156).

Competitive yields were obtained compared to previous reactions involving Pd catalysts, proving to be a robust and efficient system in the C(sp^2)–C(sp^2) coupling across multiple functionalities (*139*, *156*, *163*, *164*). This early study demonstrated the feasibility of a Au^{I}/Au^{III} redox catalytic cycle and the success of Au as a catalyst. Along the subject of C–C reductive elimination, a report in 2006 elucidated the capability of C(*sp*)–C(*sp*) reductive elimination from Au–acetylide complexes (*165*). These complexes were prepared from conventional Au^{I}–phosphine complexes and were shown to have selective cis-reductive elimination (*165*), giving rise to easy access to conventional rudimentary steps. Another recent example demonstrated the use of aryl-trimethylsilanes in C–C coupling (*166*). The C–Si auration allowed high chemoselectivity in the catalytic process and mechanistic insights suggest a classical Au^{III}/Au^{I} redox cycle, which can be considered in future developments.

Figure 26. Synthetic scheme illustrating the facile P–C(sp^2) reductive elimination from Au^{III} (167).

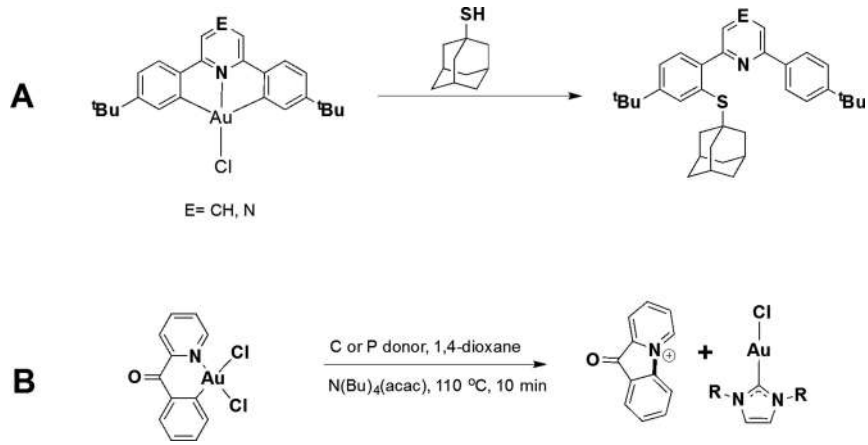

Figure 27. (a) Reductive elimination of Au^{III} thiolates. 1-adamantylthiol is oxidatively added to gold twice, inducing reductive elimination (172). (b) C(sp^2)–N(sp^2) reductive elimination from a stable cyclometaled Au^{III} complex (175).

With this success, other catalytic couplings such as C–X, where X is a heteroatom (N, O, S, P) were blossoming as researchers wanted to push the boundaries beyond typical C–C bond formation. A unique, recent example of this C–X coupling involved the reductive elimination of a phosphine ligand with an aryl ligand to form a phosphonium salt (Figure 26) (*167*). Typically phosphine ligands are found to be coordinated to the Au center for stability purposes, as phosphine ligands donate into the low-lying metal orbitals (*168*). In this particular instance, the reductive elimination forms phosphonium salts rather than neutral phosphines, which is what had largely been reported in prior work (*169–171*). This work presents a unique method of forming phosphonium salts from facile reductive elimination from Au^{III} (*167*).

Another unique example of C-heteroatom coupling in the very recent literature demonstrates the ability of gold to successfully perform C–S coupling via reductive elimination from Au^{III} (Figure 27A) (*172–175*). Prior work demonstrated this same reductive elimination; however, from palladium and rhodium catalysts, not Au^{III} transition metal complexes (*176–178*).

The C–S transformation is another example of elementary reactions applicable to Au catalysis, through reductive elimination pathway. Recent work in our laboratory demonstrates intramolecular C–N bond formation from Au^{III} (Figure 27B) (*175*). Other oxidant-free C–N and C–O coupling reactions have been studied and will be of great utility for the development of medicinal agents or materials via Au catalysis (*179–182*).

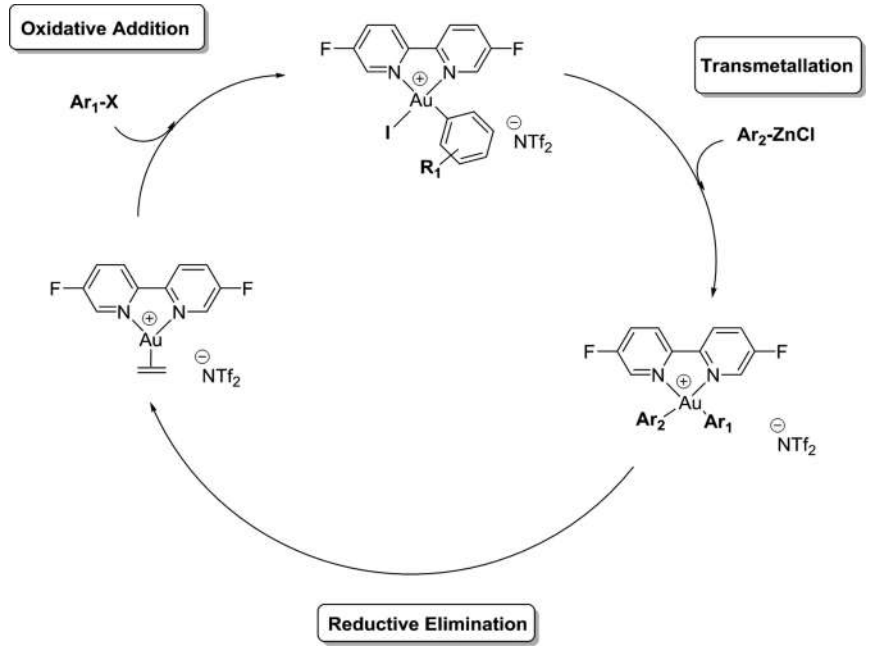

Figure 28. Catalytic scheme of the oxidative addition, transmetalation, and reductive elimination from a Au^{I} tricoordinate species to form a $C(sp^2)–C(sp^2)$ bond (*93*).

In a report that described halide-dependent mechanisms of reductive elimination from Au^{III}, two organogold complexes of the type $(Ph_3P)Au(4\text{-}Me\text{-}C_6H_4)(CF_3)(X)$ and $(Cy_3P)Au(4\text{-}F\text{-}C_6H_4)(CF_3)(X)$ (X = I, Br, Cl, F) revealed unique reactivity and kinetic selectivity toward $C_{aryl} – X$ and $C_{aryl} – CF_3$ reductive elimination (a commonly used derivative in oxidative addition reactions to Au) (*183*). Furthermore, the study showed that when the halogen, X, is iodine, there is complete selectivity to form the C(aryl)–X bond. However, when the halogen, X, is fluorine, the opposite is observed (*146*). This insight provides a potential mechanistic insight into the reductive elimination process and shows the potential to tune gold complexes in a specific way to achieve a desired transformation. Continuing on the importance of CF_3 reductive elimination, a report in 2017 further established mechanistic insight into this pathway. Toste et al. were able to identify a "rebound mechanism" in which CF_3 moiety has a fluoride abstracted, followed by migratory insertion of the alkyl substituent, and then formal reductive elimination (*184*). This insight provides further evidence of the mechanism behind Au-catalyzed reactions and allowed Toste et al. to harness this process

to synthesize ^{18}F compounds, which are useful tracers in positron emission tomography (*184*). A key example that should be discussed is the recently published by Russell and co-workers. In this work, Au^{I} complex undergoes oxidative addition, proceeds through transmetalation, and closes the catalytic cycle with reductive elimination to perform a Negishi-type reaction (Figure 28) (*93*).

This work is novel in the sense that all rudimentary catalytic steps are observed during the transformation; something that had not been previously reported in the history of gold catalysis. Another attractive point is that the Au^{I} starting material is easily accessible in moderate yields (*93*). It also employs the commonplace bidentate N–N ligand, bipyridine (bpy), as the electron donor to stabilize the gold. This ligand had been previously used in other exciting work on gold catalysis (*185*, *186*). When analyzing reaction rates, different R_1 groups, were varied to evaluate substrate dependence on the overall rate of reaction. It was found that electron-poorer substrates proceeded at a faster rate than electron-rich groups: R_1: OMe > H > CF_3 (*93*). This is consistent with previous examples as electron-poorer substrates lead to enhanced oxidative addition to Au^{I} complexes (*55*). These developments enlighten the community on fundamentals of gold during the catalytic process. It is also important to note that throughout these examples, it is evident that Au is functional group tolerant, a crucial factor needed in natural product synthesis as well as many other applications.

β-Hydride Elimination

β-hydride elimination is another classical step seen in catalysis such as in the Heck reaction or Wacker-Tsuji oxidation (*187*, *188*). This particular step is used to generate olefins and corresponding metal hydride from an alkyl group attached to the metal center (Figure 29).

Figure 29. Illustration of a general β-hydride elimination.

The mechanistic pathway is a prominent method of decomposition of metal (Pd, Ru, Pt) alkyls (*189–191*). One of the most notable uses is in the industrial production of acetaldehyde (*192*). Throughout this section, Au^{III} alkyl complexes will be discussed, and it is worth mentioning the unique synthesis carried out by Bochmann et al. in which Au^{III} alkyl complexes were synthesized from Au^{III} alkoxide complexes (*193*). Despite the in-depth studies on β-hydride elimination of these metals, studies on gold β-hydride elimination have been scarce (*194–197*), because it was long deemed impractical for gold (*198*, *199*). However, this is not the case. Recent research efforts elucidated two Au^{I} metal hydride complexes, setting a new precedent for Au-induced β-hydride elimination, previously thought impossible (Figure 30) (*200–203*).

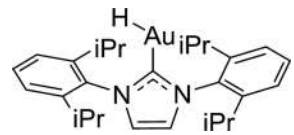

Figure 30. Example of an isolated Au-hydride complex (*201*).

Although the isolation of these hydride complexes suggests that the mechanism would work, for Au^{I} compounds it has been found not possible. Computational calculations examined the ability of Au^{I}–NHC complexes to undergo β-hydride elimination. Results indicated that the energy barrier was too large for the Au^{I} complexes to overcome (Figure 31) (*204*). Further studies show similar results, stating that the Coulomb exchange repulsion is too large of a barrier to overcome when a positively charged hydrogen atom is forced to distort the completely filled orbitals of the d^{10} Au^{I} atom; an integral part of the β-hydride elimination mechanism (*205*).

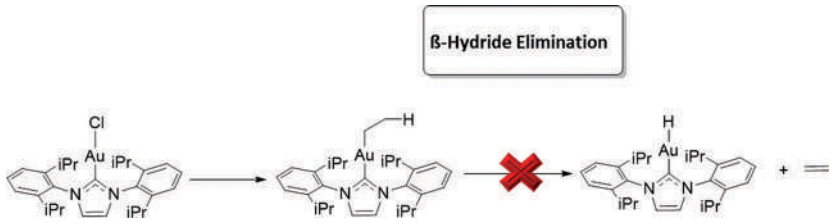

Figure 31. Theoretical insight of the elementary step of metal–alkyls to olefins with β-hydride elimination. This has been found not to be feasible for Au^{I} complexes (*204*).

Subsequently, as we have demonstrated thus far, Au^{III} is also prominent in Au catalysis. β-hydride elimination should not be completely ruled out, as Au^{III} is a d^{8} atom with unfilled d orbitals. The chemistry of Au^{III} is very different from Au^{I}, and thus β-hydride elimination should be considered for these complexes. This concept was explored in a recent study to examine the ability of Au^{III} complexes to undergo β -hydride elimination. Au^{III} catalysis of allenols using $AuCl_3$ found two products formed. The first product was an adduct of cycloisomerization (kinetic product), but the second being an adduct of β-hydride elimination (thermodynamic product) (Figure 32) (*197*). This transformation is quite exciting as it shows the capability of Au^{III} to facilitate β-hydride elimination.

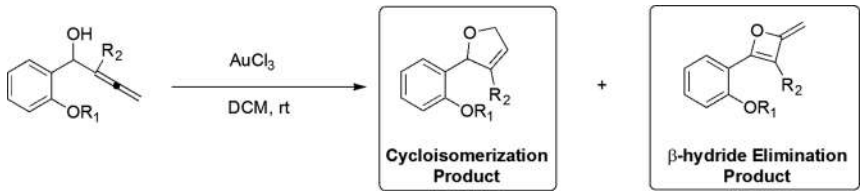

Figure 32. Synthetic scheme of the synthesis of oxytenes from allenols featuring a Au^{III}-catalyzed β -hydride elimination step.

Because the use of $AuCl_3$, which gained no benefits from external ligand stability and tuning, showed promise, it was thought that stabilizing the metal could potentially improve the success in the ability to perform β-hydride elimination. In 2012, a study by Toste's group attested to this. Although the main goal was to achieve C(sp^2)–F reductive elimination via their Au^{III} compounds, the observed outcome was preference for the β-hydride eliminated product (Figure 33). Further studies showed that more sterically demanding cyclohexyl derivatives indeed disfavored β-hydride elimination product formation and the C(sp^2)–F product was observed in the majority. Overall, C(sp^2)–F reductive elimination is less facile than C(sp^2)–I reductive elimination, and further research could give insight into the kinetics of this mechanism. A key takeaway from this preliminary study

revealed Au^{III} complexes are capable of C(sp^2)–F reductive elimination; however, dependence on variance of the halide and R group does exist.

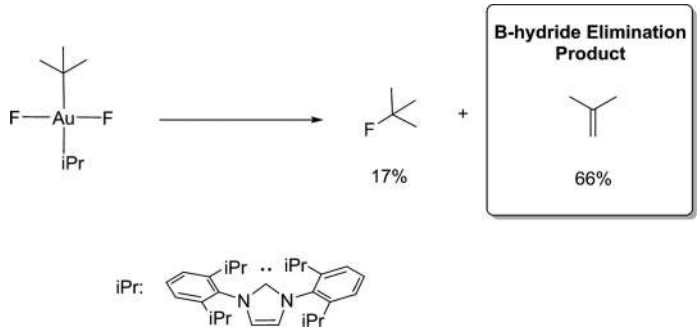

Figure 33. Attempted synthesis of C(sp^2)–F reductive elimination products in a study revealed the preference for β-hydride elimination with Au^{III} complexes bearing alkyl chains (*206*).

Further research expanded on this discovery by trying to design a Au^{III} alkyl complex particularly for the exploration of β-hydride elimination. Au^{III} alkyl complexes are limited throughout the literature and so the development of this complex is a unique advancement. (Figure 34) (*207*).

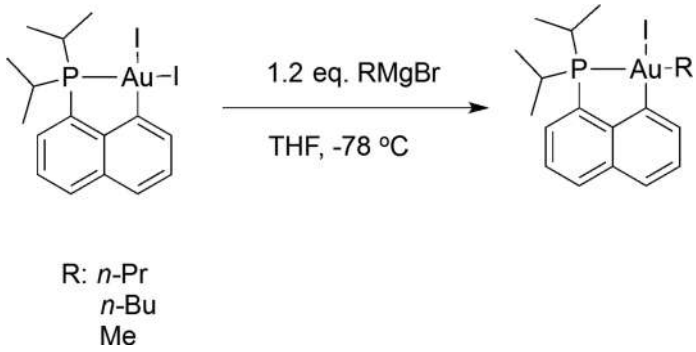

Figure 34. Synthetic scheme illustrating the synthesis of Au^{III} alkyl complexes.

By means of a stabilizing (P,C) pincer type ligand, a Au^{III} alkyl was isolated. Using phosphorus and a strongly donating carbon atom increases donation to the metal center, thus stabilizing the compound. Treatment of this Au^{III} alkyl complex with a silver salt at very cold temperatures followed by temperature elevation led to the isolation of β-hydride elimination products (Figure 35) (*207*).

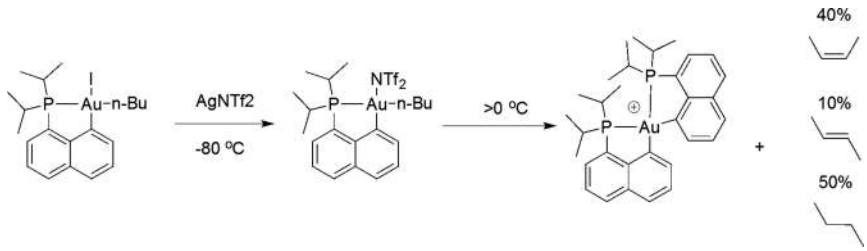

Figure 35. Isolation of β-hydride elimination products via Au^{III} alkyl complexes. Upon warming the four-coordinate Au^{III} complex the β-hydride elimination occurs (*207*).

One of the most recent examples in this field comes in 2017, where a stable Au^{III} formate complex is able to undergo β-hydride elimination to produce formic acid (Figure 36) (*208*).

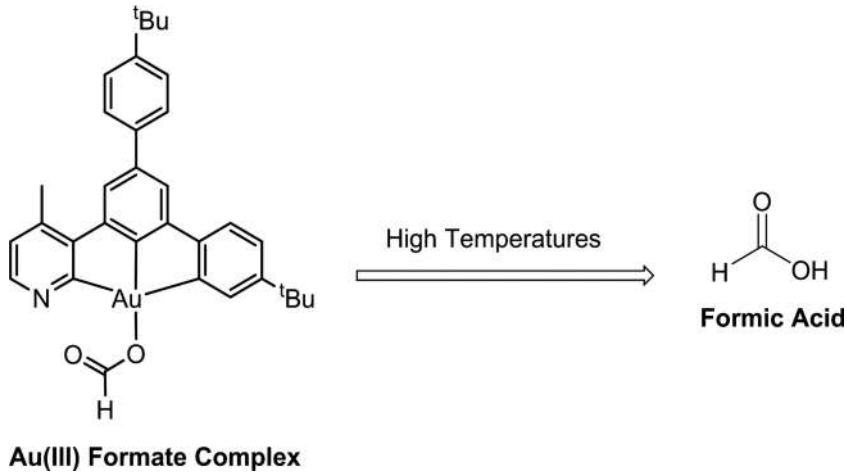

Figure 36. Isolatable Au^{III} formate complex leads to β-hydride elimination to formic acid (*208*).

The strategy not only isolates the first Au^{III} formate complex, it also establishes further concrete evidence in the viability of Au^{III}–metal complexes to undergo β-hydride elimination. It is mentioned that although the established reaction (as seen in Figure 35) is viable, it is not as synthetically applicable for this specific catalytic transformation (*208–211*). It is a very exciting time for gold catalysis as increasing curiosity has led to a stark of new discoveries. In the case of β-hydride elimination, a once unreachable goal has now become a feasible reality.

Migratory Insertion

Migratory insertion (Figure 37) is another rudimentary step in catalysis that is key in several different catalytic cycles, such as the Ziegler–Natta polymerization olefin, which was awarded a Nobel Prize (*212*, *213*) as well as the Mizoroki–Heck coupling to form substituted olefins from unsaturated alkenes (*187*, *214*).

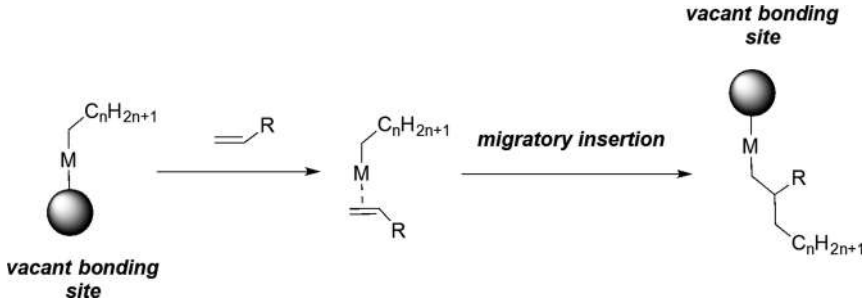

Figure 37. Generic illustration of migratory insertion of an olefin into a metal complex. The square in the figure represents a vacant coordination site to the metal. Note that oxidation states do not change during migratory insertion.

Recent developments in Au catalysis have also explored the ability of Au to perform this rudimentary step. One advancement shows successful migratory insertion of olefins into a Au–O bond (Figure 38) (*215–218*).

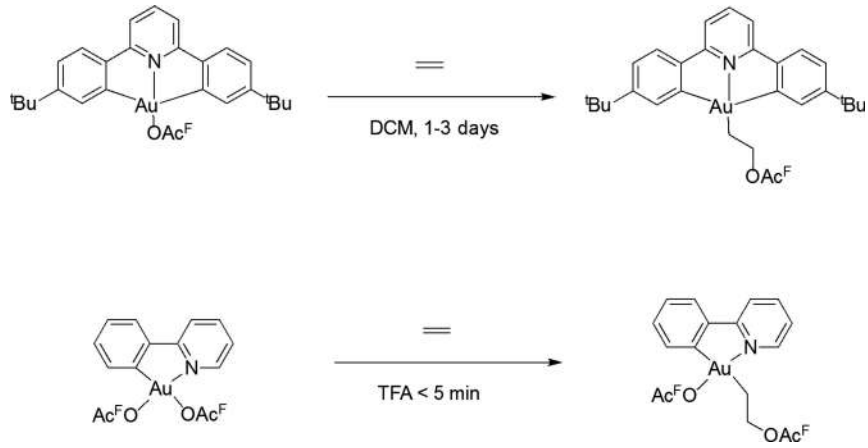

Figure 38. Illustration of the most recent advancements of migratory insertion into a Au^{III}–O bond (216, 217).

The success of the work presented sparked further interest in research of Au's capability to do formal migratory insertion across other systems. Recent developments include formal migratory insertion into Au–C bonds, which is underdeveloped (Figure 39) (*219*, *220*).

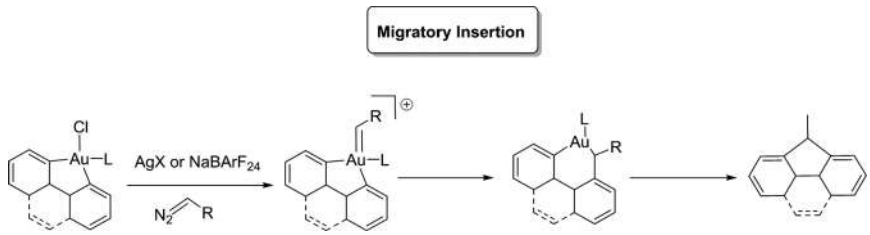

Figure 39. Synthetic scheme of formal migratory insertion into a Au^{III}–C bond (*220*).

Similarly, Bourissou for the first time isolated a Au^{III}–arene complex as a function of formal migratory insertion. Surprisingly, these complexes had not been previously reported even though Au^{III} has clearly shown favorable interactions with π-systems (*221*). This reveals that migratory insertion of olefins is catalytically feasible. This work is significant as it gives researchers a new tool to work with and more applications for Au^{III} catalysis as a whole. These studies indicate novel catalytic capabilities of Au^{III}. With the groundwork laid out, further developments are sure to follow with innovative science in the field of Au catalysis.

Summary

We have highlighted elementary reactions underlying gold chemistry including: oxidative addition, transmetalation, reductive elimination, β-hydride elimination, and migratory insertion. A number of these organometallic transformations were thought to be impossible for gold a few years ago. This presentation unveils invaluable opportunities for Au catalysis of which catalyst design is critically needed. When considering the development of a catalyst, each step shows dependence

on several factors: sterics, electronics, geometries, temperature, and the intended product outcome. Optimizing these conditions gives rise to robust Au catalysts that are able to perform classical cross-coupling reactions and are competitive with the traditional Pd or Pt catalysts. Au catalysis has seen an exponential growth in discovery within recent years and the field is bursting with new insights on the exact chemistry behind it. The use of Au is becoming more and more attractive for researchers and new developments are sure to come in the immediate future. We believe this work will contribute to the advancement of Au catalysis.

Acknowledgments

This work was supported by the University of Kentucky (UK), Department of Chemistry for Start-up Funds and the UK, Igniting Research Collaboration Fund.

References

1. Gorin, D. J.; Toste, F. D. Relativistic Effects in Homogeneous Gold Catalysis. *Nature* **2007**, *446*, 395.
2. Li, Z.; Brouwer, C.; He, C. Gold-Catalyzed Organic Transformations. *Chem. Rev.* **2008**, *108*, 3239–3265.
3. Huang, H.; Zhou, Y.; Liu, H. Recent Advances in the Gold-Catalyzed Additions to C–C Multiple Bonds. *Beilstein J. Org.Chem.* **2011**, *7*, 897–936.
4. Rudolph, M.; Hashmi, A. S. K. Gold Catalysis in Total Synthesis—an Update. *Chem. Soc. Rev.* **2012**, *41*, 2448–2462.
5. Braun, I.; Asiri, A. M.; Hashmi, A. S. K. Gold Catalysis 2.0. *ACS Catalysis* **2013**, *3*, 1902–1907.
6. Hashmi, A. S. K. Dual Gold Catalysis. *Acc. Chem. Res.* **2014**, *47*, 864–876.
7. Pflästerer, D.; Hashmi, A. S. K. Gold Catalysis in Total Synthesis – Recent Achievements. *Chem. Soc. Rev.* **2016**, *45*, 1331–1367.
8. Shahzad, S. A.; Sajid, M. A.; Khan, Z. A.; Canseco-Gonzalez, D. Gold Catalysis in Organic Transformations: A Review. *Synth. Commun.* **2017**, *47*, 735–755.
9. Harris, D. C.; Lucy, C. A. ; University of North Carolina at Chapel Hill; Department of Chemistry; *Quantitative Chemical Analysis*; Freeman Custom Publishing: New York, NY, 2016.
10. Schwerdtfeger, P.; Hermann, H. L.; Schmidbaur, H. Stability of the Gold(I)−Phosphine Bond. A Comparison with Other Group 11 Elements. *Inorg. Chem.* **2003**, *42*, 1334–1342.
11. Baenziger, N. C.; Bennett, W. E.; Soborofe, D. M. Chloro(Triphenylphosphine)Gold(I). *Acta Crystallogr., Sect. B* **1976**, *32*, 962–963.
12. Dorel, R.; Echavarren, A. M. Gold(I)-Catalyzed Activation of Alkynes for the Construction of Molecular Complexity. *Chem. Rev.* **2015**, *115*, 9028–9072.
13. Wu, C.-Y.; Horibe, T.; Jacobsen, C. B.; Toste, F. D. Stable Gold(III) Catalysts by Oxidative Addition of a Carbon–Carbon Bond. *Nature* **2015**, *517*, 449.
14. Fukuda, Y.; Utimoto, K. Preparation of 2,3,4,5-Tetrahydropyridines from 5-Alkynylamines under the Catalytic Action of Gold(III) Salts. *Synthesis* **1991**, 975–978.
15. Yukitoshi Fukuda, K. U.; Nozaki, Hitoshi Preparation of 2,3,4,5-Tetrahydropyridines from 5-Alkynylamines under the Catalytic Action of Au(III). *Heterocycles* **1987**, *25*, 297–300.

16. Usón, R.; Laguna, A.; Laguna, M.; Jiménez, J.; Jones, P. G. A Mixed-Valent Pentanuclear Gold Complex Containing a Linear Au Chain. *Angew. Chem., Int. Ed.* **1991**, *30*, 198–199.
17. Leary, K.; Zalkin, A.; Bartlett, N. Crystal Structure of [Xe2f11]+[Auf6]. *J. Chem. Soc., Chem. Commun.* **1973**, 131–132.
18. Murray, H. H.; Fackler, J. P.; Mazany, A. M.; Porter, L. C.; Shain, J.; Falvello, L. R. Synthesis and X-Ray Crystallographic Characterization of the Gold(II) Ylide Dimers [Au(Ch2)2pph2] 2(Ch2cn)Br and [Au(Ch2)2pph2] 2(Ch2c(O)Ph)Br. Unusually Stable Functionalized Alkyl Halide Adducts. *Inorg. Chim. Acta* **1986**, *114*, 171–178.
19. Bennett, M. A.; Bhargava, S. K.; Hockless, D. C. R.; Welling, L. L.; Willis, A. C. Dinuclear Cycloaurated Complexes Containing Bridging (2-Diphenylphosphino)Phenylphosphine and (2-Diethylphosphino)Phenylphosphine, C6h4pr2 (R = Ph, Et). Carbon−Carbon Bond Formation by Reductive Elimination at a Gold(II)−Gold(II) Center. *J. Am. Chem. Soc.* **1996**, *118*, 10469–10478.
20. Bardají, M.; Blascoa, A.; Jiménez, J.; G. Jones, P.; Laguna, A.; Laguna, M.; Francisco Merchán, G. Di- and Tetranuclear Gold(II) Complexes with Dithiocarbamate and Related Ligands. X-Ray Structure of Au2(M-Ch2pph2ch2)2(S2cnme2)2]. *Inorg. Chim. Acta* **1994**, *223*, 55–61.
21. Murray, H. H.; Fackler, J. P. The Reactivity of Bromoform with [Au(Ch2)2pph2]2. The Completion of the Halomethane Series Chyx4−Y (Y=3,2,1,0; X=Cl, Br, I) and Reactivity with [Au(Ch2)2pph2]2. *Inorg. Chim. Acta* **1986**, *115*, 207–209.
22. Preiß, S.; Förster, C.; Otto, S.; Bauer, M.; Müller, P.; Hinderberger, D.; Hashemi Haeri, H.; Carella, L.; Heinze, K. Structure and Reactivity of a Mononuclear Gold(II) Complex. *Nature Chem.* **2017**, *9*, 1249.
23. Christopher Corti, R. H. *Gold: Science and Applications*, 1st ed.; CRC Press, Taylor and Francis Group: 6000 Broken Sound Parkway NW, Suite 300, Boca Raton, FL, 2009; p 444 (accessed Sept 28, 2018).
24. Wickleder, M. S. Auso4: A True Gold(II) Sulfate with an Au24+ Ion. *Z. Anorg. Allg. Chem.* **2001**, *627*, 2112–2114.
25. Calabro, D. C.; Harrison, B. A.; Palmer, G. T.; Moguel, M. K.; Rebbert, R. L.; Burmeister, J. L. Thiocyanation, Selenocyanation, and Halogenation Reactions of Dithiocarbamate Complexes of Gold(I) and Silver(I). Generation of Gold(II) and Silver(II) Complexes. *Inorg. Chem.* **1981**, *20*, 4311–4316.
26. Khan, M. N. I.; Wang, S.; Fackler, J. P. Synthesis and Structural Characterization of the Gold Complex, [N-Bu4n]2[Au2(I-Mnt)2] (I-Mnt = 1,1-Dicyanoethylene-2,2-Dithiolate) and Its Oxidative-Addition Products [Ph4as]2[Au2(I-Mnt)2cl2], [N-Bu4n]2[Au2(I-Mnt)2br2], and [N-Bu4n][Au(I-Mnt)2]. Spectral Studies of the Disproportionation of [N-Bu4n]2[Au2(I-Mnt)2x2] (X = Cl-, Br-, I-) into [N-Bu4n][Aux2] and [N-Bu4n][Au(I-Mnt)2]. *Inorg. Chem.* **1989**, *28*, 3579–3588.
27. Abdou, H. E.; Mohamed, A. A.; Fackler, J. P. Oxidative Addition of Small Molecules to a Dinuclear Au(I) Amidinate Complex, Au2[(2,6-Me2ph)2n2ch]2. Syntheses and Characterization of Au(II) Amidinate Complexes Including One Which Possesses Au(II)−Oxygen Bonds. *Inorg. Chem.* **2007**, *46*, 9692–9699.
28. Basil, J. D.; Murray, H. H.; Fackler, J. P.; Tocher, J.; Mazany, A. M.; Trzcinska-Bancroft, B.; Knachel, H.; Dudis, D.; Delord, T. J.; Marler, D. Experimental and Theoretical Studies of Dinuclear Gold(I) and Gold(II) Phosphorus Ylide Complexes. Oxidative Addition, Halide

Exchange, and Structural Properties Including the Crystal and Molecular Structures of [Au(Ch2)2pph2]2 and [Au(Ch2)2pph2]2(Ch3)Br. *J. Am. Chem. Soc.* **1985**, *107*, 6908–6915.

29. Usón, R.; Laguna, A.; Laguna, M.; Fraile, M. N.; Jones, P. G.; Sheldrick, G. M. Mono- and Bi-Nuclear Gold(I), Gold(II), and Gold(III) Perhalogenoaryl Complexes with the Ligand Bis(Diphenylphosphino)Amine. Crystal and Molecular Structure of μ-[Bis(Diphenylphosphino)Amine]-Dichlorobis(Pentafluorophenyl)Digold(II). *J. Chem. Soc., Dalton Trans.* **1986**, 291–296.
30. Leary, K.; Bartlett, N. A New Oxidation State of Gold: The Preparation and Some Properties of [Auf6]– Salts. *J. Chem. Soc., Chem. Commun.* **1972**, 903–904.
31. Rice, G. W.; Tobias, R. S. Synthesis of Tetramethylaurate(III). Structures of Lithium Dimethylaurate and Lithium Tetramethylaurate in Solution. *Inorg. Chem.* **1975**, *14*, 2402–2407.
32. Rice, G. W.; Tobias, R. S. Isolation of Thermally Stable Compounds Containing the Dimethylaurate(I) and Tetramethylaurate(III) Anions. *Inorg. Chem.* **1976**, *15*, 489–490.
33. Gambarotta, S.; Floriani, C.; Chiesi-Villa, A.; Guastini, C. A Homoleptic Arylgold(I) Complex: Synthesis and Structure of Pentanuclear Mesitylgold(I). *J. Chem. Soc., Chem. Commun.* **1983**, 1304–1306.
34. Kharasch, M. S.; Isbell, H. S. The Chemistry of Organic Gold Compounds. III. Direct Introduction of Gold into the Aromatic Nucleus (Preliminary Communication). *J. Am. Chem. Soc.* **1931**, *53*, 3053–3059.
35. Kharasch, M. S.; Beck, T. M. The Chemistry of Organic Gold Compounds. V. Auration of Aromatic Nitriles. *J. Am. Chem. Soc.* **1934**, *56*, 2057–2060.
36. Norman, R. O. C.; Parr, W. J. E.; Thomas, C. B. The Reactions of Alkynes, Cyclopropanes, and Benzene Derivatives with Gold(III). *J. Chem. Soc., Perkin Trans. 1* **1976**, 1983–1987.
37. Jack Sugar, A. M. Energy Levels of Copper, Cu I through Cu XXIX. *J. Phys. Chem. Ref. Data* **1990**, *19*, 527–616.
38. Loock, H.-P.; Beaty, L. M.; Simard, B. Reassessment of the First Ionization Potentials of Copper, Silver, and Gold. *Phys. Rev. A* **1999**, *59*, 873–875.
39. Benschop, H.; Joshi, Y. N.; Vankleef, T. A. M. Second Spectrum of Silver: Ag Ii. *Can. J. Phys.* **1975**, *53*, 700–706.
40. Brown, C. M.; Ginter, M. L. Absorption Spectrum of Au I between 1300 and 1900 Å. *J. Opt. Soc. Am.* **1978**, *68*, 243–246.
41. Maria, R.; Jean-Francois, W. The Spectrum of Singly Ionized Gold, Au II. *Phys. Scr.* **1997**, *55*, 690.
42. Chen, E. C. M.; Wentworth, W. E. The Experimental Values of Atomic Electron Affinities. Their Selection and Periodic Behavior. *J. Chem. Educ.* **1975**, *52*, 486.
43. Ding, D.; Mou, T.; Feng, M.; Jiang, X. Utility of Ligand Effect in Homogenous Gold Catalysis: Enabling Regiodivergent Π-Bond-Activated Cyclization. *J. Am. Chem. Soc.* **2016**, *138*, 5218–5221.
44. Nkosi, B.; Coville, N. J.; Hutchings, G. J.; Adams, M. D.; Friedl, J.; Wagner, F. E. Hydrochlorination of Acetylene Using Gold Catalysts: A Study of Catalyst Deactivation. *J. Catal.* **1991**, *128*, 366–377.
45. Schmidbaur, H. *Naturewiss. Rundsch.* **1995**, *48*, 443.

46. Hashmi, A. S. K. The Catalysis Gold Rush: New Claims. *Angew. Chem., Int. Ed.* **2005**, *44*, 6990–6993.
47. Dyker, G. An Eldorado for Homogeneous Catalysis? *Angew. Chem., Int. Ed.* **2000**, *39* (23), 4237–4239.
48. Hashmi, A. S. K.; Frost, T. M.; Bats, J. W. Highly Selective Gold-Catalyzed Arene Synthesis. *J. Am. Chem. Soc.* **2000**, *122*, 11553–11554.
49. Hashmi, A. S. K.; Frost, T. M.; Bats, J. W. Gold Catalysis: On the Phenol Synthesis. *Org. Lett.* **2001**, *3*, 3769–3771.
50. Pearson, R. G. Hard and Soft Acids and Bases. *J. Am. Chem. Soc.* **1963**, *85*, 3533–3539.
51. Pearson, R. G. Hard and Soft Acids and Bases, Hsab, Part 1: Fundamental Principles. *J. Chem. Educ.* **1968**, *45*, 581.
52. Pearson, R. G. Hard and Soft Acids and Bases, Hsab, Part II: Underlying Theories. *J. Chem. Educ.* **1968**, *45*, 643.
53. Abdou, H. E.Mohamed, A. A.Fackler, J. P.,Jr. Gold(I) Nitrogen Chemistry. In *Gold Chemistry*; Mohr, P. D. F. , Ed.; John Wiley & Sons: 2009.
54. Henrique, T. J.; Stefan, B.; Mathieu, C. Cationic Gold(I) Complexes: Highly Efficient Catalysts for the Addition of Alcohols to Alkynes. *Angew. Chem., Int. Ed.* **1998**, *37*, 1415–1418.
55. Joost, M.; Zeineddine, A.; Estévez, L.; Mallet–Ladeira, S.; Miqueu, K.; Amgoune, A.; Bourissou, D. Facile Oxidative Addition of Aryl Iodides to Gold(I) by Ligand Design: Bending Turns on Reactivity. *J. Am. Chem. Soc.* **2014**, *136*, 14654–14657.
56. Martell, A. E. The Chelate Effect. In *Werner Centennial*; American Chemical Society: 1967; Vol. 62, pp 272–294.
57. Crespo, O.; Gimeno, M. C.; Laguna, A.; Jones, P. G. Two-, Three- and Four-Co-Ordinate Gold(I) Complexes of 1,2-Bis(Diphenylphosphino)-1,2-Dicarba-Closo-Dodecaborane. *J. Chem. Soc., Dalton Trans.* **1992**, 1601–1605.
58. Wang, W.; Hammond, G. B.; Xu, B. Ligand Effects and Ligand Design in Homogeneous Gold(I) Catalysis. *J. Am. Chem. Soc.* **2012**, *134*, 5697–5705.
59. Ebule, R. E.; Deepika, M.; Hammond, G. B.; Xu, B. Ligand Effects in the Gold Catalyzed Hydration of Alkynes. *Adv. Syn. Catal.* **2016**, *358*, 1478–1481.
60. Roth, K. E.; Blum, S. A. Relative Kinetic Basicities of Organogold Compounds. *Organometallics* **2010**, *29*, 1712–1716.
61. Markham, J. P.; Staben, S. T.; Toste, F. D. Gold(I)-Catalyzed Ring Expansion of Cyclopropanols and Cyclobutanols. *J. Am. Chem. Soc.* **2005**, *127*, 9708–9709.
62. Wang, Z. J.; Benitez, D.; Tkatchouk, E.; Goddard, W. A., 3rd; Toste, F. D. Mechanistic Study of Gold(I)-Catalyzed Intermolecular Hydroamination of Allenes. *J. Am. Chem. Soc.* **2010**, *132*, 13064–13071.
63. Leyva, A.; Zhang, X.; Corma, A. Chemoselective Hydroboration of Alkynes Vs. Alkenes over Gold Catalysts. *Chem. Commun.* **2009** (33), 4947–4949.
64. Leyva, A.; Corma, A. Isolable Gold(I) Complexes Having One Low-Coordinating Ligand as Catalysts for the Selective Hydration of Substituted Alkynes at Room Temperature without Acidic Promoters. *J. Org. Chem.* **2009**, *74*, 2067–2074.

65. Zhang, D. H.; Yao, L. F.; Wei, Y.; Shi, M. Gold(I)-Catalyzed Cycloisomerization of 1,6-Diynes: Synthesis of 2,3-Disubstituted 3-Pyrroline Derivatives. *Angew. Chem., Int. Ed. Engl.* **2011**, *50*, 2583–2587.
66. Leyva-Perez, A.; Cabrero-Antonino, J. R.; Cantin, A.; Corma, A. Gold(I) Catalyzes the Intermolecular Hydroamination of Alkynes with Imines and Produces α,α′,N-Triarylbisenamines: Studies on Their Use as Intermediates in Synthesis. *J. Org. Chem.* **2010**, *75*, 7769–7780.
67. Wang, Y.; Wang, Z.; Li, Y.; Wu, G.; Cao, Z.; Zhang, L. A General Ligand Design for Gold Catalysis Allowing Ligand-Directed Anti-Nucleophilic Attack of Alkynes. *Nat. Commun.* **2014**, *5*, 3470.
68. Livendahl, M.; Goehry, C.; Maseras, F.; Echavarren, A. M. Rationale for the Sluggish Oxidative Addition of Aryl Halides to Au(I). *Chem. Commun.* **2014**, *50*, 1533–1536.
69. Shiotani, A.; Schmidbaur, H. Organogold-Chemie Ix. Versuche Zur Oxydativen Addition an Organogold-Komplexen. *J. Organomet. Chem.* **1972**, *37*, C24–C26.
70. Tamaki, A.; Kochi, J. K. Catalytic Mechanism Involving Oxidative Addition in the Coupling of Alkylgold(I) with Alkyl Halides. *J. Organomet. Chem.* **1972**, *40*, C81–C84.
71. Johnson, A.; Puddephatt, R. J. Oxidative Addition Reactions of Methylgold (I) Compounds. *Inorg. Nucl. Chem. Lett.* **1973**, *9*, 1175–1177.
72. Tamaki, A.; Kochi, J. K. Dialkylaurate(I) Complexes and the Synthesis of Trialkylgold(III) Compounds. *J. Organomet. Chem.* **1973**, *51*, C39–C42.
73. Tamaki, A.; Kochi, J. K. Reactions of Dialkylaurate(I) with Electrophiles: Synthesis of Trialkylgold(III) Compounds. *J. Chem. Soc., Dalton Trans.* **1973**, 2620–2626.
74. Tamaki, A.; Kochi, J. K. Oxidative Addition in the Coupling of Alkylgold(I) with Alkyl Halides. *J. Organomet. Chem.* **1974**, *64*, 411–425.
75. Johnson, A.; Puddephatt, R. J. Oxidative Addition Reactions of Methyl Iodide with Some Methylgold(I) Compounds. *J. Organomet. Chem.* **1975**, *85*, 115–121.
76. Schuster, O.; Schmidbaur, H. The Course of Oxidative Addition Reactions of Haloalkynes and Haloalkenes to Dimethyl- and Dialkynylaurate(I) Anions $[RAuR]^-$. *Inorg. Chim. Acta* **2006**, *359*, 3769–3775.
77. Corma, A.; Juárez, R.; Boronat, M.; Sánchez, F.; Iglesias, M.; García, H. Gold Catalyzes the Sonogashira Coupling Reaction without the Requirement of Palladium Impurities. *Chem. Commun.* **2011**, *47*, 1446–1448.
78. Robinson, P. S. D.; Khairallah, G. N.; da Silva, G.; Lioe, H.; O'Hair, R. A. J. Gold-Mediated C-I Bond Activation of Iodobenzene. *Angew. Chem., Int. Ed.* **2012**, *51*, 3812–3817.
79. Lauterbach, T.; Livendahl, M.; Rosellón, A.; Espinet, P.; Echavarren, A. M. Unlikeliness of Pd-Free Gold(I)-Catalyzed Sonogashira Coupling Reactions. *Org. Lett.* **2010**, *12*, 3006–3009.
80. Cerrada, E.; Jones, P. G.; Laguna, A.; Laguna, M. Synthesis and Reactivity of Heteroleptic Complexes of Gold with 2-Thioxo-1,3-Dithiole-4,5-Dithiolate (Dmit). X-Ray Structure of [Au2(M-Dmit)(Pph3)2], (Nbu4)[Au(Dmit)(Pph3)], and (Ppn)[Au(Dmit)(C6f5)2]. *Inorg. Chem.* **1996**, *35*, 2995–3000.
81. Guenther, J.; Mallet-Ladeira, S.; Estevez, L.; Miqueu, K.; Amgoune, A.; Bourissou, D. Activation of Aryl Halides at Gold(I): Practical Synthesis of (P,C) Cyclometalated Gold(III) Complexes. *J. Am. Chem. Soc.* **2014**, *136*, 1778–1781.

82. Fernandez, I.; Wolters, L. P.; Bickelhaupt, F. M. Controlling the Oxidative Addition of Aryl Halides to Au(I). *J. Comput. Chem.* **2014**, *35*, 2140–2145.
83. Parish, R. V. Organogold Chemistry: II Reactions. *Gold Bull.* **1997**, *30*, 55–62.
84. Schmidbaur, H.; Schier, A. Aurophilic Interactions as a Subject of Current Research: An up-Date. *Chem. Soc. Rev.* **2012**, *41*, 370–412.
85. Yoshinari, N.; Kitani, N.; Tsukuda, T.; Konno, T. [M-1,2-Bis(Diphenylphosphanyl)Benzene-K(2) P:P′]Bis[Chloridogold(I)]. *Acta Crystallogr., Sect. E: Struct. Rep.* **2011**, *67* (Pt 1), m121–m121.
86. Partyka, D. V.; Updegraff Iii, J. B.; Zeller, M.; Hunter, A. D.; Gray, T. G. Gold(I) Halide Complexes of Bis(Diphenylphosphine)Diphenyl Ether Ligands: A Balance of Ligand Strain and Non-Covalent Interactions. *Dalton Trans.* **2010**, *39*, 5388–5397.
87. Besenyei, G.; Bitter, I.; Párkányi, L.; Szalontai, G.; Baranyai, P.; Kunsági-Máté, É.; Faigl, F.; Grün, A.; Kubinyi, M. A New Xantphos-Type Ligand and Its Gold(I) Complexes: Synthesis, Structure, Luminescence. *Polyhedron* **2013**, *55*, 57–66.
88. Schmidbaur, H.; Schier, A. A Briefing on Aurophilicity. *Chem. Soc. Rev.* **2008**, *37*, 1931–1951.
89. Fackler, J. P. Metal-Metal Bond Formation in the Oxidative Addition to Dinuclear Gold(I) Species. Implications from Dinuclear and Trinuclear Gold Chemistry for the Oxidative Addition Process Generally. *Polyhedron* **1997**, *16*, 1–17.
90. Bennett, M. A.; Welling, L. L.; Willis, A. C. Synthesis and Structure of [Au5(C6h4pph2)4]+: A Cycloaurated Cation Containing a Pair of Ipso-Carbon−Digold Interactions. *Inorg. Chem.* **1997**, *36*, 5670–5672.
91. Henrique, T. J. Oxidative Addition to Gold(I): A New Avenue in Homogeneous Catalysis with Au. *Angew. Chem., Int. Ed.* **2015**, *54*, 5556–5558.
92. Zeineddine, A.; Estévez, L.; Mallet-Ladeira, S.; Miqueu, K.; Amgoune, A.; Bourissou, D. Rational Development of Catalytic Au(I)/Au(III) Arylation Involving Mild Oxidative Addition of Aryl Halides. *Nat. Commun.* **2017**, *8*, 565.
93. Harper, M. J.; Arthur, C. J.; Crosby, J.; Emmett, E. J.; Falconer, R. L.; Fensham-Smith, A. J.; Gates, P. J.; Leman, T.; McGrady, J. E.; Bower, J. F.; Russell, C. A. Oxidative Addition, Transmetalation, and Reductive Elimination at a 2,2′-Bipyridyl-Ligated Gold Center. *J. Am. Chem. Soc.* **2018**, *140*, 4440–4445.
94. Joost, M.; Estévez, L.; Miqueu, K.; Amgoune, A.; Bourissou, D. Oxidative Addition of Carbon–Carbon Bonds to Gold. *Angew. Chem., Int. Ed.* **2015**, *54*, 5236–5240.
95. Huang, L.; Rominger, F.; Rudolph, M.; Hashmi, A. S. K. A General Access to Organogold(III) Complexes by Oxidative Addition of Diazonium Salts. *Chem. Commun.* **2016**, *52*, 6435–6438.
96. Winston, M. S.; Wolf, W. J.; Toste, F. D. Photoinitiated Oxidative Addition of CF_3I to Gold(I) and Facile Aryl-CF_3 Reductive Elimination. *J. Am. Chem. Soc.* **2014**, *136*, 7777–7782.
97. Tlahuext-Aca, A.; Hopkinson, M. N.; Daniliuc, C. G.; Glorius, F. Oxidative Addition to Gold(I) by Photoredox Catalysis: Straightforward Access to Diverse (C,N)-Cyclometalated Gold(III) Complexes. *Chem.—Eur. J.* **2016**, *22*, 11587–11592.
98. Hopkinson, M. N.; Tlahuext-Aca, A.; Glorius, F. Merging Visible Light Photoredox and Gold Catalysis. *Acc. Chem. Res.* **2016**, *49*, 2261–2272.
99. Shu, X.-z.; Zhang, M.; He, Y.; Frei, H.; Toste, F. D. Dual Visible Light Photoredox and Gold-Catalyzed Arylative Ring Expansion. *J. Am. Chem. Soc.* **2014**, *136*, 5844–5847.

100. Patil, D. V.; Yun, H.; Shin, S. Catalytic Cross-Coupling of Vinyl Golds with Diazonium Salts under Photoredox and Thermal Conditions. *Adv. Synth. Catal.* **2015**, *357*, 2622–2628.
101. Huang, L.; Rudolph, M.; Rominger, F.; Hashmi, A. S. K. Photosensitizer-Free Visible-Light-Mediated Gold-Catalyzed 1,2-Difunctionalization of Alkynes. *Angew. Chem., Int. Ed.* **2016**, *55*, 4808–4813.
102. Chinchilla, R.; Nájera, C. The Sonogashira Reaction: A Booming Methodology in Synthetic Organic Chemistry. *Chem. Rev.* **2007**, *107*, 874–922.
103. Stille, J. K. The Palladium-Catalyzed Cross-Coupling Reactions of Organotin Reagents with Organic Electrophiles [New Synthetic Methods (58)]. *Angew. Chem., Int. Ed.* **1986**, *25*, 508–524.
104. King, A. O.; Okukado, N.; Negishi, E.-i. Highly General Stereo-, Regio-, and Chemo-Selective Synthesis of Terminal and Internal Conjugated Enynes by the Pd-Catalysed Reaction of Alkynylzinc Reagents with Alkenyl Halides. *J. Chem. Soc., Chem. Commun.* **1977**, 683–684.
105. Casado, A. L.; Espinet, P. A Novel Reversible Aryl Exchange Involving Two Organometallics: Mechanism of the Gold(I)-Catalyzed Isomerization of Trans-[Pdr2l2] Complexes (R = Aryl, L = Sc4h8). *Organometallics* **1998**, *17*, 3677–3683.
106. Jones, L. A.; Sanz, S.; Laguna, M. Gold Compounds as Efficient Co-Catalysts in Palladium-Catalysed Alkynylation. *Catal. Today* **2007**, *122*, 403–406.
107. Sonogashira, K.; Tohda, Y.; Hagihara, N. A Convenient Synthesis of Acetylenes: Catalytic Substitutions of Acetylenic Hydrogen with Bromoalkenes, Iodoarenes and Bromopyridines. *Tetrahedron Lett.* **1975**, *16*, 4467–4470.
108. Elangovan, A.; Wang, Y.-H.; Ho, T.-I. Sonogashira Coupling Reaction with Diminished Homocoupling. *Org. Lett.* **2003**, *5*, 1841–1844.
109. Hashmi, A. S. K.; Döpp, R.; Lothschütz, C.; Rudolph, M.; Riedel, D.; Rominder, F. Scope and Limitations of Palladium-Catalyzed Cross-Coupling Reactions with Organogold Compounds. *Adv. Synth. Catal.* **2010**, *352*, 1307–1314.
110. Shi, Y.; Roth, K. E.; Ramgren, S. D.; Blum, S. A. Catalyzed Catalysis Using Carbophilic Lewis Acidic Gold and Lewis Basic Palladium: Synthesis of Substituted tenolides and Isocoumarins. *J. Am. Chem. Soc.* **2009**, *131*, 18022–18023.
111. Garcia-Dominguez, P.; Nevado, C. Au-Pd Bimetallic Catalysis: The Importance of Anionic Ligands in Catalyst Speciation. *J. Am. Chem. Soc.* **2016**, *138*, 3266–3269.
112. Hashmi, A. S. K.; Lothschütz, C.; Döpp, R.; Ackermann, M.; De Buck Becker, J.; Rudolph, M.; Scholz, C.; Rominger, F. On Homogeneous Gold/Palladium Catalytic Systems. *Adv. Synth. Catal.* **2012**, *354*, 133–147.
113. Hashmi, A. S. K.; Lothschütz, C.; Döpp, R.; Matthias, R.; Ramamurthi, D. T.; Rominger, F. Gold and Palladium Combined for Cross-Coupling. *Angew. Chem., Int. Ed.* **2009**, *48*, 8243–8246.
114. Shi, Y.; Peterson, S. M.; Haberaecker, W. W.; Blum, S. A. Alkynes as Stille Reaction Pseudohalides: Gold- and Palladium-Cocatalyzed Synthesis of Tri- and Tetra-Substituted Olefins. *J. Am. Chem. Soc.* **2008**, *130*, 2168–2169.
115. Müller, D. S.; Marek, I. Copper Mediated Carbometalation Reactions. *Chem. Soc. Rev.* **2016**, *45*, 4552–4566.

116. Shirakawa, E.; Yoshida, H.; Kurahashi, T.; Nakao, Y.; Hiyama, T. Carbostannylation of Alkynes Catalyzed by an Iminophosphine−Palladium Complex. *J. Am. Chem. Soc.* **1998**, *120*, 2975–2976.
117. Sladek, A.; Hofreiter, S.; Paul, M.; Schmidbaur, H. Sodium Tetraphenylborate as a Phenylating Agent for Gold(I) Complexes. *J. Organomet. Chem.* **1995**, *501*, 47–51.
118. Forward, J. M.; Fackler, J. P.; Staples, R. J. Synthesis and Structural Characterization of the Luminescent Gold(I) Complex [(Metpa)3aui]I3. Use of Nabph4 as a Phenyl-Transfer Reagent to Form [(Metpa)Auph](Bph4) and (Tpa)Auph. *Organometallics* **1995**, *14*, 4194–4198.
119. Cresswell, A. J.; Lloyd-Jones, G. C. Room-Temperature Gold-Catalysed Arylation of Heteroarenes: Complementarity to Palladium Catalysis. *Chem.—Eur. J.* **2016**, *22*, 12641–12645.
120. Cambeiro, X. C.; Ahlsten, N.; Larrosa, I. Au-Catalyzed Cross-Coupling of Arenes Via Double C–H Activation. *J. Am. Chem. Soc.* **2015**, *137*, 15636–15639.
121. Hofer, M.; Genoux, A.; Kumar, R.; Nevado, C. Gold-Catalyzed Direct Oxidative Arylation with Boron Coupling Partners. *Angew. Chem., Int. Ed. Engl* **2017**, *56*, 1021–1025.
122. Kumar, R.; Linden, A.; Nevado, C. Evidence for Direct Transmetalation of Au(III)-F with Boronic Acids. *J. Am. Chem. Soc.* **2016**, *138*, 13790–13793.
123. Maity, A.; Sulicz, A. N.; Deligonul, N.; Zeller, M.; Hunter, A. D.; Gray, T. G. Suzuki–Miyaura Coupling of Arylboronic Acids to Gold(III). *Chem. Sci.* **2015**, *6*, 981–986.
124. Smith, D. A.; Roşca, D.-A.; Bochmann, M. Selective Au–C Cleavage in (C^N^C)Au(III) Aryl and Alkyl Pincer Complexes. *Organometallics* **2012**, *31*, 5998–6000.
125. Roşca, D.-A.; Smith, D. A.; Bochmann, M. Cyclometallated Gold(Iii) Hydroxides as Versatile Synthons for Au–N, Au–C Complexes and Luminescent Compounds. *Chem. Commun.* **2012**, *48*, 7247–7249.
126. Hofer, M.; Gomez-Bengoa, E.; Nevado, C. A Neutral Gold(III)–Boron Transmetalation. *Organometallics* **2014**, *33*, 1328–1332.
127. Shi, Y.; Blum, S. A. Gold and Rhodium Transmetalation: Mechanistic Insights and Dual-Metal Reactivity. *Organometallics* **2011**, *30*, 1776–1779.
128. LaLonde, R. L.; Brenzovich, J. W. E.; Benitez, D.; Tkatchouk, E.; Kelley, K.; Goddard, I. I. I. W. A.; Toste, F. D. Alkylgold Complexes by the Intramolecular Aminoauration of Unactivated Alkenes. *Chem. Sci.* **2010**, *1*, 226–233.
129. Weber, D.; Tarselli, M. A.; Gagné, M. R. Mechanistic Surprises in the Gold(I)-Catalyzed Intramolecular Hydroarylation of Allenes. *Angew. Chem., Int. Ed.* **2009**, *48*, 5733–5736.
130. Liu, L.-P.; Xu, B.; Mashuta, M. S.; Hammond, G. B. Synthesis and Structural Characterization of Stable Organogold(I) Compounds. Evidence for the Mechanism of Gold-Catalyzed Cyclizations. *J. Am. Chem. Soc.* **2008**, *130*, 17642–17643.
131. Goldberg, K. I.; Yan, J.; Breitung, E. M. Energetics and Mechanisms of Carbon-Carbon and Carbon-Iodide Reductive Elimination from a Pt(Iv) Center. *J. Am. Chem. Soc.* **1995**, *117*, 6889–6896.
132. Roy, A. H.; Hartwig, J. F. Directly Observed Reductive Elimination of Aryl Halides from Monomeric Arylpalladium(II) Halide Complexes. *J. Am. Chem. Soc.* **2003**, *125*, 13944–13945.

133. Joost, M.; Amgoune, A.; Bourissou, D. Reactivity of Gold Complexes Towards Elementary Organometallic Reactions. *Angew. Chem., Int. Ed.* **2015**, *54*, 15022–15045.
134. Brown, M. P.; Puddephatt, R. J.; Upton, C. E. E. Mechanism of Reductive Elimination of Ethane from Some Halogenotrimethylbis(Tertiary Phosphine)Platinum(IV) Complexes. *J. Chem. Soc., Dalton. Trans.* **1974**, 2457–2465.
135. Komiya, S.; Kochi, J. K. Electrophilic Cleavage of Organogold Complexes with Acids. The Mechanism of the Reductive Elimination of Dialkyl(Aniono)Gold(III)Species. *J. Am. Chem. Soc.* **1976**, *98*, 7599–7607.
136. Komiya, S.; Albright, T. A.; Hoffmann, R.; Kochi, J. K. Reductive Elimination and Isomerization of Organogold Complexes. Theoretical Studies of Trialkylgold Species as Reactive Intermediates. *J. Am. Chem. Soc.* **1976**, *98*, 7255–7265.
137. Tamaki, A.; Magennis, S. A.; Kochi, J. K. Catalysis by Gold. Alkyl Isomerization, *Cis-Trans* Rearrangement, and Reductive Elimination of Alkygold(III) Complexes. *J. Am. Chem. Soc.* **1974**, *96*, 6140–6148.
138. Kuch, P. L.; Tobias, R. S. Synthesis of Cationic Dialkylgold(III) Complexes: Nature of the Facile Reductive Elimination of Alkane. *J. Organomet. Chem.* **1976**, *122*, 429–446.
139. Vicente, J.; Dolores Bermudez, M.; Escribano, J. Gold in Organic Synthesis. Preparation of Symmetrical and Unsymmetrical Biaryls Via Carbon-Carbon Coupling from Cis-Diarylgold(III) Complexes. *Organometallics* **1991**, *10*, 3380–3384.
140. Vicente, J.; Bermúdez, M. D.; Escribano, J.; Carrillo, M. P.; Jones, P. G. Synthesis of Intermediates in the C–H Activation of Acetone with 2-Phenylazophenylgold(III) Complexes and in the C–C Coupling of Aryl Groups from Diarylgold(III) Complexes. Crystal and Molecular Structures of [Au{C6h3(N=Nc6h4me-4′)-2-Me-5}(Acac-C)Cl](Acac = Acetylacetonate), Cis-[Au(C6h4n=Nph-2)Cl2(Pph3)] and [Au(C6h4ch2nme2-2)(C6f5)Cl]. *J. Chem. Soc., Dalton. Trans.* **1990**, 3083–3089.
141. Ball, L. T.; Lloyd-Jones, G. C.; Russell, C. A. Gold-Catalyzed Direct Arylation. *Science* **2012**, *337* (6102), 1644–1648.
142. Lawrence Kuch, P.; Stuart Tobias, R. Synthesis of Cationic Dialkylgold(III) Complexes: Nature of the Facile Reductive Elimination of Alkane. *J. Organomet. Chem.* **1976**, *122*, 429–446.
143. Komiya, S.; Ozaki, S.; Shibue, A. Leaving Group Selectivity in Reductive Elimination from Organogold(Iii) Complexes. *J. Chem. Soc., Chem. Commun.* **1986**, 1555–1556.
144. Schuster, O.; Schmidbaur, H. Preparative Routes to the First Tri- and Tetra(Alkynyl)Gold(III) Compounds: (L)Au(C⋮Cr)3 and [Er4]+ [Au(C⋮Cr)4]. *Organometallics* **2005**, *24*, 2289–2296.
145. Wolf, W. J.; Winston, M. S.; Toste, F. D. Exceptionally Fast Carbon-Carbon Bond Reductive Elimination from Gold(Iii). *Nat. Chem* **2014**, *6*, 159–164.
146. Winston, M. S.; Wolf, W. J.; Toste, F. D. Halide-Dependent Mechanisms of Reductive Elimination from Gold(III). *J. Am. Chem. Soc.* **2015**, *137*, 7921–7928.
147. Mankad, N. P.; Toste, F. D. C(Sp(3))-F Reductive Elimination from Alkylgold(III) Fluoride Complexes. *Chem. Sci.* **2012**, *3*, 72–76.
148. Komiya, S.; Albright, T. A.; Hoffmann, R.; Kochi, J. K. Reductive Elimination and Isomerization of Organogold Complexes. Theoretical Studies of Trialkylgold Species as Reactive Intermediates. *J. Am. Chem. Soc.* **1976**, *98*, 7255–7265.

149. Kleinhans, G.; Hansmann, M. M.; Guisado-Barrios, G.; Liles, D. C.; Bertrand, G.; Bezuidenhout, D. I. Nucleophilic T-Shaped (Lxl)Au(I)-Pincer Complexes: Protonation and Alkylation. *J. Am. Chem. Soc.* **2016**, *138*, 15873–15876.
150. Wu, Q.; Du, C.; Huang, Y.; Liu, X.; Long, Z.; Song, F.; You, J. Stoichiometric to Catalytic Reactivity of the Aryl Cycloaurated Species with Arylboronic Acids: Insight into the Mechanism of Gold-Catalyzed Oxidative C(Sp2)–H Arylation. *Chem. Sci.* **2015**, *6*, 288–293.
151. Komiya, S.; Kochi, J. K. Electrophilic Cleavage of Organogold Complexes with Acids. The Mechanism of the Reductive Elimination of Dialkyl(Aniono)Gold(III) Species. *J. Am. Chem. Soc.* **1976**, *98*, 7599–7607.
152. Tolman, C. A. Phosphorus Ligand Exchange Equilibriums on Zerovalent Nickel. Dominant Role for Steric Effects. *J. Am. Chem. Soc.* **1970**, *92*, 2956–2965.
153. Komiya, S.; Shibue, A. Steric and Electronic Effects of the Tertiary Phosphine Ligand on the Dissociative Reductive Elimination from Cis-Aryldimethyl(Triarylphosphine)Gold(III). *Organometallics* **1985**, *4*, 684–687.
154. Tolman, C. A. Steric Effects of Phosphorus Ligands in Organometallic Chemistry and Homogeneous Catalysis. *Chem. Rev.* **1977**, *77*, 313–348.
155. Sonogashira, K. Development of Pd–Cu Catalyzed Cross-Coupling of Terminal Acetylenes with Sp2-Carbon Halides. *J. Organomet. Chem.* **2002**, *653*, 46–49.
156. Qian, D.; Zhang, J. Au(I)/Au(III)-Catalyzed Sonogashira-Type Reactions of Functionalized Terminal Alkynes with Arylboronic Acids under Mild Conditions. *Beilstein J. Org. Chem.* **2011**, *7*, 808–812.
157. Zhou, M.-B.; Wei, W.-T.; Xie, Y.-X.; Lei, Y.; Li, J.-H. Palladium-Catalyzed Cross-Coupling of Electron-Poor Terminal Alkynes with Arylboronic Acids under Ligand-Free and Aerobic Conditions. *J. Org. Chem.* **2010**, *75*, 5635–5642.
158. Hashmi, A. S. K. Gold-Catalyzed Organic Reactions. *Chem. Rev.* **2007**, *107*, 3180–3211.
159. Gorin, D. J.; Sherry, B. D.; Toste, F. D. Ligand Effects in Homogeneous Au Catalysis. *Chem. Rev.* **2008**, *108*, 3351–3378.
160. Jiménez-Núñez, E.; Echavarren, A. M. Gold-Catalyzed Cycloisomerizations of Enynes: A Mechanistic Perspective. *Chem. Rev.* **2008**, *108*, 3326–3350.
161. Levin, M. D.; Toste, F. D. Gold-Catalyzed Allylation of Aryl Boronic Acids: Accessing Cross-Coupling Reactivity with Gold. *Angew. Chem., Int. Ed.* **2014**, *53*, 6211–6215.
162. Mankad, N. P.; Toste, F. D. C−C Coupling Reactivity of an Alkylgold(III) Fluoride Complex with Arylboronic Acids. *J. Am. Chem. Soc.* **2010**, *132*, 12859–12861.
163. Corrie, T. J. A.; Ball, L. T.; Russell, C. A.; Lloyd-Jones, G. C. Au-Catalyzed Biaryl Coupling to Generate 5- to 9-Membered Rings: Turnover-Limiting Reductive Elimination Versus Π-Complexation. *J. Am. Chem. Soc.* **2017**, *139*, 245–254.
164. Cambeiro, X. C.; Boorman, T. C.; Lu, P.; Larrosa, I. Redox-Controlled Selectivity of C-H Activation in the Oxidative Cross-Coupling of Arenes. *Angew. Chem., Int. Ed.* **2013**, *52*, 1781–1784.
165. Schuster, O.; Liau, R.-Y.; Schier, A.; Schmidbaur, H. Preparation, Structure and Decomposition of Gold(I) and Gold(III) Acetylide Complexes. *Inorg. Chim. Acta* **2005**, *358*, 1429–1441.

166. Ball, L. T.; Lloyd-Jones, G. C.; Russell, C. A. Gold-Catalyzed Oxidative Coupling of Arylsilanes and Arenes: Origin of Selectivity and Improved Precatalyst. *J. Am. Chem. Soc.* **2014**, *136*, 254–264.
167. Kawai, H.; Wolf, W. J.; DiPasquale, A. G.; Winston, M. S.; Toste, F. D. Phosphonium Formation by Facile Carbon–Phosphorus Reductive Elimination from Gold(III). *J. Am. Chem. Soc.* **2016**, *138*, 587–593.
168. *CRC Handbook of Chemistry and Physics*, 96th ed.; CRC Press: Boca Raton, FL, 2015.
169. Xu, Y.; Zhang, J. Stereochemistry at the Phosphorus Atom During Palladium-Catalysed Formation of Carbon–Phosphorous Bonds and Mechanistic Implications. *J. Chem. Soc., Chem. Commun.* **1986**, 1606–1606.
170. Barbaro, P.; Peruzzini, M.; Ramirez, J. A.; Vizza, F. Rhodium-Mediated Functionalization of White Phosphorus: A Novel Formation of C−P Bonds. *Organometallics* **1999**, *18*, 4237–4240.
171. Gelman, D.; Jiang, L.; Buchwald, S. L. Copper-Catalyzed C−P Bond Construction Via Direct Coupling of Secondary Phosphines and Phosphites with Aryl and Vinyl Halides. *Org. Lett.* **2003**, *5*, 2315–2318.
172. Currie, L.; Rocchigiani, L.; Hughes, D. L.; Bochmann, M. Carbon–Sulfur Bond Formation by Reductive Elimination of Gold(III) Thiolates. *Dalton Trans.* **2018**, *47*, 6333–6343.
173. Kung, K. K.-Y.; Ko, H.-M.; Cui, J.-F.; Chong, H.-C.; Leung, Y.-C.; Wong, M.-K. Cyclometalated Gold(III) Complexes for Chemoselective Cysteine Modification Via Ligand Controlled C–S Bond-Forming Reductive Elimination. *Chem. Commun.* **2014**, *50*, 11899–11902.
174. Messina, M. S.; Stauber, J. M.; Waddington, M. A.; Rheingold, A. L.; Maynard, H. D.; Spokoyny, A. M. Organometallic Gold(III) Reagents for Cysteine Arylation. *J. Am. Chem. Soc.* **2018**, *140*, 7065–7069.
175. Kim, J. H.; Mertens, R. T. Amal Agarwal, Parkin, S.; Berger, G.; Awuah, S. G. *Direct Intramolecular Carbon(sp^2)-Nitrogen(sp^2) Reductive Elimination*. *Unpublished*, 2018.
176. Eichman, C. C.; Stambuli, J. P. Transition Metal Catalyzed Synthesis of Aryl Sulfides. *Molecules* **2011**, *16*, 590.
177. Qiao, Z.; Jiang, X. Recent Developments in Sulfur–Carbon Bond Formation Reaction Involving Thiosulfates. *Org. Biomol. Chem.* **2017**, *15*, 1942–1946.
178. Timpa, S. D.; Pell, C. J.; Ozerov, O. V. A Well-Defined (Pocop)Rh Catalyst for the Coupling of Aryl Halides with Thiols. *J. Am. Chem. Soc.* **2014**, *136*, 14772–14779.
179. Serra, J.; Parella, T.; Ribas, X. Au(III)-Aryl Intermediates in Oxidant-Free C–N and C–O Cross-Coupling Catalysis. *Chem. Sci.* **2017**, *8*, 946–952.
180. Serra, J.; Whiteoak, C. J.; Acuña-Parés, F.; Font, M.; Luis, J. M.; Lloret-Fillol, J.; Ribas, X. Oxidant-Free Au(I)-Catalyzed Halide Exchange and Csp2–O Bond Forming Reactions. *J. Am. Chem. Soc.* **2015**, *137*, 13389–13397.
181. Marchetti, L.; Kantak, A.; Davis, R.; DeBoef, B. Regioselective Gold-Catalyzed Oxidative C–N Bond Formation. *Org. Lett.* **2015**, *17*, 358–361.
182. Lavy, S.; Miller, J. J.; Pažický, M.; Rodrigues, A-S.; Rominger, F.; Jäkel, C.; Serra, D.; Vinokurov, N.; Limbach, M. Stoichiometric Reductive C-N Bond Formation of Arylgold(III) Complexes with N-Nucleophiles. *Adv. Synth. Catal.* **2010**, *352*, 2993–3000.

183. García-Monforte, M. A.; Martínez-Salvador, S.; Menjón, B. The Trifluoromethyl Group in Transition Metal Chemistry. *Eur. J. Inorg. Chem.* **2012**, 4945–4966.
184. Levin, M. D.; Chen, T. Q.; Neubig, M. E.; Hong, C. M.; Theulier, C. A.; Kobylianskii, I. J.; Janabi, M.; O'Neil, J. P.; Toste, F. D. A Catalytic Fluoride-Rebound Mechanism for $C(sp^3)$-CF_3 Bond Formation. *Science* **2017**, *356*, 1272–1276.
185. Cai, R.; Lu, M.; Aguilera, E. Y.; Xi, Y.; Akhmedov, N. G.; Peterson, J. L.; Chen, H.; Shi, X. Ligand-Assisted Gold-Catalyzed Cross-Coupling with Aryldiazonium Salts: Redox Gold Catalysis without an External Oxidant. *Angew. Chem., Int. Ed.* **2015**, *54*, 8772–8776.
186. Peng, H.; Cai, R.; Xu, C.; Chen, H.; Shi, X. Nucleophile Promoted Gold Redox Catalysis with Diazonium Salts: C–Br, C–S and C–P Bond Formation through Catalytic Sandmeyer Coupling. *Chem. Sci.* **2016**, *7*, 6190–6196.
187. Heck, R. F.; Nolley, J. P. Palladium-Catalyzed Vinylic Hydrogen Substitution Reactions with Aryl, Benzyl, and Styryl Halides. *J. Org. Chem.* **1972**, *37*, 2320–2322.
188. Tsuji, J. *Palladium Reagents and Catalysts*. 1st ed.; Wiley: 2004.
189. Chen, X.; Engle, K. M.; Wang, D-H.; Yu, J-Q. Palladium(II)-Catalyzed C-H Activation/C-C Cross-Coupling Reactions: Versatility and Practicality. *Angew. Chem., Int. Ed.* **2009**, *48*, 5094–5115.
190. Lemke, F. R.; Bullock, R. M. Insertion And .Beta.-Hydride Elimination Reactions of Ruthenium/Zirconium Complexes Containing C2 Bridges with Bond Orders of 1, 2, and 3. *Organometallics* **1992**, *11* (12), 4261–4267.
191. Alexanian, E. J.; Hartwig, J. F. Pt-Mechanistic Study of the B-Hydrogen Elimination from Organoplatinum(II) Enolate Complexes. *J. Am. Chem. Soc.* **2008**, *130*, 15627.
192. Acetaldehyde. In *Ullmann's Encyclopedia of Industrial Chemistry*.
193. Chambrier, I.; Roşca, D.-A.; Fernandez-Cestau, J.; Hughes, D. L.; Budzelaar, P. H. M.; Bochmann, M. Formation of Gold(III) Alkyls from Gold Alkoxide Complexes. *Organometallics* **2017**, *36*, 1358–1364.
194. Tamaki, A.; Magennis, S. A.; Kochi, J. K. Catalysis by Gold. Alkyl Isomerization, Cis-Trans Rearrangement, and Reductive Elimination of Alkylgold(III) Complexes. *J. Am. Chem. Soc.* **1974**, *96*, 6140–6148.
195. Tamaki, A.; Kochi, J. K. Formation and Decomposition of Alkyl-Gold(I) Complexes. *J. Organomet. Chem.* **1973**, *61*, 441–450.
196. Ting, C.-M.; Hsu, Y.-L.; Liu, R.-S. Gold-Catalyzed Isomerization of Unactivated Allenes into 1,3-Dienes under Ambient Conditions. *Chem. Commun.* **2012**, *48*, 6577–6579.
197. Alcaide, B.; Almendros, P.; del Campo, T. M.; Fernández, I. Fascinating Reactivity in Gold Catalysis: Synthesis of Oxetenes through Rare 4-Exo-Dig Allene Cyclization and Infrequent B-Hydride Elimination. *Chem. Commun.* **2011**, *47*, 9054–9056.
198. Gaël, U.; Guy, B. A- Und B-Hydridabstraktion in Gold(I)-Alkylkomplexen. *Angew. Chem.* **2013**, *125*, 11599–11602.
199. Hashmi, A. S. K.; Schwarz, L.; Ji-Hyun, C.; Frost, T. M. A New Gold-Catalyzed C−C Bond Formation. *Angew. Chem., Int. Ed.* **2000**, *39*, 2285–2288.
200. Escalle, A.; Mora, G.; Gagosz, F.; Mézailles, N.; Le Goff, X. F.; Jean, Y.; Le Floch, P. Cationic Dimetallic Gold Hydride Complex Stabilized by a Xantphos-Phosphole Ligand: Synthesis,

X-Ray Crystal Structure, and Density Functional Theory Study. *Inorg. Chem.* **2009**, *48*, 8415–8422.

201. Tsui, E. Y.; Müller, P.; Sadighi, J. P. Reactions of a Stable Monomeric Gold(I) Hydride Complex. *Angew. Chem., Int. Ed.* **2008**, *47*, 8937–8940.
202. Crawford, M-J.; Klapötke, T. M. Hydrides and Iodides of Gold. *Angew. Chem., Int. Ed.* **2002**, *41*, 2269–2271.
203. Wang, X.; Andrews, L. Gold Hydrides AuH and (H2)AuH and the AuH3 Transition State Stabilized in (H2)AuH3: Infrared Spectra and Dft Calculations. *J. Am. Chem. Soc.* **2001**, *123*, 12899–12900.
204. Klatt, G.; Xu, R.; Pernpointner, M.; Molinari, L.; Quang Hung, T.; Rominger, F.; Hashmi, A. S. K.; Köppel, H. Are β-H-Eliminations or Alkene Insertions Feasible Elementary Steps in Catalytic Cycles Involving Gold(I) Alkyl Species or Gold(I) Hydrides? *Chem.—Eur. J.* **2013**, *19*, 3954–3961.
205. Castiñeira Reis, M.; López, C. S.; Kraka, E.; Cremer, D.; Faza, O. N. Rational Design in Catalysis: A Mechanistic Study of B-Hydride Eliminations in Gold(I) and Gold(III) Complexes Based on Features of the Reaction Valley. *Inorg. Chem.* **2016**, *55*, 8636–8645.
206. Mankad, N. P.; Toste, F. D. C(Sp3)–F Reductive Elimination from Alkylgold(III) Fluoride Complexes. *Chem. Sci.* **2012**, *3*, 72–76.
207. Rekhroukh, F.; Estevez, L.; Mallet-Ladeira, S.; Miqueu, K.; Amgoune, A.; Bourissou, D. B-Hydride Elimination at Low-Coordinate Gold(III) Centers. *J. Am. Chem. Soc.* **2016**, *138*, 11920–11929.
208. Kumar, R.; Krieger, J. P.; Gómez-Bengoa, E.; Fox, T.; Linden, A.; Nevado, C. The First Gold(III) Formate: Evidence for B-Hydride Elimination. *Angew. Chem., Int. Ed.* **2017**, *56*, 12862–12865.
209. Zheng, Z.; Tachikawa, T.; Majima, T. Plasmon-Enhanced Formic Acid Dehydrogenation Using Anisotropic Pd–Au Nanorods Studied at the Single-Particle Level. *J. Am. Chem. Soc.* **2015**, *137*, 948–957.
210. Liu, Q.; Yang, X.; Huang, Y.; Xu, S.; Su, X.; Pan, X.; Xu, J.; Wang, A.; Liang, C.; Wang, X.; Zhang, T. A Schiff Base Modified Gold Catalyst for Green and Efficient H2 Production from Formic Acid. *Energy Environ. Sci.* **2015**, *8*, 3204–3207.
211. Yang, X.; Pachfule, P.; Chen, Y.; Tsumori, N.; Xu, Q. Highly Efficient Hydrogen Generation from Formic Acid Using a Reduced Graphene Oxide-Supported Aupd Nanoparticle Catalyst. *Chem. Commun.* **2016**, *52*, 4171–4174.
212. Ziegler, K.; Krupp, F.; Zosel, K. Eine Einfache Synthese Primärer Alkohole Aus Olefinen. *Angew. Chem., Int. Ed.* **1955**, *67*, 425–426.
213. Natta, G.; Pino, P.; Corradini, P.; Danusso, F.; Mantica, E.; Mazzanti, G.; Moraglio, G. Crystalline High Polymers of A-Olefins. *J. Am. Chem. Soc.* **1955**, *77*, 1708–1710.
214. Tsutomu, M.; Kunio, M.; Atsumu, O. Arylation of Olefin with Aryl Iodide Catalyzed by Palladium. *Bull. Chem. Soc. Jpn.* **1971**, *44*, 581–581.
215. Cinellu, M. A.; Giovanni, M.; Fabio, C.; Sergio, S.; Antonio, Z.; Mario, M. Reactions of Gold(III) Oxo Complexes with Cyclic Alkenes. *Angew. Chem., Int. Ed.* **2005**, *44*, 6892–6895.

216. Langseth, E.; Nova, A.; Tråseth, E. A.; Rise, F.; Øien, S.; Heyn, R. H.; Tilset, M. A Gold Exchange: A Mechanistic Study of a Reversible, Formal Ethylene Insertion into a Gold(III)–Oxygen Bond. *J. Am. Chem. Soc.* **2014**, *136*, 10104–10115.
217. Savjani, N.; Roşca, D. A.; Schormann, M.; Bochmann, M. Gold(III) Olefin Complexes. *Angew. Chem., Int. Ed.* **2013**, *52*, 874–877.
218. Cinellu, M. A.; Giovanni, M.; Fabio, C.; Sergio, S.; Antonio, Z.; Mario, M. Reactions of Gold(III) Oxo Complexes with Cyclic Alkenes. *Angew. Chem., Int. Ed.* **2005**, *117*, 7052–7055.
219. Feriel, R.; Rémy, B.; Abderrahmane, A.; Didier, B. Cationic Gold(III) Alkyl Complexes: Generation, Trapping, and Insertion of Norbornene. *Angew. Chem., Int. Ed.* **2015**, *54*, 1266–1269.
220. Zhukhovitskiy, A. V.; Kobylianskii, I. J.; Wu, C.-Y.; Toste, F. D. Migratory Insertion of Carbenes into Au(III)–C Bonds. *J. Am. Chem. Soc.* **2018**, *140*, 466–474.
221. Rekhroukh, F.; Blons, C.; Estévez, L.; Mallet-Ladeira, S.; Miqueu, K.; Amgoune, A.; Bourissou, D. Gold(III)–Arene Complexes by Insertion of Olefins into Gold–Aryl Bonds. *Chem. Sci.* **2017**, *8*, 4539–4545.

Chapter 3

Computational Investigations into the Mechanisms of Trans-Selective Hydrogenation and Hydrometalation of Alkynes

Lawrence M. Wolf*,[1] and Walter Thiel[2]

[1]Department of Chemistry, University of Massachusetts Lowell, 1 University Avenue, Lowell, Massachusetts 01854, United States

[2]Max-Planck-Institute für Kohlenforschung, D-45470 Mülheim/Ruhr, Germany

***E-mail: Lawrence_Wolf@uml.edu**

An overview on the mechanisms of the trans-selective hydrogenation and hydrometalation of alkynes using a CpRuL catalyst is provided. Unlike the more common mode of hydrogenation, syn, this select ruthenium catalyst system uniquely favors the products resulting from anti-addition across the alkyne π-system. The primary focus is summarizing the results of computational studies on the mechanism of these reactions, including key experimental supporting evidence. This chapter addresses hydrogenation, hydrosilylation, hydrostannation, and hydroboration. An overview of the mechanisms for all of these processes is highlighted.

Introduction

Hydrogenation and hydrometalation of unsaturated systems are reliable synthetic disconnections for complex molecule synthesis. These transformations normally proceed with syn addition of the [M]–H bond across the alkyne π-system. The stereocomplementary anti-addition has been far less established. The development of *E*-selective hydrogenation and hydrometalation has been enabled by the discovery of [Cp*RuL]. Remarkably, this catalyst is capable of delivering H–H and H–[M] across an alkyne in a stepwise but reliably trans-selective manner. The mechanism of these additions has been studied both experimentally and computationally. The combination of computation with experiment has uncovered a level of mechanistic detail that could not have been revealed with either approach alone. The new strategies for trans hydrogenation and hydrometalation have proven to be highly effective in the synthesis of complex natural products (*1*).

Trans-Selective Hydrosilylation

The reduction of alkynes to alkenes belongs to the category of immutable synthetic transformations, invaluable to synthetic chemistry (*2*). The stereoselective semihydrogenation of alkynes to form alkenes has traditionally followed one of two well-established methods: syn delivery of hydrogen to form the cis-configured product or dissolving metal reduction to form the trans product from anti-addition (Scheme 1). The classical Lindlar catalyst is a proven effective method for accessing cis alkenes. While dissolving metal reductions exclusively give the trans alkenes, particularly narrow functional group tolerance hinders its utility for complex molecules with diverse functionality. A more functional group tolerant method for accessing trans alkenes from alkynes will have widespread applicability.

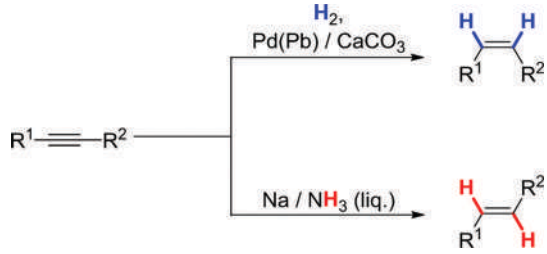

Scheme 1. Classical approaches for the semihydrogenation of alkynes to cis- and trans-configured alkenes.

In 2001, the Trost group developed an indirect method for trans-selective delivery of H_2 across an alkyne involving an initial trans-selective hydrosilylation, followed by protodesilylation (Scheme 2) (*3*). This powerful strategy has widespread utility and has increased the available scope for accessing trans products indirectly (*1*). Nevertheless, the use of tetrabutylammonium fluoride limits the substrate's scope, including sensitivity to base labile functional groups. Hydrosilylation of an internal alkyne can be performed selectively by carefully selecting a substrate that exploits intramolecular hydrogen-bonding-type interactions (*4*).

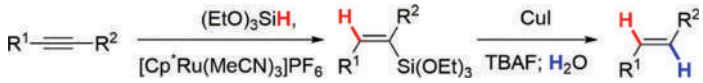

Scheme 2. An indirect strategy for accessing trans alkenes through hydrosilylation (*3*).

The mechanism of adding the H–[Si] moiety in a trans-selective manner is unorthodox and worthy of closer investigation. In an early computational study performed at the B3LYP/6-31G(d)(LANL2DZ) level of theory, Wu et al. focused on the order of insertion (H or SiR_3 first), as well as the regioselectivity (internal or terminal initial delivery) of hydrosilylation of terminal alkynes (Figure 1) (*5*). The oxidative addition and hydride insertion were predicted to take place concertedly. Initial hydride insertion was computed to be favored over silyl insertion by 7.3 kcal/mol. Importantly, Markovnikov regioselectivity was found to be favored over anti-Markovnikov by 1.5 kcal/mol. Interestingly, the intermediate from the initial hydride migration was a low-lying 18-electron metallocyclopropane. The existence of metallocyclopropane intermediates in rhenium–alkyne complexes has been supported both experimentally and theoretically (*6*). The formation of a metallocyclopropene obtained from this study represents a deviation from both the classical and modified Chalk–Harrod mechanisms. The classical Chalk–Harrod mechanism begins with an oxidative addition of the silane to the metal center with hydride migration to the alkyne

occurring first, while the modified version begins with silyl migration (*7*, *8*). In contrast to alternative transition-metal-catalyzed hydrosilylations, this provides the hydrosilylated product resulting from Markovnikov addition. The *E*-selectivity arises from the rotation about the C–C bond that positions the transferred hydride proximal to the Cp ligand. The preference for initial silyl migration over hydride migration was probed using acetylene and was calculated to be 6.6 kcal·mol^{-1}.

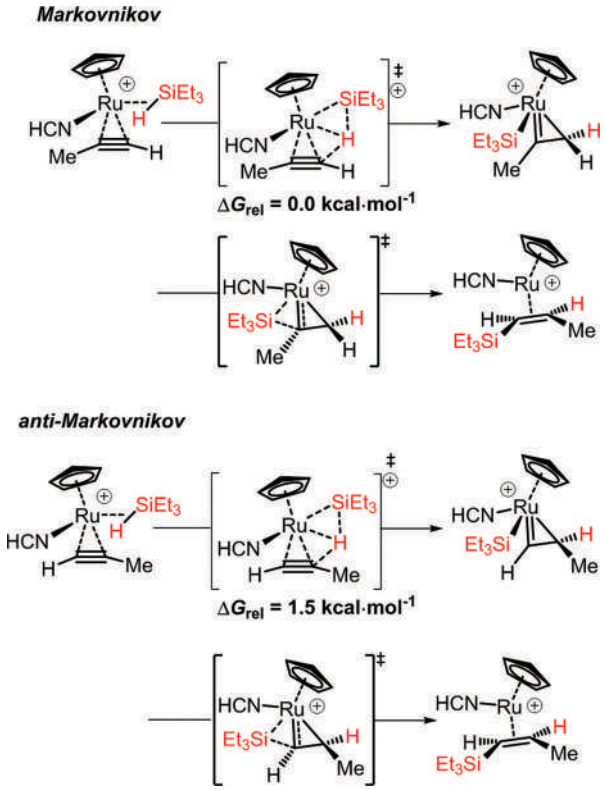

Figure 1. Density functional theory (DFT)-located pathways for Markovnikov and anti-Markovnikov hydrosilylation. The relative energies for the rate-determining TSs are given (*5*).

Encouraged by the results of this previous study, a more detailed computational investigation was conducted on the role of ligand effects on reactivity and selectivity, particularly with respect to ligand sterics (*9*). The study was performed at the solvation model based on density (SMD)($CHCl_3$ or CH_3COCH_3) M06/6-311G(2d,2p) (def2-TZVP) level of theory. The M06's function was determined suitable for accurately predicting geometries and energies of ruthenium–alkyne complexes in a benchmark study that used spectroscopic data (*10*). Again, terminal alkynes were the focus, with the origins of the regioselectivity also of interest. The catalysts studied were cationic $[LRuCp]^+$ where L was either acetonitrile, the bulky iPr_3P ligand, or the moderately bulky Me_3P ligand (Figure 2). Since the oxidative migration TS was found to be rate determining in the former computational study, these TSs were located for each catalyst first to determine the preferred migration sequence and target (i.e., to which alkyne carbon atom, internal or external, the migration will take place). With the bulky phosphine ligand complex, the large SiR_3 group is first delivered to the β-carbon (26.7 kcal·mol^{-1}), with the hydride subsequently migrating to the α-carbon. Initial silyl migration reduces the steric interaction between the bulky $PiPr_3$ ligand and the silyl group, which

overrides the intrinsic electronic preference for the initial hydride migration sequence identified by the prior studies. With the moderately bulky PMe_3 ligand, there is a slight preference for initial hydride migration to the β-carbon, due to a slight steric interaction between the propyne methyl and the PMe_3 ligand. The catalyst with the least bulky CH_3CN ligand prefers to migrate the hydride to the β-carbon first, as expected based on minimal steric interactions and the intrinsic electronic preference.

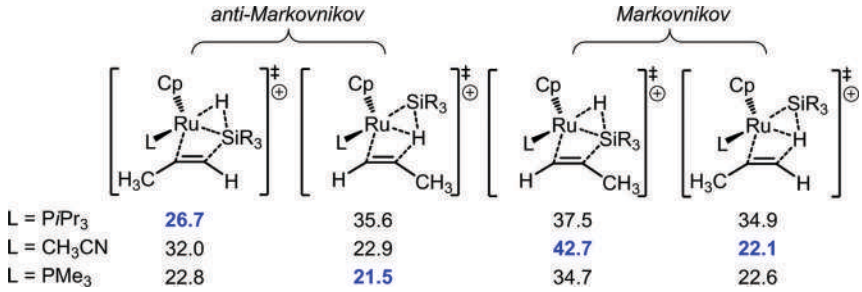

Figure 2. TS and energies (kcal·mol^{-1}) for either silyl or hydride migration. The energies are relative to the starting CpRuL(CH$_3$CN)$_2^+$(SiR$_3$ = SiMe$_2$Ph) (10).

With a terminal alkyne, DFT predicted that a bulky phosphine ligand would give the greatest selectivity and thus, the full mechanistic profile was more fully explored (Figure 3). Ligand exchange of the 2 acetonitrile ligands for H_2 and the alkyne is uphill in energy by 17.3 kcal·mol^{-1}. The subsequent rate-determining oxidative silyl migration transition state is traversed with a height of 26.7 kcal·mol^{-1} that results in a C–C bond rotation to position the silyl group proximal to the Cp ligand. A series of bond rotations results in the formation of the metallocyclopropene that positions the hydride proximal to the α-carbon, followed by a very facile reductive elimination of the hydride to form the bound product.

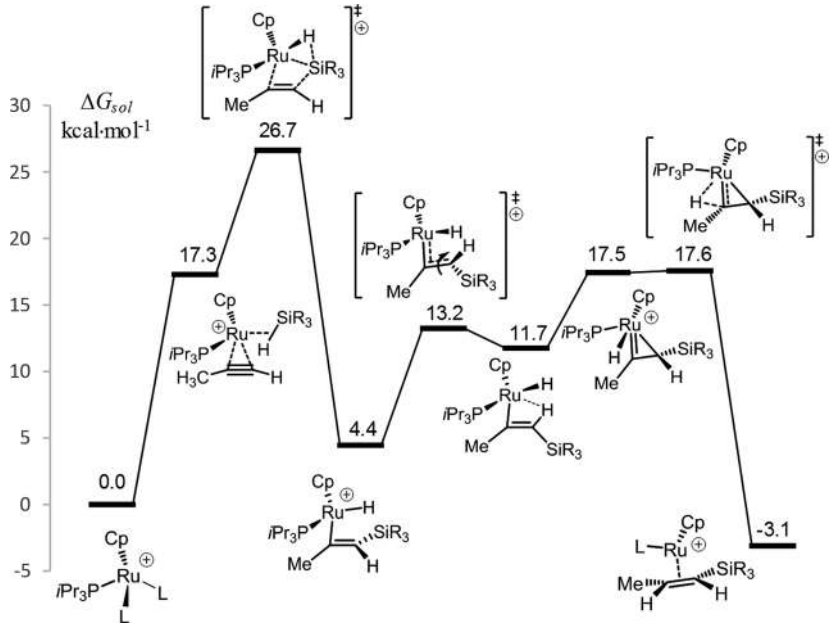

Figure 3. M06-computed energy profile (kcal·mol^{-1}) for hydrosilylation of propyne (10).

Hydrosilylation can also be carried out using a ruthenium–hydride complex $(PCy_3)_2CORuHCl$ on terminal alkynes to produce vinyl silanes in good *E*/*Z* selectivity (*11*). The favored diastereomer can be controlled by the sterics of the alkyne in that sterically undemanding terminal alkynes give *E*-products, while sterically demanding alkynes give *Z*-products. This catalyst was initially used for the oxidative silylation of terminal alkenes to *E*-vinylsilanes (*12*). A quantum mechanical and molecular mechanical strategy was used to computationally investigate the mechanism at the ONIOM-B3LYP/CEP-121G(d):UFF level, where UFF is the universal force field. The phosphine ligands were treated with the UFF, and the rest of the complex was treated with DFT. The preference for *Z*-products originates from an isomerization of the ruthenium–vinyl complex intermediates to a more stable complex, benefiting from an agostic interaction of the ruthenium with a vinyl C–H bond, despite the energetic cost in placing the phenyl and $SiMe_3$ groups in a cis relationship (Figure 4). If the alkyne is more sterically demanding, the cost of placing the bulky group cis to the $SiMe_3$ group is too costly and results in the *E*-product. Ruthenacyclopropene-type intermediates have not been observed in this system, making it different from the CpRuL system investigated by Wu and Trost. Rather, a metallocyclopropene-like transition state was located for the isomerization of the ruthenium–vinyl intermediates.

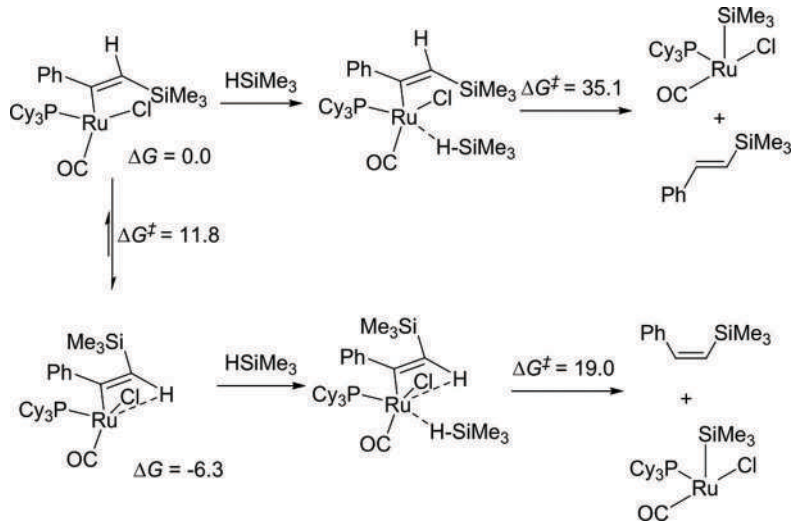

Figure 4. Pathway to isomerization of the key ruthenium–vinyl intermediate complexes that dictates E/Z-product selectivity (*11*).

Another study reported an interesting regiodivergent hydrosilylation of silyl alkynes that can be performed with high diastereoselectivity and regioselectivity (*13*). The effects of both Cp and Cp* ligands were explored. The less bulky Cp ligand gave the *E*-product (syn addition), while the bulkier Cp* ligand gave the *Z*-product, arising from anti-addition of the $HSi(OEt)_3$ (Scheme 3). The DFT-computed mechanisms revealed that the process follows a familiar route that includes oxidative hydrometalation, isomerization, and reductive silyl migration. In both cases, the addition sequence involving initial hydride migration was preferred. With the less bulky Cp ligand, the oxidative hydrometalation step disfavored α-addition and resulted in a preference for an overall syn addition attributed to a reduced barrier for silyl migration to the same side as the migrating hydride that is the rate-determining step. The preferred pathway of Cp* involved the hydride migrating to the less sterically hindered α-carbon, despite migration to the β-carbon being lower in energy for this step.

This preference was explained by the final step involving silyl migration that was rate determining and lower in energy with initial hydride migration to the α-carbon. Taken together, the interplay between the sterics of the bulky substrate silyl group with the steric variation in the ligand (Cp or Cp*) dictated the regio- and diastereoselectivity.

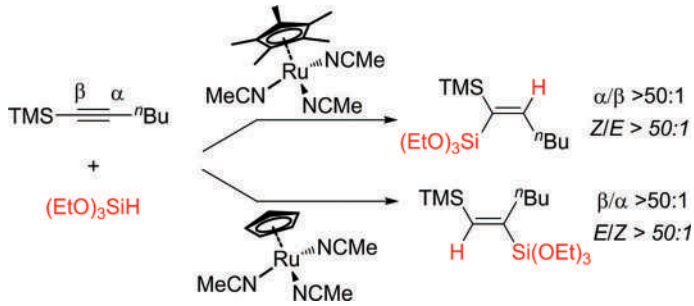

Scheme 3. Regiodivergent hydrosilylation of silyl alkynes dependent on the steric bulk of the catalyst.

Hydrosilylation of thioalkynes was also explored using the $[Cp^*Ru(MeCN)_3]^+$ cationic complex (*14*). Interestingly, the silylation proceeds with syn addition to the alkyne and is highly regioselective. With these unique substrates, the thio group serves to stabilize the ruthenacyclopropane intermediate through positive charge delocalization. This charge stabilization largely explains the high regioselectivity determined by the migration sequence. Opening of the metallocyclopropene to a vinyl–ruthenium complex is also facile and downhill in energy by 9 kcal·mol^{-1}, which is attributed to stabilization through α-coordination of the thio group to the Ru center.

Trans-Selective Hydrogenation

Inspired by the initial discovery of the pivotal trans-selective hydrosilylation of alkynes, the Fürstner group wondered whether the [Cp*RuL] catalyst system might be capable of promoting an antidelivery of H–H across a π-system of the alkyne directly, bypassing the intermediacy of a vinyl silane (Scheme 4). Excluding methods that produce trans products formally through isomerization of the initially formed cis products (*15*), a direct antiselective hydrogenation manifold would be of great value to complement the more established and traditional syn-selective hydrogenation methods.

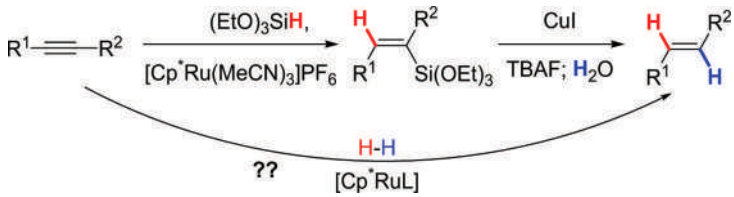

Scheme 4. An alternative strategy for accessing trans alkenes directly from alkynes through direct hydrogenation.

The concept was fully realized as subjection of an internal alkyne to the catalyst Cp*Ru(cod)Cl in the presence of H_2 resulted in the formation of the *E*-alkene in excellent yields and diastereoselectivity (Scheme 5). The substrate scope is broad but limited to internal alkynes. Preliminary investigations into the mechanism revealed that a σ–H_2 complex, $[Cp^*Ru(H_2)(cod)]$ (*16*), is catalytically competent in the reaction, furnishing the same selectivity as the precatalyst (*17*).

A dimeric dihydride complex gave cis–trans alkenes with very poor selectivity. Both results suggest that the mechanism likely proceeds through a monomeric dihydride complex intermediate.

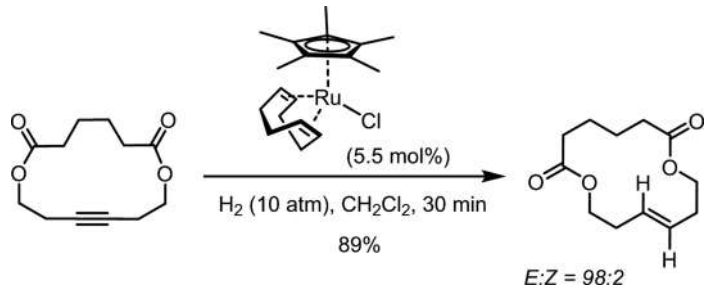

*Scheme 5. Trans-selective semihydrogenation of a functionalized alkyne using the Cp*Ru(cod)Cl catalyst (16).*

More detailed experimental and computational investigations were performed on the nature of the mechanism of this unorthodox, trans-selective semihydrogenation (*18–20*). An NMR technique that uses parahydrogen-induced polarization transfer was used to help identify key intermediates of the mechanism (*21*). Subjecting a functionalized alkyne (Figure 5) to the Cp*Ru(cod)Cl catalyst in the presence of parahydrogen led to the identification of a ruthenium–carbene intermediate arising from an unusually formal gem-hydrogenation. The complex could be crystallized, thus unambiguously confirming the carbene structure. Further NMR results from 2D ^{1}H-OPSY-EXSY experiments with a similar alkyne substrate indicated that this carbene complex does lead to the formation of the desired *E*-alkene; however, it also links the complex to side products from the reaction often observed in small amounts, namely isomerized alkene products and the fully saturated alkane side products.

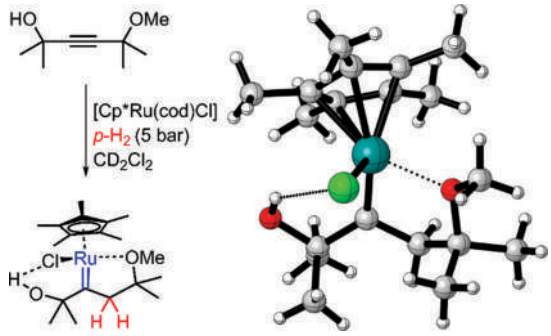

*Figure 5. Isolation of a key ruthenium–carbene species during the [Cp*Ru(cod)Cl] hydrogenation (18).*

With this information in hand, combined with coupled cluster theory, DFT was used to probe the mechanism. The mechanistic pathway was investigated at the DLPNO-CCSD(T)/def2-TZVP//M06/def2-TZVP level of theory (Figure 6). Beginning from the precatalyst **A0**, the substrate alkyne and H_2 are loaded onto the Ru center to give the heteroleptic complex **A1** in which H_2 coordinates through its σ-bond. The mechanism resembles that obtained in hydrosilylation (*9*). The fleeting intermediacy of a dihydride species (**A2**) resulting from oxidative addition of H–H is unique to this case. Upon passing though the low-lying transition state $\mathbf{TS_{A2\text{-}A3}}$ ($\Delta G^{\ddagger} = 0.8$ kcal·mol^{-1}), this short-lived dihydride complex quickly transfers the H-atom proximal to the Cp* to

an alkyne carbon. The η^1-vinyl complex **A3** quickly collapses to the ruthenacyclopropane **E1**. Two pathways of nearly equal preference are available to **E1**. The first pathway involves direct reductive elimination to deliver the Ru–H to form the associated *E*-alkene associated complex **E2.** The second pathway proceeds through initial rotation about the Ru–C bond to form **C1** in which the Ru–H is positioned above and proximal to and is subsequently delivered to the β-carbon with little to no energy barrier to produce the ruthenium–carbene **C2**.

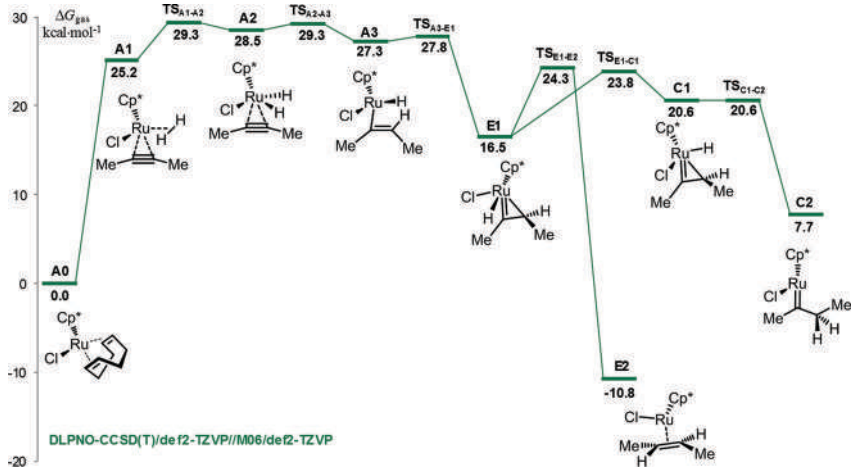

Figure 6. Computed energy profile for the semihydrogenation of 2-butyne (18).

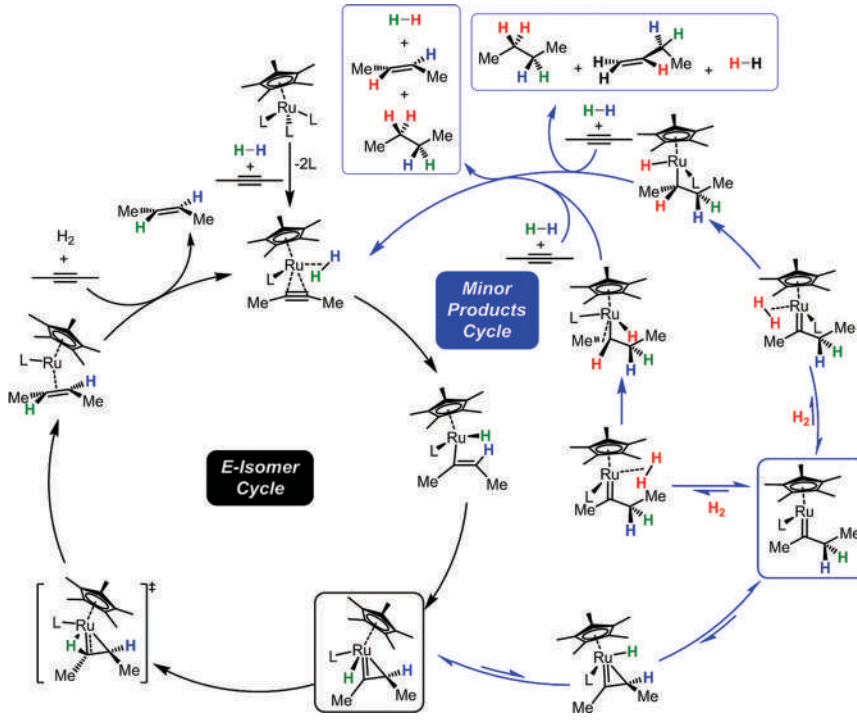

Scheme 6. The overall predicted mechanism highlighting the productive cycle (black) and unproductive cycle that leads to side product formation (blue).

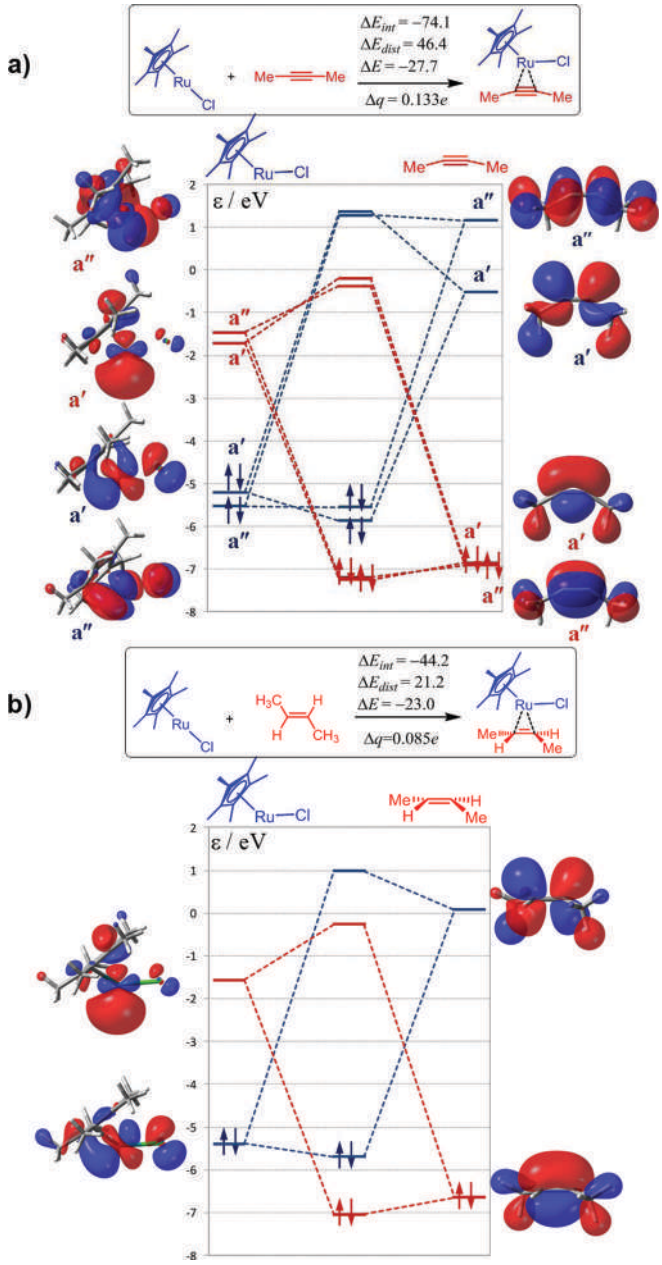

*Figure 7. Orbital interaction diagrams describing the bonding between Cp*RuCl and (a) 2-butyne and (b) 2-butene* (*20*).

The competency of the ruthenium–carbene complex to deliver product was also probed computationally. Indeed, the desired product and side products were predicted to arise from the carbene through an associative mechanism involving H_2 association to the unsaturated 16-electron complex **C2**. The overall catalytic cycle was determined by a detailed mechanistic investigation that combined theory with experiment (Scheme 6). The left cycle describes the formation of the desired *E*-alkene and the right cycle details all pathways that led to side product formation. The exit channel off the main catalytic cycle involves a simple low-barrier rotation about the formal Ru=C bond.

Future efforts to optimize this important hydrogenation process should focus on disfavoring this rotation through catalyst modification.

The nature of the alkyne coordination to the Cp*RuCl center was investigated using orbital interaction theory (Figure 7) (*20*). Donation from the alkyne to the Ru center and backdonation from the Cp*RuCl to the alkyne occured. Both π-systems of the alkyne participated in the bonding, as they interacted equally with the LUMO(a′) (mostly 5*s* character with σ-symmetric bonding) and the LUMO-1(a″) (π-symmetric bonding of the Ru fragment). The σ-bonding to the carbon distal to the Cl ligand was enhanced via the σ-symmetric interaction between the alkyne π* LUMO(a′) and the Cp*RuCl HOMO(a′) (mostly $3d_z2$ character) and amounted to the strongest mixing interaction. A net charge transfer of $\Delta q = 0.133e$ from the alkyne to the Cp*RuCl was calculated from natural bond order partial charges. These results support the claim that the alkyne behaving as a four-electron donor outcompetes the alkene for the metal center that can only behave as a two-electron donor. This also explains why the alkene product does not react further.

Trans-Selective Hydrostannation

Similar reactivity might be expected to be accessible to other metal hydride reagents capable of coordinating to the Ru center through their σ-bonds similar to H–SiR_3 and H–H. One such example involves hydrostannanes (Scheme 7) (*4*, *20*, *22*, *23*). An analogous σ-coordination had been observed in the manganese complex $MeCp(CO)_2MnHSnPh_3$ (*24*). Mechanistic investigations into hydrostannation led to the isolation of σ-stannane–ruthenium complexes (*4*). The hydrostannation proceeded with excellent *E*/*Z*- and regioselectivity in the presence of a hydroxyl directing group.

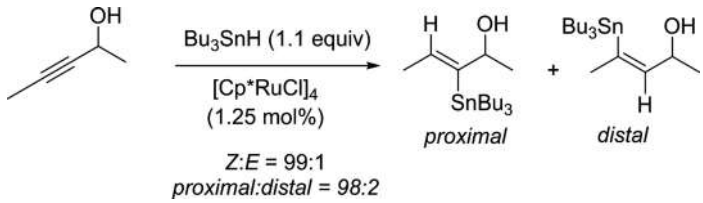

*Scheme 7. Directed hydrostannation of propargyl alcohols catalyzed by [Cp*RuCl]$_4$ (4).*

The origins of both the regio- (proximal versus distal) and diastereoselectivity were investigated using DFT at the SMD(DCM)-M06/def2-TZVP//M06-def2-SVP level of theory (Figure 8) (*20*). Both the proximal (black) and distal pathways (grey) were explored. Initial complexation of the propargyl alcohol produced **INT0** and **INT0′**. Complex **INT0** is favored over **INT0′** by 4.8 kcal·mol^{-1}, largely as a result of the hydrogen bonding between the hydroxyl group of the substrate and the chloro ligand in **INT0**. The subsequent binding of Me_3SnH through the Sn–H σ-bond produced **INT1** in accordance with experimental solid-state structure data. The subsequent step involved a concerted breaking of the Sn–H bond followed by concomitant transfer of the hydride to the ligated substrate, all in a concerted manner. The hydride was delivered proximal to the Cp* consistent with the mechanisms of both hydrogenation and hydrosilylation. The resulting ruthenacyclopropane **INT2** underwent a direct reductive elimination of the $SnMe_3$ group to the remaining carbon of the alkyne to produce the *Z*-product. Since the barrier height for the interconversion of **INT0** and **INT0′** was similar in magnitude to the highest barrier heights leading to the proximal and distal products, the regioselectivity largely depended on the ground-state energy difference between **INT0** and **INT0′** rather than on the barrier to interconversion.

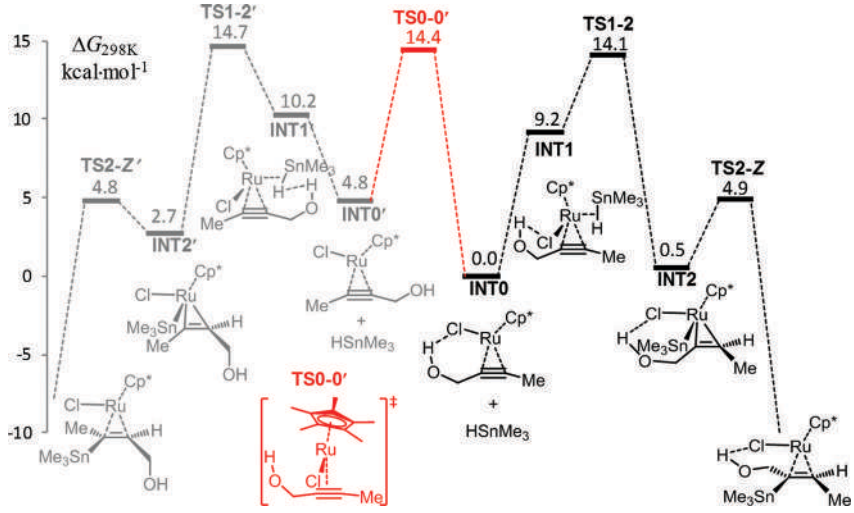

*Figure 8. Energy profile describing the regioselectivity in the Cp*RuCl catalyzed hydrostannation of propargyl alcohol* (*20*).

Trans-Selective Hydroboration

Hydroboration of alkynes in the absence of a metal catalyst is well established to proceed with a syn addition of the $X_2B–H$ bond across the π-system (*25*). This syn addition mode has rarely been violated, with such violations restricted to secondary processes.

An antiselective hydroboration manifold of alkynes could be accessed through the use of the Cp^*RuL_n catalyst (Scheme 8) (*26*). The reaction proceeds with excellent diastereoselectivity for most substrates. The regioselectivity in unsymmetrical substrates depends entirely on the presence of directing functionality. The reaction does not proceed with terminal alkynes.

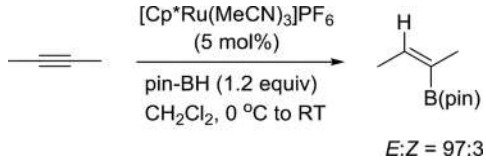

*Scheme 8. Hydroboration of internal alkynes using a [Cp*Ru(MeCN)$_3$]PF$_6$ catalyst* (*26*).

The mechanism for this enabling hydroboration reaction was investigated using DFT at the SMD(DCM)-M06/6-311++G(3df,2pd)(def2-TZVP)//B3LYP/6-31G(d) (LANL2DZ) level of theory (Figure 9) (*27*). The catalyst chosen for this study was $[Cp^*Ru(CH_3CN)_3]^+$. The overall mechanism was found to be similar to that for hydrosilylation. The addition sequence proceeding by initial hydride migration was predicted to be lower in energy by 1.7 kcal·mol^{-1} than the sequence involving initial boron migration (black versus red pathway). This oxidative hydroboration step was predicted to be rate limiting. Boron migration takes places on the face opposite to that of the prior hydride migration consistent with an overall anti-addition mechanism.

Terminal alkynes' inability to undergo hydroboration was also investigated computationally by exploring alternative pathways. The lowest-energy pathway was predicted to be an oxidative coupling of two alkynes to generate a ruthenacyclopentadiene intermediate that introduces a pathway to arene side products. An ion mobility mass spectrometric study combined with collision-induced

dissociation analysis supported the presence of the ruthenacyclopentadiene intermediate as well as the cyclotrimerized product complexed to ruthenium.

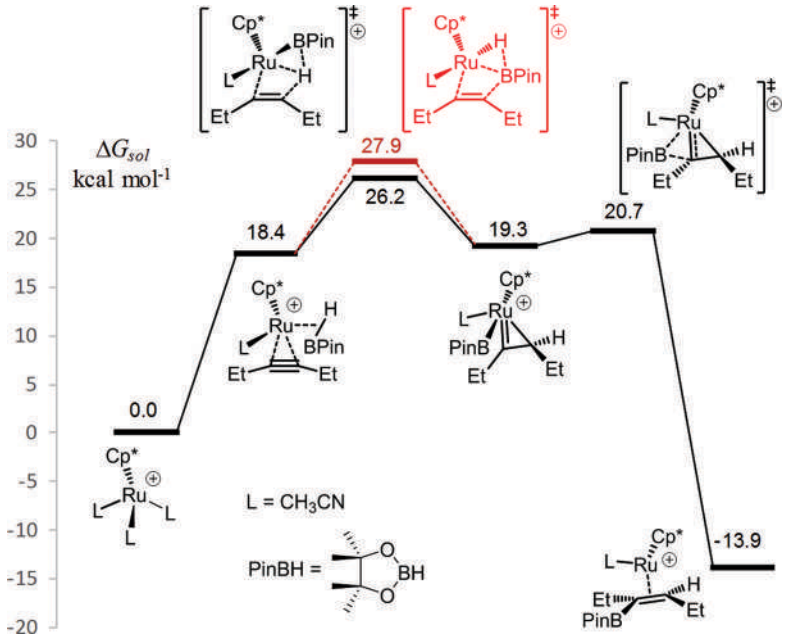

*Figure 9. Computed energy profile for the Cp*Ru(CH_3CN)$_3$ catalyzed hydroboration of internal alkynes (27).*

Summary

Hydrometalation and hydrogenation of alkynes catalyzed by a [Cp*RuL] complex lead to selectivity patterns that few other catalysts impart. The unique selectivity results from divergent mechanisms that are highly dependent on both ligand and substrate effects. The substrate can be tailored to influence the regioselectivity through directing group bias. The diastereoselectivity is dependent on the torsional dynamics of the initial insertion step. Computational investigations and experiments combined with advanced spectroscopic techniques have uncovered many of the key features and interactions that control selectivity, reactivity, and side product formation. Without the powerful synergy between computation and experiment, the mechanistic subtleties that control selectivity in these important transformations would have remained obscure.

Acknowledgments

The authors would like to thank all collaborators and give special thanks to Prof. Alois Fürstner. Financial support by the MPG is greatly acknowledged. L.M.W. acknowledges UML for financial support.

References

1. Fürstner, A.; Frihed, T. G. *Bull. Chem. Soc. Jpn.* **2016**, *89*, 135–160.
2. Rummelt, S. M.; Cheng, G. J.; Gupta, P.; Thiel, W.; Fürstner, A. *Angew. Chem., Int. Ed.* **2017**, *56*, 3599–3604.
3. Trost, B. M.; Ball, Z. T. *J. Am. Chem. Soc.* **2001**, *123*, 12726–12727.

4. Rummelt, S. M.; Radkowski, K.; Rosca, D. A.; Fürstner, A. *J. Am. Chem. Soc.* **2015**, *137*, 5506–5519.
5. Chung, L. W.; Wu, Y.-D.; Trost, B. M.; Ball, Z. T. *J. Am. Chem. Soc.* **2003**, *125*, 11578–11582.
6. Casey, C. P.; Brady, J. T.; Boller, T. M.; Weinhold, F.; Hayashi, R. K. *J. Am. Chem. Soc.* **1998**, *120*, 12500–12511.
7. Chalk, A. J.; Harrod, J. F. *J. Am. Chem. Soc.* **1965**, *87*, 16–21.
8. Harrod, J. F.; Chalk, A. J. *J. Am. Chem. Soc.* **1965**, *87*, 1133–1135.
9. Yang, Y. F.; Chung, L. W.; Zhang, X.; Houk, K. N.; Wu, Y.-D. *J. Org. Chem.* **2014**, *79*, 8856–8864.
10. Škríba, A.; Jašík, J.; Andris, E.; Roithova, J. *Organometallics* **2016**, *35*, 990–994.
11. Gao, R.; Pahls, D. R.; Cundari, T. R.; Yi, C. S. *Organometallics* **2014**, *33*, 6937–6944.
12. Yi, C. S.; He, Z.; Lee, D. W.; Rheingold, A. L.; Lam, K-C. *Organometallics* **2009**, *19*, 2036–2039.
13. Ding, S.; Song, L. J.; Chung, L. W.; Zhang, X.; Sun, J.; Wu, Y.-D. *J. Am. Chem. Soc.* **2013**, *135*, 13835–13842.
14. Ding, S.; Song, L. J.; Wang, Y.; Zhang, X.; Chung, L. W.; Wu, Y.-D.; Sun, J. *Angew. Chem., Int. Ed.* **2015**, *54*, 5632–5635.
15. Swamy, K. C. K.; Reddy, A. S.; Sandeep, K.; Kalyani, A. *Tetrahedron* **2018**, *59*, 419–429.
16. Jia, G.; Ng, W. S.; Lau, C. P. *Organometallics* **1998**, *17*, 4538–4540.
17. Radkowski, K.; Sundararaju, B.; Fürstner, A. *Angew. Chem., Int. Ed.* **2013**, *52*, 355–360.
18. Leutzsch, M.; Wolf, L. M.; Gupta, P.; Fuchs, M.; Thiel, W.; Fares, C.; Fürstner, A. *Angew. Chem., Int. Ed.* **2015**, *54*, 12431–12436.
19. Guthertz, A.; Leutzsch, M.; Wolf, L. M.; Gupta, P.; Rummelt, S. M.; Goddard, R.; Fares, C.; Thiel, W.; Fürstner, A. *J. Am. Chem. Soc.* **2018**, *140*, 3156–3169.
20. Rosca, D. A.; Radkowski, K.; Wolf, L. M.; Wagh, M.; Goddard, R.; Thiel, W.; Fürstner, A. *J. Am. Chem. Soc.* **2017**, *139*, 2443–2455.
21. Schleyer, D.; Niessen, H. G.; Bargon, J. *New J. Chem.* **2001**, *25*, 423–426.
22. Sommer, H.; Hamilton, J. Y.; Fürstner, A. *Angew. Chem., Int. Ed.* **2017**, *56*, 6161–6165.
23. Rummelt, S. M.; Fürstner, A. *Angew. Chem., Int. Ed.* **2014**, *53*, 3626–3630.
24. Schubert, U.; Kunz, E.; Harkers, B.; Willnecker, J.; Meyer, J. *J. Am. Chem. Soc.* **1989**, *111*, 2572–2574.
25. Brown, H. C. *Hydroboration*; W. A. Benjamin Inc.: New York, 1962.
26. Sundararaju, B.; Fürstner, A. *Angew. Chem., Int. Ed.* **2013**, *52*, 14050–14054.
27. Song, L-J.; Wang, T.; Zhang, X.; Chung, L. W.; Wu, Y-D. *ACS Catal.* **2017**, *7*, 1361–1368.

Chapter 4

A Biomimetic System for Studying Salicylate Dioxygenase

Atanu Banerjee,[1] Jia Li,[1] Monika A. Molenda,[1] William W. Brennessel,[2] and Ferman A. Chavez*[,2]

[1]Department of Chemistry, Oakland University, Rochester, Minnesota 48309-4477, United States

[2]Department of Chemistry, University of Rochester, Rochester, New York 14627-0216, United States

***E-mail: chavez@oakland.edu**

We report the characterization of [Fe(T1Et4iPrIP)(sal)] (**2**) (T1Et4iPrIP = tris(1-ethyl-4-isopropyl-imidazolyl)phosphine; sal^{2-} = salicylate dianion), which serves as a model for substrate-bound salicylate dioxygenase (SDO). Complex **2** crystallizes in the monoclinic space group $P2_1/n$ with a = 10.7853(12) Å, b = 16.5060(19) Å, c = 21.217(2) Å, β = 94.489(2)°,and V = 3765.5(7) Å^3. The structure consists of Fe^{II} bonded in distorted square pyramidal geometry (τ = 0.32) with two salicylate oxygens and two T1Et4iPrIP nitrogens serving as the base and the apical position occupied by the other ligand nitrogen. [Fe(T1Et4iPrIP)$(OTf)_2$] (**1**), the precursor for **2**, catalyzes the cleavage of 1,4-dihydroxy-2-naphthoate in the presence of O_2. Complex **1** is also capable of cleaving the salicylate aromatic ring in the presence of H_2O_2. The progression of this reaction toward product formation involves an Fe^{III}–phenoxide species.

Introduction

The deposition of aromatic waste products into the environment by either intentional or accidental means is a threat to human health and may be responsible for a number of acute or chronic diseases. Sources of these hydrocarbons include vehicle emissions and industrial exhaust while other sources include wild fires, burning of plastics and pesticides, incomplete burning of coal or other fuels, and oil spills (*1*, *2*). Bacteria have evolved to utilize these waste products as a carbon source. Activation of an aromatic substrate in aerobic microorganisms is usually affected by hydroxylation of the ring and subsequent dearomatization. The typical ring-fission substrates are catechol, protocatechuate, homoprotocatechuate, hydroquinone, gentisate, or homogentisate. These substrates are converted to either mono- or dicarboxylic acids, depending on the mode of

cleavage (*3*). Hydroquinones, homogentisate, and gentisate undergo fission of the aromatic ring adjacent to the hydroxyl group by dioxygenases. For hydroquinones-bearing carboxyl groups (e.g., homogentisate and gentisate), cleavage usually occurs at the 1,2-position between the carboxyl and hydroxyl group (*4*, *5*). Intradiol Fe^{III} dioxygenases are usually present in these ring-fission dioxygenases while Fe^{II} is present for para-substituted diols-cleaving enzymes and extradiol-cleaving enzymes (*3*, *6–8*). A third type of dioxygenase that cleaves aromatic compounds (*9–11*) has been assigned to a new class (Class III) (*12*). These enzymes catalyze the dioxygenation of gentisate, homogentisate, 3-hydroxy-anthranilate, 1-hydroxy-2-naphthoate, 2-aminophenol, salicylate, 5-aminosalicylate, 5-chlorosalicylate, and 5-nitrosalicylate (*13*). Gentisate, salicylate, 5-aminosalicylate, and 5-chlorosalicylate are converted via the Class III dioxygenases while the rest are oxidized by Class I and II enzymes. The Class III ring-cleaving dioxygenases are part of the cupin superfamily (*14*, *15*). Enzymes containing a 3His metal binding site are gentisate 1,2-dioxygenase (GDO), salicylate 1,2-dioxygenase (SDO), 3-hydroxyanthranilate 3,4-dioxygenases, 1-hydroxy-2-naphthoate dioxygenase (HNDO), and Type II hydroquinone 1,2-dioxygenase.

Gentisate 1,2-dioxygenase converts gentisate to maleylpyruvate (Scheme 1) (*16*, *17*). GDO contains Fe^{II} and has a high specificity for gentisate. Alternately, SDO (Scheme 1) catalyzes the dioxygenation of many monohydroxylated aromatic substrates, which include 3-, 4-, and 5-chlorosalicylate, and 1-hydroxy-2-naphthoate (*9*, *18*). Other substrates include: 5-fluorosalicylate; 3,5-dichlorosalicylate; 3-, 4-, 5-bromosalicylate; 3-, 4-, and 5-methylsalicylate (*9*); 1-hydroxy-2-naphthoate; 3- and 5-aminosalicylate; and 3- and 4-hydroxysalicylate (*9*, *18*). Figure 1 shows the structures of GDO (PDB 3BU7) (*19*) and SDO with bound gentisate (PDB 3NL1), bound salicylate (PDB 3NJZ), and bound hydroxy naphthoate (PDB 3NKT) (*12*). No substrate-bound adduct has been structurally characterized for GDO; however, hydrogen bonding interactions between the active site residues (His162, Tyr190, Gln108, and Asp175) and two iron-bound water ligands are clearly seen.

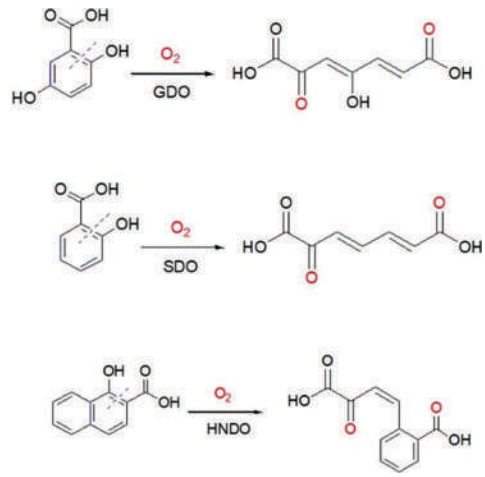

Scheme 1. Class III Dioxygenase Enzymes: GDO, SDO, and HNDO

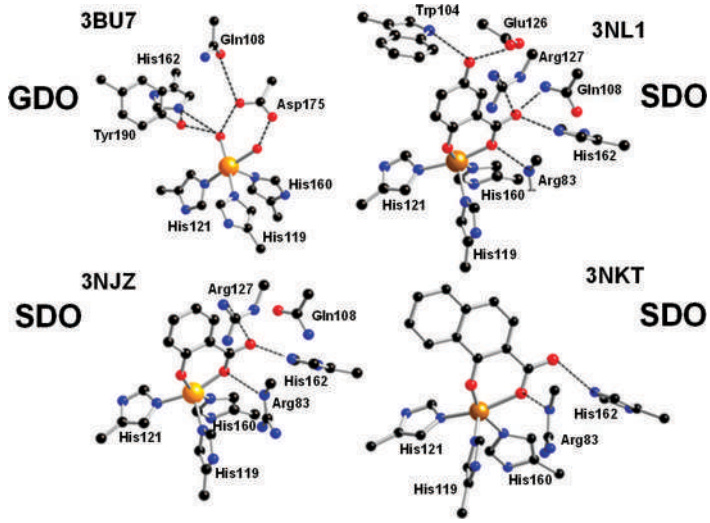

Figure 1. X-ray structure for the active site of GDO (PDB 3BU7) and SDO with bound gentisate (PDB 3NL1), salicylate (PDB 3NJZ), and naphthoate (PDB 3NKT).

Substrate-bound SDO active site structures also exhibit extensive hydrogen bonding interactions between active site residues and substrates. In all cases, His162 is within bonding distance to the carbonyl oxygen of the substrate and Arg83 also provides an H-donor to the bound substrate oxygen of the carboxylate group. Arg127 also interacts in the salicylate and gentisate structures. In the case of SDO, it has been proposed that His162 acts as proton donor to the evolving peroxidate intermediate (*20*). It is quite probable that successful synthetic models for these active sites will require outer-sphere H-bonding interactions. Interestingly, Eppinger et al. reported that a GDO mutant (Ala112Gly) allowed GDO to function as SDO in its substrate preference (*21*). This suggests that in GDO, salicylate is unable to bind productively (with both the deprotonated carboxyl and hydroxyl groups) due to the Ala112 group (located distally to the active site); therefore, no turnover is observed.

The catalytic mechanism for GDO is believed to first involve coordination of the substrate followed by dioxygen binding. The O_2 attacks at carbon-1 of the bound gentisate to form an alkylperoxo intermediate (Scheme 2). Heterolytic cleavage of the O–O bond and insertion of one oxygen atom into the ring C1–C2 bond (Criegee rearrangement) would be enhanced by conversion of the hydroxyl group to a ketone at C5 and would result in formation of a cyclic lactone. Hydrolysis by coordinated hydroxide could occur, resulting in formation of the final product (*19*, *22*, *23*).

For SDO, gentisate and 5-aminosalicylate are converted to products at a much faster rate (>100-fold for gentisate) to products compared to salicylate. The rate constant for wild-type SDO (0.9 s^{-1}) (*24*) corresponds to ~68 kJ/mol. The key factor responsible for the enhanced catalytic rate could be that gentisate possesses a hydroxyl group at the 5-position. The presence of an amino group for 5-aminosalicylate could also be key since deprotonation could occur here to stabilize the forming intermediate. The hydrophobic active site pocket could be important in transferring electron density to the ring. For gentisate-bound SDO (Figure 1, 3NL1), Trp104 is typically a tyrosine in many GDOs. The presence of extensive H-bonding interactions in SDO between the substrate and binding pocket could be an important factor in activation of the substrate; however, this point must be investigated with model chemistry. The mechanism believed operative in GDO may not account for the reactivity toward salicylate since no 5-OH group is present. The mechanism for salicylate 1,2-dioxygenase has been investigated by a quantum mechanical and molecular mechanical (QM/MM)

study (25). The study reveals that an active site His (His162) plays a role as an acid/base catalyst supplying a proton to the substrate during catalysis. Roy et al. also conducted QM/MM calculations on the mechanism of SDO and found that it is possible for a GDO-like mechanism to occur (Scheme 2) without the need for the 5-OH group (*26*).

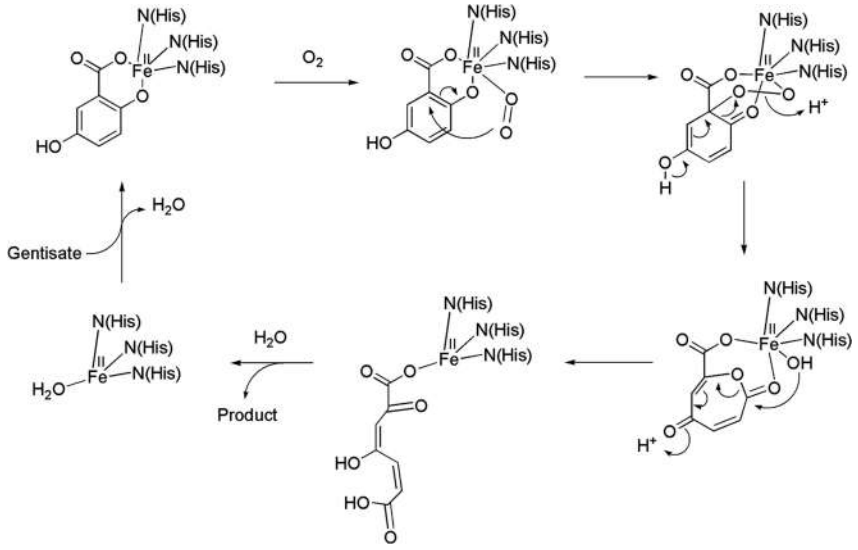

Scheme 2. Proposed Mechanism for Dioxygenation of Gentisate by GDO (*23*)

To study and provide support for mechanistic proposals we have utilized tris(1-ethyl-4-isopropyl-imidazolyl)phosphine (T1Et4iPrIP, Scheme 3) as our 3His metal binding site and have synthesized [Fe(T1Et4iPrIP)$(OTf)_2$] (**1**) to serve as a model for the iron site in SDO.

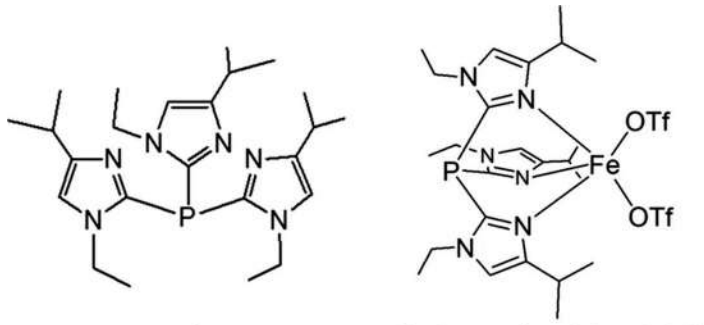

*Scheme 3. Structures of T1Et4iPrIP and [Fe(T1Et4iPrIP)$(OTf)_2$] (**1**)*

Results and Discussion

Complex **1**, first reported by our group (*27*), was reported to be a good model for iron–3His sites from a structural and electronic standpoint. Complex **1** was shown to reversibly bind NO (similar to other iron–3His enzyme active sites such as GDO and other mononuclear iron sites) (*23*, *28*). We studied the LFe + NO ↔ LFeNO equilibrium process spectroscopically by titrating a solution of NO (7 mM) in THF at 25 °C with **1**. The study yielded the equilibrium constant (K_{eq} = 470 M^{-1}) (*29*) and is in line with similar studies (*30*).

We sought to synthesize a model for the enzyme-substrate adduct to investigate and understand the mechanism for SDO. To do this we reacted **1** with one equiv bis(tetraethylammonium) salicylate in dichloromethane. After diffusion in an ether chamber and crystallization at -20 °C, light-green crystals of [Fe(T1Et4iPrIP)(sal)] (**2**) deposited and were isolated in moderate yield. The crystallographic parameters (Table 1) and bond distances and angles (Table 2) for **2** are given. The structure is shown in Figure 2. The structure reveals Fe^{II} in distorted square pyramidal geometry ($\tau =$ 0.32) (*31*). The base comprises oxygens from phenoxy and carboxy groups of the salicylate and two nitrogens from the imidazole groups of the ligand. The apical position is occupied by a third nitrogen from T1Et4iPrIP. The average Fe–N bond distance (2.190 Å) is slightly longer compared to **1** (2.140 Å) (*27*) while the Fe–O distances (1.9519(12) and 2.0456(11) Å) are slightly shorter compared to another iron salicylate complex (1.958(1) and 2.060(1) Å) (*32*).

Table 1. Crystallographic Data for [Fe(T1Et4iPrIP)(sal)]·(Et_2O) (2·Et_2O)

Complex	*2·Et_2O*
chemical formula	$C_{35}H_{53}FeN_6O_4P$
formula weight (g/mol)	708.65
temperature /K	100.0(5)
λ/Å	0.71073
Crystal system	Monoclinic
space group	$P2_1/n$
a /Å	10.7853(12)
b /Å	16.5060(19)
c /Å	21.217(2)
α/°	90
β/°	94.489(2)
γ/°	90
V /Å3	3765.5(7)
Z	4
μ/mm^{-1}	0.487
D_{calcd} /Mg/m^3	1.250
$R1$ ($(I > 2\sigma(I))$)	0.0485
$wR2$ ($(I > 2\sigma(I))$)	0.1017

$R1 = \Sigma||F_o|-|F_c||/\Sigma|F_o|$, $wR2 = [\Sigma[w(F_o^2-F_c^2)^2]/\Sigma[w(F_o^2)^2]]^{1/2}$ $w = q/[\sigma^2(F_o^2)+(a\cdot P)^2+b\cdot P+d+e\cdot\sin(\theta)]$.

Reactivity Studies

A model for SDO has previously been reported (*32*). $[Fe^{II}(Tp^{Ph2})]^+$ (Tp^{Ph2} = hydrotris(3,5-diphenylpyrazole-1-yl)borate) has been shown to catalyze the aromatic ring scission of 1,4-dihydroxy-2-naphthoate using O_2 as the oxidant (Scheme 4) (*33*). Incorporation of both oxygen

atoms into the substrate was demonstrated. It was noted that the presence of 4-hydroxy group was critical for the reaction and that substitution by $–NH_2$ or $–OCH_3$ did not lead to ring scission.

Table 2. Selected Bond Lengths (Å) and Angles (°) for [Fe(T1Et4iPrIP)-(sal)]·(Et_2O) (2·Et_2O)

Bond Lengths (Å)			
Fe(1)–O(2)	1.9519(12)	P(1)–C(1)	1.8157(16)
Fe(1)–O(1)	2.0456(11)	P(1)–C(2)	1.8219(15)
Fe(1)–N(2)	2.1598(13)	O(1)–C(25)	1.2805(18)
Fe(1–)N(1)	2.1786(13)	O(2)–C(31)	1.3147(19)
Fe(1)–N(3)	2.2320(12)	O(3)–C(25)	1.2457(18)
P(1)–C(3)	1.8142(15)		
Bond Angles (°)			
O(2)–Fe(1)–O(1)	87.07(5)	N(2)–Fe(1)–N(3)	84.16(5)
O(2)–Fe(1)–N(2)	151.58(5)	N(1)–Fe(1)–N(3)	89.82(5)
O(1)–Fe(1)–N(2)	93.40(5)	C(3)–P(1)–C(1)	97.93(7)
O(2)–Fe(1)–N(1)	117.36(5)	C(3)–P(1)–C(2)	99.21(7)
O(1)–Fe(1)–N(1)	99.34(5)	C(1)–P(1)–C(2)	97.49(7)
N(2)–Fe(1)–N(1)	90.64(5)	C(25)–O(1)–Fe(1)	130.69(10)
O(2)–Fe(1)–N(3)	90.75(5)	C(31)–O(2)–Fe(1)	128.11(10)
O(1)–Fe(1)–N(3)	170.56(5)		

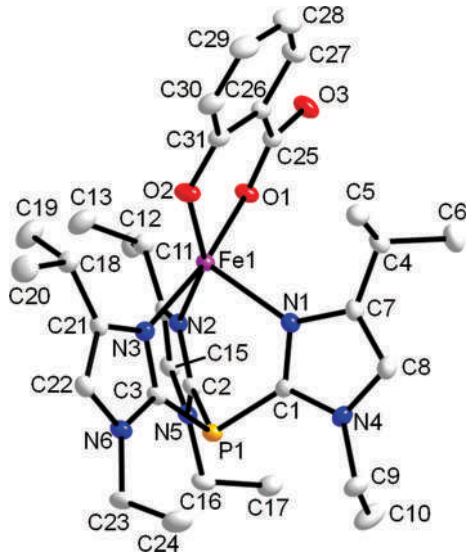

Figure 2. Oak Ridge thermal ellipsoid plot of **2** *(50% probability). H-atoms have been removed for clarity.*

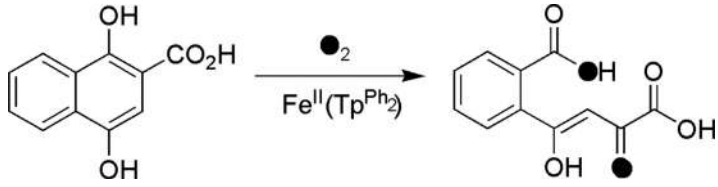

Scheme 4. Dioxygenation of 1,4-Dihydroxy-2-naphthoate (33)

The model complex was not capable of degrading salicylate or 1-hydroxy-2-naphthoate as is the case with SDO and HNDO. In the reaction, the absorption band at 340 nm disappears and two new charge-transfer bands appear at 720 nm and 920 nm, following a pseudo-first order rate. The proposed mechanism (Scheme 5) (33) involves initial outer-sphere oxidation of Fe^{II} to Fe^{III} by oxygen followed by an internal redox reaction where iron is reduced back to Fe^{II} creating a radical on the ligand. Oxygen then reacts with the iron center affording an Fe^{III} alkyl peroxide moiety. The 4-hydroxy group then directs heterolytic cleavage of the O–O bond via a Criegee type rearrangement to generate an anhydride intermediate. The resulting coordinated hydroxide participates in hydrolysis of the anhydride yielding the ring-opened product. $[Fe^{II}(Tp^{Ph2})]^+$ was also shown to be unreactive toward 4-methylsalicylate and 5-aminosalicylate (33). Using complex **1**, we were also able to catalyze the oxidative scission of 1,4-dihydroxy-2-naphthoate using O_2 as the oxidant in CH_2Cl_2. Next, we focused our attention on examining whether **1** is capable of catalyzing the ring scission of salicylate in the presence of O_2. NMR studies and gas chromatography–mass spectrometry (GCMS) analysis indicated that although the solution quickly changes in color from yellow to brownish-red upon exposure to oxygen, the salicylate was unaffected in these reactions. We then pursued using H_2O_2 as the oxidant. The addition of 20 equiv H_2O_2 to **1** and bis(tetraethylammonium) salicylate in methanol or CH_2Cl_2 at 25 °C resulted in the immediate formation of a deep reddish-purple solution (Figure 3). After 10 min the reaction became reddish-brown. Analysis of the reaction mixture by acidification and extraction with CH_2Cl_2 indicated that the aromatic ring had been cleaved (Figure 4).

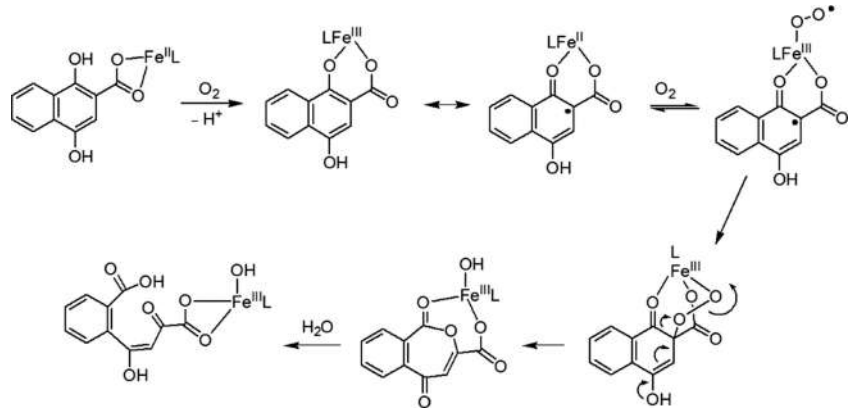

Scheme 5. Proposed Mechanism for the Dioxygenation of 1,4-Dihydroxy-2-naphthoate (33)

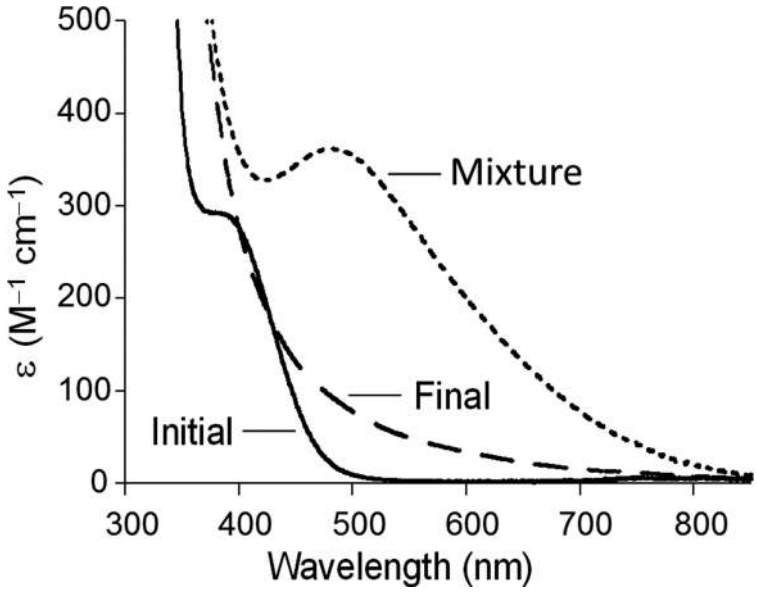

*Figure 3. Initial UV–vis spectrum of **1** and bis(tetraethylammonium) salicylate at a ratio of 1:1 in methanol (−), spectrum in methanol after addition of 20 equiv H_2O_2 (···), and spectrum after 10 min (- - -).*

A control experiment was run by replacing **1** with $Fe(OTf)_2{\cdot}2MeCN$. This reaction showed no cleavage of the salicylate aromatic ring (Figure 4). The intermediate spectrum in Figure 3 is anticipated to be related to an Fe^{III}–phenoxide band arising from oxidation of the Fe by H_2O_2 (*34*, *35*). The disappearance of this band is expected coincide with the cleavage of the aromatic ring.

Summary and Conclusions

In this work we reported the synthesis and characterization of **2**, a structural model for substrate-bound SDO. The precursor complex **1**, was found to be active in the cleavage of 1,4-dihydroxy-2-naphthoate in the presence of O_2 and to affect the ring scission of salicylate in the presence of H_2O_2. An intermediate species was observed during the oxidation of salicylate in the presence of H_2O_2, and is believed to be an Fe^{III}–phenoxide species with an intermediate in the ring scission reaction. Low temperature studies are planned to determine if any intermediates are present prior to the intermediate observed at 25 °C. Density functional theory studies will also help generate a proposed mechanism for the reaction.

Experimental

$Fe(OTf)_2{\cdot}2CH_3CN$ was prepared according to literature procedure (*36*). **1** was also prepared according to a published method (*37*). Anhydrous THF, pentane, dichloromethane, and ether were obtained using a solvent purification system (Innovative Technologies, Inc., Amesbury, MA). Methanol (CH_3OH) was dried and distilled according to published procedures (*38*). Elemental analysis was performed on pulverized crystalline samples that were placed under vacuum and sealed in a glass ampule prior to submission (Atlantic Microlabs, Inc., Norcross, GA). H_2O_2 (80%, v/v) was

prepared by adding anhydrous $MgSO_4$ to 30% H_2O_2 (Alfa Aesar, Haverhill, MA) and storing this mixture at 5 °C. The purity was determined by density measurements. Unless otherwise noted, all the reaction chemicals and tetramethylsilane were AR grade (Sigma-Aldrich, St. Louis, MO or Alfa Aesar) and used as received.

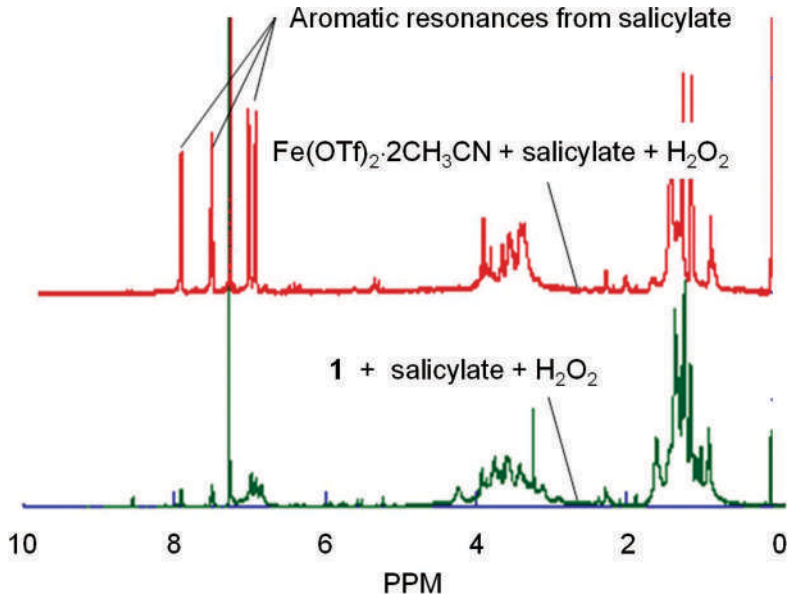

*Figure 4. ^1H NMR spectra (25 °C) of extracted reaction mixtures in $CDCl_3$. $Fe(OTf)_2{\cdot}2CH_3CN$ (control, top) and **1** reacted with **1** equiv bis(tetraethylammonium) salicylate and 20 equiv H_2O_2 in methanol. After 14 h, reactions were acidified with **1** N HCl and extracted with CH_2Cl_2. The CH_2Cl_2 was removed in vacuo and the residues were redissolved in $CDCl_3$ for analysis.*

Synthesis

Bis(tetraethylammonium) Salicylate

To a stirred solution of salicylic acid (2.76 g, 0.02 mol) in CH_3OH (10 mL) was added aqueous $Et_4N(OH)$ (wt.% = 20%, 29.45 g, 0.04 mol). The solution was stirred for 30 min, evaporated under high vacuum overnight to remove the solvent and affording a pale-white solid as the product. Yield: 7.54 g (95%). ^1H NMR (400 MHz, $CDCl_3$, δ (ppm)) = 7.92 (d, J = 2.0 Hz, 1H), 7.18–7.22 (m, 1H), 6.78 (d, J = 4.0 Hz, 1H), 6.69–6.73 (m, 1H), 3.29–3.34 (m, 16H), 1.27–1.30 (m, 24H).

*[Fe(T1Et4iPrIP)(sal)] (**2**)*

To a stirred solution of [Fe(T1Et4iPrIP)$(OTf)_2$] (50 mg, 0.063 mmol) in CH_3CN (2 mL) was added a prepared solution of bis(tetraethylammonium) salicylate (25 mg, 0.063 mmol) with 2.5 equiv trimethylamine (22 μL, 0.158 mmol) in CH_3CN (2 mL) under dry nitrogen. The solution was stirred for 30 min then filtered. Ether was added to the filtrate until it became slightly cloudy. The resulting mixture was filtered and placed at –30 °C. After a few days, light-green crystals were deposited as the product. Yield: 25 mg (75%). IR (KBr pellet, cm^{-1}): $\tilde{\nu}$ = 3124 (m), 3072(m), 2960 (s), 2932 (sh), 2869 (m), 2575(w), 1601 (vs), 1571(vs), 1465(vs), 1447 (vs), 1424 (s), 1383

(s), 1352 (vs), 1323 (sh), 1259 (s), 1201(m), 1195 (m), 1147 (m), 1132 (m), 1107 (w), 1084(w), 1031(w), 1101(w), 965(w), 923(w), 879(m), 818(m), 757(m), 727(w), 707(w), 655(w), 610 (w), 569 (w), 541 (s), 490 (w), 446 (w), 407 (w). UV–vis [λ_{max}, nm (ε, M^{-1} cm^{-1}) in CH_3OH] 409 (598), 262 (130500). Anal. Calcd for $C_{31}H_{43}N_6O_3PFe$: C, 58.68; H, 6.83; N, 13.24. Found: C, 58.03; H, 6.75; N, 12.86. Magnetic measurements, μ_{eff} ($CDCl_3$ solution, 298 K): 5.20 μ_B.

Physical Measurements

A Cary 50 ultraviolet–visible (UV–vis) spectrophotometer was used to collect optical spectra. FT-IR spectra were acquired on a Varian 3100 Excalibur Series and a Bruker ATR Alpha P spectrometer. NMR spectra were monitored at 25 °C on a Brüker Avance II 400 MHz instrument and sample peaks were referenced to tetramethylsilane ($CDCl_3$). GCMS experiments were performed on an Hewlett-Packard 6890/5973 GCMS. Solution magnetic susceptibility measurements on **1** at 298 K were obtained using the Evans NMR method (*39*) with $CDCl_3$ containing 5% CH_3CN as the reference. Mass susceptibility, χ_g, was calculated from the following equation:

$$\chi_g = \frac{-3\Delta f}{4\pi f m} + \chi_o\left[1 + \frac{(d_o - d_s)}{m}\right] \quad (1)$$

Where Δf is the frequency shift in Hz of the reference compound, f is the fixed probe frequency of the spectrometer, χ_o is the mass susceptibility in cm^3 g^{-1} of the solvent, m is the mass in g of the complex in 1 mL of solution, and d_o and d_s are the densities of the solvent and solution, respectively.

X-ray Crystallography

Green blocks of **2** were obtained by allowing a saturated CH_3CN solution of **2** with ether to cool at –30 °C. A crystal of **2** was placed onto the tips of a thin glass optical fiber and mounted on a Bruker SMART APEX II CCD platform diffractometer for data collection at 100.0(5) K (*40*). The full data collection was carried out using MoKα radiation (graphite monochromator). The intensity data were corrected for absorption (*41*). Final cell constants were calculated from the xyz centroids after integration (*42*). The structures were solved using *SIR2011* (*43*) and refined using *SHELXL-2014/7* (*44*). A direct-methods solution was calculated and provided most nonhydrogen atoms from the E-map. Full-matrix least squares/difference Fourier cycles were performed which located the remaining nonhydrogen atoms. All nonhydrogen atoms were refined with anisotropic displacement parameters. All other hydrogen atoms were placed in ideal positions and refined as riding atoms with relative isotropic displacement parameters. The asymmetric unit for each compound contains one iron complex and one cocrystallized diethyl ether molecule, both in general positions. Refer to Table 1 for additional crystal and refinement information. Selected bond lengths and angles are listed in Table 2.

Acknowledgments

FAC acknowledges the receipt of an OU-REF grant. JL acknowledges a graduate fellowship from OU. MAM acknowledges an OU Provost Award. NIH Grant No. R15GM112395 and NSF Grant Nos. CHE-0748607 and CHE-0821487 are gratefully acknowledged.

References

1. Lerner, J. E. C.; Kohajda, T.; Aguilar, M. E.; Massolo, L. A.; Sanchez, E. Y.; Porta, A. A.; Opitz, P.; Wichmann, G.; Herbarth, O.; Mueller, A. Improvement of Health Risk Factors after Reduction of VOC Concentrations in Industrial and Urban Areas. *Environ. Sci. Pollut. Res.* **2014**, *21*, 9676–9688.
2. Shi, S. S.; Zhao, B. Modeled Exposure Assessment via Inhalation and Dermal Pathways to Airborne Semivolatile Organic Compounds (SVOCs) in Residences. *Environ. Sci. Technol.* **2014**, *48*, 5691–5699.
3. Vaillancourt, F. H.; Bolin, J. T.; Eltis, L. D. The Ins and Outs of Ring-Cleaving Dioxygenases. *Crit. Rev. Biochem. Mol. Biol.* **2006**, *41*, 241–267.
4. Lack, L. The Enzymic Oxidation of Gentisic Acid. *Biochim. Biophys. Acta* **1959**, *34*, 117–123.
5. Knox, E.; Edwards, S. W. The Properties of Maleylacetate, the Initial Product of Homogentisate Oxidation in Liver. *J. Biol. Chem.* **1955**, *216*, 489–498.
6. Harpel, M. R.; Lipscomb, J. D. Gentisate 1,2-Dioxygenase from *Pseudomonas*. Purification, Characterization, and Comparison of the Enzymes from *Pseudomonas testosteroni* and *Pseudomonas acidovorans*. *J. Biol. Chem.* **1990**, *265*, 6301–6311.
7. Miyauchi, K.; Adachi, Y.; Nagata, Y.; Takagi, M. Cloning and Sequencing of a Novel *meta*-Cleavage Dioxygenase Gene whose Product is Involved in Degradation of g-Hexachlorocyclohexane in *Sphingomonas paucimobilis*. *J. Bacteriol.* **1999**, *181*, 6712–6719.
8. Veldhuizen, E. J. A.; Vaillancourt, F. H.; Whiting, C. J.; Hsiao, M. M. Y.; Gingras, G.; Xiao, Y. F.; Tanguay, R. M.; Boukouvalas, J.; Eltis, L. D. Steady-State Kinetics and Inhibition of Anaerobically Purified Human Homogentisate 1,2-Dioxygenase. *Biochem. J.* **2005**, *386*, 305–314.
9. Hintner, J. P.; Remtsma, T.; Stolz, A. Biochemical and Molecular Characterization of a Ring Fission Dioxygenase with the Ability to Oxidize (substituted) Salicylate(s) from *Pseudaminobacter salicylatoxidans*. *J. Biol. Chem.* **2004**, *279*, 37250–37260.
10. Qu, Y.; Spain, J. C. Biodegradation of 5-Nitroanthranilic Acid by *Bradyrhizobium sp* Strain JS329. *Appl. Environ. Microbiol.* **2010**, *76*, 1417–1422.
11. Qu, Y.; Spain, J. C. Molecular and Biochemical Characterization of the 5-Nitroanthranilic Acid Degradation Pathway in *Bradyrhizobium sp* Strain JS329. *J. Bacteriol.* **2011**, *193*, 3057–3063.
12. Ferraroni, M.; Matera, I.; Steimer, L.; Burger, S.; Scozzafava, A.; Stolz, A.; Briganti, F. Crystal Structures of Salicylate 1,2-Dioxygenase-Substrates Adducts: A Step Towards the Comprehension of the Structural Basis for Substrate Selection in Class III Ring Cleaving Dioxygenases. *J. Struct. Biol.* **2012**, *177*, 431–438.
13. Buongiorno, D.; Straganz, G. D. Structure and Function of Atypically Coordinated Enzymatic Mononuclear Non-Heme-Fe(II) Centers. *Coord. Chem. Rev.* **2013**, *257* (2), 541–563.
14. Fetzner, S. Ring-Cleaving Dioxygenases with a Cupin Fold. *Appl. Environ. Microbiol.* **2012**, *78*, 2505–2514.
15. Ferraroni, M.; Da Vela, S.; Kolvenbach, B. A.; Corvini, P. F. X.; Scozzafava, A. The Crystal Structures of Native Hydroquinone 1,2-Dioxygenase from *Sphingomonas sp* TTNP3 and of Substrate and Inhibitor Complexes. *Biochim. Biophys. Acta Proteins Proteomics* **2017**, *1865*, 520–530.

16. Hopper, D. J.; Chapman, P. J. Gentisic Acid and its 3- and 4-Methyl Substituted Homologues as Intermediates in the Bacterial Degradation of *m*-Cresol, 3,5-Xylenol and 2,5-Xylenol. *Biochem. J.* **1971**, *122*, 19–28.
17. Poh, C. L.; Bayly, R. C. Evidence of Isofunctional Enzymes used in *m*-Cresol and 2,5-Xylenol Degradation via the Gentisate Pathway. *J. Bacteriol.* **1980**, *143*, 59–69.
18. Hintner, J. P.; Lechner, C.; Riegert, U.; Kuhm, A. E.; Storm, T.; Reemtsma, T.; Stolz, A. Direct Ring Fission of Salicylate by a Salicylate 1,2-Dioxygenase Activity from *Pseudaminobacter salicylatoxidans*. *J. Bacteriol.* **2001**, *183*, 6936–6942.
19. Chen, J.; Li, W.; Wang, M.; Zhu, G.; Liu, D.; Sun, F.; Hao, N.; Li, X.; Rao, Z.; Zhang, X. C. Crystal Structure and Mutagenic Analysis of GDOsp, a Gentisate 1,2-Dioxygenase from *Silicibacter Pomeroyi*. *Prot. Sci.* **2008**, *17*, 1362–1373.
20. Straganz, G. D.; Diebold, A. R.; Egger, S.; Nidetzky, B.; Solomon, E. I. Kinetic and CD/MCD Spectroscopic Studies of the Atypical, three-His-Ligated, Non-Heme Fe^{2+} Center in Diketone Dioxygenase: The Role of Hydrophilic Outer Shell Residues in Catalysis. *Biochemistry* **2010**, *49*, 996–1004.
21. Eppinger, E.; Stolz, A. Expansion of the Substrate Range of the Gentisate 1,2-Dioxygenase from *Corynebacterium glutamicum* for the Conversion of Monohydroxylated Benzoates. *Protein Eng. Des. Sel.* **2017**, *30*, 57–65.
22. Adams, M. A.; Singh, V. K.; Keller, B. O.; Jia, Z. Structural and Biochemical Characterization of Gentisate 1,2-Dioxygenase from *Escherichia coli* O157:H7. *Mol. Microbiol.* **2006**, *61*, 1469–1484.
23. Harpel, M. R.; Lipscomb, J. D. Gentisate 1,2-Dioxygenase from *Pseudomonas*. Substrate Coordination to Active-Site Fe^{2+} and Mechanism of Turnover. *J. Biol. Chem.* **1990**, *265*, 22187–22196.
24. Ferraroni, M.; Steimer, L.; Matera, I.; Burger, S.; Scozzafava, A.; Stolz, A.; Briganti, F. The Generation of a 1-Hydroxy-2-Naphthoate 1,2-Dioxygenase by Single Point Mutations of Salicylate 1,2-Dioxygenase - Rational Design of Mutants and the Crystal Structures of the A85H and W104Y Variants. *J. Struct. Biol.* **2012**, *180*, 563–571.
25. Dong, G.; Ryde, U. O_2 Activation in Salicylate 1,2-Dioxygenase: A QM/MM Study Reveals the Role of His162. *Inorg. Chem.* **2016**, *55*, 11727–11735.
26. Roy, S.; Kastner, J. Catalytic Mechanism of Salicylate Dioxygenase: QM/MM Simulations Reveal the Origin of Unexpected Regioselectivity of the Ring Cleavage. *Chem.—Eur. J.* **2017**, *23*, 8949–8962.
27. Li, J.; Banerjee, A.; Pawlak, P. L.; Brennessel, W. W.; Chavez, F. A. Highest Recorded N-O Stretching Frequency for 6-Coordinate $\{Fe\text{-}NO\}^7$ Complexes: An Iron Nitrosyl Model for His_3 Active Sites. *Inorg. Chem.* **2014**, *53*, 5414–5416.
28. Orville, A. M.; Chen, V. J.; Krauciunas, A.; Harpel, M. R.; Fox, B. G.; Munck, E.; Lipscomb, J. D. Thiolate Ligation of the Active Site Iron(II) of Isopenicillin *N*-Synthase Derives from Substrate Rather than Endogenous Cysteine: Spectroscopic Studies of Site-Specific Cys-Ser Mutated Enzymes. *Biochemistry* **1992**, *31*, 4602–4612.
29. Banerjee, A.; Li, J.; Speelman, A. L.; White, C. J.; Pawlak, P. L.; Brennessel, W. W.; Lehnert, N.; Chavez, F. A. A Structural Model for the Iron-Nitrosyl Adduct of Gentisate Dioxygenase. *Eur. J. Inorg. Chem.* **2018**, *44*, 4797–4804.

30. Begel, S.; Puchta, R.; Sutter, J.; Heinemann, F. W.; Dahlenburg, L.; van Eldik, R. Studies on the Reaction of Iron(II) with NO in a Noncoordinating Ionic Liquid. *Inorg. Chem.* **2015**, *54*, 6763–6775.
31. Addison, A. W.; Rao, T. N.; Reedijk, J.; van Rijn, J.; Verschoor, G. C. Synthesis, Structure, and Spectroscopic Properties of Copper(II) Compounds Containing Nitrogen–Sulphur Donor Ligands; the Crystal and Molecular Structure of Aqua[1,7-bis(N-methylbenzimidazol-2-yl)-2,6-dithiaheptane]-Copper(II) Perchlorate. *J. Chem. Soc., Dalton Trans.* **1984**, 1349–1356.
32. Bittner, M. M.; Baus, J. S.; Lindeman, S. V.; Fiedler, A. T. Synthesis and Structural Characterization of Iron(II) Complexes with Tris(imidazolyl)phosphane Ligands: A Platform for Modeling the 3-Histidine Facial Triad of Nonheme Iron Dioxygenases. *Eur. J. Inorg. Chem.* **2012**, 1848–1856.
33. Rahaman, R.; Chakraborty, B.; Paine, T. K. Mimicking the Aromatic-Ring-Cleavage Activity of Gentisate-1,2-Dioxygenase by a Nonheme Iron Complex. *Angew. Chem., Int. Ed.* **2016**, *55*, 13838–13842.
34. Kerber, W. B.; Perez, K. A.; Ren, C.; Siegler, M. A. Speciation of Ferric Phenoxide Intermediates During the Reduction of Iron(III)-μ-oxo Dimers by Hydroquinone. *Inorg. Chem.* **2014**, *53*, 11507–11516.
35. Aniscough, E. W.; Brodie, A. M.; Plowman, J. E.; Brown, K. L.; Addison, A. W.; Gainsford, A. R. Small Molecule Analogues for the Specific Iron-Binding Site of Lactoferrin: A Single-Crystal X-ray Structure of Bis(methanol)bis[2- (5-methylpyrazol-3-yl) phenolato]iron(III) Nitrate-Methanol and Spectroscopic Studies on Iron(III) Phenolate Complexes. *Inorg. Chem.* **1980**, *19*, 3655–3663.
36. Hagen, K. S. Iron(II) Triflate Salts as Convenient Substitutes for Perchlorate Salts: Crystal Structures of $[Fe(H_2O)_6](CF_3SO_3)_2$ and $Fe(MeCN)_4(CF_3SO_3)_2$. *Inorg. Chem.* **2000**, *39*, 5867–5869.
37. Korendowych, E.; Crown, A. L.; Harbuz, M. S.; Jessop, D. S.; Lightman, S. L.; Kirwan, J. R. Hypothalamic-Pituitary-Adrenal Axis Dysregulation in Patients with Rheumatoid Arthritis following the Dexamethasone-Corticotrophin Releasing Factor Test. *Rheumatology* **2001**, *40*, 22–22.
38. Armarego, W. L. F.; Perrin, D. D. *Purification of Laboratory Chemicals*, 4th ed.; Butterworth Heinemann: New York, 2002.
39. Piguet, C. Paramagnetic Susceptibility by NMR: The "Solvent Correction" Removed for Large Paramagnetic Molecules. *J. Chem. Educ.* **1997**, *74*, 815–816.
40. *APEX2,* version 2011.4-1; Bruker AXS: Madison, WI, 2011.
41. Sheldrick, G. M. *SADABS*, version 2014/5; University of Göttingen: Göttingen, Germany, 2014.
42. *SAINT*, version 8.32B; Bruker AXS: Madison, WI, 2014.
43. Burla, M. C.; Caliandro, R.; Camalli, M.; Carrozzini, B.; Cascarano, G. L.; Giacovazzo, C.; Mallamo, M.; Mazzone, A.; Polidori, G.; Spagna, R. *SIR2011: A New Package for Crystal Structure Determination and Refinement*, version 1.0; Instituto di Cristallografia: Bari, Italy, 2012. 2012, 32, 115.
44. Sheldrick, G. M. *SHELXL*, version 2014/7; University of Göttingen: Göttingen, Germany, 2014.

Chapter 5

Recent Advances in Ru-Catalyzed Olefin and C–H Bond Oxidation

Hashini N. K. Herath and Alexander R. Parent*

Department of Chemistry and Biochemistry, North Dakota State University, Fargo, North Dakota 58108-6050, United States

***E-mail: alexander.parent@ndsu.edu**

A brief summary of recent (2011–2018) reports on olefin epoxidation and C–H bond oxidation by ruthenium (Ru) complexes is presented herein. Emphasis is on studies reporting mechanistic information with an overview of the techniques used. This chapter is designed to provide foundational knowledge for those beginning work in this area.

Designing and characterizing catalysts for the activation of C–H bonds is one of the most active areas in chemical research today. New catalysts for the selective conversion of C–H to C–C (*1*–*3*), C–N (*2*), C–X (*4*), and C–O (*2*) bonds seem to be reported daily in the chemical literature. Each of these chemical transformations has been significantly developed and warrants an in-depth review of the recent advances pertaining to their catalysis. For the purposes of this review, we will focus on the oxidation of C–H bonds to C–O bonds (i.e., C–H bond hydroxylation) and the related oxidation of C=C bonds to epoxides (i.e., olefin epoxidation). Specifically, this review will focus on C–H bond oxidation by ruthenium (Ru) complexes, as a number of recent reviews have been published on C–H bond oxidation by first-row transition metal catalysts (*5*–*11*). Recently, a number of new and improved Ru catalysts have been reported . This chapter aims to offer a brief overview of these developments and provide the reader with a foundation on which to start exploring the field.

Mechanism of Catalysis by Ru^{IV}–Oxo and Ru^{III}–Oxyl Species

C–H bond oxidation mechanisms can be divided into two broad categories: inner- and outer-sphere mechanisms. Inner-sphere mechanisms involve direct coordination between the catalyst and substrate, which is typically followed by the oxidative addition of the C–H bond to form an organometallic metal hydride species, followed by ligand exchange, and reductive elimination of product (*12*, *13*). In contrast, outer-sphere mechanisms typically involve an electrophilic attack of the metal complex on the C–H bond to form the product, which may or may not be transiently coordinated to the metal center (*13*). All known cases of C–H bond hydroxylation and olefin

epoxidation follow outer-sphere pathways; therefore, inner-sphere mechanisms will not be discussed in detail.

Ruthenium–oxo (Ru=O) and Ru–oxyl (Ru–O●) species are key intermediates during C–H bond hydroxylation and olefin epoxidation (Scheme 1). These species are typically formed by the oxidation of a Ru^{II} or Ru^{III} complex by a sacrificial chemical oxidant, although there are a few examples of such species being formed electrochemically in the field of water oxidation (*14*). Following formation of the Ru–oxo or hydroxo species, C–H bond hydroxylation can proceed via two distinct pathways: radical rebound and oxene insertion. Similarly, alkene epoxidation can proceed via a concerted two-electron nucleophilic attack on the Ru–O● or Ru=O intermediate, or via two consecutive one-electron transfers with the formation of a substrate radical as an intermediate. Significant effort has been devoted to identifying which factors influence the pathway followed during catalysis, as the mechanism followed by oxidation catalysts is the most important factor in determining overall stereoselectivity.

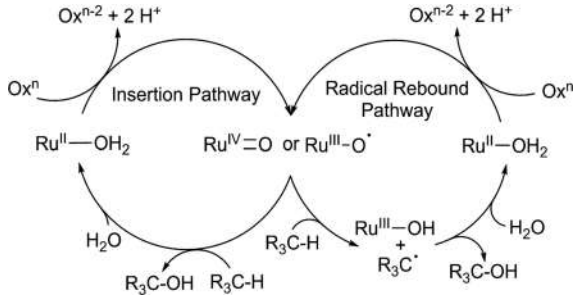

Scheme 1. General mechanisms of C–H bond hydroxylation. Adapted with permission from reference (*15*). *Copyright 2018 The Royal Society of Chemistry.*

Radical Rebound Mechanism of C–H Bond Hydroxylation

The most common mechanism of C–H bond hydroxylation is the radical rebound. Originally proposed by Groves (*16*, *17*), the rebound mechanism involves initial H-atom abstraction from an aliphatic substrate by the high-valent metal–oxo or hydroxo species (Scheme 1). The substrate radical species formed then further reacts with the Ru catalyst to form the C–O bond. Under this mechanism, the rate-determining step (RDS) is typically H-atom abstraction by the high-valent Ru catalyst. As such, the overall rate of the reaction is directly controlled by the overall strength of the C–H bond dissociation energy (BDE), as well as the oxidizing potential of the catalyst. Excellent reviews on the relationship between BDE and H-atom abstraction by transition metals have been published by Mayer (*18*, *19*) (details on this relationship will not be discussed in-depth herein). It is sufficient to say that for any particular catalyst, the rate of the reaction follows that predicted by the Evans–Polanyi correlation (*20*) (i.e., the log of the rate constant [*k*] varies linearly with the BDE of the substrate C–H bond). Thus, the rebound mechanism selectively oxidizes weaker C–H bonds in preference to stronger C–H bonds and greater selectivity is predicted for catalysts with lower oxidizing potentials.

In the rebound mechanism, stereoselectivity is determined in the moments following H-atom abstraction. If the nascent substrate radical reacts quickly with the newly formed Ru–OH, the original configuration of the C-atom can be retained leading to a retention of stereochemistry. Conversely, with even a momentary delay in the rebound, the substrate radical can isomerize, resulting in a racemic product mixture.

Oxene Insertion Mechanism of C–H Bond Hydroxylation

Direct insertion mechanisms involve inserting an active ligand (such as a carbene, nitrene, or oxene) between the C–H bond without forming a metal–alkyl intermediate. While well-established as a mechanism for the formation of C–C and C–N bonds (*3*, *21*), relatively few examples of C–O bond formation via insertion have been reported. As originally proposed by Shaik for H_2 oxidation (*22*), the insertion mechanism for the Ru=O or Ru–O● species reacts with the substrate in a single two-electron step to form a bound product alcohol in the RDS (Scheme 1). This bound product then exchanges for solvent and the Ru center can be re-oxidized to its high-valent state by the oxidizing agent. Oxene insertion provides several advantages over radical rebound, most importantly there is no opportunity of isomerization in the transition state and, therefore, no racemization during the formation of the C–O bond.

Alkene Epoxidation via One- and Two-Electron Mechanisms

Similar to C–H bond hydroxylation, alkene epoxidation can follow either a one-electron stepwise or two-electron concerted pathway (Scheme 2) (*23*, *24*). For epoxidation by Ru=O and Ru–O● species, kinetic and computational results suggest that the one-electron stepwise pathway typically dominates (*25*), with the overall enantioselectivity of the reaction determined by the rate of radical rebound and the relative energies of the radical conformations. Unlike C–H bond hydroxylation, there is no general RDS, with either oxidation of the metal center or nucleophilic attack by the alkene being rate determining, depending on the catalyst and reaction conditions (*26*).

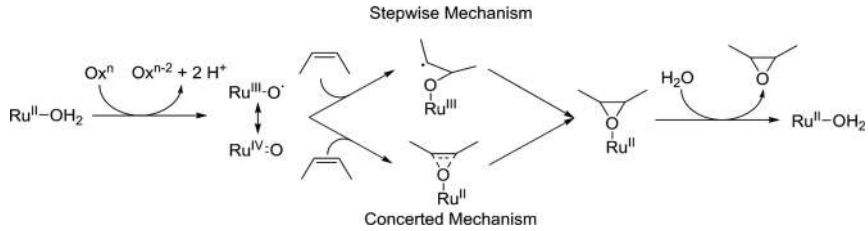

Scheme 2. General mechanisms of alkene epoxidation by Ru complexes.

Alkene Epoxidation

Alkene epoxidation is responsible for the synthesis of numerous industrially important materials and is thus a prime target for improved synthetic methods (*23*, *27*). Historically, organic peracids have been employed as oxidants for the alkene epoxidation reactions (*28*); however, use of these oxidants has major drawbacks including the generation of organic waste, narrow substrate scopes, and difficulty separating the epoxide from byproducts (*29*). To overcome these problems, a number of transition metal catalysts have been developed to enable efficient and selective alkene epoxidation using more benign oxidants (*23*, *26*, *27*). Among these catalysts, those based on Ru have been demonstrated to serve among the most as efficient and long-lived (*23*, *26*). A number of improved Ru catalysts have been reported since the comprehensive review by Chatterjee (*26*). This section focuses on those catalysts reported since 2008 and refers readers to the aforementioned review for details on earlier work in this area.

Table 1. Relative Turnover Frequencies (TOF) and Turnover Numbers (TON) for Epoxidation Catalysts

Complex	*Substrate*	*Oxidant*	*TOF (h^{-1})*	*TON*[a]	*Reference*
1[b]	Styrene	$PhI(OAc)_2$	6.3[c]	49.6	(*30*)
2a[b]	Styrene	$PhI(OAc)_2$	3.4[c]	41.5	(*30*)
2b[b]	Styrene	$PhI(OAc)_2$	5.3[c]	60.5	(*30*)
3a[d]	Styrene	H_2O_2	1.9	15	(*31*)
3b[d]	Styrene	H_2O_2	0.25	2.0	(*31*)
4a[e]	*trans*-Stilbene	$PhI(OAc)_2$	2.6	61	(*32*)
4b[e]	*trans*-Stilbene	$PhI(OAc)_2$	2.0	47	(*32*)
5a[e]	*trans*-Stilbene	$PhI(OAc)_2$	1.4	33	(*32*)
5b[e]	*trans*-Stilbene	$PhI(OAc)_2$	1.7	42	(*32*)
6[e]	*trans*-Stilbene	$PhI(OAc)_2$	0.56	13	(*32*)
7[e]	*trans*-Stilbene	$PhI(OAc)_2$	0.53	16	(*32*)
8[f]	Styrene	$PhI(OAc)_2$	520[g]	440[g]	(*33*)
9a[b]	*trans*-Stilbene	$PhI(OAc)_2$	13.6[c]	80.1	(*39*)
9b[b]	*trans*-Stilbene	$PhI(OAc)_2$	7.7[c]	59.4	(*39*)
10[b]	*trans*-Stilbene	$PhI(OAc)_2$	250[c]	100	(*39*)
11a[h]	*trans*-Stilbene	PhIO	78	680	(*40*)
11b[h]	*trans*-Stilbene	PhIO	66	596	(*40*)
12[h]	*trans*-Stilbene	PhIO	18	148	(*40*)
13[h]	*trans*-Stilbene	PhIO	12	136	(*40*)

[a] Mols epoxide/mols catalyst. [b] Reaction conditions: 24 h, 298 K, 500 μM catalyst, 50 mM substrate, 100 mM oxidant, 15 mM biphenyl standard in dichloromethane (DCM). [c] Measured initial rate in μmol substrate/h. [d] Reaction conditions: 8 h, 293 K, 8.3 mM catalyst, 167 mM substrate, 500 mM oxidant in ethanol. [e] Reaction conditions: 24 h, room temperature (RT), 0.8 mM catalyst, 80.0 mM substrate, 160.0 mM oxidant in DCM. [f] Reaction conditions: 1.0 mM catalyst, 2.0 M substrate, 4.0 M oxidant, 4.0 M water, 165 mM dodecane standard in 1:1 DCM/ethanol. [g] Per Ru center. [h] Reaction conditions: 910 mM $PhI(OAc)_2$, 910 mM water, and 0.5 mM catalyst were stirred at RT for 2 h in 5 mL of 1,2-dichloroethane to hydrolyze the $PhI(OAc)_2$ to PhIO. Substrate was then added to a final concentration of 455 mM, and the reaction was stirred at RT with samples analyzed for product formation every 5–30 min.

One important development in the field since 2008 is the report by Dakkach et al. (*30*) reporting on a family of Ru terpyridyl (tpy) complexes with (pyridyl)pyrazol and (pyridyl)pyrollidine ligands (Figure 1). Compound **1** was determined to have a concerted two-electron $Ru^{II/IV}$ couple between pH 1.21 and 9.75, while compounds **2a** and **2b** were found to possess slightly separated one-electron

$Ru^{II/III}$ and $Ru^{III/IV}$ redox couples. Each of these catalysts showed epoxidation activity in the presence of (diacetoxyiodo)benzene, ($PhI(OAc)_2$) (Table 1). Interestingly, there is a competition between steric and electron effects for epoxidation in this family of catalysts. Electronically, **1** has the highest oxidizing potential and **2a** has the lowest; therefore, with sterically unhindered epoxides such as styrene, the overall rate of epoxidation is **1** > **2b** > **2a**. On the other hand, **2b** possesses a sterically bulky methyl group near the Ru=O species, inhibiting more sterically hindered epoxides from approaching and greatly diminishing its rate of reaction relative to **1** and **2a** (Table 1).

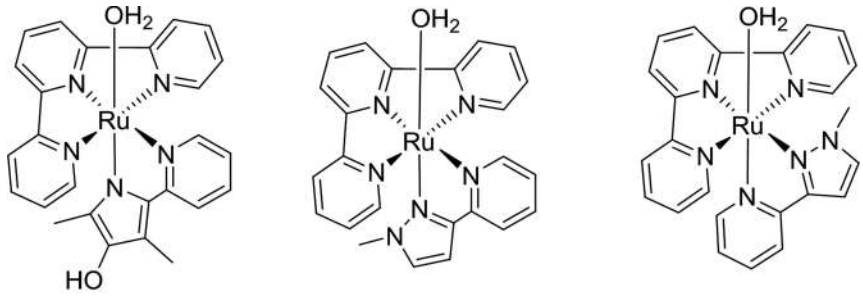

*Figure 1. Structure diagrams of **1**, **2a**, and **2b** (30).*

In 2011 Chowdhury et al. (*31*) reported a related series of Ru complexes bearing tpy and 2-quinolinecarboxylate ligands (Figure 2). The different isomers of this complex show significantly different catalytic activity for alkene epoxidation, with **3a** showing good activity for epoxidation using hydrogen peroxide as the oxidant, and **3b** requiring *meta*-chloroperbenzoic acid to catalyze epoxidation (Table 1). This difference in reactivity between the isomers is attributed to the relatively lower energy of Ru^{IV}=O observed for **3a**, indicating the RDS for these catalysts is oxidation of the Ru^{II}–OH_2 resting state by the oxidant. On the basis of density functional theory (DFT) calculations and radical scavenger competition experiments, these complexes were each proposed to follow the stepwise – rather than concerted mechanism for epoxidation (Scheme 2).

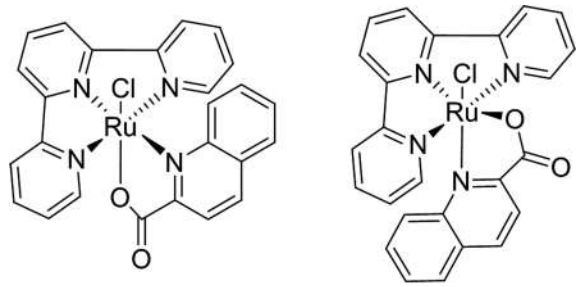

*Figure 2. Structure diagrams of Ru(tpy)(2-quinolinecarboxylate)Cl isomers **3a** and **3b** (31).*

Also in 2011, Ru complexes bearing either tris(pyrazolyl)methane or tpy and bis(oxazoline) (BOX) ligands were investigated by Serrano et al. (*32*) for selectivity in substrates containing multiple alkene moieties (Figure 3). Intriguingly, the selectivity of these catalysts for ring versus vinyl epoxidation in 4-vinylcyclohexene was found to vary dramatically with small changes in ligand (Table 2). This selectivity was investigated via DFT, where it was found that the RDS in these reactions

was an initial complexation between the catalysts and one of the C=C bonds in 4-vinylcyclohexene, and that switching from the benzyl side chains of **4a** to the ^{i}Pr side chains of **4b** increased the barrier to activation at the cyclohexene C=C bond by 1.4 kcal/mol (Figure 4). Stereochemical retention was observed for these catalysts in the oxidation of *cis*-stilbene, suggesting a concerted mechanism; however, it is not possible to exclude a stepwise mechanism with rapid rebound based on the experimental data provided.

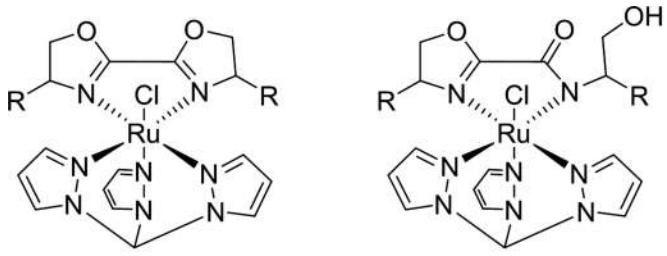

4a: R = Bz
4b: R = ^{i}Pr

5a: R = Bz
5b: R = ^{i}Pr

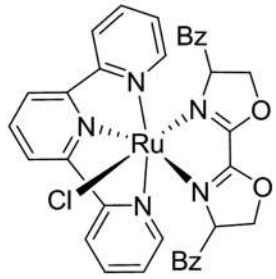

6

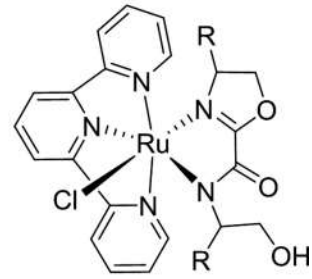

7

Figure 3. Structure diagrams of BOX ligand epoxidation catalysts ***4****–****7*** *(32).*

In 2013 Di Giovanni et al. reported a dinuclear Ru complex, $\{[Ru^{II}(tpy)(H_2O)]_2(\mu\text{-pyridazine-3,6-dicarboxylate})\}^{2+}$ **8**, with exceptionally high epoxidation activity (Figure 5) (*33*). The high activity of this catalyst is attributed to through-space cooperative effects enabled by electronic communication through the pyridazine ligand (*34*, *35*). Support for a cooperative mechanism was demonstrated by comparison to the monomeric $[Ru^{II}(tpy)(picolinate)(H_2O)]^{+}$ complex, which showed much lower activity. The overall mechanism of epoxidation by **8** was proposed to be concerted nucleophilic attack by the alkene on one of the Ru^{IV}=O sites due to retention of stereochemistry. As with the BOX catalysts, a stepwise process with rapid rebound cannot be excluded because of the experimental results.

Table 2. Selectivity for Ring versus Vinyl Epoxidation of 4-Vinylcyclohexene by Ru–BOX Catalysts

Catalyst	*Conversion (%)*	*Ring Oxidation (%)*	*Vinyl Oxidation (%)*
4a	74.1	97.4	2.6
4b	21.2	0	100

Reaction conditions: 24 h, RT, 0.80 mM catalyst, 80.0 mM substrate, 160.0 mM oxidant in DCM.

While often discounted as too prone to oxidation to serve as ligands during oxidation catalysis, N-heterocyclic carbenes (NHC) have been demonstrated to serve admirably under the extremely harsh conditions required for water oxidation (*36*, *37*). With this powerful demonstration of their resistance to oxidation, NHCs have begun to be investigated for their efficacy as ligands in other oxidation reactions, including akene epoxidation and C–H bond hydroxylation. Early examples of NHCs are those reported by the two groups led by Romero and Rodríguez in groups **9**–**10** (Figure 6) (*38*, *39*). Each of these complexes was determined to have a concerted two-electron two-proton $Ru^{II/IV}$ redox potential in aqueous solution, with the potential varying in the order **10** < **9b** < **9a**. In this family, **10** typically exhibited the greatest initial rate and turnover despite its lower redox potential (Table 2). This was attributed to a combination of the amine ligand in **10** providing a more nucleophilic Ru=O species relative to that formed by the terpyridine ligands in **9a** and **9b**, as well as the potential for π–π interactions between **10** and aromatic substrates.

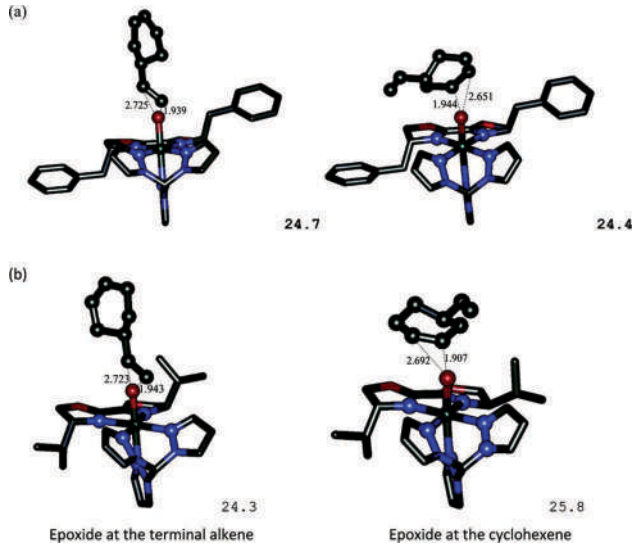

Figure 4. DFT optimized transition states of the RDS for epoxidation of 4-vinylcyclohexene by ***4a*** *(a) and* ***4b*** *(b). Energy barriers are given in kcal/mol and interatomic distances are given in Å. Reprinted with permission from reference* (32). *Copyright 2011 American Chemical Society.*

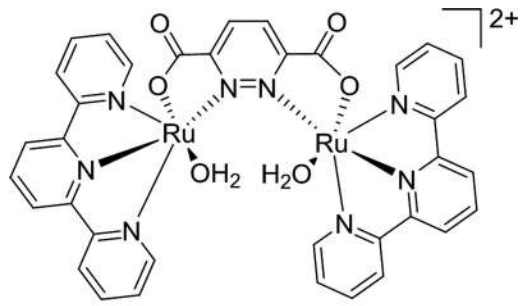

8

Figure 5. Structure diagram of {[Ru^{II}(tpy)(H_2O)]$_2$(μ-pyridazine-3,6-dicarboxylate)}$^{2+}$ ***8*** *(33).*

In 2017 Liu et al. (*40*) reported some of the best characterized Ru–NHC complexes to catalyze alkene epoxidation (Figure 6). In their report, the authors describe a family of Ru–NHC complexes containing either a meridional tpy ligand or a facial *N,N*-bis(pyridin-2-ylmethyl)ethanamine ligand. It was found that the mer complexes **11a** and **11b** were significantly more active for epoxidation than the fac complexes **12** and **13** (Table 1). This is attributed to the ability of **11a** and **11b** to participate in concerted two-electron transfers ($\Delta E_{1/2}$ ~30 mV), whereas **12** and **13** are limited to one-electron chemistry ($\Delta E_{1/2}$ > 200 mV). Due to this ability to participate in two-electron chemistry, **11a** and **11b** are proposed to catalyze epoxidation via a concerted mechanism (Scheme 2), whereas **12** and **13** are proposed to catalyze the reaction via a stepwise mechanism (Scheme 2). Although, it should be noted that retention of stereochemistry is observed during the epoxidation of *cis*-*β*-methylstyrene for all catalysts in this family, indicating that if **12** and **13** follow a stepwise mechanism, then the rebound is faster than rotation around the C–C bond in the radical intermediate, demonstrating the difficulty of using only retention of stereochemistry to determine catalytic mechanisms in these reactions.

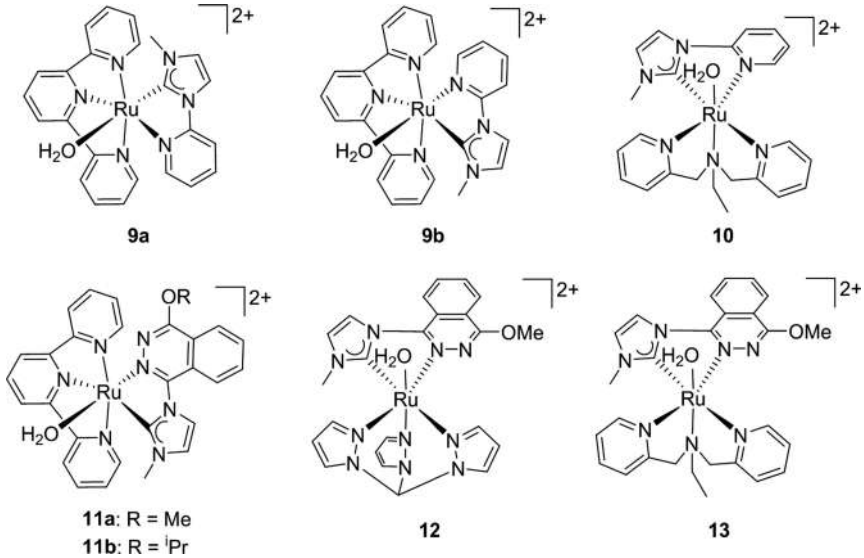

9a **9b** **10**

11a: R = Me
11b: R = ^{i}Pr

12 **13**

Figure 6. Structure diagrams of Ru–NHC epoxidation catalysts ***9–10*** *(38, 39) and* ***11a–13*** *(40).*

An excellent joint experimental theoretical study by Dhuri et al. (*41*) in 2015 describes the unusual case of a Ru complex catalyzing either epoxidation or C–H bond hydroxylation, depending on the substrate. Briefly, this complex, [Ru^{IV}(tpy)(2,2′-bipyrimidine)(O)]$^{2+}$ **14** (Figure 7), was

found to epoxidize styrene via a stepwise nucleophilic attack, but hydroxylates cyclohexene to 2-cyclohexen-1-ol via rate-determining H-atom abstraction. Support for these mechanisms was provided because of DFT energy barrier calculations in combination with kinetic isotope effect (KIE) studies. Further discussion of this catalyst's C–H bond hydroxylation activity is provided in the following section.

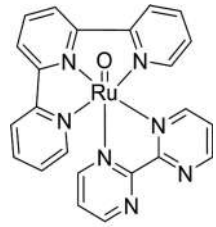

14

Figure 7. Structure diagram of [Ru^{IV}(tpy)(2,2′-bipyrimidine)(O)]$^{2+}$ ***14*** *(41).*

Alkane Hydroxylation

Alkane hydroxylation (i.e., the conversion of C–H to C–OH groups) is one of the most active areas in catalysis research today (*42*). This is due to the combined importance of installing functional groups at unactivated sites in organic synthesis (*13*, *43*) and the relevance to the synthesis of liquid fuels from renewable resources (*44*). With regards to Ru complexes synthesized for this reaction, a wide variety of ligand scaffolds have been employed, including porphyrins (*45*), amines (*46*), phosphines (*47*), and even polyoxometalates (*48*). Among these scaffolds, polypyridyl ligands are among the best studied due to their oxidation resistance and synthetic accessibility (*49*).

For our first example of alkane hydroxylation complexes using polypyridyl ligands, we return to the work of Dhuri et al. (*41*) discussed in the previous section (Figure 7). In this report **14** was found to catalyze the hydroxylation of allylic and aliphatic C–H bonds. The RDS for each of these reactions is H-atom abstraction, although Ru^{III} rather than the Ru^{II} expected from the rebound mechanism (Scheme 1) was found as the product during stoichiometric oxidation experiments. Further kinetic experiments revealed that the mechanism involved a "radical non-rebound" mechanism, where the initially formed Ru^{III}–OH species dissociates from the carbon radical. The carbon radical is then further oxidized to the alcohol by a second Ru^{IV}=O molecule (Scheme 3). This mechanism is chemically distinct from the rebound mechanism yet may be indistinguishable from a slow rebound under catalytic conditions, demonstrating the value of stoichiometric kinetics studies.

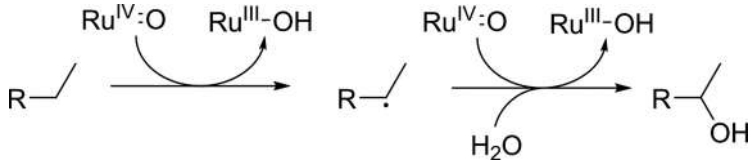

Scheme 3. General mechanism of radical non-rebound C–H bond hydroxylation.

More recently, Du Bois and Sigman et al. have demonstrated selective C–H bond oxidation using periodic acid and Ru complexes of bpy, **15**, and 4,4′-di-*tert*-butyl-2,2′-bipyridine (dtbpy), **16** (Figure 8) (*50*). This complex was found to selectively hydroxylate only the most electron rich sites in a variety of substrates, i.e. the catalysts show a strong preference for benzylic and tertiary

aliphatic sites. Of particular note is the tolerance of **16** for nitrogen-containing functional groups (Table 3), which may be oxidized to N-oxides or coordinate to the metal center of the catalyst, inhibiting the reaction. Key to this tolerance is the addition of an acid cocatalyst. It is hypothesized that this acid additive inhibits binding of and oxidation at N-sites by protonating them, although further investigation into this mechanism is ongoing. Oxidation of chiral substrates by **16** shows nearly complete retention of stereochemistry, suggesting an oxene insertion mechanism (Scheme 1); however, a radical mechanism with rapid rebound cannot be precluded on this basis alone.

Table 3. Relative TOF and TON for C–H Bond Hydroxylation Catalysts

Complex	*Substrate*	*Oxidant*	*TOF (h^{-1})*	*TON*[a]	*Reference*
15[b]	2-isohexylpyridine	H_5IO_6	3.5	14	(*50*)
16[b]	2-isohexylpyridine	H_5IO_6	4.1	16.2	(*50*)
16[c]	2-isohexylpyridine	H_5IO_6	4.5	17.8	(*50*)
16[c]	4′-isopropylacetophenone	H_5IO_6	4.6	18.4	(*50*)
17[d]	ethylbenzene	$NaIO_4$	4.2	25	(*51*)
18[e]	ethylbenzene	electrode	133	1600	(*52*)
21[f]	4-ethylbenzenesulfonate	CAN[g]	38	38	(*54*)
22[f]	4-ethylbenzenesulfonate	CAN[g]	35	35	(*54*)
23[f]	4-ethylbenzenesulfonate	CAN[g]	33	33	(*54*)

[a] Mols alcohol (ketone/aldehyde)/mol catalyst. [b] Reaction conditions: 60 mM substrate, 3.0 mM catalyst, 180 mM oxidant, 360 mM triflic acid, 4 h at RT in 1.67 mL 1:1 acetic acid:water solvent. [c] Reaction conditions: 60 mM substrate, 3.0 mM catalyst, 120 mM oxidant, 360 mM triflic acid, 4 h at RT in 1.67 mL 1:1 acetic acid:water solvent. [d] Reaction conditions: 55.6 mM substrate, 560 mM oxidant, 1.7 mM catalyst, in 4.5 mL 2:1 acetonitrile:water solvent for 6 h at 70 °C. [e] Reaction conditions: 10 nmol catalyst on a 1 cm^2 nano-ITO electrode (ITO = Indium-doped Tin Oxide), 20.0 mM substrate, 100.0 mM $LiClO_4$ electrolyte, 1.0% water in propylene carbonate solvent, 1.74 V constant potential for 12 h at 23 °C. [f] Reaction conditions: 100 mM substrate, 200 mM oxidant, 1 μM catalyst in D_2O for 1 h at 23 °C. [g] CAN = cerium(IV) ammonium nitrate.

In 2017, Gupta and Choudhury reported an NHC-based Ru catalyst, **17**, for oxidation at benzylic C–H bonds (Figure 9) (*51*). On the basis of electrospray ionization mass spectrometry (ESI-MS) and ultraviolet-visible spectroscopy is time-course studies, **17** was found to form a *cis*-dioxo Ru^{VI} species when oxidized with $NaIO_4$, which then proceeds to abstract a benzylic H-atom in the RDS. This RDS was further supported by an observed hydrogen/deuterium (H/D) KIE of 3.4, indicating involvement of the substrate H-atom in the RDS. Addition of a radical trap to the reaction mixture resulted in a significant reduction in TOF and TON, strongly suggesting a radical rebound mechanism for this catalyst (Scheme 1). As is common in C–H bond oxidation, hydroxylation at secondary sites was not observed as any product alcohols were likely rapidly oxidized to the corresponding ketones.

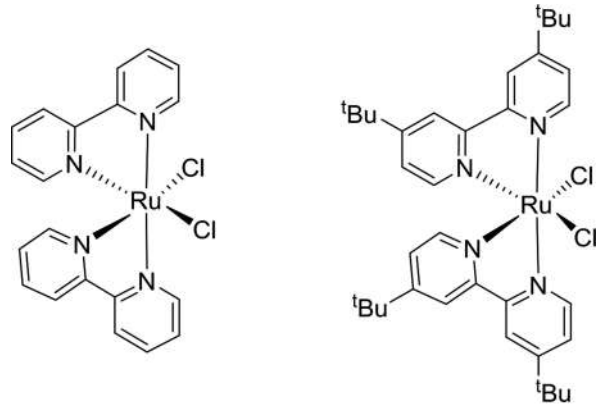

15 **16**

Figure 8. Structure diagram of [Ru(bpy)$_2$Cl$_2$] ***15*** *and [Ru(dtbpy)$_2$Cl$_2$]* ***16*** *(50).*

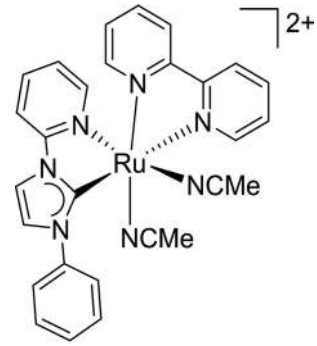

17

Figure 9. Structure diagram of [Ru(NHC)(bpy)(MeCN)$_2$](OTf)(PF$_6$) ***17*** *(51).*

A rare example of electrochemical C–H bond oxidation by a well-defined Ru catalyst was reported in 2012 by Meyer et al. (52). In this report, the bpy ligand of a known C–H bond oxidation catalyst, [Ru(Mebimpy)(bpy)(OH$_2$)](PF$_6$)$_2$ (Mebimpy = 2,6-bis(1-methylbenzimidazol-2-yl)pyridine), was modified with phosphonate groups to generate **18** (Figure 10). When attached to a nano-ITO electrode, **18** was found to exhibit significant catalytic activity for the conversion of ethylbenzene to acetophenone (Table 3). Remarkably, the catalyst remains stable for hours on the electrode surface, leading to turnover numbers significantly greater than typically seen for homogeneous catalysts and demonstrating the advantages of heterogenizing known catalysts. KIE studies showed only a minor H/D KIE of 1.2. In conjunction with a lack of inhibition of the reaction in the presence of O$_2$, this result suggests **18** operates via the oxene insertion mechanism (Scheme 1). Unfortunately, no alcohol products are observed to form during C–H bond oxidation by **18**. This is attributed to rapid oxidation of the alcohol intermediate by **18** at the electrode surface before diffusion can occur.

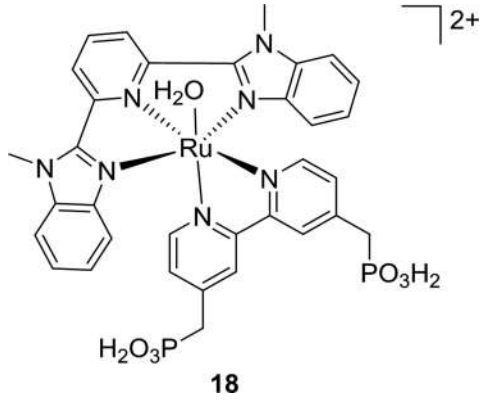

18

Figure 10. Structure diagram of the phosphonate functionalized [Ru(Mebimpy)(bpy)(OH$_2$)]$^{2+}$ derivative, ***18*** *(52).*

In 2011, Kojima and Fukuzumi reported a particularly well characterized C–H bond hydroxylation catalyst based on tpa, [Ru(tpaH)(bpy)(O)](PF$_6$)$_3$ **19** (Figure 11) (53). Kinetic analysis of C–H bond oxidation of cumene by **19** revealed two distinct steps: the observed rate constant for the first of which exhibited linear dependence on the concentration of cumene and an H/D KIE of 12, and an observed rate constant for the second of which was independent of cumene concentration and an H/D KIE of 1. Varying the substrate further revealed that the observed rate constant for the first step decreased linearly with the substrates' C–H BDE. Based on these kinetic experiments, **19** was found to follow the radical rebound mechanism (Scheme 1) with H-atom abstraction serving as the RDS in the catalytic cycle. Additionally, the inclusion of radical traps in the catalytic mixture had no effect on the rate or product distribution of **19**, further supporting the rebound over the non-rebound mechanisms. Remarkably, using ESI-MS the authors were able to identify the initial product of the rebound reaction with cumene, i.e. the bound cumyl alcohol species **20** (Figure 11). Further investigation of the products via ESI-MS determined that the second observable step in the C–H bond hydroxylation by **19** is irreversible ligand exchange between the bound, oxidized substrate, and the acetonitrile used as solvent.

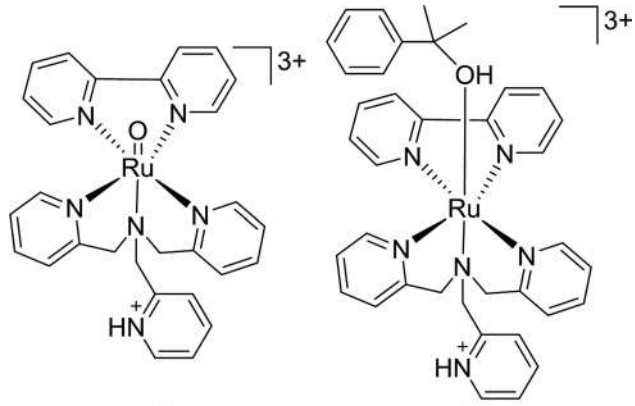

19 **20**

Figure 11. Structure diagrams of [Ru(tpaH)(bpy)(O)](PF$_6$)$_3$, ***19****, and its rebound product with cumene,* ***20*** *(53).*

Based on this work, in 2012 Fukuzumi and Kojima reported on the C–H bond oxidation activity of several Ru(tpa)-based complexes (Figure 12) (*54*). These complexes were found to serve as very active catalysts for the oxidation of alcohol to aldehydes and ketones and were also capable of oxidizing benzylic C–H bonds to the corresponding ketones (Table 3). H/D isotope studies on the oxidation of methanol by the corresponding Ru^{IV}–oxo species showed KIEs of 1.7–2.5, depending on the catalyst. These values indicate that the RDS in C–H bond oxidation by these complexes is H-atom abstraction which is followed by radical rebound (Scheme 1).

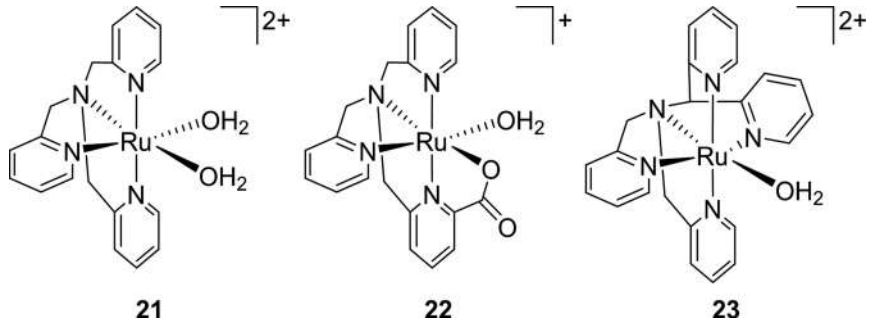

21 **22** **23**

*Figure 12. Structure diagrams of Ru(tpa)-based C–H bond oxidation catalysts **21**–**23** (54).*

Summary

C–H bond hydroxylation and alkene epoxidation are two of the most active areas in catalysis today. These reactions share high-valent oxo species in their mechanism, and thus mechanistic insights into one of these reactions can lead to insights in the other. In the past decade, a number of new strategies using Ru catalysts have been employed to understand the mechanism of these reactions. These strategies, including the use of NHC ligands and heterogenizing known homogeneous catalysts, have led to remarkable improvements in catalytic activity.

While much of the current effort is focused on first-row transition metals, considerable work remains to improve our understanding of the mechanism C–H bond oxidation and alkene epoxidation by Ru. As our understanding improves, new opportunities to improve the sustainability of these reactions will become possible through use of greener reaction conditions. This selection of catalytic developments demonstrates the significant progress made toward this goal in the last ten years. It is the authors' hope that this article assists a new generation of researchers to employ Ru catalysts toward improving our understanding of this vital reaction.

References

1. Topczewski, J. J.; Sanford, M. S. Carbon–Hydrogen (C–H) Bond Activation at PdIV: A Frontier in C–H Functionalization Catalysis. *Chem. Sci.* **2014**, *6*, 70–76.
2. Song, G.; Wang, F.; Li, X. C–C, C–O and C–N Bond Formation via Rhodium(III)-Catalyzed Oxidative C–H Activation. *Chem. Soc. Rev.* **2012**, *41*, 3651–3678.
3. Davies, H. M. L.; Beckwith, R. E. J. Catalytic Enantioselective C−H Activation by Means of Metal−Carbenoid-Induced C−H Insertion. *Chem. Rev.* **2003**, *103*, 2861–2904.
4. Neufeldt, S. R.; Sanford, M. S. Controlling Site Selectivity in Palladium-Catalyzed C–H Bond Functionalization. *Acc. Chem. Res.* **2012**, *45*, 936–946.

5. Shaik, S.; Hirao, H.; Kumar, D. Reactivity of High-Valent Iron–Oxo Species in Enzymes and Synthetic Reagents: A Tale of Many States. *Acc. Chem. Res.* **2007**, *40*, 532–542.
6. Krebs, C.; Galonić Fujimori, D.; Walsh, C. T.; Bollinger, J. M. Non-Heme Fe(IV)–Oxo Intermediates. *Acc. Chem. Res.* **2007**, *40*, 484–492.
7. Nam, W.; Lee, Y.-M.; Fukuzumi, S. Tuning Reactivity and Mechanism in Oxidation Reactions by Mononuclear Nonheme Iron(IV)-Oxo Complexes. *Acc. Chem. Res.* **2014**, *47*, 1146–1154.
8. McCann, S. D.; Stahl, S. S. Copper-Catalyzed Aerobic Oxidations of Organic Molecules: Pathways for Two-Electron Oxidation with a Four-Electron Oxidant and a One-Electron Redox-Active Catalyst. *Acc. Chem. Res.* **2015**, *48*, 1756–1766.
9. Gagnon, N.; Tolman, W. B. [CuO]+ and [CuOH]2+ Complexes: Intermediates in Oxidation Catalysis? *Acc. Chem. Res.* **2015**, *48*, 2126–2131.
10. Oloo, W. N.; Que, L. Bioinspired Nonheme Iron Catalysts for C–H and C-C Bond Oxidation: Insights into the Nature of the Metal-Based Oxidants. *Acc. Chem. Res.* **2015**, *48*, 2612–2621.
11. Milan, M.; Salamone, M.; Costas, M.; Bietti, M. The Quest for Selectivity in Hydrogen Atom Transfer Based Aliphatic C–H Bond Oxygenation. *Acc. Chem. Res.* **2018**, *51*, 1984–1995.
12. Crabtree, R. H. Alkane C–H Activation and Functionalization with Homogeneous Transition Metal Catalysts: A Century of Progress—a New Millennium in Prospect. *J. Chem. Soc., Dalton Trans.* **2001** (17), 2437–2450.
13. Hartwig, J. F.; Larsen, M. A. Undirected, Homogeneous C–H Bond Functionalization: Challenges and Opportunities. *ACS Cent. Sci.* **2016**, *2*, 281–292.
14. Concepcion, J. J.; Jurss, J. W.; Brennaman, M. K.; Hoertz, P. G.; Patrocinio, A. O. T.; Murakami Iha, N. Y.; Templeton, J. L.; Meyer, T. J. Making Oxygen with Ruthenium Complexes. *Acc. Chem. Res.* **2009**, *42*, 1954–1965.
15. Nilles, C. K.; Herath, H. N. K.; Fanous, H.; Ugrinov, A.; Parent, A. R. Electrochemical Properties and C-H Bond Oxidation Activity of [Ru(Tpy)(Pyalk)Cl]+ and [Ru(Tpy)(Pyalk)(OH)]+. *Dalton Trans.* **2018**, *47*, 9701–9708.
16. Groves, J. T.; Van der Puy, M. Stereospecific Aliphatic Hydroxylation by an Iron-Based Oxidant. *J. Am. Chem. Soc.* **1974**, *96*, 5274–5275.
17. Groves, J. T.; McClusky, G. A. Aliphatic Hydroxylation via Oxygen Rebound. Oxygen Transfer Catalyzed by Iron. *J. Am. Chem. Soc.* **1976**, *98*, 859–861.
18. Mayer, J. M. Hydrogen Atom Abstraction by Metal−Oxo Complexes: Understanding the Analogy with Organic Radical Reactions. *Acc. Chem. Res.* **1998**, *31*, 441–450.
19. Mayer, J. M. Understanding Hydrogen Atom Transfer: From Bond Strengths to Marcus Theory. *Acc. Chem. Res.* **2011**, *44*, 36–46.
20. Evans, M. G.; Polanyi, M. Inertia and Driving Force of Chemical Reactions. *Trans. Faraday Soc.* **1938**, *34*, 11–24.
21. Ping, L.; Chung, D. S.; Bouffard, J.; Lee, S. Transition Metal-Catalyzed Site- and Regio-Divergent C–H Bond Functionalization. *Chem. Soc. Rev.* **2017**, *46*, 4299–4328.
22. Filatov, M.; Shaik, S. Theoretical Investigation of Two-State-Reactivity Pathways of H−H Activation by FeO+: Addition−Elimination, "Rebound", and Oxene-Insertion Mechanisms. *J. Phys. Chem. A* **1998**, *102*, 3835–3846.

23. Faveri, G. D.; Ilyashenko, G.; Watkinson, M. Recent Advances in Catalytic Asymmetric Epoxidation Using the Environmentally Benign Oxidant Hydrogen Peroxide and Its Derivatives. *Chem. Soc. Rev.* **2011**, *40*, 1722–1760.
24. Cussó, O.; Ribas, X.; Costas, M. Biologically Inspired Non-Heme Iron-Catalysts for Asymmetric Epoxidation; Design Principles and Perspectives. *Chem. Commun.* **2015**, *51*, 14285–14298.
25. Benet-Buchholz, J.; Comba, P.; Llobet, A.; Roeser, S.; Vadivelu, P.; Wadepohl, H.; Wiesner, S. Iron vs. Ruthenium—a Comparison of the Stereoselectivity in Catalytic Olefin Epoxidation. *Dalton Trans.* **2009**, 5910–5923.
26. Chatterjee, D. Asymmetric Epoxidation of Unsaturated Hydrocarbons Catalyzed by Ruthenium Complexes. *Coord. Chem. Rev.* **2008**, *252*, 176–198.
27. Lane, B. S.; Burgess, K. Metal-Catalyzed Epoxidations of Alkenes with Hydrogen Peroxide. *Chem. Rev.* **2003**, *103*, 2457–2474.
28. Rose, E.; Andrioletti, B.; Zrig, S.; Quelquejeu-Ethève, M. Enantioselective Epoxidation of Olefins with Chiral Metalloporphyrin Catalysts. *Chem. Soc. Rev.* **2005**, *34*, 573–583.
29. Tse, M. K.; Klawonn, M.; Bhor, S.; Döbler, C.; Anilkumar, G.; Hugl, H.; Mägerlein, W.; Beller, M. Convenient Method for Epoxidation of Alkenes Using Aqueous Hydrogen Peroxide. *Org. Lett.* **2005**, *7*, 987–990.
30. Dakkach, M.; López, M. I.; Romero, I.; Rodríguez, M.; Atlamsani, A.; Parella, T.; Fontrodona, X.; Llobet, A. New Ru(II) Complexes with Anionic and Neutral N-Donor Ligands as Epoxidation Catalysts: An Evaluation of Geometrical and Electronic Effects. *Inorg. Chem.* **2010**, *49*, 7072–7079.
31. Chowdhury, A. D.; Das, A.; K, I.; Mobin, S. M.; Lahiri, G. K. Isomeric Complexes of [RuII(Trpy)(L)Cl] (Trpy = 2,2′:6′,2″-Terpyridine and HL = Quinaldic Acid): Preference of Isomeric Structural Form in Catalytic Chemoselective Epoxidation Process. *Inorg. Chem.* **2011**, *50*, 1775–1785.
32. Serrano, I.; López, M. I.; Ferrer, Í.; Poater, A.; Parella, T.; Fontrodona, X.; Solà, M.; Llobet, A.; Rodríguez, M.; Romero, I. New Ru(II) Complexes Containing Oxazoline Ligands As Epoxidation Catalysts. Influence of the Substituents on the Catalytic Performance. *Inorg. Chem.* **2011**, *50*, 6044–6054.
33. Di Giovanni, C.; Vaquer, L.; Sala, X.; Benet-Buchholz, J.; Llobet, A. New Dinuclear Ruthenium Complexes: Structure and Oxidative Catalysis. *Inorg. Chem.* **2013**, *52*, 4335–4345.
34. Planas, N.; Christian, G.; Roeser, S.; Mas-Marzá, E.; Kollipara, M.-R.; Benet-Buchholz, J.; Maseras, F.; Llobet, A. Substitution Reactions in Dinuclear Ru-Hbpp Complexes: An Evaluation of Through-Space Interactions. *Inorg. Chem.* **2012**, *51*, 1889–1901.
35. Roeser, S.; Ertem, M. Z.; Cady, C.; Lomoth, R.; Benet-Buchholz, J.; Hammarström, L.; Sarkar, B.; Kaim, W.; Cramer, C. J.; Llobet, A. Synthesis, Structure, and Electronic Properties of RuN6 Dinuclear Ru-Hbpp Complexes. *Inorg. Chem.* **2012**, *51*, 320–327.
36. Bernet, L.; Lalrempuia, R.; Ghattas, W.; Mueller-Bunz, H.; Vigara, L.; Llobet, A.; Albrecht, M. Tunable Single-Site Ruthenium Catalysts for Efficient Water Oxidation. *Chem. Commun.* **2011**, *47* (28), 8058–8060.

37. Crabtree, R. H. Abnormal, Mesoionic and Remote N-Heterocyclic Carbene Complexes. *Coord. Chem. Rev.* **2013**, *257*, 755–766.
38. Dakkach, M.; Fontrodona, X.; Parella, T.; Atlamsani, A.; Romero, I.; Rodríguez, M. A Novel Carbene Ruthenium Complex as Reusable and Selective Two-Electron Catalyst for Alkene Epoxidation. *Adv. Synth. Catal.* **2011**, *353*, 231–238.
39. Dakkach, M.; Atlamsani, A.; Parella, T.; Fontrodona, X.; Romero, I.; Rodríguez, M. New Aqua N-Heterocyclic Carbene Ru(II) Complexes with Two-Electron Process as Selective Epoxidation Catalysts: An Evaluation of Geometrical and Electronic Effects. *Inorg. Chem.* **2013**, *52*, 5077–5087.
40. Liu, H.-J.; Gil-Sepulcre, M.; Francàs, L.; Nolis, P.; Parella, T.; Benet-Buchholz, J.; Fontrodona, X.; García-Antón, J.; Romero, N.; Llobet, A.; Escriche, L.; Bofill, R.; Sala, X. Mononuclear Ruthenium Compounds Bearing N-Donor and N-Heterocyclic Carbene Ligands: Structure and Oxidative Catalysis. *Dalton Trans.* **2017**, *46*, 2829–2843.
41. Dhuri, S. N.; Cho, K.-B.; Lee, Y.-M.; Shin, S. Y.; Kim, J. H.; Mandal, D.; Shaik, S.; Nam, W. Interplay of Experiment and Theory in Elucidating Mechanisms of Oxidation Reactions by a Nonheme RuIVO Complex. *J. Am. Chem. Soc.* **2015**, *137*, 8623–8632.
42. White, M. C. Adding Aliphatic C–H Bond Oxidations to Synthesis. *Science* **2012**, *335*, 807–809.
43. Newhouse, T.; Baran, P. S. If C-H Bonds Could Talk: Selective C-H Bond Oxidation. *Angew. Chem., Int. Ed.* **2011**, *50*, 3362–3374.
44. Hashiguchi, B. G.; Bischof, S. M.; Konnick, M. M.; Periana, R. A. Designing Catalysts for Functionalization of Unactivated C–H Bonds Based on the CH Activation Reaction. *Acc. Chem. Res.* **2012**, *45*, 885–898.
45. Ito, R.; Umezawa, N.; Higuchi, T. Unique Oxidation Reaction of Amides with Pyridine-N-Oxide Catalyzed by Ruthenium Porphyrin: Direct Oxidative Conversion of N-Acyl-l-Proline to N-Acyl-l-Glutamate. *J. Am. Chem. Soc.* **2005**, *127*, 834–835.
46. Yip, W.-P.; Yu, W.-Y.; Zhu, N.; Che, C.-M. Alkene Cis-Dihydroxylation by [(Me3tacn)(CF3CO2)RuVIO2]ClO4 (Me3tacn = 1,4,7-Trimethyl-1,4,7-Triazacyclononane): Structural Characterization of [3 + 2] Cycloadducts and Kinetic Studies. *J. Am. Chem. Soc.* **2005**, *127*, 14239–14249.
47. Marmion, M. E.; Takeuchi, K. J. Preparation and Characterization of Stable Ruthenium(IV)-Oxo Complexes That Contain Tertiary Phosphine Ligands. *J. Am. Chem. Soc.* **1986**, *108*, 510–511.
48. Neumann, R.; Dahan, M. Molecular Oxygen Activation by a Ruthenium-Substituted "Sandwich" Type Polyoxometalate. *J. Am. Chem. Soc.* **1998**, *120*, 11969–11976.
49. Kojima, T.; Hayashi, K.; Iizuka, S.; Tani, F.; Naruta, Y.; Kawano, M.; Ohashi, Y.; Hirai, Y.; Ohkubo, K.; Matsuda, Y.; Fukuzumi, S. Synthesis and Characterization of Mononuclear Ruthenium(III) Pyridylamine Complexes and Mechanistic Insights into Their Catalytic Alkane Functionalization with m-Chloroperbenzoic Acid. *Chem.—Eur. J.* **2007**, *13*, 8212–8222.
50. Mack, J. B. C.; Gipson, J. D.; Du Bois, J.; Sigman, M. S. Ruthenium-Catalyzed C–H Hydroxylation in Aqueous Acid Enables Selective Functionalization of Amine Derivatives. *J. Am. Chem. Soc.* **2017**, *139*, 9503–9506.

51. Gupta, S. K.; Choudhury, J. A Mixed N-Heterocyclic Carbene/2,2′-Bipyridine-Supported Robust Ruthenium(II) Oxidation Precatalyst for Benzylic C–H Oxidation. *ChemCatChem* **2017**, *9*, 1979–1984.
52. Vannucci, A. K.; Chen, Z.; Concepcion, J. J.; Meyer, T. J. Nonaqueous Electrocatalytic Oxidation of the Alkylaromatic Ethylbenzene by a Surface Bound RuV(O) Catalyst. *ACS Catal.* **2012**, *2*, 716–719.
53. Kojima, T.; Nakayama, K.; Ikemura, K.; Ogura, T.; Fukuzumi, S. Formation of a Ruthenium(IV)-Oxo Complex by Electron-Transfer Oxidation of a Coordinatively Saturated Ruthenium(II) Complex and Detection of Oxygen-Rebound Intermediates in C–H Bond Oxygenation. *J. Am. Chem. Soc.* **2011**, *133*, 11692–11700.
54. Ohzu, S.; Ishizuka, T.; Hirai, Y.; Jiang, H.; Sakaguchi, M.; Ogura, T.; Fukuzumi, S.; Kojima, T. Mechanistic Insight into Catalytic Oxidations of Organic Compounds by Ruthenium(IV)-Oxo Complexes with Pyridylamine Ligands. *Chem. Sci.* **2012**, *3*, 3421–3431.

Chapter 6

Characterizations of Surface Ligands and Stabilizers on Metallic Nanoparticles

Meng Zhou*

Department of Natural Sciences, Lawrence Technological University, 21000 West Ten Mile Road, Southfield, Michigan 48075, United States

***E-mail: mzhou@ltu.edu**

Despite the well-established techniques to characterize the core structure and composition of metallic nanoparticles (NPs), the characterizations of surface stabilizers on metallic NPs remain very challenging. Such NPs are active catalysts for the hydrogenation of alkene, alkyne, aromatic, nitro, ketone, and aldehyde groups. The stabilizers affect the size, solubility, stability, and catalytic activity of NPs. A variety of stabilizers have been characterized using infrared spectroscopy (IR), NMR, elemental analysis, X-ray photoelectron microscopy, energy-dispersive X-ray spectroscopy, thermogravimetric analysis, and mass spectrometry. These stabilizers include carbonyl, phosphine, *N*-heterocyclic carbene, amine, aniline, thiolate, citrate, and phosphine oxide. This chapter focuses on developments for the qualitative and quantitative analyses of NP stabilizers, which are discrete molecules or ions.

Introduction

This chapter illustrates many spectroscopic and titration methods to characterize and quantify surface ligands and stabilizers on metallic nanoparticles (NPs). Although the characterizations of the core structure and composition of zerovalent, metallic NPs are well established, the characterizations of the surface ligands or stabilizers on NPs remain a great challenge (*1*, *2*). These zerovalent, metallic NPs represent the most active NP catalysts for the hydrogenation of alkene (*3*), aromatic (*4*), nitro (*5*), alkyne (*6*), ketone (*7*), and aldehyde (*7*) groups. The surface ligands or stabilizers can determine or influence the stability and activity of NP catalysts. They prevent NPs from aggregating and forming bulk material (*1*, *2*), which leads to the loss of surface area and catalytic activity. Meanwhile, the surface ligands or stabilizers can block the surface binding sites and poison the catalyst.

For the sake of brevity, surface ligands or stabilizers will simply be referred to as stabilizers in this chapter. The term ligand implies the presence of a surface metal–ligand coordinate covalent bond. These ligands can be small organic molecules such as amine (*8*–*10*), carboxylate (*11*–*18*), and thiolate (*6*, *11*, *15*, *19*–*27*). The more general term stabilizer has no such implication, and

it includes ionic or Derjaguin–Landau–Verwey–Overbeek (DLVO) stabilizers, such as chloride, acetate, ammonium, sodium, and hydroxide, which may or may not be involved in a coordinate covalent bond (*1*, *2*, *18*, *28*–*30*). The distinction between a ligand and an uncoordinated stabilizer can only be determined by experiment. In this chapter, the term ligand is used only when the presence of a surface metal–ligand coordinate covalent bond is supported by direct spectroscopic evidence.

The characterizations of stabilizers are discussed in this chapter using examples. The sections are organized by the atomic number of elements, from ruthenium to gold. The sections are further organized by the stabilizers, with the established stabilizers discussed first, followed by the novel ones. In each case, brief background information is provided regarding the synthesis, purification, characterizations on the NP core, catalytic activity, and theory of NPs. The detailed characterizations of stabilizers follow, and specific characterizations data is included for reference and comparison. The NPs are labeled using the metal element followed by the stabilizers in parentheses. Unless otherwise specified, the NP size refers to the average diameter rather than the radius.

Except for a few highly cited works from the 1990s, the scope of this chapter is limited to studies published since the year 2000 (*27*, *31*, *32*). For earlier studies, readers are referred to the 1985 *ACS Symposium Series Volume 288, Catalyst Characterization Science: Surface and Solid State Chemistry* by Marvin L. Deviney and John L. Gland and a 2007 review by Ott and Finke (*2*, *33*). Techniques that require highly specialized equipment are avoided; interested readers are referred to reviews on NP characterizations using a custom-built mass spectrometer (*34*) or a synchrotron radiation facility for X-ray absorption spectroscopy (*2*). Instead, this work is dedicated to the most general techniques accessible to chemists, only highlighting a selected group of studies focused on the characterizations of stabilizers. The characterizations of atomically precise, subnanometer molecular gold clusters are beyond the scope of this chapter. Such a cluster is best described as a multinuclear metal complex rather than NPs.

The well-established methods to characterize the structure of the NP core include high-resolution transmission electron microscopy (HRTEM), selected area electron diffraction (SAED), and powder X-ray diffraction (PXRD). The compositional analysis is performed using elemental analysis (EA), X-ray photoelectron microscopy (XPS), energy-dispersive X-ray spectroscopy (EDX), and atomic absorption spectroscopy. The general techniques to characterize the stabilizers include (listed in descending order according to accessibility): IR spectroscopy, EA, mass spectrometry (MS), solution-phase proton NMR spectroscopy, diffusion-ordered NMR spectroscopy (DOSY), two-dimensional (2D) NMR, multinuclear NMR spectroscopy, thermogravimetric analysis (TGA), XPS, EDX, and solid-state magic-angle-spinning NMR (MAS NMR) spectroscopy.

The abbreviations, rather than full names, will be used to describe these common spectroscopic techniques. Additional abbreviations, listed in alphabetical order, include: attenuated total reflectance (ATR), carbonyl ligand (CO), 1,5-cyclooctadiene (cod), 1,3,5,7-cyclooctatetraene (cot), and an organic alkyl or aryl group (R).

Case Studies

Ru (Phosphine)

Chaudret, Philippot, Salmeron, and co-workers have carried out extensive studies on the characterizations of surface organic ligands on the Ru NP catalysts (*10*, *35*–*39*). The authors have streamlined the surface ligand characterizations on Ru NPs, using solution-phase proton NMR, ^{1}H–^{13}C heteronuclear single quantum coherence 2D NMR spectroscopy, solid-state ^{13}C and ^{31}P

MAS NMR spectroscopy with or without cross-polarization, XPS analysis of binding energies, EA, FT-IR, and titration of surface hydrides using an olefin.

Typically, the Ru NPs are made by the decomposition of an Ru complex, Ru(cod)(cot), under H_2 (*38*). A small organic ligand is present in the reaction mixture and stabilizes the NPs. The reaction is carried out using air-free techniques by degassing the solvent using freeze-pump-thaw cycles and an argon protective atmosphere. A variety of Ru NPs are made by varying the ligand (e.g., phosphine and *N*-heterocyclic carbene) and reaction conditions, and the surface structure is thoroughly characterized.

In 2014, Martínez-Prieto et al. reported (*37*) the synthesis of Ru NPs stabilized by bis(diphenylphosphino)butane (dppb), as shown in Figure 1. The synthesis was carried out using a one-pot, two-step protocol starting from the Ru(cod)(cot) precursor. The reaction conditions included using degassed heptanol as the solvent at room temperature in a Fisher–Porter reactor under 3 bar H_2. The reaction mixture quickly turned from yellow to dark, indicating the formation of NPs. The heptanol-stabilized Ru NPs formed initially, and, 1 h later, a solution of dppb in tetrahydrofuran (THF) was added to replace heptanol with dppb. The reaction continued for 14 h at room temperature to form Ru NPs stabilized by dppb.

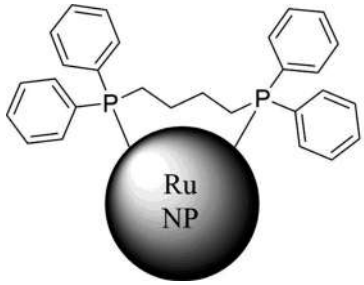

Characterizations of the stabilizer:
solid-state ^{31}P and ^{13}C NMR, EA, and XPS

Figure 1. Ru NPs stabilized by dppb ligands.

The solution was concentrated by evaporation at 70 °C to purify the NPs. The dppb-stabilized NPs were precipitated using pentane. A second pentane wash was performed to remove any free organic molecules such as heptanol and phosphine that were not adsorbed to NPs. Finally, after solvent removal under vacuum, the NPs were isolated in a dry powder form.

The Ru–Pt NPs catalyzed styrene hydrogenation in a degassed THF solution at 25 °C and under 3 bar H_2. Complete styrene hydrogenation to ethylcyclohexane was achieved with a turnover frequency (TOF) of 2.1 h^{-1}. By monitoring the product formation, the authors found that styrene hydrogenation to ethylbenzene occurred first, followed by arene hydrogenation to ethylcyclohexane as the final product.

The 3.1 $\pm$ 0.4 nm NPs formed and have a crystalline hexagonal close-packed (hcp) structure, similar to Ru bulk metal, with a roughly spherical shape under HRTEM. The XPS binding energy (280.5 eV for the $3d_{5/2}$ peak) of the Ru NPs was higher than metallic Ru (280.0 eV for the $3d_{5/2}$ peak). The π-acceptor ligand dppb coordinated to Ru could increase its binding energy by lowering the energy of d orbitals. The binding energy calibration is conducted using the Au $4f_{7/2}$ peak at 84.0 eV and the Fermi level edge at 0 eV.

The dppb surface ligand was characterized by solid-state MAS NMR. In the proton-decoupled ^{31}P MAS NMR spectrum of the Ru NPs, the peak at 34.5 ppm was assigned to the phosphorous atom. In the proton-decoupled ^{13}C MAS NMR of the Ru NPs, shown in the bottom spectrum of Figure 2, peaks near 25 ppm were assigned to the alkyl groups of dppb and possibly the alkyl groups

of residual heptanol ligands. The synthesis of Ru(dppb) was achieved by the ligand replacement of Ru(heptanol) with dppb; however, the exchange may not be complete. Peaks near 130 ppm were assigned to the aryl groups. ^{13}C-labeled CO was added and adsorbed onto the Ru NPs to study their surface structure by ^{13}C MAS NMR, shown in the top spectrum of Figure 2. The peak at 195.7 ppm was assigned to the terminal carbonyl group, and the peak at 229.9 ppm was assigned to the bridging carbonyl group. The ^{13}C-labeled CO adsorption experiment suggests the availability of two distinct binding sites on the surface of Ru NPs.

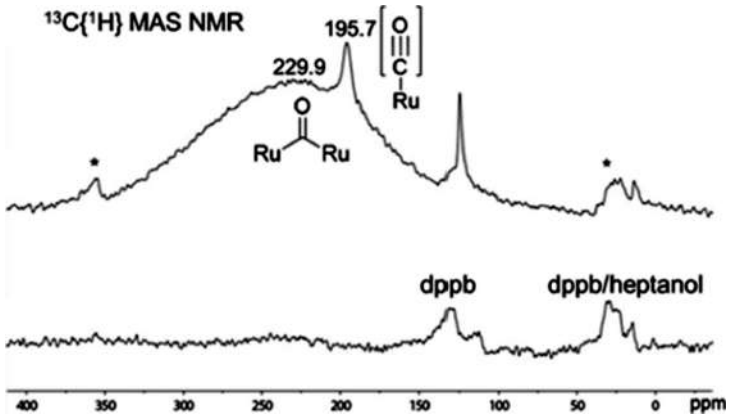

Figure 2. The proton-decoupled ^{13}C solid-state MAS NMR spectrum of the Ru(dppb) NPs before adding ^{13}CO (bottom) and after adsorption of CO (top). Spinning side bands of the 195.7 ppm peak are marked with asterisks. Reaction conditions for ^{13}CO adsorption: 25 °C, 3 bar H_2, and 20 h. Reproduced with permission from ref (36). Copyright 2014 American Chemical Society.

Elemental and inductively coupled plasma–atomic emission spectroscopy analyses found 10.48% of carbon, 2.48% of phosphorous, and 2.48% of hydrogen attributed to the phosphine ligand. The NPs consisted of 69.99% of ruthenium. XPS binding energies confirmed the presence of carbon and phosphorous elements. The binding energy of phosphorous (134.4 eV) is higher than that of free and uncoordinated dppb ligands (130 eV). The high binding energy suggests that the dppb ligands are directly coordinated to surface Ru atoms and rules out the presence of free dppb ligands.

The Ru(dppb) NPs catalyzed the Fischer–Tropsch synthesis of C1–C4 alkanes from H_2 and CO. Up to 1.3×10^{-5} s^{-1} TOF was detected in the formation of C2–C4 alkanes at a temperature of 150 °C, which is relatively low for the Fischer–Tropsch reaction.

Ru–Pt (Phosphine)

Dppb was also used to stabilize Ru–Pt bimetallic NPs (*40*). Two organometallic complexes in a 1:1 ratio were used in the synthesis of the Ru–Pt NPs. Ru(cod)(cot) served as the source of Ru and [Pt(Me)$_2$(cod)] (Me = methyl) served as the source of Pt. They were mixed in a THF solution in the presence of the dppb ligand (*40*). The reaction was carried out in a Fisher–Porter reactor at room temperature and under 3 bars H_2.

To isolate the NPs in a dry powder form, pentane was added to precipitate the NPs at −30 °C. The NPs were washed twice with pentane under argon, using a cannula, and dried under vacuum.

The Ru–Pt NPs catalyzed styrene hydrogenation in a degassed THF solution at 25 °C and under 3 bar H_2. Complete styrene hydrogenation to ethylcyclohexane was achieved with a TOF of 2.1 h^{-1}. By monitoring the product formation, shown in Figure 3, the authors found that styrene hydrogenation to ethylbenzene occurred first, followed by arene hydrogenation to ethylcyclohexane as the final product.

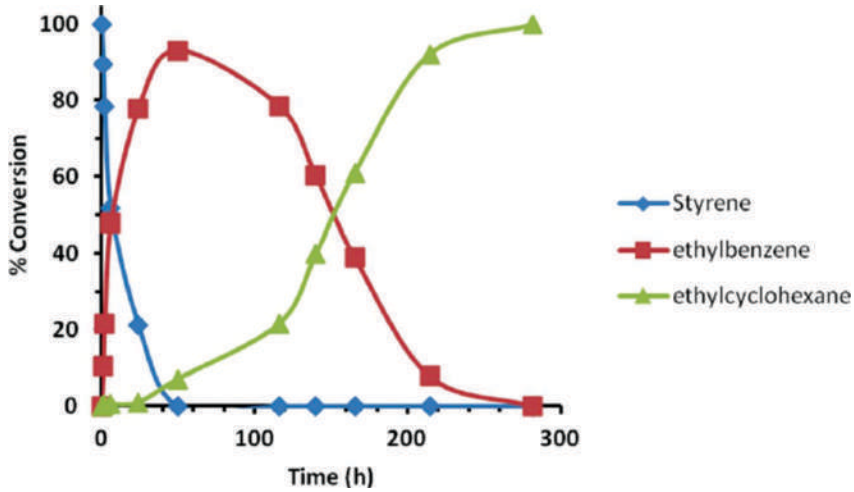

Figure 3. The formation of ethylbenzene, followed by ethylcyclohexane in the styrene hydrogenation catalyzed by Ru–Pt (dppb) NPs. Reaction conditions: 25 °C, 3 bar H_2, and 0.03 mmol total Ru–Pt metal. Reproduced with permission from ref (39). Copyright 2013 Royal Society of Chemistry.

TEM analysis showed that the Ru–Pt NPs have the size of 1.8 ± 0.2 nm. HRTEM revealed both hcp and face-centered cubic (fcc) structure in these NPs. Inductively coupled plasma–atomic emission spectroscopy analysis showed a Ru to Pt ratio of 1.2:1.

The FT-IR and solid-state MAS NMR studies confirmed the presence of dppb ligands on Ru–Pt NPs. The stretches at 1884 cm^{-1} and 3070–2850 cm^{-1} were assigned to the C=C and C–H stretching modes of the dppb ligand. Proton-decoupled ^{31}P MAS NMR showed four peaks at 4.78 ppm, 37.63 ppm, and 25.57 ppm, which were assigned to dppb ligands coordinated to Ru at different Ru sites, as well as the hydrogenated dppb ligand, presumably due to the hydrogenation of the aryl group of dppb. In the proton-decoupled ^{13}C MAS NMR spectrum of the NPs, peaks from 10 to 40 ppm were assigned to the alkyl carbons of the dppb ligand, and peaks at 110 and 135 ppm were assigned to the aryl carbons.

Ru (*N*-Heterocyclic Carbene)

N-Heterocyclic carbene (NHC) ligands are well known for the homogeneous Ru catalyst in olefin metathesis (*41*), and studies have emerged using NHC ligands to stabilize NPs (*42*). Chaudret and co-workers have made seminal contributions to the synthesis and surface ligand characterizations of Ru NPs stabilized by NHC ligands (*36*, *38*, *39*, *43*).

In 2011, Ru NPs (*36*) stabilized by *t*Bu·NHC and IPr·NHC ligands (Figure 4) were synthesized using Ru(cod)(cot) as the precursor organometallic complex. Ru (NHC) NPs were made at room temperature under 3 bar H_2 in pentane solvent and in the presence of *t*Bu·NHC·HCl or IPr·NHC·HCl imidazolium chloride salts, which generated the NHC ligands in situ. The NPs were

purified by removing the pentane solvent under vacuum. The Ru NPs catalyzed the complete hydrogenation of styrene to ethylbenzene at 25 °C and under 3 bar H_2.

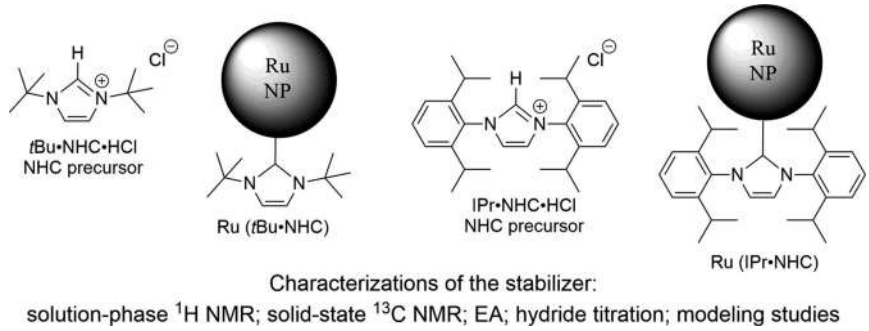

Figure 4. The imidazolium salts, tBu·NHC·HCl (left) and IPr·NHC·HCl (right), and the Ru NPs stabilized by the corresponding NHC ligands.

Under otherwise identical conditions, Ru NPs made from *t*Bu·NHC·HCl and those from IPr·NHC·HCl both have a size of 1.7 ± 0.2 nm, as shown by TEM imaging. HRTEM analyses detected crystalline NPs with hcp structure.

Surface hydride ligands on the NHC-stabilized Ru NPs were detected and quantified using an olefin titration method (*36*). In the absence of H_2, Ru NPs react with 2-norbornene to form 2-norbornane in pentane solvent. Due to the lack of H_2, the authors argue that the only source of hydrogen responsible for norbornene hydrogenation is the surface hydride on Ru NPs. For the 1.7 nm NPs, the ratios of surface hydride to surface Ru atoms are 1.1:1 for NPs made with *t*Bu·NHC·HCl and 1.3:1 for those made with IPr·NHC·HCl. The surface Ru atoms are calculated based on modeling studies (*27*, *44*). Similar modeling studies are discussed in the sections on the Pd (dodecylthiolate), Ir (polyoxoanion), and Au (dodecylthiolate) NPs.

The percentage of surface ligand coverage can be calculated by dividing the number of hydrides by the number of surface Ru atoms. Therefore, high surface ligand coverages of 110% and 130% were determined. Elemental analyses showed the significant presence of carbon and nitrogen, which is expected when NHC ligands are present. The Ru (*t*Bu·NHC) NPs contained 18.7% carbon, 3.3% hydrogen, and 2.0% nitrogen. The Ru (IPr·NHC) NPs contained 37% carbon, 5% hydrogen, and 2.2% nitrogen.

The solution-phase ^{1}H NMR analysis was carried out for a C_6D_6 solution suspension of *t*Bu·NHC-stabilized Ru NPs. A broad signal was detected at 1.4 ppm, assigned to the *t*butyl group. No signals were detected in the 6–7 ppm region. This region would give the aromatic protons on the imidazole ring. The absence of these proton NMR signals was attributed to the immobilized nature of NP surface ligands, as opposed to a free ligand in solution. For the IPr·NHC-stabilized Ru NPs, only the methyl groups can be identified with a very broad signal from 1.0 to 1.8 ppm. A variety of mechanisms, such as slow tumbling rate, surface heterogeneity (a variety of binding sites), Knight shift, paramagnetism, and ferromagnetism, can lead to a broad solution NMR signal (*28*, *36*, *38*, *45*).

Tightly bound surface ligands tend to have broader solution NMR signals than unbound, free ligands (*45*); however, without further solution NMR analysis using DOSY and nuclear Overhauser effect spectroscopy (NOESY) techniques, this evidence alone does not suggest that the ligand is tightly bound (*45*). A lack of broadening also does not necessarily suggest unbound free ligands. An example of surface ligands that give sharp NMR signals is discussed in the section on the Pt (NHC)

NPs. The NHC ligands on Ru were resistant to ligand exchange by thiols and appeared to be tightly bound.

Solid-state ^{13}C MAS NMR spectroscopy enabled much more accurate analysis of the surface ligand than solution-phase proton NMR spectroscopy. ^{1}H–^{13}C cross-polarization was used to enhance the signal-to-noise ratio. The spectrum of *t*Bu·NHC-stabilized NPs showed the vinylic carbons at 120 ppm, the quaternary carbons at 55 ppm, and the methyl carbons at 30 ppm. To identify the C2 carbene carbon (NCN) coordinated to Ru NPs, Ru NPs made from ^{13}C-labeled *t*Bu·NHC (N^{13}CN) ligand were synthesized and analyzed. The carbene carbon appeared at 190 ppm. For the IPr·NHC-stabilized NPs, signals were assigned to alkyl carbons at 25 ppm, aromatic carbons at 135–150 ppm, and carbene carbons at 205 ppm.

Continuing work on Ru (NHC) NPs, Martínez–Prieto et al. reported (*39*) various NHC surface ligands bearing long-chain alkyl groups and cholesterol moieties. Similar methods using ^{13}C MAS NMR and elemental analyses were carried out to characterize the surface ligands. Notably, for the NPs stabilized by cholesterol-derived NHC ligands, the ruthenium content was only 50% by weight, as shown by atomic absorption spectroscopy. These NPs catalyzed the complete hydrogenation of many organic molecules, such as phenol to cyclohexanol and acetophenone to 1-cyclohexylethanol, at room temperature and under 5 bar H_2.

Rh (NHC and Imidazolium Salt)

Martinez-Espinar et al. reported (*4*) the synthesis and surface ligand characterizations of Rh NPs stabilized by IPr·NHC ligands, shown in Figure 5. Rh NPs with a TEM size of 1.68 ± 0.26 nm were made using [Rh(η^3-C_3H_5)$_3$] (with C_3H_5 being the allyl group) as the precursor complex in THF solvent at 35 °C for 16 h under 4 bar H_2 and in the presence of IPr·NHC·HCl imidazolium chloride. Purification was performed by three cycles of washing–precipitation by pentane, followed by solvent removal under vacuum.

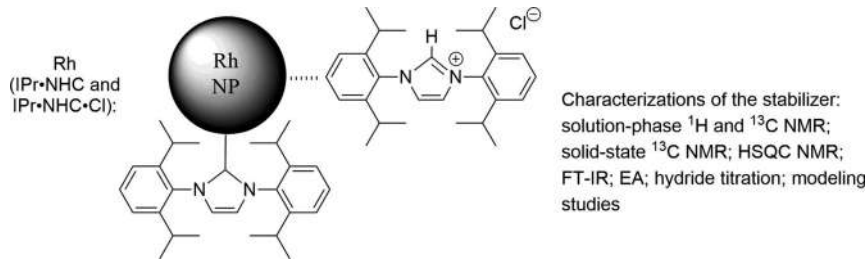

Figure 5. Rh NPs stabilized by the IPr·NHC ligand and the imidazolium salt.; the hashed line indicates physical adsorption of an ionic stabilizer.

HRTEM showed that the NPs were highly crystalline with an fcc structure. PXRD confirmed the size and crystallinity of fcc Rh. XPS analyses of the binding energies of Rh 3d electrons suggested that the surface of the NPs contained 97– 99% of zerovalent Rh atoms, where the $3d_{5/2}$ peak was found at 306.7 eV and the $3d_{3/2}$ peak was found at 311.40 eV. The instrument was calibrated using the $3d_{5/2}$ line of Ag with a full width at half maximum (FWHM) of 0.8 eV.

The IPr·NHC-stabilized Rh NPs catalyzed the hydrogenation of phenol at 30 °C in 3 h. At 1.7 bar H_2, a TOF of 23 h^{-1} was measured (based on the mole number of the product divided by the mole number of surface Rh atoms). The selectivity was 75% with respect to the partial hydrogenation

product (i.e., cyclohexanone) and 25% with respect to the complete hydrogenation product (i.e., cyclohexanol). When the H_2 pressure was raised to 30 bar, TOF rose to 81 h^{-1}, and the selectivity, with respect to cyclohexanol, increased to 68%. The catalyst was also active in the hydrogenation of a variety of benzene and pyridine derivatives.

The olefin titration method, described previously for Ru (NHC) NPs, was again used to quantify the surface hydride ligands. The method reacts Rh NPs directly with 2-norbornene in the absence of H_2. On average, 0.58 surface hydride was detected per surface Rh atom for the 1.68 ± 0.26 nm NPs, giving a surface hydride ligand coverage of 58%, a much lower value than the 110% and 130% values determined for Ru NPs of a similar size (1.7 nm). FT-IR analyses detected alkyl C–H stretches at 2850–2960 cm^{-1} and aromatic C=C stretching and C–H bending modes at 1500–1700 cm^{-1} and 680–860 cm^{-1}, respectively.

The NP surface structure was studied by FT-IR upon adsorption of ^{13}CO ligands. Carbonyl stretches at 2067 and 2026 cm^{-1} were assigned to the germinal CO ligands in an $Rh(CO)_2$ surface moiety. Carbonyl stretches at 1995 and 1845 cm^{-1} were assigned to the terminal and bridging CO ligands, respectively.

Solution-phase proton NMR spectroscopy was performed for the Rh NPs in d8–THF; a broad signal was observed between 6.75 and 7.75 ppm, assigned to the protons on the phenyl ring. A signal at 7.94 ppm was assigned to the vinylic protons on the imidazole ring. The methyl signals on isopropyl groups were found at 0.82 and 1.29 ppm. Upfield chemical shifts at 0.5–2 ppm were assigned to aliphatic protons, possibly originated from the hydrogenation of the aromatic groups of the IPr·NHC ligand. The broad 10.23 ppm peak was assigned to the NCHN proton of the imidazolium cations, which, presumably, are physically adsorbed to Rh NPs without being coordinated to the surface Rh.

To verify that this 10.23 ppm chemical shift belongs to the IPr·NHC·HCl imidazolium salt, solution-phase proton NMR spectroscopy was used on a sample of Rh NPs made from ^{13}C-labeled IPr·NHC·HCl, with ^{13}C isotope at the C2 ($N^{13}CHN$) position. Strong ^{13}C–^{1}H coupling was observed between the labeled carbon and the 10.23 ppm peak, consistent with the presence of an imidazolium salt. In the ^{13}C NMR spectrum of the ^{13}C-labeled Rh NPs, the 140 ppm and 170 ppm peaks were assigned, respectively, to the C2 carbon ($N^{13}CHN$) of the imidazolium salt and the carbene carbon ($N^{13}CN$) coordinated to Rh. Analysis by heteronuclear single quantum coherence 2D NMR spectroscopy shows the ^{1}H–^{13}C correlations between the 10.23 ppm proton NMR shift and the 140 ppm ^{13}C NMR shift. This 10.23 ppm peak persists even after washing the Rh NPs with water and reacting with PPh_3 and $P(OPh)_3$ in an unsuccessful attempt at ligand exchange, presumably because the ligand is tightly bound to the surface of NPs without the help of a surface metal–ligand bond.

In solid-state ^{13}C MAS NMR, a signal at 25.57–29.83 ppm was assigned to methyl carbons, 32.6 ppm was assigned to methine (tertiary) carbons, and 28 ppm assigned to aromatic carbons. The downfiled signals at 140 and 170 ppm were assigned to the carbene carbons of the coordinated NHC ligand and the noncoordinated imidazolium NCHN carbons, consistent with the findings from solution-phase ^{13}C NMR spectroscopy.

Rh [Bis(imino)pyridine]

An Rh^I complex (Figure 6) with an [*N,N,N*-Bis(imino)pyridine] pincer ligand served as the precursor to Rh metallic NPs (*46*). The Rh NPs were prepared by the hydrogenation of the pincer complex in the presence of KO*t*Bu, in 2-propanol solvent, at 60 °C in 7 h and under 1 atm H_2. Both ligand and metal are from the same complex in this synthesis, and purification of the NPs was performed by washing them with 2-propanol and drying. TEM images showed 1.5 ± 0.2 nm NPs. The Rh NPs that formed in situ and in a solution suspension from the precursor complex catalyzed the aromatic hydrogenation reactions. The hydrogenation reactions are similar to those of the Rh (NHC) NPs discussed in the previous section.

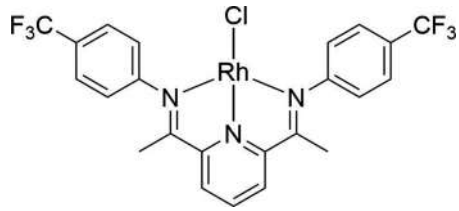

Figure 6. A Rh^I pincer complex as a precursor for the Rh NPs.

The reaction conditions were very mild. Under 1 atm H_2 at 60 °C in 5 h and using a 2% catalyst loading (based on Rh), phenol was reduced to cyclohexanone with a quantitative yield. Benzene was reduced to cyclohexane in quantitative yield in 4 h under otherwise identical conditions. The NPs also catalyzed the dehalogenation of 1,4-dichlorobenzene to benzene with 86% yield in 4 h. Control experiments, including the Hg adsorption test, suggest that the dehalogenation reaction is catalyzed by both homogeneous and NP catalysts. Aromatic hydrogenation was only catalyzed by the NP catalyst.

Solution-phase proton NMR spectroscopy in $CDCl_3$ showed broad aromatic peaks from 6.3 to 7.6 ppm and aliphatic peaks from 0.5 to 2.3 ppm. The proton-decoupled ^{19}F NMR spectrum showed a singlet at –61.1 ppm, assigned to the CF_3 groups on the two phenyl rings. These results suggest that the Rh NPs are stabilized by the partially hydrogenated *N,N,N*-bis(imino)pyridine ligand originated from the precursor complex.

Pd (Dodecylthiolate)

Shon and co-workers have performed extensive studies (*11*, *19*, *20*, *26*, *47*) on the synthesis, catalysis, and characterizations of several surface thiolate ligands on Pd NPs. The thiolate ligands (RS^-) on the surface of Pd NPs are made from the $NaBH_4$ reduction of a ligand precursor molecule, S-alkanethiosulfate ($RS–SO_3^-$). In the synthesis of Pd NPs, alkanethiosulfate ligands initially attached to the surface of Pd NPs but were then reduced by $NaBH_4$ to thiolate via the cleavage of the S–S bond and the loss of a sulfite (SO_3^-) group. The authors streamlined the surface ligand characterizations using solution-phase proton NMR, TGA, and FT-IR analyses. They estimated the surface ligand coverage using a truncated octahedron model (*26*, *27*).

This indirect approach using S-alkanethiosulfate ligands was developed to produce Pd NPs with a lower surface ligand coverage than Pd NPs made using thiolate ligands directly (*27*). Since the ligands block the active sites, high coverage of thiolate ligands on NPs is undesirable for NP catalysts

(*28*). The surface ligands stabilize the NPs from agglomeration; however, they can poison the catalyst simultaneously. The authors studied the NPs for their selectivity in catalytic hydrogenation and isomerization of olefins.

A review (*19*) by San and Shon discussed a variety of metal NPs stabilized by thiolate ligands that are generated in situ from S-alkanethiosulfate, including Au, Pd, Pt, and Ir NPs. The catalytic activity and selectivity were also discussed. To avoid duplication, only three key studies are highlighted herein that focus on the characterizations and quantitation of the surface thiolate ligands.

Gavia et al. reported the initial work (*26*) on the synthesis of dodecylthiolate-stabilized Pd NPs (Figure 7), using a modified Brust–Schiffrin method (*26*, *31*). Alkanethiosulfate was used as the precursor to alkanethiolate instead of attaching alkanethiolate ligands directly to Pd NPs.

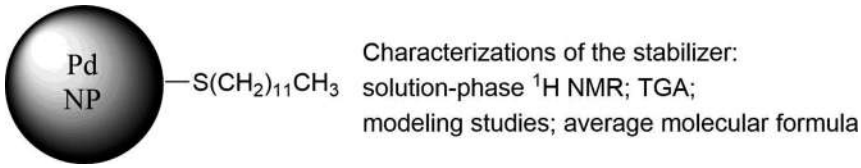

Figure 7. Dodecylthiolate [$S(CH_2)_{11}CH_3$]-stabilized Pd NPs.

First, a water-soluble potassium tetrachloropalladate(II) complex (K_2PdCl_4) underwent cation exchange with tetra-*N*-octylammonium bromide (TOAB), a phase-transfer agent. Organic-soluble tetra-*N*-octylammonium tetrachloropalladate was formed. The water-soluble thiolate ligand, sodium S-dodecylthiosulfate, was also brought into the organic layer by cation exchange using TOAB. NP formation occurred in an aqueous–organic biphasic system when $NaBH_4$ reduced Pd^{II} to Pd^0. Pd NPs with a size of 2.59 ± 1.15 nm were made at 22 °C in 3 h. Pd NPs with different sizes were also prepared by varying the reaction conditions and purified by removing the aqueous layer, drying under vacuum, and repeatedly washing with ethanol, acetonitrile, and acetone. The NPs were isolated in a powder form after volatiles were removed under vacuum.

Solution-phase proton NMR analysis showed broad peaks at 1.2 and 0.8 ppm, assigned to methylene and methyl hydrogens, respectively. Hydrogens at the α- ($RC\underline{H}_2–S^-$) and β- ($RC\underline{H}_2CH_2–S^-$) positions cannot be detected. Presumably, the signals were broadened beyond recognition (see the sections on Ru (NHC) and Pt (NHC) NPs for additional discussions on broadening).

TGA was performed at room temperature to 600 °C. The weight loss during thermolysis was attributed to the loss of organic thiolate surface ligands. A weight loss of 31.4% was detected in the thiolate-stabilized 2.59 ± 1.15 nm Pd NPs. Therefore, the authors believe that the NPs has a 68.6% Pd content. Based on a truncated octahedron model (*26*, *27*), the NP size and the surface ligand quantity were used to estimate the average molecular formula of Pd NPs. The average molecular formula for the 2.59 ± 1.15 nm Pd NPs was Pd_{586}(dodecylthiolate)$_{142}$ with a surface ligand coverage of 0.52 per surface Pd atom, or 52%. Pd NPs ranging from 1.51 to 3.38 nm were made by varying reaction conditions (temperature, number of reagents, and ligands). Increasing the NP size resulted in decreasing ligand surface coverage from 75% (0.75 ligands per surface Pd atom) for the 1.51 nm NPs to 34% for the 3.38 nm NPs.

The 2.59 ± 1.15 nm Pd NPs catalyzed the isomerization of allylic alcohol to propanal with 90% conversion, 81% selectivity, and 12% of hydrogenation product, 1-propanol, in 4 h and 12 mmol H_2. The catalyst loading was 5%, based on total Pd relative to allylic alcohol; the TOF was 407 h^{-1},

based on the mole number of the isomerized product, propanal, per Pd atom. As expected, the TOF increased with the decrease in surface ligand coverage in all five samples of NPs. For example, the 1.51 nm NPs had the highest ligand surface coverage of 75% and gave the lowest TOF of 61 h^{-1}. NPs with a size of 3.38 nm had a ligand surface coverage of 34% and the highest TOF of 449 h^{-1}. This increase in catalytic reactivity with an increase in NP size is remarkable and counterintuitive because smaller NPs were believed to be more active (due to higher surface area) than larger NPs.

The studies suggest that surface ligand coverage can be more important than size in determining catalyst activity. In this case, the 1.51 nm Pd NPs were more poisoned than 3.38 nm NPs. Further lowering the ligand coverage may increase catalyst activity; however, during synthesis, when the ligand to palladium ratio is lower than 1:1, no NPs can form. Instead, Pd bulk material precipitates.

Pd (Alkylthiolate and Arylthiolate)

The method for the synthesis of thiolate-stabilized Pd NPs, discussed in the previous section, was used to synthesize three types of Pd NPs (*20*), each bearing a different ligand: hexylthiolate, (2-cyclohyexylethyl) thiolate, and 2-phenylethyl thiolate. The size of the NPs were 2.3 ± 1.1 nm, 2.9 ± 1.3 nm, and 1.7 ± 0.8 nm, respectively.

Solution-phase proton NMR analyses were performed on these NPs. The chemical shifts of the ligands were assigned using the proton NMR chemical shifts of the free, unbound ligands (e.g., the spectrum of sodium S-hexylthiosulfate was compared to the Pd NPs stabilized by hexylthiolate).

In the NMR spectrum of the hexylthiolate-stabilized Pd NPs, the β-methylene protons ($RC\underline{H}_2CH_2–S^-$) at 1.66 ppm for the free ligand were used to assign a broad signal found at this region for the bound ligand of Pd NPs. Two very broad peaks at 1.3 and 0.9 ppm were assigned to the rest of the methylene groups and the terminal methyl group, respectively. The assignments were based on the chemical shifts of methylene and methyl protons for the free, unbound sodium S-hexylthiosulfate. Protons at the α-position ($RC\underline{H}_2–S^-$) were expected at 3.00 ppm for the Pd NPs, but the signal could not be detected and was possibly broadened beyond recognition (see the sections on Ru (NHC) and Pt (NHC) NPs for additional discussions on broadening).

The proton NMR chemical shifts of the other two types of NPs could not be accurately assigned due to signal broadening beyond recognition. For the NPs stabilized by (2-cyclohyexylethyl) thiolate ligands, three very broad alkyl chemical shifts were observed from 0.9 to 1.7 ppm. No distinct chemical shifts could be identified at all for the NPs stabilized by 2-phenylethylthiolate ligands. An extremely broad signal from 6.6 to 7.5 ppm was detected, which could be due to the aryl protons.

TGA determined the Pd content for the thiolate-stabilized NPs was 88% for Pd (hexylthiolate), 84% for Pd [(2-cyclohyexylethyl)thiolate], and 83% for Pd (2-phenylethyl thiolate). Using the respective NP core size of 2.3 nm, 2.9 nm, and 1.7 nm, the surface ligand coverage was estimated to be respectively 0.35, 0.41, and 0.32 ligands per surface Pd atom, or 35%, 41%, and 32%.

All three types of NPs catalyzed the isomerization reaction of allylic alcohol to propanal with higher than 92–98% yield. However, the Pd (2-phenylethylthiolate) catalyst appeared to be more selective than the Pd (hexylthiolate) catalyst for the isomerization of 1-phenyl-2-propen-1-ol to the ketone, propiophenone. Pd (2-phenylethylthiolate) was less selective, giving 78% yield of ketone and 22% of hydrogenation products. Pd (hexylthiolate) was the least selective catalyst, giving 46% yield of ketone and 54% of hydrogenation products.

Water-soluble Pd NPs (*47*) were synthesized using sodium *ω*-carboxyl-S-undecanethiosulfate as the ligand precursor to the *ω*-carboxyl-undecanethiolate ligand. Previously, the thiolate-stabilized Pd NPs were only soluble in an organic hydrocarbon solvent (*20*, *26*, *27*). Using these water-soluble

Pd NPs, catalytic isomerization of allylic alcohols to aldehydes can be carried out in a biphasic solvent mixture. Allylic alcohols dissolved in the organic layer can be hydrogenated using the Pd NPs dissolved in the aqueous layer. At the end of the reaction, the catalyst in the aqueous layer can be easily removed and recycled.

TEM images showed that the Pd NPs stabilized by ω-carboxyl-undecanethiolate had a size of 2.4 ± 1.15 nm and were well dispersed. Proton NMR analyses and TGA similar to those used for Pd (alkylthiolates) NPs were carried out.

The presence of the carboxylate group of the ω-carboxyl-undecanethiolate ligand was verified by FT-IR analyses of Pd NPs stabilized by this ligand. For the Pd NPs, stretches at 3000–2850 cm^{-1} were consistent with the presence of alkyl groups of the 11-mercaptoundecanoate ligand. The strong antisymmetric and symmetric $-COO^-$ stretches were identified at 1550 cm^{-1} and 1440 cm^{-1}, respectively. The O–H stretch near 3300 cm^{-1} and a shoulder near 1700 cm^{-1} could be consistent with the carboxylic acid group (–COOH), in addition to the carboxylate group ($-COO^-$).

Ir (Polyoxoanion)

The stabilization of NPs from aggregation and formation of bulk material (*1*) is believed to be due to steric or electrostatic effects (*1*, *2*); however, the stabilization by the van der Waals force and by the surface metal–ligand bonding can also contribute. The zerovalent metallic NPs are vulnerable to oxidation by air (*32*).

The all-inorganic Ir NPs stabilized by polyoxoanion have a mode of stabilization called an electrosteric effect, which is the result of large size and the multiple negative charges of a polyoxoanion such as $[P_4W_{30}Nb_6O_{123}]^{16-}$. Finke and Lin (*2*, *32*) reported the synthesis and thorough characterizations of Ir NPs stabilized by $[P_4W_{30}Nb_6O_{123}]^{16-}$ polyoxoanions, shown in Figure 8. A variety of of spectroscopic techniques, including TEM, EA, FT-IR, mass spectrometry, NMR spectroscopy, and modeling studies, allow the authors to establish a molecular formula for the NPs, $[Ir^0{}_{900}(P_4W_{30}Nb_6O_{123}{}^{16-})_{60}](Bu_4N)_{660}Na_{300}$ (Bu = butyl). These NPs are referred to as the Ir 900 NPs. The square bracket indicates an anionic NP core with polyoxoanion stabilizers. The tetra-*N*-butyl ammonium and sodium cations serve as counter ions. A zeta-potential of –40 mV, measured using an electrophoresis experiment, is consistent with the proposed model in which the polyoxoanions are adsorbed to the surface. The sodium and tetra-*N*-butylammonium cations serve as counter ions in the outer diffusion layer of NPs.

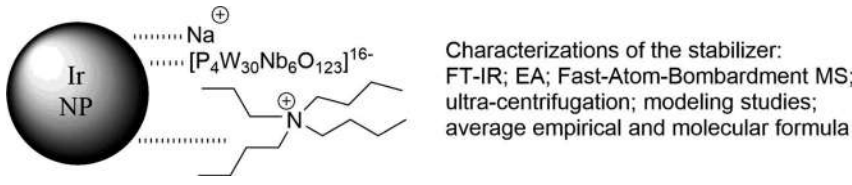

Figure 8. Ir NPs stabilized by $[P_4W_{30}Nb_6O_{123}]^{16-}$ polyoxoanions and the counter ions: sodium and tetrabutylammonium cations.

The synthesis of the polyoxoanion-stabilized Ir NPs was carried out using an organometallic precursor complex, $(Bu_4N)_5Na_3[(cod)Ir{\cdot}P_2W_{15}Nb_3O_{62}]$, at room temperature in an acetone solvent and under 2.7 atm of H_2. The decomposition of the precursor complex led to NP formation.

Purification of the NPs was performed to remove free, uncoordinated tetra-*N*-butylammonium cations and polyoxoanions. This was done by precipitation of the NPs using hexane, discarding the supernatant that contains impurities, dissolving the NPs in acetone, and drying under vacuum. TEM images of these Ir NPs showed that they have a size of 3.0 ± 0.4 nm. SAED studies indicate that the crystalline NPs have an fcc structure, similar to bulk Ir metal. The Ir NPs catalyzed the hydrogenation of cyclohexene. This "reporter reaction" is studied in great detail by Finke and coworkers to determine the kinetic mechanism of NP nucleation and growth (*2*, *32*).

The FT-IR spectrum of the polyoxoanion-stabilized Ir NPs showed stretches at 1088, 947, 920, 896, and 774 cm^{-1}. They are characteristic of $P_2W_{15}Nb_3O_{62}^{9-}$ or its dimer, $[P_4W_{30}Nb_6O_{123}]^{16-}$.

EA found in the Ir NPs 14.48% C, 2.67% H, 1.02% N, 20.1% Ir, 0.84% P, and 14.5% O. Based on EA, the authors calculated the average empirical formula for the Ir 900 NPs to be $[Ir_{15}(P_4W_{30}Nb_6O_{123})(Bu_4N)_{11}Na_5]_n$. This formula gives a very similar composition of 15.28% C, 2.89% H, 1.11% N, 20.8% Ir, 0.89% P, and 14.23% O. The average empirical formula describes the relative ratios of all the elements in a molecule; however, it is not the average molecular formula for the NPs. EA does not provide information regarding the number *n* in the average empirical formula, which is an integer that determines the average total atoms of NPs.

The average molecular formula of the Ir 900 NPs was determined with the help of a theoretical model (*27*). Using the 3.0 ± 0.4 nm NP size from TEM measurements, the average empirical formula from EA, and a theoretical model of NPs (*26*, *27*, *32*), the authors calculated the average molecular formula to be $[Ir_{15}(P_4W_{30}Nb_6O_{123})(Bu_4N)_{11}Na_5]_{60}$, or the algebraically equivalent $[Ir^0{}_{900}(P_4W_{30}Nb_6O_{123}{}^{16-})_{60}](Bu_4N)_{660}Na_{300}$.

The theoretical model approximates the fcc Ir NPs as a truncated octahedron. Depending on the size or diameter of a truncated octahedron, the corresponding number of atoms is known. These numbers are called "magic numbers" and have different values depending on the size of NPs. For example, a 3.0 nm truncated octahedron is made of Ir 900 atoms, where the magic number is 900.

The average molecular weight was measured directly, using the sedimentation-equilibrium method at an ultracentrifugation speed of 20,000 rpm (*32*). The measured value of 180,000 ± 8,000 g/mol is close to the molecular weight based on the average molecular formula from theoretical modeling, 170,000 g/mol. Fast-atom bombardment mass spectrometry of the Ir NPs detected two broad peaks corresponding to the polyoxoanion ligands. The one at 5000 m/z was attributed to the $P_2W_{15}Nb_3O_{62}^{9-}$ anion, and the one at 10,000 m/z was attributed to the $P_4W_{30}Nb_6O_{123}^{16-}$ anion. The molecular weight measurement suggests that the stabilizer is the dimeric form, $P_4W_{30}Nb_6O_{123}^{16-}$.

Ir (Dodecylthiolate)

The synthetic method for the formation of Pd NPs also enabled the synthesis of 1.2 nm thiolate-stabilized Ir NPs, shown in Figure 9 (*25*). The S-alkanethiosulfate ligands ($R–S–SO_3^-$) used by Gavia et al. served as a precursor to thiolate ligands. This indirect route of NP synthesis was developed for Ir because the direct attachment of the thiolate ligand failed to give Ir metallic NPs.

The NP synthesis was carried out in a biphasic mixture of 1:1 toluene and water at 60 °C. Water-soluble potassium hexachloroiridate (K_2IrCl_6) served as the iridium precursor and TOAB as the phase tansfer agent. This agent is responsible for bringing the $[IrCl_6]^{2-}$ complex anion to the organic phase by the formation of tetra-*N*-octylammonium hexachloroiridate. Sodium S-dodecylthiosulfate

$[CH_3(CH_2)_{11}S–SO_3Na]$ was also brought to the organic layer by TOAB. $NaBH_4$ reduced Ir^{IV} to Ir^0, en route to NP formation. $NaBH_4$ also reduced the S-dodecylthiosulfate ligand to form thiolates in situ that stabilized the Ir NPs.

The organic layer containing the NP was washed repeatedly with water and collected using a separatory funnel. The organic solvent was removed under vacuum, and the NPs were washed thoroughly with ethanol, methanol, and acetone to remove organic molecules that were not tightly bound to the NP surface. The NPs were isolated in a powder form after drying under vacuum.

TEM images showed that the average particle size was 1.2 ± 0.3 nm. XPS analysis showed Ir ($4f_{7/2}$) and ($4f_{5/2}$) peaks at 60.8 eV and 63.8 eV, respectively, consistent with metallic Ir^0 (*16*). The binding energy was calibrated using the oxygen 1s peak at 528.5 eV. These Ir NPs have strong magnetic properties, unlike Ru NPs, which are believed to be diamagnetic (*38*).

The solution-phase proton NMR spectrum of the alkanethiosulfate-stabilized Ir NPs in $CDCl_3$ showed broad peaks at 1.80–1.60 ppm, 1.50–1.20 ppm, and 0.9–0.8 ppm, assigned respectively to the β-methylene group (–CH_2–CH_2–S–), methylene groups further away from the β position, and the terminal methyl group. In contrast to Ir NPs, the β-methylene groups in Pd NPs stabilized by thiolate ligands are broadened beyond recognition. The broadening of solution-phase proton NMR peaks is commonly associated with organic ligands bound to the surface rather than with free ligands (*25*).

Due to the thorough purification procedures by aqueous-organic extraction and by washing with a variety of polar organic solvents, free ligands that were not bound to the surface of Ir were not observed in the solution-phase proton NMR spectrum. These unbound, free species include tetra-*N*-octylammonium with the α–CH_2–N at 3.40 ppm, didodecyldisulfide with the α–CH_2–S–SR at 2.54 ppm, and dodecanethiolate with the α–CH_2–S^- at 2.18 ppm.

FT-IR analysis of the thiolate-stabilized Ir NPs showed alkyl stretches of thiolates ligands at 3000–2800 cm^{-1} (stretching mode) and 1450 cm^{-1} (bending mode). Stretches associated with sulfonate (RSO_3^-) were absent (1350 cm^{-1} and 1175 cm^{-1} for the antisymmetric and symmetric S=O stretches), which indicates the absence of the alkanethiosulfate precursor ligand. It was proposed that $NaBH_4$ carried out reductive S–S cleavage to convert alkanethiosulfate to thiolate ligands that stabilized Ir NPs.

TGA detected a weight loss of 38.5% when the sample was heated from 150 to 600 °C. The result suggests that the NPs contain 61.5% of Ir and 38.5% of organic compounds and volatiles. The XPS binding energy for S (2p) is found at 162.2 eV, attributed to the sulfur atom coordinated to Ir.

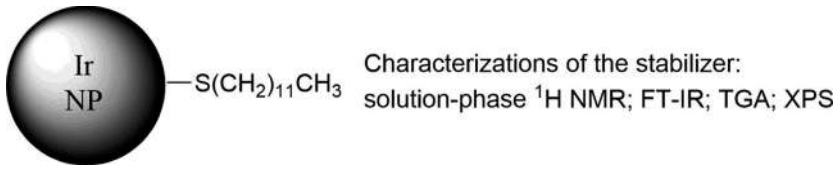

Figure 9. Dodecylthiolate-stabilized Ir NPs.

Ir (Citrate)

To study the surface-enhanced Raman scattering activity of Ir metallic NPs, Cui et al. synthesized citrate-stabilized 2.5 nm Ir NPs, shown in Figure 10 (*16*). Under nitrogen, a diluted aqueous solution (1%) of trisodium citrate was combined with Ir^{III} trichloride (0.03%). The pH of

the solution was adjusted to 7–9 using NaOH. The reaction was heated to reflux, and a 1 M $NaBH_4$ aqueous solution was used to reduce Ir^{III} to Ir^0.

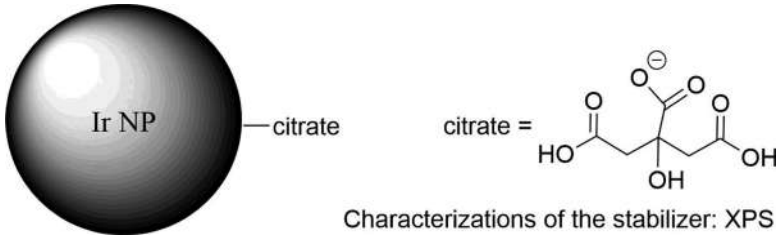

Figure 10. Ir NPs stabilized by citrate anions. The precise binding mode is unclear, and the most acidic proton is removed in the citrate anion.

The Ir NPs were purified by precipitation with ethanol. HRTEM analysis showed that these NPs were crystalline and were 2.5 ± 0.5 nm. The SAED and PXRD spectrum showed the (111), (200), (220), and (311) reflections of fcc metallic Ir. XPS analysis showed the $4f_{7/2}$ and $4f_{5/2}$ binding energies of Ir at 61.2 and 64.1 eV, attributed to Ir^0. Binding energies at 62.3 eV and 65.2 were attributed to an oxidized Ir^{n+} species. The presence of an oxidized Ir^{n+} species could be due to the incomplete reduction by $NaBH_4$ or possibly oxidation during the purification–characterization stage.

XPS analysis showed C 1s binding energies at 284.6 and 288.3 eV, which were assigned to the citrate stabilizer. The 284.6 eV peak was assigned to the methylene carbon bonded only to other carbons. The 288.3 eV peak was assigned to carbons bonded to oxygen. XPS analysis showed O 1s binding energies at 531.3, 532.2, and 533.1 eV, which were assigned to the oxygens of the citrate stabilizer. The 531.3 and 532.2 eV peaks were assigned to the carbonyl (C=O) and hydroxyl (C–OH) oxygen. The 533.1 eV peak was assigned to the negatively charged O^- of citrate anions. The binding energy calibration was conducted using the C 1s peak at 284.8 eV.

The precise binding mode of citrate to Ir NPs is unclear. Based on the pKa value, the proton of the central carboxylic acid group, as shown in Figure 10, is the most acidic (*48*) and most likely to be removed. The zeta-potential of –25 mV is consistent with a citrate anion-stabilized NP core.

Pt (Carbonyl and Hydroxide)

In 2000, Wang et al. (*29*) reported the synthesis of stable, 1–2 nm Pt NPs in basic ethylene glycol solution at 160 °C for 3 h and under argon or N_2. The Pt NPs were made without using any conventional stabilizer to prevent aggregation. The conventional stabilizers are, for example, a small organic ligand such as phosphine, a surfactant such as oleic acid or dodecylthiol, or a polymer such as polyvinyl alcohol or polyvinylpyrrolidone (*1*). PXRD analysis showed that the NPs have a crystalline fcc structure.

The Pt NPs were considered "unprotected" due to the lack of conventional stabilizer. Wang et al. emphasized that these unprotected NPs were not "truly bare," which describes metal-only NPs that have no stabilizers. Without stabilizers, the NPs would quickly aggregate and precipitate (*28*, *29*). In contrast, the Pt NPs were stable enough to stay suspended in solution for months (*28*, *29*, *49*). XPS analysis did not detect any chloride in NPs, ruling out the possibility of a chloride stabilizer (*2*). EA showed less than 0.8% of carbon, which could be due to ethylene glycol. Consequently, the authors proposed hydroxide anions from NaOH and ethylene glycol from the solvent as the stabilizers.

Approximately 15 years later, Baquero (*49*) et al. and Schrader (*28*) et al. reported the direct characterizations of the surface ligands of the Pt NPs (Figure 11), where ethylene glycol, hydroxide, and CO have been detected directly. In 2014, Baquero et al. reported a 2050 cm^{-1} stretch in the FT-IR spectrum of the Pt NPs made with the Wang method. This stretch corresponds to a linearly adsorbed, terminal CO ligand (*49*, *50*). Vibrations at 3000–2790 cm^{-1} and 1770–1400 cm^{-1} were assigned to C–H stretching and bending modes of surface-bound ethylene glycol, which could not be removed by washing the NPs with an organic solvent. The FT-IR studies were performed in the transmission mode on NPs drop-casted on a CaF_2 substrate.

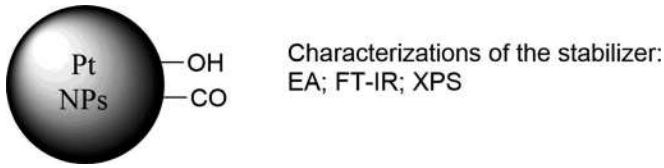

Figure 11. Hydroxide- and carbonyl-stabilized Pt NPs.

In 2015, Schrader et al. reported (*28*) that a strong IR stretch at 2026 cm^{-1} was observed for the Pt NPs made with the Wang method and attributed to the linearly adsorbed, terminal (*50*) CO ligand from the oxidation of ethylene glycol, as shown in Figure 12. In a control experiment, the Pt NPs made in water without ethylene glycol lacked this 2026 cm^{-1} stretch. A stretch at 1830 cm^{-1} was assigned to a bridging (*50*) carbonyl ligand, and a stretch at 1730 cm^{-1} was assigned to the C=O stretching mode of a carboxylate group (*28*), although the stretch appears to be consistent with a carboxylic acid group instead (*50*). The presence of carboxylic acid could be due to the oxidation of ethylene glycol to glycolic acid. In contrast to Baquero et al.'s studies, Schrader et al. could not identify IR stretches or solution-phase proton NMR signals that corresponded to the ethylene glycol stabilizer, ruling out this stabilizer. The FT-IR studies were performed in the ATR mode on a solution suspension of NPs in ethylene glycol and used ethylene glycol as a reference.

The hydroxide ligand overlapped with water in the IR spectrum. To resolve this issue, the presence of hydroxide ligands was indirectly characterized by IR (*28*), using the surface hydroxide-induced CO shift from 2046 to 2020 cm^{-1}, when the NaOH concentration during synthesis increased from 0.0625 M to 0.5 M. The shift in CO stretch was attributed to an increase in the surface hydroxide coverage and a decrease in CO coverage. The decrease in CO coverage led to a reduction in the dipole–dipole coupling of adjacent CO ligands (*28*). On the other hand, hydroxide ligands probably increased the π-basicity (*51*) of surface Pt atoms and weakened the CO bond due to metal-to-ligand back-bonding (*51*). The back-bonding weakened the C=O bond and caused a redshift of the CO stretch. Pt NPs with a densely packed monolayer of CO ligands had a blueshifted IR stretch at 2060 cm^{-1} (*28*).

To suppress the dipole–dipole coupling effect, which blueshifts the CO stretch when the surface ligand coverage is high, Altmann (*49*) et al. measured the "singleton frequency" of surface CO ligands at a theoretical surface ligand coverage of CO approaching 0%. By diluting ^{12}CO with ^{13}CO, ^{12}CO surface ligands were separated from one another by ^{13}CO. The authors made the Pt NPs in ethylene glycol and deposited them on a TiO_2 support for analysis using diffuse-reflectance infrared Fourier transform spectroscopy. The singleton frequency of linearly bonded, terminal ^{12}CO was found at 2039 cm^{-1} (*50*). Minor stretches at 1839 and 2114 cm^{-1} were also detected, attributed to

bridging ^{12}CO coordinated to Pt^0 and ^{12}CO coordinated to an oxidized Pt^{n+} species, respectively (*50*). The ^{13}CO stretch was found at 2024 cm^{-1}.

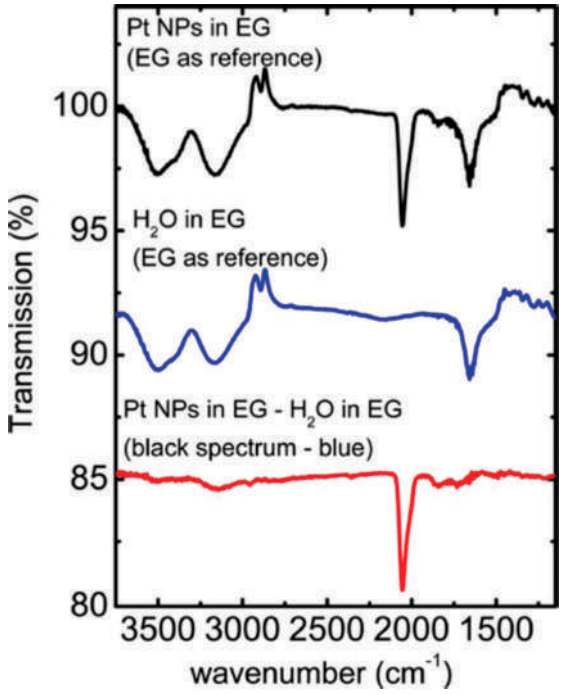

Figure 12. Infrared spectra of Pt NPs made in ethylene glycol (top), Pt NPs made in water without ethylene glycol (middle), and Pt NPs made in ethylene glycol and water (bottom). The carbonyl stretch appears near 2000 cm^{-1}. The hydroxide stabilizer cannot be distinguished from water. Reproduced with permission from ref (28). Copyright 2015 American Chemical Society.

Pt (Amine or Pyridine)

Based on Wang's method for synthesis of Pt NPs stabilized by carbonyl and hydroxide ligands, Bäumer and co-workers et al. further introduced amine and pyridine stabilizers to these Pt NPs, shown in Figure 13, and performed detailed FT-IR studies (*8*, *52*). The Pt NPs are therefore stabilized by amine or pyridine, in addition to carbonyl and possibly hydroxide.

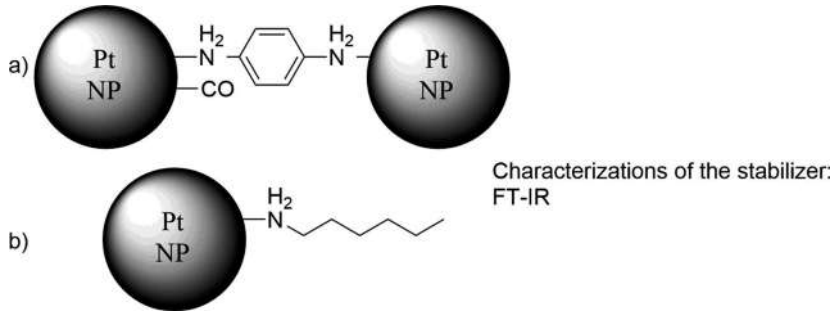

Figure 13. (a) p-Phenylenediamine and carbonyl stabilizers on Pt NPs, (b) Hexyldecylamine stabilizer on Pt NPs without carbonyl.

Bäumer and co-workers studied these NPs for the Pt-catalyzed H_2 oxidation by O_2 in the context of developing a hydrogen gas sensor. A hydrogen gas sensor made of Pt NPs detects hydrogen via the exothermic reaction between hydrogen and oxygen that generates heat as a signal for detection. Pt NPs catalyze this reaction and also catalyze the selective hydrogenation of crotonaldehyde.

The synthesis of Pt NPs, stabilized by hexadecylamine or aniline, started with Wang's synthesis of Pt NPs in basic ethylene glycol solvent, discussed in detail in the previous section. At the end of the reaction, a solution of hexadecylamine or aniline in toluene was added to a solution suspension of Pt NPs in ethylene glycol. A biphasic ethylene glycol–toluene mixture formed. After 3 h at room temperature, the amine stabilizer binds to the Pt NPs, leading to a change of solubility in the NPs. The dark Pt NPs transferred from the polar ethylene glycol phase to the nonpolar toluene phase.

The NPs were purified by removing the ethylene glycol phase and washing the toluene layer with water and ethanol. Pt NPs with various nitrogen-based stabilizers attached were made. The stabilizers included hexadecylamine, aniline, 1,8-diaminooctane, and *p*-Phenylenediamine. The TEM images showed that, before adding an amine, the NPs had a size of 1.8 ± 0.5 nm. After attaching aniline ligands, the size of the NPs did not change significantly (1.9 ± 0.3 nm).

As discussed in the previous section, the Pt NPs synthesized in ethylene glycol gave FT-IR stretches that can be attributed to the surface CO stretching mode (2050 cm^{-1}); ethylene glycol C–H stretching and bending modes (3000–2790 cm^{-1} and 1770–1440 cm^{-1}, respectively); and carboxylic acid C=O stretching mode (1730 cm^{-1}). After adsorption of the *p*-Phenylenediamine ligand, FT-IR analysis of the NPs showed the amine $-NH_2$ stretching and bending modes at 3420–3340 cm^{-1} and 1630 cm^{-1}, respectively. Aromatic C=C stretches were found at 1510 cm^{-1}. Upon the adsorption of *p*-Phenylendiamine, the CO stretch shifted from 2050 cm^{-1} to a lower frequency of 2020 cm^{-1}. The redshift could be due to a combination of a reduction in dipole–dipole coupling from adjacent CO and an increased electron density on Pt leading to a greater π back-bonding (*51*) to CO (see the previous section for additional discussions on back-bonding) (*49*). Since CO formation originates from the Pt oxidation of ethylene glycol (*28*, *52*), the presence of CO ligands on Pt NPs may indicate the presence of free surface binding sites that catalyzed the oxidation of ethylene glycol to CO.

In contrast to *p*-Phenylenediamine, when hexyldecylamine was used as the stabilizer, no CO stretch was found for the Pt NPs. The absence of CO ligand is rationalized by the full ligand coverage by hexyldecylamine and the lack of any binding sites that would catalyze the oxidation of ethylene glycol to CO.

Based on electron microscopy imaging, the authors suggest that the *p*-Phenylendiamine serves as a bifunctional stabilizer with two binding sites that can bridge two Pt NPs and form a three-dimensional network structure, as shown in Figure 14 on the right. The NPs stabilized by the monofunctional stabilizer hexyldecylamine can only form a 2D planar structure, as shown on the left.

To develop a hydrogen gas sensor (*8*, *52*), the authors studied the catalytic aerobic oxidation of H_2 using these Pt NPs. The NPs stabilized by *p*-Phenylenediamine were much more active than NPs stabilized by hexyldecylamine. The higher activity was attributed to the more available surface binding sites for catalysis. The importance of the available binding sites for catalysis is also observed in the Pd NPs by Gavia et al. (*26*).

The Pt NP catalyst with *p*-Phenylenediamine ligands was also more stable than the NP catalyst stabilized by hexyldecylamine ligands (*8*, *52*). Morsbach et al. studied the details of ligand

degradation of these Pt NPs using FT-IR (*8*). Analyses before and after catalytic aerobic oxidation of H_2 were performed on the Pt NPs for comparisons.

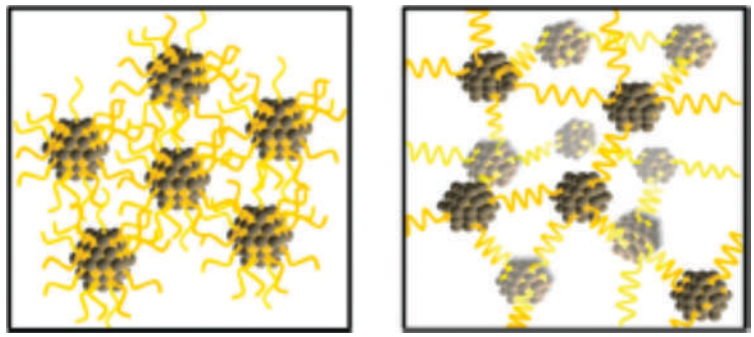

Figure 14. Hexyldecylamine-stabilized Pt NPs (left) and p-Phenylenediamine-stabilized Pt NPs (right). Reproduced with permission from ref (*52*). *Copyright 2014 American Chemical Society.*

For the Pt (hexadecylamine) NPs, the N–H bending modes (1640–1550 cm^{-1}) and C–N stretching modes (1100 cm^{-1}) vanished in the postmortem analysis, suggesting the cleavage of the C–N bond. The stretches for C–H bending (1470 cm^{-1}) and rocking modes (720 cm^{-1}) diminished, and a new C=O vibration appeared at 1720 cm^{-1}, consistent with the oxidation of alkyl C–H bonds to ketone or aldehyde. Similarly, for the Pt (1,8-octandiamine) NPs, the loss of CH_2 rocking modes (720 cm^{-1}) and C–N stretching (1270 cm^{-1}) occurred. Formation of stretches above 3000 cm^{-1} and C–O vibration at 1070 cm^{-1} suggested the formation of an epoxide. Overall, the alkyl amine and diamine ligands underwent loss of the amino groups and oxidation of the alkyl groups.

For the Pt (aniline) NPs, the loss of C–N vibration at 1260 cm^{-1} and the retention of aromatic C=C stretches at 1600–1500 cm^{-1} suggested that the phenyl ring may be stable against degradation under H_2 oxidation conditions in the presence of a Pt NP catalyst. For the Pt (*p*-Phenylenediamine) NPs, the postmortem IR spectrum showed that the *p*-Phenylenediamine stabilizer remained intact. The N–H (3411 and 3327 cm^{-1}), C=C (1575 cm^{-1}), C–N (1290 cm^{-1}), and N–H (1614 cm^{-1}) all retained. The authors concluded that the high stability of Pt (*p*-Phenylenediamine) NP catalyst over 13 h is due to the stability of the *p*-Phenylenediamine ligand, which prevents Pt NPs from aggregation and loss of catalytic activity. In this case, catalyst stability correlates activity.

Pt {NHC Ligand and $Na_3[Pt^{II}Me(OH_2)(NHC)_2]$ Ionic Stabilizer}

Baquero et al. found (*53*) that Pt NPs can be dually stabilized by surface ligands and by ionic DLVO stabilizers (*1*, *2*). As discussed in this chapter's introduction, an NP stabilizer can be either a surface ligand or an ionic DLVO stabilizer (*1*, *2*). The Pt NPs reported by Baquero et al. are stabilized by both mechanisms.

The authors synthesized the Pt NPs using an NHC-ligated Pt^{II} complex, as shown in Figure 15 (*53*). Each NHC ligand contains two sulfonate groups that enable the synthesis to be carried out in water to form water-soluble Pt (NHC) NPs. No external reductant was used to convert the Pt^{II} complex to Pt^0 NPs. Instead, the reductive elimination (*51*) of the two methyl groups occured to form ethane, where Pt lowered its oxidation state by two. The Pt NPs range from 1.3 to 2.0 nm.

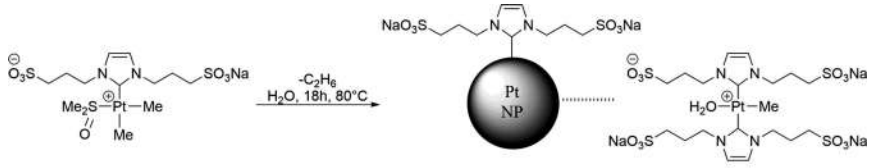

Figure 15. The synthesis of Pt NPs that are dually stabilized by the NHC ligands and the $Na_3[Pt^{II}Me(OH_2)(NHC)_2]$ ionic stabilizers. The hashed line indicates physical adsorption.

The authors identified an NHC surface ligand and an ionic DLVO stabilizer, $Na_3[Pt^{II}Me(OH_2)(NHC)_2]$ (*1*, *2*). The NHC ligand contained two sulfonate groups and is a dianion, which makes the complex, $[Pt^{II}Me(OH_2)(NHC)_2]^{3-}$, a trianion. The NHC surface ligands are chemically adsorbed to surface Pt via coordinate covalent bonds, but the ionic stabilizers are physically adsorbed without a chemical bond to surface Pt.

FT-IR and solution-phase proton NMR spectroscopy confirmed the presence of the NHC ligands. No CO stretch was found in these Pt NPs because they were synthesized in water rather than ethylene glycol, as in the previously discussed system investigated by Wang et al. (*29*), Bäumer and co-workers (*49*, *52*), and Schrader et al. (*28*). In D_2O, the proton NMR spectrum of the Pt (NHC) NPs showed broad signals that can be assigned based on the NMR spectrum of the NHC-ligated Pt complex. The imidazole vinylic (CH=CH) protons were detected at 7.4–7.1 ppm, and the b- and a-methylene groups were found at 2.9 and 2.2 ppm, respectively.

^1H–^{13}C cross-polarization magic angle carbon NMR spectroscopy of the Pt NPs was performed. Signals from the imidazole vinylic (CH=CH) carbons (124–122 ppm) and the α-, β-, and γ-methylene groups (49, 26, and 49 ppm) were detected. The carbene (NCN) signal was very weak, and therefore, it was measured using a ^{13}C–labeled NHC ligand, where the C2 position ($N^{13}CN$) was labeled. The carbene ($N^{13}CN$) signal was found at 177 ppm. A 940 Hz ^{13}C–^{195}Pt coupling was observed, suggesting a direct C–Pt bond on the surface of the NPs.

Notably, even after purification by dialysis for 72 h, the solution-phase proton NMR spectrum still showed sharp signals in addition to the broad signals coming from the surface-bound NHC ligands. This finding suggests the presence of tightly bound stabilizers that do not cause line broadening. NP stabilizers do not necessarily give rise to broadened solution-phase proton NMR shifts, even though they often coincide (*28*, *45*, *54*). Indeed, DOSY (*45*) found that these sharp signals belong to a species that has a diffusion coefficient of 2.5×10^{-10} m^2s^{-1}. This coefficient is similar to that of the surface-coordinated NHC ligands that give broad solution-phase proton NMR signals. The diffusion coefficient is about half that of the molecular complex bearing the same NHC ligand. The diffusion coefficient of the solvent water molecule is close to 20×10^{-10} m^2s^{-1}.

The Stokes–Einstein equation (*55*) relates the hydrodynamic radii (size) of a molecule with its diffusion coefficient. Surface ligands bound to NPs diffuse at a much lower rate than unbound, free ligands (*45*). DOSY is often used in semiconductor NPs (*45*) to distinguish between free molecules and NP surface ligands in the same solution. The results suggest that the two species are both adsorbed to the Pt NPs, despite having very different line width in solution-phase proton NMR spectroscopy.

Electrospray ionization–mass spectrometry detected a species consistent with the $\{Na_2[Pt^{II}Me(NHC)_2]\}^{2-}$ anion. Based on the NMR chemical shifts and electrospray

ionization–mass spectrometry studies, the structure of this second stabilizer was determined to be $Na_3[Pt^{II}Me(OH_2)(NHC)_2]$. The sharp solution-phase proton NMR signals were attributed to this complex anion. The authors believed that the Pt complex anion was not directly coordinated to a surface Pt atom, consistent with a DLVO (or ionic) stabilizer for the NPs (*1*, *2*).

Au (Dodecylthiolate)

Hostetler et al. (*27*) made thiolate-stabilized Au NPs, shown in Figure 16, in a biphasic toluene–water solvent (*19*, *27*, *31*). In the synthesis, $HAuCl_4$ hydrate was dissolved in water and a phase-transfer agent, TOAB, was dissolved in toluene. After mixing the two solutions, phase transfer of the $[AuCl_4]^-$ anion from the aqueous to the organic phase occurred. The aqueous layer was removed, the organic layer was collected, and dodecanethiol was added to stabilize NPs.

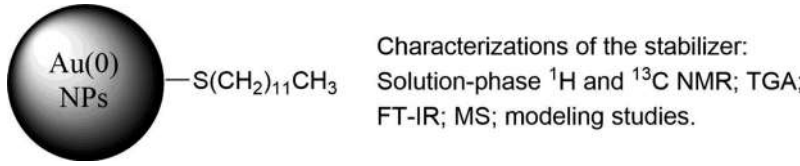

Figure 16. Dodecylthiolate-stabilized Au NPs.

Upon addition of an aqueous $NaBH_4$ solution to the organic layer, NPs formed under a biphasic condition. Au NPs from 1.5 to 5.2 nm in diameter were made by systematic variations on three reaction conditions: (1) temperature at the time $NaBH_4$ was added, (2) the mole ratio of dodecanethiol versus $HAuCl_4$ hydrate, and (3) the rate at which $NaBH_4$ was added. The authors found that the NP size was affected most significantly by the ratio of ligand to $HAuCl_4$ hydrate. Increasing the ligand-to-metal ratio resulted in smaller NPs. XPS analyses on Au $4f_{7/2}$ showed that the relatively large 2.8 nm NPs had binding energy at 84.0 eV, the same as that of bulk gold metal. The very small 1.5 nm NPs had binding energy at 84.4 eV, approaching that of Au^I alkanethiolate polymer at 84.9 eV. The binding energy was calibrated using the carbon 1s peak of the methylene carbon of the dodecylthiolate ligands at 284.9 eV.

The shape of these NPs resembled truncated octahedrons (*44*); therefore, the authors estimated the number of total atoms and surface atoms for the deodecylthiolate-stabilized Au NPs, ranging from 1.5 to 5.2 nm, using the "magic number" (*44*) of atoms in truncated octahedron models that matched the size of the NPs.

The modeling studies (*27*, *44*) showed that the NPs with a size from 1.5 to 5.2 nm had 110 to 4800 Au atoms. For example, calculations showed that a 2.0 nm truncated octahedron made of Au consisted of 314 Au atoms, and a 4.0 nm octahedron consisted of 2406 Au atoms. Out of the total 314 atoms for a 2.0 nm truncated octahedron made of Au, 174 of them were surface atoms, and the number of surface atoms was 752 for the 4.0 nm truncated octahedron made of Au.

The number of dodecylthiolate ligands was calculated theoretically and compared with the experimental values. The number of ligands ranged from 53 to 520 for NPs from 1.5 to 5.2 nm in size.

Only the surface of the truncated octahedron can bind ligands. Each dodecylthiolate ligand has a theoretical "footprint," or the minimal surface area taken up by the ligand. Based on the 19.46 nm^2 surface area of the 2.0 nm truncated octahedron and the 0.214 nm^2 footprint of a single

dodecylthiolate ligand, the theoretical maximum ligand coverage is 91 ligands (19.476 nm^2 divided by 0.214 nm^2) for a 2.0 nm truncated octahedron and 326 ligands for a 4.0 nm truncated octahedron.

The NP size was measured using HRTEM and small-angle X-ray scattering. The calculated maximum number of surface ligands matched well with the experimental values for the average number of ligands measured using TGA. For example, for 4.0 nm Au NPs, the calculated percentage for the ligand was 12.2% wt. The experimental value measured using TGA was 12.8% wt. The loss of mass when heating the sample was attributed to the loss of the surface thiolate ligands.

The limit of this model is that it assumes an ideal polyhedral geometry with flat surfaces for the NPs. Realistically, NP surfaces can be rough and contain more corners, steps, and surfaces than an ideal polyhedron (*1*, *27*). The corners, steps, and additional surfaces lead to a greater surface area than that suggested by the model. Therefore, the model can underestimate the maximum number of surface ligands of an NP.

Thiolate signals from solution-phase ^1H and ^{13}C NMR spectra are characteristically broader than a free, unbound thiolate. This broadening is due to low tumbling rates and surface heterogeneity. The latter is attributed to the different Au binding sites at terraces, edges, and corners on the uneven NP surface (*45*). The degree of signal broadening is different across the deodecylthiolate chain. In C_6D_6, the 38 ppm methylene carbon signal at the β-position ($\underline{C}H_2–CH_2–S^-$) was broadened nearly beyond recognition. The proton signal of the methyl group at the end of the thiolate alkyl chain was the sharpest at 0.4 ppm.

FT-IR analysis measured the antisymmetric stretching frequency of the methylene groups of dodecylthiolate surface ligands on Au NPs. For NPs with an average size from 1 to 4 nm, the stretching frequencies varied only slightly and were detected at 2919 to 2924 cm^{-1}. The stretching frequency was comparable to that of crystalline polyethylene, where the methylene antisymmetric stretching frequency is at 2920 cm^{-1}. The dodecylthiolate ligands are believed to adopt a densely packed structure of crystalline solid (*27*, *56*). The C–S bond vibration was found at 720 cm^{-1}, where the C–S bond is at the antiposition to the adjacent ($^-S–C–\underline{C}–\underline{C}$) C–C bond. The C–S bond vibration was also found at 640 cm^{-1} for some of the NPs, where the C–S bond is at the gauche (defect) position relative to the adjacent C–C bond.

Thermolysis of the dodecylthiolate-stabilized NPs was performed at 240–260 °C. Dodecyl disulfide formed and was detected by mass spectrometry. The formation of disulfide was attributed to the oxidation of two molecules of dodecylthiolate. No thiol ligand (the conjugate acid of thiolate) was detected, consistent with the presence of thiolate rather than thiol ligands.

Au (Citrate, Citric Acid, and Thiolate)

The Brust–Schiffrin method (*31*) was used to make very small Au NPs ranging from 1.5 to 5.2 nm (*27*). To make thiolate-stabilized Au NPs in the 5–100 nm range, a method (*17*) was developed based on the ligand replacement of citrate-stabilized Au NPs with thiols. The effectiveness of this ligand exchange was rationalized by the higher Au–thiolate bond energy than that of the Au–carboxylate bond. It was assumed that citrate surface ligands were completely displaced by thiols using this synthetic method.

Park and Shumaker–Parry reported (*17*, *18*) that the NPs formed by this ligand replacement method contained a significant number of citrate ligands. Therefore, the ligand replacement was incomplete. The carboxylate and carboxylic acid groups of citrate ligands formed a stable hydrogen-bonded network that resisted the ligand replacement by thiols. Al-Johani et al. studied the complex

surface Au–carboxylate binding mode in detail using solid-state ^{13}C and ^{23}Na NMR spectroscopy and computational modeling (*57*).

The 40 nm Au NPs stabilized by citrate and thiolate ligands were made using a two-step procedure. The citrate-stabilized Au NPs were synthesized first, followed by the ligand displacement reaction with thiols. The citrate-stabilized Au NPs were made using the Frens method (*18*), where $HAuCl_4 \cdot 3H_2O$ and trisodium citrate in an aqueous solution were heated at reflux for 1 h. The citrate anion reduced Au^I to Au^0 (*18*). To perform the ligand replacement of citrate with thiolate, an aqueous solution-suspension of Au NPs was centrifuged to form a pellet. A solution of thiols in ethanol was mixed with the citrate-stabilized Au NPs. The replacement reaction occurred over 2 h at room temperature. Purification of the thiolate-stabilized Au NPs was performed by three cycles of centrifugation, discarding the supernatant, and resuspending the NPs in ethanol.

ATR-IR analysis of the 40 nm Au NPs showed a hydrogen-bonded carboxylic acid C=O stretch at 1704 cm^{-1}, attributed to the hydrogen-bonded cyclic dimer of carboxylic acid groups between a bound citrate and a citric acid. Another C=O stretch at 1734 cm^{-1} was attributed to the hydrogen-bonded acyclic dimer of carboxylic acid groups (*58*). The antisymmetric stretch of the η^1-carboxylate coordinated to surface Au appeared at 1611 cm^{-1}. The antisymmetric stretch of the η^2-carboxylate coordinated to surface Au in a bidentate fashion appeared at 1540 cm^{-1}. The antisymmetric stretch of the carboxylate attached to the middle quaternary carbon appeared at 1575 cm^{-1}.

In XPS spectroscopy, the carbon 1s peak appeared at 287–291 eV, which is a higher binding energy for a carboxylic acid or carboxylate group than the carbon 1s peak for a hydrocarbon at 284.8 eV. A carbon 1s binding energy was detected at 287.6 eV, assigned to the carboxylate ligand coordinated to Au. The peak at 289.4 eV was assigned to the uncoordinated carboxylic acid group.

Au (Phosphine Oxide)

Cano et al. (*7*) developed Au NPs stabilized by secondary phosphine oxide ligands **L1** to **L6**, shown in Figure 17. These Au NPs are air-stable and catalyze the selective hydrogenation of aldehyde groups over alkene, arene, nitro, and ketone groups.

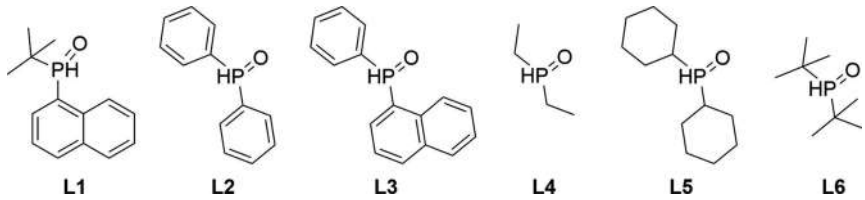

Figure 17. Secondary phosphine oxide ligands as stabilizers for Au NPs.

Pentavalent secondary phosphine oxide ($R_2HP{=}O$) is at a tautomeric equilibrium with the trivalent phosphinous acid ($R_2P–OH$). The phosphine oxide form is more stable than the phosphinous acid form. In general, the equilibrium shifts to the phosphinous acid form in the presence of a metal, due to the formation of a metal–phosphorus bond. Removal of a proton of phosphinous acid gives an oxygen-centered anion, which is capable of carrying out an outer-sphere heterolytic cleavage of dihydrogen. This reaction produces a metal hydride intermediate capable of hydrogenation of aldehyde.

NPs with different sizes and various secondary phosphine surface ligands were made by varying only the ligand and using otherwise identical reaction conditions. Different Au NPs ranging from

1.2 to 2.2 nm were made using ligands **L1** to **L5** at ambient temperature over 15 h and in aqueous THF solvent. The very bulky ligand **L6** failed to stabilize Au NPs; Au precipitated with **L6** instead of forming NPs. Two-coordinate gold complexes ligated by chloride and different secondary phosphine ligands served as the source of both metal and ligand. The reduction of Au^{I} complex to metallic Au NPs was carried out by 14 equivalents of $NaBH_4$. The NPs were purified by three cycles of centrifugation, removal of the supernatant, and resuspension. Residual solvent was removed under vacuum. TEM analyses showed that the NPs had a narrow size distribution. For example, **L1** gave 1.24 ± 0.16 nm NPs, and **L2** gave 1.6 ± 0.16 nm NPs.

Quantitative EA, TGA, and EDX were carried out. The Au NPs stabilized by various secondary phosphine ligands consisted of 44–66% gold and a large amount of ligand. For example, Au NPs stabilized by **L1** contained carbon in 35.12%, hydrogen in 5.35%, phosphorous in 4.42%, and gold in 46.28%. EDX detected carbon in 33.93%, oxygen in 4.79%, gold in 47.00%, and phosphorous in 5.54%. TGA detected up to 52.72% of organic ligands.

The authors reported a metal-to-ligand ratio of 1.48:1 for the NPs stabilized by **L1**, without fully disclosing the details. The ratio was probably calculated using the Au/P mole ratio. The metal-to-ligand ratio calculated based solely on the mole of Au divided by the mole of P was 1.64:1 using the data obtained from the EA. The ratio was instead 1.33:1 when using the EDX data. The average of these two values is 1.49:1. The average empirical formula of the NPs based on the TGA alone can be estimated as $Au_{1.06}$ **L1**$_1$ with an Au-to-ligand ratio of 1.06:1, which assumes that all mass loss during thermolysis is due to the desorption of phosphine ligand and that no other ligand is present. Cano et al. reported ratios ranging from 1.32:1 to 2.88:1 for the five samples of Au NPs.

Modeling studies by van Hardeveld and Hartog calculated the number of surface atoms corresponding to the size of metal crystals in hcp, body-centered cubic (bcc), or cubic close-packed (ccp) structures (*44*). Cano et al. found a close to 1:1 ratio of surface metal atoms versus ligands for NPs made using **L1** to **L4**. This result suggests that the surface ligand coverage, calculated by the number of surface atoms divided by the number of ligands, is 100%. For the 2.2 nm NPs stabilized by **L4**, the 100% coverage is more than twice the ligand coverage of the Au (dodecylthiolate) NPs with a similar size (*27*).

This much higher ligand coverage of **L4** may be rationalized by a much smaller ligand footprint of the secondary phosphine and a greater surface area of Au NPs stabilized by secondary phosphine oxide ligand **L4** than Au NPs, which are the same size but are stabilized by dodecylthiolates.

XPS analyses of the NPs stabilized by **L1** and **L2** gave 84.8 and 84.9 eV, significantly higher than the thiolate-stabilized Au NPs of similar size at 84.0 eV or 83.8 eV. Binding energy of Au^{I} species ranges from 85.5 to 86 eV. The binding energies of Au NPs stabilized by **L1** and **L2** approached the value of a Au^{I} species. The binding energy was calibrated using the $3d_{5/2}$ line of Ag with a FWHM of 0.8 eV. Therefore, the authors suggested that the phosphine-stabilized Au NPs consist of a mixture of Au^{I} and Au^{0} species.

Summary

IR, NMR, and elemental analyses are the most general methods to characterize stabilizers. All examples involve at least one of these techniques, and Table 1 summarizes these approaches to characterizing NP stabilizers.

The elemental composition of NP stabilizers can be identified and quantified through EA, XPS, and EDX. The structure of the stabilizers can be determined using IR, NMR, XPS, MS, and titration. With the help of a quantitative model of NPs, the ligand coverage can be calculated, or estimated, using EA or TGA. NMR and IR studies have been used to distinguish coordinated surface ligands from uncoordinated surface stabilizers.

The average empirical formula of NPs, including stabilizers, can be calculated from EA or TGA. The average molecular formula can be measured directly using ultracentrifugation or calculated using the average core size of NPs and the average empirical formula of NPs.

New strategies have been developed to synthesize thiolate-stabilized NPs using S-alkanethiosulfate ligand precursors [in the sections on the Pd and Ir (dodecylthiolate) NPs]. As techniques evolve and interest in identifying stabilizers grows, new stabilizers are revealed even for NPs initially reported years ago [in the sections on the Pt (carbonyl and hydroxide) and Au (citrate, citric acid, and thiolate) NPs]. Multiple species can costabilize the NPs [in the sections on the Rh (NHC), Pt, and Au (citrate, citric acid, and thiolate) NPs]. NHC and secondary phosphine oxide ligands, which are well known for homogeneous catalysts (*51*) but unconventional for NPs, are currently being explored as stabilizers of well-defined metallic NP catalysts {in the sections on the Ru (NHC), Rh (NHC), Rh [bis(imino)pyridine], Pt (NHC), and Au (phosphine oxide) NPs}.

Characterizing the stabilizers on metallic NPs is difficult and has yet to become a common practice. FT-IR spectroscopy is an accessible and sensitive technique, but the spectrum can be misinterpreted when the fingerprint region is crowded. An FT-IR analysis should be corroborated by an orthogonal method (e.g., EA or XPS).

EA is routinely used to characterize metal complexes but rarely performed on NPs. An investigator should discard the assumption that metallic NPs have the same composition as bulk metal, free of stabilizers and made of nearly 100% metal. Nanomaterials can have different structures, compositions, and properties from their bulk counterparts (*1*).

The accuracy of an XPS binding energy measurement depends on the reference material used for instrument calibration. The carbon 1s peak, from adventitious carbon under ultrahigh vacuum conditions, is often the reference with a binding energy at 284.7 eV (*59*), but the value can vary by 1 eV or more (*59*). This is a significant variation when used to distinguish the oxidation states. In addition, the adventitious carbon signal can overlap with the carbon peaks of the organic stabilizers. Alternatively, sputtered gold or a piece of gold foil as an XPS support material is a common reference, giving the Au $4f_{7/2}$ peak at 83.98 eV (*59*). Cu $2p_{3/2}$ at 932.66 eV and Ag $3d_{5/2}$ at 368.26 eV are also common references.

Solution-phase proton NMR spectroscopy has been used successfully for characterizations of the stabilizers on semiconductor NPs (quantum dots), and DOSY, one-dimensional and 2D NOESY, and rotating-frame Overhauser spectroscopy have also been implemented (*45*). Progress using NMR spectroscopy on noble metallic NPs was reported in 2015 (*60*). The solution-phase ^{1}H NMR spectra of the dodecylthiolate ligand for Pd, Ir, and Au NPs have very broad signals for the methylene protons that are overlapped. The chemical shifts for the protons at the α- and β-positions can be broadened beyond recognition. However, the methyl peaks of dodecylthiolate are relatively sharp, and the line widths (FWHM) increase with the core size of Au NPs (*27*). Moreover, a DOSY study was carried out for the Pt(NHC) NPs costabilized by NHC ligand and a bis-NHC Pt complex, which is likely physically adsorbed onto the NPs (*53*). The latter gave very sharp chemical shifts. The chemical shifts of the NHC protons were well separated. Similar diffusion coefficients, 2.5×10^{-10} versus 2.8×10^{-10} m^2/s, were respectively determined for the two stabilizers.

Table 1. Summary and References of the Stabilizer Characterizations

	Compositional Analysis	
EA	Ru (Phosphine), Ru (NHC), Ir (Polyoxoanion), Pt (Carbonyl and Hydroxide), and Au (Phosphine Oxide)	(*7*, *29*, *32*, *36*, *37*)
XPS	Ru (Phosphine), Ir (Dodecylthiolate), Ir (Citrate), Pt (Carbonyl and Hydroxide),and Au (Citrate, Citric Acid, and Thiolate)	(*16*, *25*, *29*, *37*, *58*)
EDX	Au (Phosphine Oxide)	(*7*)
	Structural Analysis	
IR, NMR, XPS, or MS	Ru (Phosphine), Ru (NHC), Rh (NHC), Pd (Dodecylthiolate), Ir (Dodecylthiolate), Ir (Polyoxoanion), Ir (Citrate), Pt (Carbonyl and Hydroxide), Pt (Amine or Pyridine), Pt (NHC), Au (Dodecylthiolate), and Au (Citrate, Citric Acid, and Thiolate)	(*4*, *16*, *25–28*, *32*, *36*, *37*, *49*, *52*, *53*)
	Ligand Coverage Analysis	
EA or TGA	Pd (Dodecylthiolate), Pd (Alkylthiolate and Arylthiolate), Ir (Dodecylthiolate), Au (Dodecylthiolate), and Au (Phosphine Oxide)	(*7*, *11*, *20*, *25–27*, *47*)
Hydride Titration	Ru (NHC) and Rh (NHC)	(*4*, *36*)
Modeling Studies	Ru (NHC), Rh (NHC), Pd (Dodecylthiolate), Pd (Alkylthiolate and Arylthiolate), Ir (Polyoxoanion), Au (Dodecylthiolate), and Au (Phosphine Oxide)	(*4*, *7*, *26*, *27*, *32*, *36*)
	Determination of Average Empirical or Molecular Formula	
EA	Ir (Polyoxoanion)	(*32*)
TGA	Pd (Dodecylthiolate) and Au (Dodecylthiolate)	(*26*, *27*)
Ultra-Centrifugation	Ir (Polyoxoanion)	(*32*)

The solid-state ^{13}C NMR spectrum of NP stabilizers can have relatively sharp peaks, but the technique has yet to be widely used for the characterizations of the stabilizers. The $^{1}H–^{13}C$ cross-polarization in solid-state ^{13}C NMR spectroscopy can increase signal-to-noise ratio and reduce experiment time (*61*); however, the $^{1}H–^{13}C$ cross-polarization cannot be carried out without hydrogen (*61*). The quaternary carbene carbon in the NHC-stabilized Ru, Rh, and Pt NPs were only detected using NPs made with ^{13}C-labeled NHC ligands. For a comprehensive discussion on solid-state NMR spectroscopy, readers are referred to the book *Solid-State NMR: Basic Principles and Practice* (*58*).

The NMR Knight shift, named after Walter Knight (*62*), refers to the coupling of a nucleus by the unpaired conduction electrons on the metallic NP surface. The carbonic–carbon signal of the NHC-stabilized 3.8 nm Pd NPs was shifted downfield dramatically to 600 ppm and severely broadened (*36*), which was attributed to the Knight shift. The downfield shift and peak broadening were consistent with a surface Pd–C bond. For further reading on the NMR Knight shift in noble metal NPs, please refer to the review article by Marbella et al. (*60*).

The direct characterizations of the metal hydrides on metallic NPs are rare, but the species is likely an important intermediate in catalysis. The proton chemical shifts of metal hydrides on Ru NPs could not be observed directly by NMR spectroscopy (*38*). The hydrides are identified by titrating the Ru NPs with an olefin, where a hydrogenation reaction occurred in the absence of H_2. Notably, the protons of hydroxide ligands on anatase TiO_2 nanocrystals have been studied by Jeantelot et al. using solid-state ^1H NMR spectroscopy (*63*).

Currently, the average molecular formula of metallic NPs is rarely determined or estimated (*26*, *32*). The direct measurement or estimate of the average molecular weight of metallic NPs is extremely rare, but possible approaches include ultracentrifugation (*32*), static light scattering (*64*), and polyacrylamide gel electrophoresis (*65*). Time-of-flight mass spectrometry has emerged as a technique for the characterizations of relatively complex organic stabilizers on NPs (*66*). The field of computational chemistry has grown rapidly, but in general, computational studies have yet to be implemented for the stabilizers in this chapter. The development of computational methods for nanomaterials appears to have a fascinating outlook (*67*).

References

1. Cao, G.; Wang, Y. *Nanostructures and Nanomaterials: Synthesis, Properties, and Applications*; World Scientific: Singapore, 2011.
2. Ott, L. S.; Finke, R. G. Transition-Metal Nanocluster Stabilization for Catalysis: A Critical Review of Ranking Methods and Putative Stabilizers. *Coord. Chem. Rev.* **2007**, *251*, 1075–1100.
3. Alley, W. M.; Hamdemir, I. K.; Johnson, K. A.; Finke, R. G. Ziegler-Type Hydrogenation Catalysts Made from Group 8–10 Transition Metal Precatalysts and Alr3 Cocatalysts: A Critical Review of the Literature. *J. Mol. Catal., A: Chem.* **2010**, *315*, 1–27.
4. Martinez-Espinar, F.; Blondeau, P.; Nolis, P.; Chaudret, B.; Claver, C.; Castillón, S.; Godard, C. NHC-Stabilised Rh Nanoparticles: Surface Study and Application in the Catalytic Hydrogenation of Aromatic Substrates. *J. Catal.* **2017**, *354*, 113–127.
5. Chadha, R.; Das, A.; Maiti, N.; Kapoor, S. Synthesis of Silver Nanoparticles: Effects of Anionic Ligands on Formation and Catalytic Activity. *Mater. Chem. Phys.* **2014**, *148*, 1124–1130.
6. San, K. A.; Chen, V.; Shon, Y.-S. Preparation of Partially Poisoned Alkanethiolate-Capped Platinum Nanoparticles for Hydrogenation of Activated Terminal Alkynes. *ACS Appl. Mater. Interfaces* **2017**, *9*, 9823–9832.
7. Cano, I.; Huertos, M. A.; Chapman, A. M.; Buntkowsky, G.; Gutmann, T.; Groszewicz, P. B.; van Leeuwen, P. W. N. M. Air-Stable Gold Nanoparticles Ligated by Secondary Phosphine Oxides as Catalyst for the Chemoselective Hydrogenation of Substituted Aldehydes: A Remarkable Ligand Effect. *J. Am. Chem. Soc.* **2015**, *137*, 7718–7727.
8. Morsbach, E.; Brauns, E.; Kowalik, T.; Lang, W.; Kunz, S.; Bäumer, M. Ligand-Stabilized Pt Nanoparticles (NPs) as Novel Materials for Catalytic Gas Sensing: Influence of the Ligand on Important Catalytic Properties. *Phys. Chem. Chem. Phys.* **2014**, *16*, 21243–21251.
9. Zhou, L.; He, B.; Huang, J. One-Step Synthesis of Robust Amine- and Vinyl-Capped Magnetic Iron Oxide Nanoparticles for Polymer Grafting, Dye Adsorption, and Catalysis. *ACS Appl. Mater. Interfaces* **2013**, *5*, 8678–8685.

10. Jansat, S.; Picurelli, D.; Pelzer, K.; Philippot, K.; Gómez, M.; Muller, G.; Lecante, P.; Chaudret, B. Synthesis, Characterization and Catalytic Reactivity of Ruthenium Nanoparticles Stabilized by Chiral N-Donor Ligands. *New J. Chem.* **2006**, *30*, 115–122.
11. Maung, M. S.; Dinh, T.; Salazar, C.; Shon, Y.-S. Unsupported Micellar Palladium Nanoparticles for Biphasic Hydrogenation and Isomerization of Hydrophobic Allylic Alcohols in Water. *Colloids Surf. A* **2017**, *513*, 367–372.
12. Lawrence, K. N.; Dutta, P.; Nagaraju, M.; Teunis, M. B.; Muhoberac, B. B.; Sardar, R. Dual Role of Electron-Accepting Metal-Carboxylate Ligands: Reversible Expansion of Exciton Delocalization and Passivation of Nonradiative Trap-States in Molecule-Like Cdse Nanocrystals. *J. Am. Chem. Soc.* **2016**, *138*, 12813–12825.
13. Ikenberry, M.; Peña, L.; Wei, D.; Wang, H.; Bossmann, S. H.; Wilke, T.; Wang, D.; Komreddy, V. R.; Rillema, D. P.; Hohn, K. L. Acid Monolayer Functionalized Iron Oxide Nanoparticles as Catalysts for Carbohydrate Hydrolysis. *Green Chem.* **2014**, *16*, 836–843.
14. Xu, S.; Klama, F.; Ueckermann, H.; Hoogewerff, J.; Clayden, N.; Nann, T. Optical and Surface Characterisation of Capping Ligands in the Preparation of Inp/Zns Quantum Dots. *Sci. Adv. Mater.* **2009**, *1*, 125–137.
15. Sudipa, P.; Subrata, K.; Soumen, B.; Snigdhamayee, P.; Subhra, J.; Surojit, P.; Sujit Kumar, G.; Anjali, P.; Tarasankar, P. Cysteine Functionalized Copper Organosol: Synthesis, Characterization and Catalytic Application. *Nanotechnology* **2006**, *17*, 5461.
16. Cui, M.; Zhao, Y.; Wang, C.; Song, Q. Synthesis of 2.5 nm Colloidal Iridium Nanoparticles with Strong Surface Enhanced Raman Scattering Activity. *Microchim. Acta* **2016**, *183*, 2047–2053.
17. Louie, S. M.; Pettibone, J. M. Research Highlights: Probing Adsorbed Organic Coatings on Nanoparticle Surfaces. *Environ. Sci. Nano*. **2015**, *2*, 417–420.
18. Park, J.-W.; Shumaker-Parry, J. S. Strong Resistance of Citrate Anions on Metal Nanoparticles to Desorption under Thiol Functionalization. *ACS Nano* **2015**, *9*, 1665–1682.
19. San, K.; Shon, Y.-S. Synthesis of Alkanethiolate-Capped Metal Nanoparticles Using Alkyl Thiosulfate Ligand Precursors: A Method to Generate Promising Reagents for Selective Catalysis. *Nanomaterials* **2018**, *8*, 346.
20. Maung, M. S.; Shon, Y.-S. Effects of Noncovalent Interactions on the Catalytic Activity of Unsupported Colloidal Palladium Nanoparticles Stabilized with Thiolate Ligands. *J. Phys. Chem. C* **2017**, *121*, 20882–20891.
21. Chen, T.-A.; Shon, Y.-S. Alkanethiolate-Capped Palladium Nanoparticles for Selective Catalytic Hydrogenation of Dienes and Trienes. *Catal. Sci. Technol.* **2017**, *7*, 4823–4829.
22. Abroshan, H.; Li, G.; Lin, J.; Kim, H. J.; Jin, R. Molecular Mechanism for the Activation of Au25(SCH_2CH_2Ph)18 Nanoclusters by Imidazolium-Based Ionic Liquids for Catalysis. *J. Catal.* **2016**, *337*, 72–79.
23. Zhu, J. S.; Shon, Y.-S. Mechanistic Interpretation of Selective Catalytic Hydrogenation and Isomerization of Alkenes and Dienes by Ligand Deactivated Pd Nanoparticles. *Nanoscale* **2015**, *7*, 17786–17790.
24. Lavenn, C.; Albrieux, F.; Tuel, A.; Demessence, A. Synthesis, Characterization and Optical Properties of an Amino-Functionalized Gold Thiolate Cluster: Au10(Sph-Pnh2)10. *J. Colloid Interface Sci.* **2014**, *418*, 234–239.

25. Gavia, D. J.; Do, Y.; Gu, J.; Shon, Y.-S. Mechanistic Insights into the Formation of Dodecanethiolate-Stabilized Magnetic Iridium Nanoparticles: Thiosulfate vs Thiol Ligands. *J. Phys. Chem. C* **2014**, *118*, 14548–14554.
26. Gavia, D. J.; Shon, Y.-S. Controlling Surface Ligand Density and Core Size of Alkanethiolate-Capped Pd Nanoparticles and Their Effects on Catalysis. *Langmuir* **2012**, *28*, 14502–14508.
27. Hostetler, M. J.; Wingate, J. E.; Zhong, C.-J.; Harris, J. E.; Vachet, R. W.; Clark, M. R.; Londono, J. D.; Green, S. J.; Stokes, J. J.; Wignall, G. D.; Glish, G. L.; Porter, M. D.; Evans, N. D.; Murray, R. W. Alkanethiolate Gold Cluster Molecules with Core Diameters from 1.5 to 5.2 nm: Core and Monolayer Properties as a Function of Core Size. *Langmuir* **1998**, *14*, 17–30.
28. Schrader, I.; Warneke, J.; Neumann, S.; Grotheer, S.; Swane, A. A.; Kirkensgaard, J. J. K.; Arenz, M.; Kunz, S. Surface Chemistry of "Unprotected" Nanoparticles: A Spectroscopic Investigation on Colloidal Particles. *J. Phys. Chem. C* **2015**, *119*, 17655–17661.
29. Wang, Y.; Ren, J.; Deng, K.; Gui, L.; Tang, Y. Preparation of Tractable Platinum, Rhodium, and Ruthenium Nanoclusters with Small Particle Size in Organic Media. *Chem. Mater.* **2000**, *12*, 1622–1627.
30. Folkman, S. J.; Zhou, M.; Nicki, M.; Finke, R. G. Alcohol Solvent Effects in the Synthesis of Co_3O_4 Metal-Oxide Nanoparticles: Disproof of a Surface-Ligand Thermodynamic Effect En Route to Alternative Kinetic and Thermodynamic Explanations. *Inorg. Chem.* **2018**, *57*, 1517–1526.
31. Brust, M.; Walker, M.; Bethell, D.; Schiffrin, D. J.; Whyman, R. Synthesis of Thiol-Derivatised Gold Nanoparticles in a Two-Phase Liquid–Liquid System. *J. Chem. Soc., Chem. Commun.* **1994**, 801–802.
32. Lin, Y.; Finke, R. G. Novel Polyoxoanion- and Bu_4^{n+}-Stabilized, Isolable, and Redissolvable, 20–30–.Ang. Ir300–900 Nanoclusters: The Kinetically Controlled Synthesis, Characterization, and Mechanism of Formation of Organic Solvent-Soluble, Reproducible Size, and Reproducible Catalytic Activity Metal Nanoclusters. *J. Am. Chem. Soc.* **1994**, *116*, 8335–8353.
33. Deviney, M. L.; Gland, J. L. *Catalyst Characterization Science: Surface and Solid State Chemistry*; American Chemical Society: Washington, D.C., 1985.
34. Johnson, G. E.; Laskin, J. Understanding Ligand Effects in Gold Clusters Using Mass Spectrometry. *Analyst* **2016**, *141*, 3573–3589.
35. Chaudret, B. Organometallic Chemistry and Nanoparticles. *Actual. Chim.* **2005**, *290–291*, 33–43.
36. Lara, P.; Rivada-Wheelaghan, O.; Conejero, S.; Poteau, R.; Philippot, K.; Chaudret, B. Ruthenium Nanoparticles Stabilized by N-Heterocyclic Carbenes: Ligand Location and Influence on Reactivity. *Angew. Chem.* **2011**, *123*, 12286–12290.
37. Martínez-Prieto, L. M.; Carenco, S.; Wu, C. H.; Bonnefille, E.; Axnanda, S.; Liu, Z.; Fazzini, P. F.; Philippot, K.; Salmeron, M.; Chaudret, B. Organometallic Ruthenium Nanoparticles as Model Catalysts for Co Hydrogenation: A Nuclear Magnetic Resonance and Ambient-Pressure X-Ray Photoelectron Spectroscopy Study. *ACS Catal.* **2014**, *4*, 3160–3168.
38. Martínez-Prieto, L. M.; Chaudret, B. Organometallic Ruthenium Nanoparticles: Synthesis, Surface Chemistry, and Insights into Ligand Coordination. *Acc. Chem. Res.* **2018**, *51*, 376–384.

39. Rakers, L.; Martínez-Prieto, L. M.; López-Vinasco, A. M.; Philippot, K.; van Leeuwen, P. W. N. M.; Chaudret, B.; Glorius, F. Ruthenium Nanoparticles Ligated by Cholesterol-Derived NHCs and Their Application in the Hydrogenation of Arenes. *Chem. Commun.* **2018**, *54*, 7070–7073.
40. Lara, P.; Ayvalı, T.; Casanove, M.-J.; Lecante, P.; Mayoral, A.; Fazzini, P.-F.; Philippot, K.; Chaudret, B. On the Influence of Diphosphine Ligands on the Chemical Order in Small Rupt Nanoparticles: Combined Structural and Surface Reactivity Studies. *Dalton Trans.* **2013**, *42*, 372–382.
41. Dragutan, V.; Dragutan, I.; Demonceau, A. Ruthenium Complexes Bearing N-Heterocyclic Carbene (NHC) Ligands. *Platinum Met. Rev.* **2005**, *49*, 183–188.
42. Zhukhovitskiy, A. V.; MacLeod, M. J.; Johnson, J. A. Carbene Ligands in Surface Chemistry: From Stabilization of Discrete Elemental Allotropes to Modification of Nanoscale and Bulk Substrates. *Chem. Rev.* **2015**, *115*, 11503–11532.
43. Martínez-Prieto, L. M.; Ferry, A.; Rakers, L.; Richter, C.; Lecante, P.; Philippot, K.; Chaudret, B.; Glorius, F. Long-Chain NHC-Stabilized Runps as Versatile Catalysts for One-Pot Oxidation/Hydrogenation Reactions. *Chem. Commun.* **2016**, *52*, 4768–4771.
44. Van Hardeveld, R.; Hartog, F. The Statistics of Surface Atoms and Surface Sites on Metal Crystals. *Surf. Sci.* **1969**, *15*, 189–230.
45. Hens, Z.; Martins, J. C. A Solution Nmr Toolbox for Characterizing the Surface Chemistry of Colloidal Nanocrystals. *Chem. Mater.* **2013**, *25*, 1211–1221.
46. Buil, M. L.; Esteruelas, M. A.; Niembro, S.; Oliván, M.; Orzechowski, L.; Pelayo, C.; Vallribera, A. Dehalogenation and Hydrogenation of Aromatic Compounds Catalyzed by Nanoparticles Generated from Rhodium Bis(Imino)Pyridine Complexes. *Organometallics* **2010**, *29*, 4375–4383.
47. Gavia, D. J.; Maung, M. S.; Shon, Y.-S. Water-Soluble Pd Nanoparticles Synthesized from Ω-Carboxyl-S-Alkanethiosulfate Ligand Precursors as Unimolecular Micelle Catalysts. *ACS Appl. Mater. Interfaces* **2013**, *5*, 12432–12440.
48. Pearce, K.; Creamer, L. The Complete Ionization Scheme for Citric Acid. *Aust. J. Chem.* **1975**, *28*, 2409–2415.
49. Altmann, L.; Kunz, S.; Bäumer, M. Influence of Organic Amino and Thiol Ligands on the Geometric and Electronic Surface Properties of Colloidally Prepared Platinum Nanoparticles. *J. Phys. Chem. C* **2014**, *118*, 8925–8932.
50. Conley, R. T. *Infrared Spectroscopy*, 2nd ed.; Allyn and Bacon: Boston, 1972.
51. Crabtree, R. H. *The Organometallic Chemistry of the Transition Metals*; Wiley: Hoboken, NJ, 2014.
52. Morsbach, E.; Spéder, J.; Arenz, M.; Brauns, E.; Lang, W.; Kunz, S.; Bäumer, M. Stabilizing Catalytically Active Nanoparticles by Ligand Linking: Toward Three-Dimensional Networks with High Catalytic Surface Area. *Langmuir* **2014**, *30*, 5564–5573.
53. Baquero, E. A.; Tricard, S.; Flores, J. C.; de Jesús, E.; Chaudret, B. Highly Stable Water-Soluble Platinum Nanoparticles Stabilized by Hydrophilic N-Heterocyclic Carbenes. *Angew. Chem., Int. Ed.* **2014**, *53*, 13220–13224.
54. Grote, C.; Cheema, T. A.; Garnweitner, G. Comparative Study of Ligand Binding During the Postsynthetic Stabilization of Metal Oxide Nanoparticles. *Langmuir* **2012**, *28*, 14395–14404.

55. Edward, J. T. Molecular Volumes and the Stokes-Einstein Equation. *J. Chem. Educ.* **1970**, *47*, 261.
56. Porter, M. D.; Bright, T. B.; Allara, D. L.; Chidsey, C. E. D. Spontaneously Organized Molecular Assemblies. 4. Structural Characterization of N-Alkyl Thiol Monolayers on Gold by Optical Ellipsometry, Infrared Spectroscopy, and Electrochemistry. *J. Am. Chem. Soc.* **1987**, *109*, 3559–3568.
57. Al-Johani, H.; Abou-Hamad, E.; Jedidi, A.; Widdifield, C. M.; Viger-Gravel, J.; Sangaru, S. S.; Gajan, D.; Anjum, D. H.; Ould-Chikh, S.; Hedhili, M. N.; Gurinov, A.; Kelly, M. J.; El Eter, M.; Cavallo, L.; Emsley, L.; Basset, J.-M. The Structure and Binding Mode of Citrate in the Stabilization of Gold Nanoparticles. *Nat. Chem.* **2017**, *9*, 890–895.
58. Park, J.-W.; Shumaker-Parry, J. S. Structural Study of Citrate Layers on Gold Nanoparticles: Role of Intermolecular Interactions in Stabilizing Nanoparticles. *J. Am. Chem. Soc.* **2014**, *136*, 1907–1921.
59. Wagner, J. M. *X-Ray Photoelectron Spectroscopy*; Nova Science Publishers, Incorporated: Hauppauge, NY, 2010.
60. Marbella, L. E.; Millstone, J. E. NMR Techniques for Noble Metal Nanoparticles. *Chem. Mater.* **2015**, *27*, 2721–2739.
61. Apperley, D. C.; Harris, R. K.; Hodgkinson, P. *Solid-State NMR: Basic Principles and Practice*; Momentum Press: New York, 2012.
62. Knight, W. D. Nuclear Magnetic Resonance Shift in Metals. *Phys. Rev.* **1949**, *76*, 1259–1260.
63. Jeantelot, G.; Ould-Chikh, S.; Sofack-Kreutzer, J.; Abou-Hamad, E.; Anjum, D. H.; Lopatin, S.; Harb, M.; Cavallo, L.; Basset, J.-M. Morphology Control of Anatase TiO_2 for Well-Defined Surface Chemistry. *Phys. Chem. Chem. Phys.* **2018**, *20*, 14362–14373.
64. Brar, S. K.; Verma, M. Measurement of Nanoparticles by Light-Scattering Techniques. *TrAC, Trends Anal. Chem.* **2011**, *30*, 4–17.
65. Weber, K.; Osborn, M. The Reliability of Molecular Weight Determinations by Dodecyl Sulfate-Polyacrylamide Gel Electrophoresis. *J. Biol. Chem.* **1969**, *244*, 4406–4412.
66. Zhou, H.; Li, X.; Lemoff, A.; Zhang, B.; Yan, B. Structural Confirmation and Quantification of Individual Ligands from the Surface of Multi-Functionalized Gold Nanoparticles. *Analyst* **2010**, *135*, 1210–1213.
67. Woodley, S. M.; Bromley, S. T. *Introduction to Modeling Nanoclusters and Nanoparticles. In Frontiers of Nanoscience*; Bromley, S. T., Woodley, S. M. , Eds.; Elsevier: Amsterdam, Kidlington, and Cambridge, 2018; Vol. 12, pp 1–54.

Chapter 7

TiO_2 Nanomaterials for Enhanced Photocatalysis

Tao Peng and Jerald A. Lalman*

Department of Civil and Environmental Engineering, University of Windsor, 401 Sunset Avenue, Windsor, Ontario N9B 3P4, Canada

***E-mail: lalman@uwindsor.ca**

This chapter discusses Titanium dioxide (TiO_2) fabrication and its photocatalytic application. The review examines the basic principles of photocatalytic H_2 production, degradation of pollutants, CO_2 reduction, and N_2 reduction using TiO_2 photocatalysts under ultraviolet light conditions. The focus includes synthesis and modification of TiO_2 nanophotocatalysts for improved photocatalytic applications. The synthesis methods examined contains the sol–gel, sol, hydrothermal, solvothermal, vapor deposition, electrochemical, direct oxidation, surfactant controlled, and the plasma-assisted process. The photocatalytic activities of pure TiO_2 suffer from limitations such as the fast charge carrier recombination and its wide bandgap of approximately 3.2 eV. Improving the photocatalytic activities of TiO_2 has been the focus of many reports. Modifications of TiO_2 consist of changing the crystal structure and morphology, doping with metal and nonmetal chemicals, incorporating carbon materials (carbon nanotubes and graphene), and noncarbon materials (i.e., metals, semiconductors, dyes, and noncarbonaceous two-dimensional materials). Lastly, future prospects are discussed for the application of TiO_2.

Introduction

Titanium dioxide (TiO_2) has been a widely studied semiconducting metal oxide since the discovery of its photocatalytic water splitting on TiO_2 under ultraviolet (UV) irradiation by Fujishima and Honda in 1972 (*1*–*3*). Due to its excellent thermal stability, wide bandgap with suitable band edge, low cost, nontoxic effect, and corrosion resistant properties (*1*), TiO_2 has been used in many promising applications (such as solar harvesting and solar fuel production). The primary applications of photocatalysis include the conversion of water to generate O_2 and H_2 and the photodegradation of aqueous and atmospheric organic pollutants (*1*–*4*). The photocatalytic efficiency of TiO_2 is governed by material properties, the irradiance frequency, and irradiance intensity. In particular, the material

properties dominating photocatalytic activity include bandgap, charge transportation, crystal structure, specific surface area (SSA), and the particles' size (*5*). Understanding these properties and synthesis processes is essential in designing a high-performing photocatalyst.

Developing methods to modify TiO_2 by increasing the SSA, deceasing particle size, and optimizing crystal structure are effective strategies for enhancing the overall photocatalytic reaction efficiency (*1*, *6*–*9*). When compared to bulk TiO_2, nanostructured TiO_2 has novel properties that can be utilized to improve its photocatalytic activities (*10*). TiO_2 nanostructures are particularly interesting due to their high SSA, enhanced charge carrier conductivity, and excellent mechanical strength (*1*).

The photocatalytic activity of pure TiO_2 is limited due to the fast recombination of electrons (e^-) and holes (h^+) pairs (*4*), as well as its wide bandgap of approximately 3.2 eV, which only absorbs UV light (2–3% of the solar spectrum) (*4*, *5*). A wide variety of different methods have been developed to increase the photocatalytic activity of TiO_2. Two important aspects of these methods are based on suppressing charge recombination and extending the wavelength response range in the visible light region (*4*). These approaches include doping TiO_2 nanomaterials with other elements (*5*, *11*, *12*), sensitizing with photosensitizers such as dyes (*11*), depositing metal nanoparticles (*4*, *13*) or coupling with other semiconductors (*14*), and incorporating carbon materials (*15*, *16*).

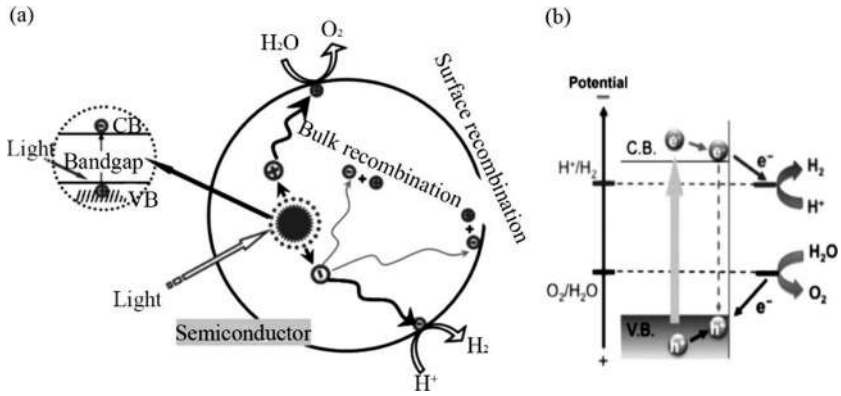

Figure 1. Schematic illustrating water splitting using TiO_2 (17, 20). (a) Charge transfer and recombination during photocatalytic water splitting, and (b) the energy position of the VB and CB. Reproduced with permission from ref (17). Copyright 2014 Elsevier.

Principles of Photocatalysis

The photocatalytic splitting of H_2O into H_2 and O_2 on TiO_2 photocatalysts is shown in Figure 1 (*17*). The three main steps of the process (Figure 1a) consist of: (1) photogeneration of e^- and h^+ when excited by photons with energy greater than the TiO_2 bandgap; (2) transportation of the charge carriers to the TiO_2 surface; and (3) surface charge transfer between carriers with reactants (e.g., H_2O). However, the photogenerated charge carriers may recombine with each other, subsequently dissipating energy without mediating the photocatalytic reaction. Recombination is the major restriction in TiO_2 photocatalysis since it reduces the overall reaction efficiency. In the case of water splitting (Figure 1b), the energy position of the lowest level in the conduction band (CB) is more

negative than the reduction potential of water (0 V versus normal hydrogen electrode [NHE] at pH = 0) ($2H^+ + 2e^- = H_2$) while the valence band's (VB) highest energy level is more positive than the oxidation potential of water (+1.23 V versus NHE at pH = 0) ($4OH^- + 4h^+ = O_2 + 2H_2O$). Photogenerated carriers can also split renewable organic chemicals (e.g., ethanol) to produce H_2 (*18*). In this case, the organic chemical functions as an electron donor. The efficiency can be measured using the gas evolution rate ($\mu mol \cdot h^{-1}$) and the quantum yield, which is defined as the number of events occurring per photon absorbed (*18*, *19*).

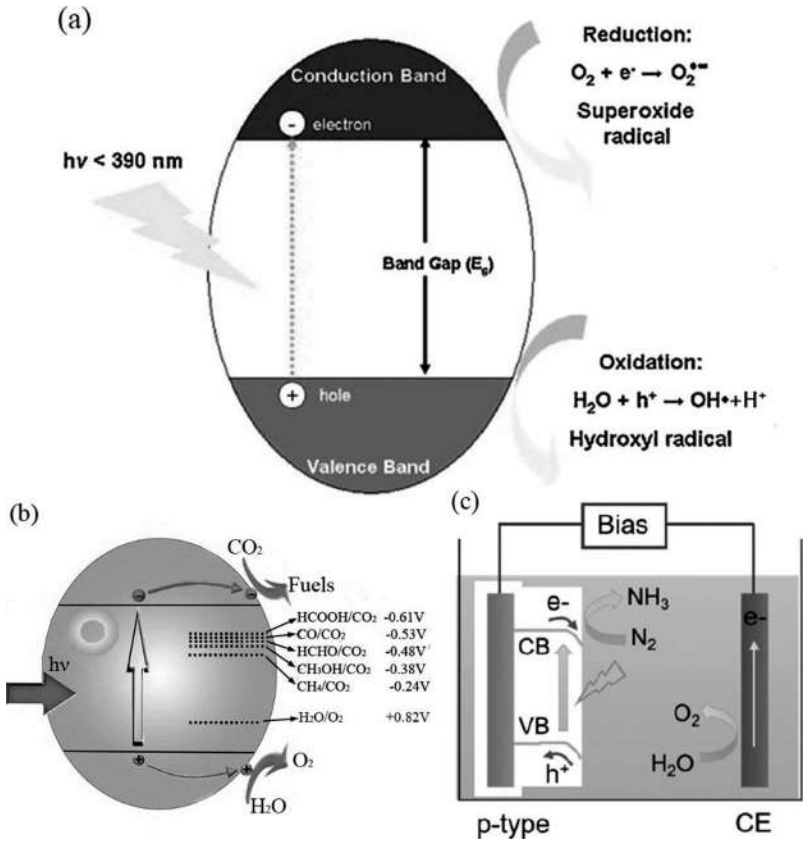

Figure 2. Schematic diagram for the reaction steps in: (a) photodegradation of aqueous organic pollutants (21), (b) photocatalytic CO_2 reduction, and (c) photocatalytic N_2 reduction (24). (a) Reproduced with permission from ref (21). Copyright 2012 Elsevier. (c) Reproduced with permission from ref (24). Copyright 2018 Royal Chemical Society.

In addition to reacting with water and ethanol to produce H_2 and O_2, the photogenerated carriers are able to degrade organic pollutants (*21*), reduce CO_2 to a fuel (*22*, *23*), reduce N_2 to NH_3 (*24*), and disinfect contaminated water. As shown in Figure 2, holes in the VB oxidize water and subsequently generate extremely powerful oxidants such as •OH radicals to oxidize organic pollutants (*21*). Electrons can be transferred to O_2 molecules and generate superoxide radical anions ($O_2^{\bullet-}$), powerful oxidants that can react with organic pollutants to produce CO_2 (*21*).

TiO_2 Nanomaterials Morphologies and Crystallographic Structures

Typical forms of bulk TiO_2 include thin films, powders, and single crystals. To increase the SSA, decreasing the TiO_2 particle size to the nanometer scale leads to nanomaterials such as nanosheets (*6*), nanoparticles, nanorods, nanowires, nanotube, nanofilms, and nanoribbons (*25*). Nanowires and nanofibers are two quasi-one-dimensional (Q1D) structures with diameters less than 100 nm and a specific growth direction, while nanorods and nanowires have similar structures, the length is shorter. Nanotubes have a hollow interior structure while nanobelts and nanoribbons are structurally similar to nanowires, but with well-defined side faces. Models for selected TiO_2 Q1D nanostructures are shown in Figure 3.

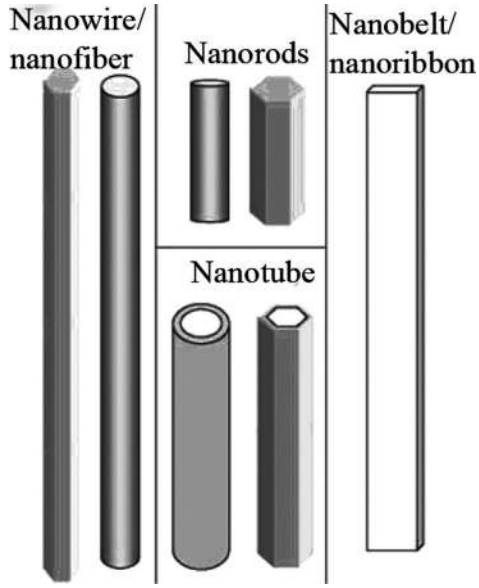

Figure 3. Models for selected TiO_2 Q1D nanostructures.

TiO_2 exists in many different crystal forms, under both standard temperature and pressure conditions, as well as other forms reported under high pressure. These include anatase (tetragonal), rutile (tetragonal), TiO_2–B (monoclinic), brookite (orthorhombic), TiO_2–R (ramsdellite-structured), TiO_2–H (hollandite-structured), TiO_2–II (columbite-type), and TiO_2–III (baddeleyite-type) (*26*). Although anatase, brookite, rutile, and TiO_2–B are known to occur naturally (*26*), the other phases that only exist under high pressure conditions are unstable under ambient conditions (*26*). Rutile is considered the most stable phase based on thermodynamics, whereas the metastable anatase, TiO_2–B, and brookite phases are transformed into rutile when treated at 600–900 °C (*27*). All the various TiO_2 phases are formed by stacking co-coordinated TiO_6 octahedral units with the Ti^{4+} ion positioned in the center of the octahedron and six oxygen atoms located at the six corners. The TiO_6 octahedron stacks oxygen atoms either via edge-sharing or corner-sharing (Figure 4) (*28*). Due to the Jahn–Teller effect, the different phase structures show distinctions in the distortion and assembly pattern of each octahedron and octahedron chain (*29*). The selected properties of anatase, rutile, brookite, and TiO_2–B are shown in Table 1.

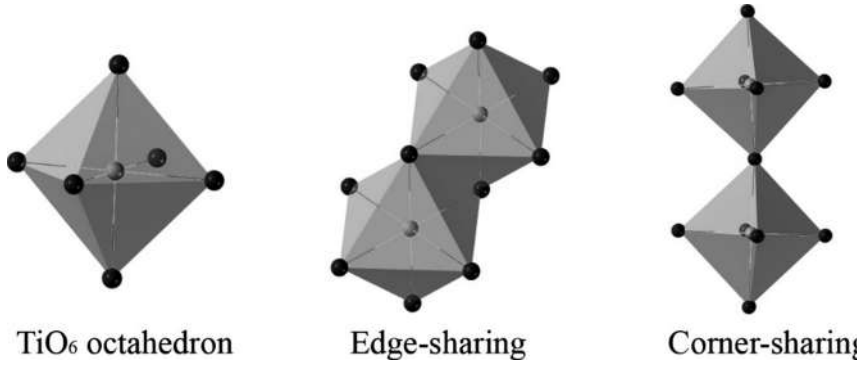

Figure 4. Model of TiO_2 octahedron showing edge-sharing and corner-sharing. Notes: black circles correspond to oxygen atom and grey circles correspond to titanium atom.

Anatase is a tetragonal structure (Figure 5) (*10*) predominantly configured with edge-sharing octahedron (*30*). Each octahedron in anatase has four sharing edges and each O^{2-} ion is closely surrounded by three Ti^{4+} ions. Anatase can be synthesized by employing the wet chemical process (*27*). The wet chemical process usually leads to the formation of anatase nanoparticles because anatase is relatively thermodynamically stable when the size is confined to the nanoscale level (*27*).

Table 1. Properties of Anatase, Rutile, Brookite, and TiO_2–B (*10*, *30*, *31*)

Property	*Anatase*	*Rutile*	*Brookite*	*TiO_2–B*
Crystal structure	Tetragonal	Tetragonal	Orthorhombic	Monoclinic
Space group	$I\frac{4}{a}md$	$P\frac{4_2}{m}nm$	Pbca	$C\frac{2}{m}$
Lattice parameters (Å)	a 3.78, c 9.51	a 4.59, c 2.96	a 5.46, b 9.18, c 5.14	a 1.218, b 3.741, c 6.525, β 107.05°
Bandgap (eV)	3.20	3.01	3.13	3.19
Hardness (Mohs Scale)	5.5–6	6–6.5	5.5–6	Unknown
Solubility in H_2O	Insoluble	Insoluble	Insoluble	Insoluble
Density	3.89	4.25	4.13	Unknown
Melting point (°C)	Converted to rutile	1855	Converted to rutile	Converted to rutile

Rutile also has a tetragonal structural configuration; however, the *c* axis is shorter in comparison to the anatase structure (Figure 6) (*10*). Rutile is composed predominantly of corner-sharing octahedron units (*30*) with octahedral apices connected to each other by edge-sharing chains parallel to the *z* axis and the chains cross-linked in a corner-sharing manner. In the rutile phase, the {011} and {100} crystal face families have the lowest energy, and thus is the most stable phase (Figure 6) (*32*). When compared to the other phases, rutile production through solution phase synthesis or transformation of other phases at 600–900 °C is due primarily to its thermodynamic stability (*27*).

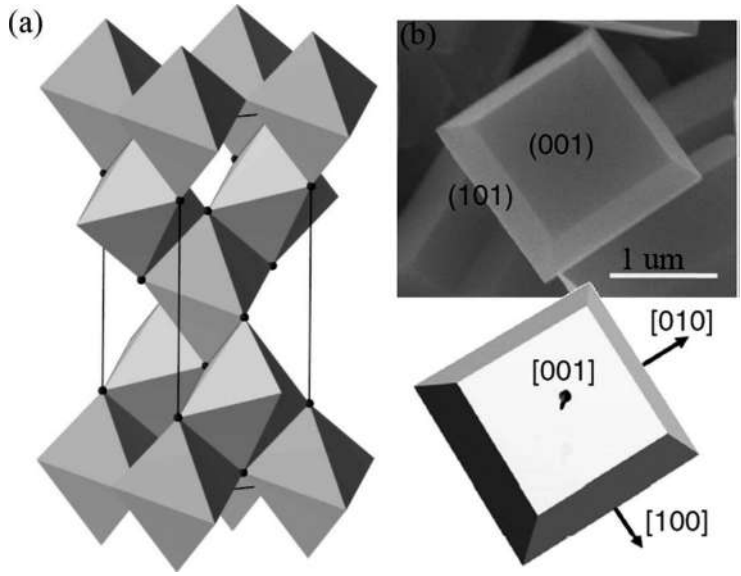

Figure 5. Anatase structure and SEM image: (a) anatase unit cell, and (b) SEM image (up) and the model (below) of truncated octahedron-shaped anatase crystal with exposed {001} and {101} facets (9). Note: black circles indicate oxygen atoms. (b) Reproduced with permission from ref (9). Copyright 2014 Springer Nature.

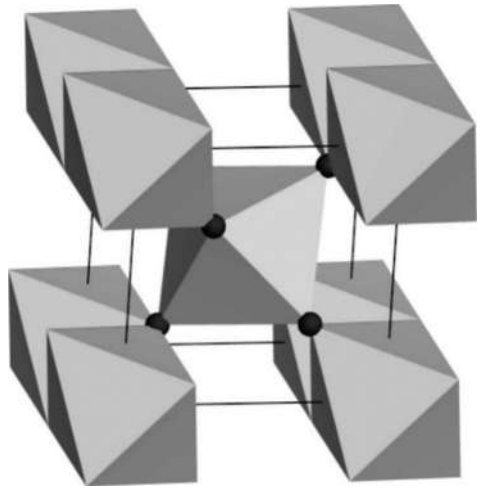

Figure 6. Rutile unit cell. Note: black circle corresponds to oxygen atoms.

TiO_2 brookite orthorhombic structure is composed of large unit cells (Figure 7) (*10*). The structure consists of distorted TiO_6 octahedrons which are connected by both edge- and corner-sharing to construct the framework shown in Figure 7. Although brookite is synthesized through the wet chemical process, it normally coexists with the rutile or anatase phases (*30*).

TiO_2–B is constructed with large unit cells (Figure 8) with a monoclinic structure with a particularly long *a* axis (*32*, *33*). TiO_2–B consists of corrugated sheets with edge- and corner-sharing TiO_6 octahedrons that are stacked to construct a 3D framework. TiO_2–B can be synthesized by proton exchange and subsequent dehydration of the titanate layers at approximately 300 °C (*33*, *34*).

TiO_2–B can be transformed into anatase or rutile at high temperatures because of its thermodynamic instability (*33*, *34*).

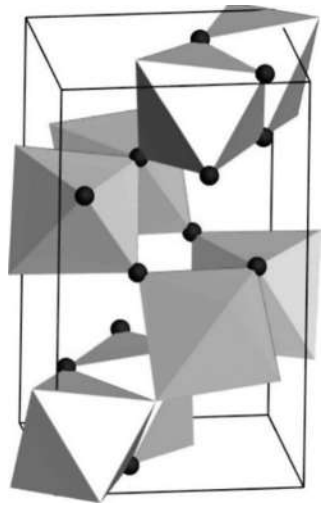

Figure 7. Brookite unit cell.

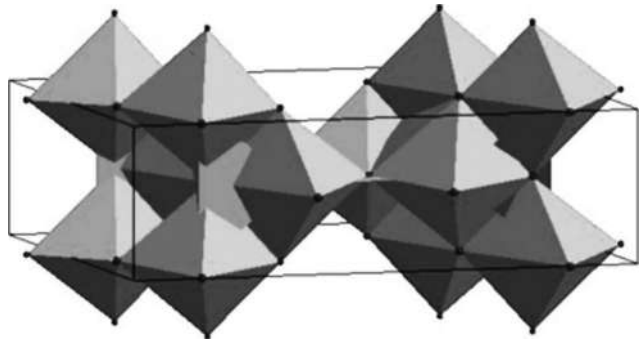

Figure 8. TiO_2–B unit cell (*32*). *Reproduced with permission from ref* (*32*). *Copyright 2014 America Chemical Society.*

TiO_2 Nanomaterials Synthesis

Methods for synthesizing TiO_2 nanostructures include sol–gel, chemical vapor deposition (CVD) and physical vapor deposition (PVD), hydro/solvothermal, direct oxidation, surfactant controlled approach, and the electrochemical route. A brief overview of various methods is discussed in the following sections.

Sol–Gel Method

The sol–gel method is commonly used to synthesize various ceramic materials (*5*). In general, a colloidal suspension is produced from the hydrolysis and polymerization reaction of precursor molecules (*5*). Subsequently, complete polymerization and removal of the solvent leads to the formation of a solid gel phase. The solid gel is then easily cast into the desired shape (e.g., nanofilms and nanofibers). Finally, the wet gel is transformed into TiO_2 by dehydration and heating treatment.

TiO_2 nanomaterials usually result from the hydrolysis of a titanium precursor. In a typical procedure to produce TiO_2 nanoparticles (*5*), a TiO_2 sol solution is produced by slowly mixing a precursor such as titanium isopropoxide in an alcoholic solution containing water. The 3D polymeric skeletons with close packing were developed by forming Ti–O–Ti chains. Next, the mixture is heated at 90–100 °C for 6 h to produce the gel. Subsequently, heating the gel at 400 °C for 2 h increases the crystallinity of the TiO_2 anatase.

Combining the sol–gel method and an anodic alumina membrane template with long nanopores is useful in producing TiO_2 nanowires (Figure 9) (*35*). A brief description of the process involves immersing porous anodic alumina membrane in a boiling TiO_2 sol followed by drying and heating. After heating at 500 °C, the TiO_2 sol is converted into anatase TiO_2. Next, the anodic alumina membrane template is removed by placing the combined TiO_2/alumina membrane template into a H_3PO_4 aqueous solution.

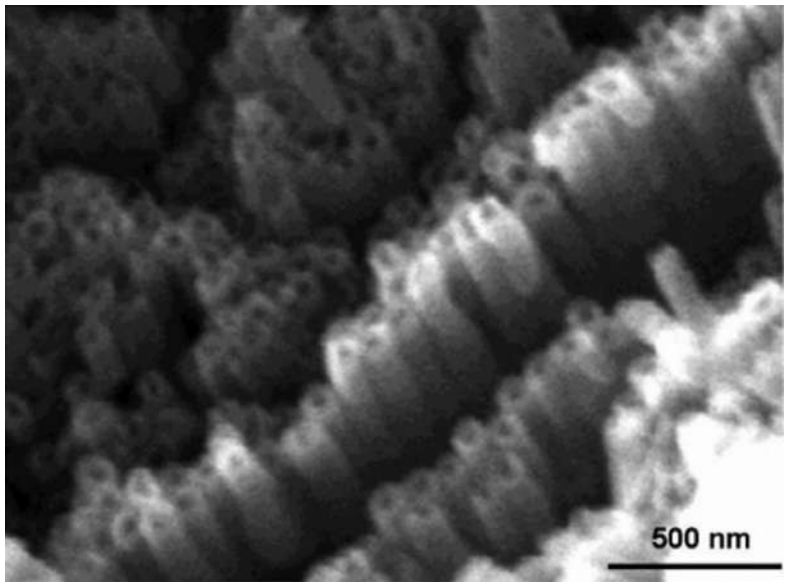

Figure 9. TiO_2 anatase nanotubes SEM image prepared by combining the sol–gel and template methods (35). Notes: synthesized using anodic alumina membrane template and TiO_2 sol, drying and heating at 60 °C for 12 h, and anodic alumina membrane template was removed in a 5wt% H_3PO_4 solution at room temperature for 3 h. Reproduced with permission from ref (35). Copyright 2002 America Chemical Society.

Sol Method

The sol method is a nonhydrolytic sol–gel process. The method involves reacting titanium chloride with a metal alkoxide such as titanium alkoxide where RO^- is an alkoxide (Eq. 1).

$$TiCl_4 + Ti(OR)_4 = 2TiO_2 + 4RCl \ (36) \qquad (1)$$

The reaction results in the formation of Ti–O–Ti bridges. The alkoxide groups are either titanium alkoxides or the products generated by in situ reacting titanium chloride with alcohols. Zhu et al. (*36*) reported mixing TiF_4 with benzyl alcohol to produce an organic-rich titanium precursor.

Next, the mixture is placed in an autoclave at 160 °C for 24 h with the subsequent formation of anatase nanosheets (Figure 10).

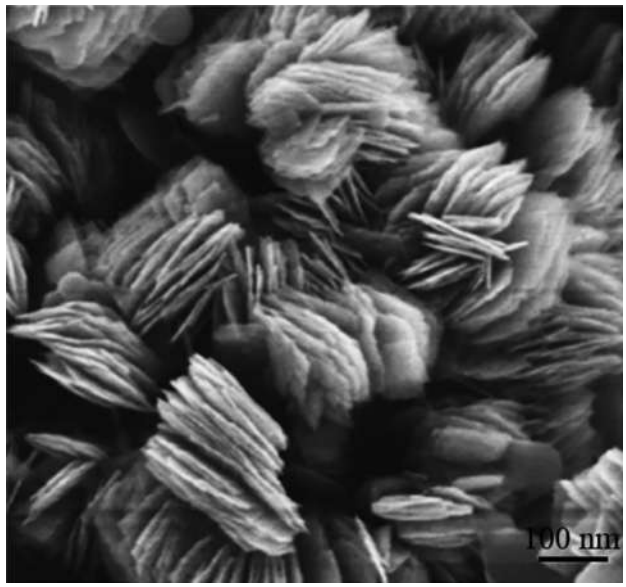

Figure 10. TiO_2 anatase nanosheet SEM image (36). Note: TiO_2 anatase nanosheet was synthesized using TiF_4 and benzyl alcohol at 160 °C for 24 h. Reproduced with permission from ref (36). Copyright 2013 America Chemical Society.

Figure 11. Commercially available, magnetically stirred stainless steel pressure vessel configured with pressure control and an external pump to control the gas flow (37). Reproduced with permission from ref (37). Copyright 2007 Elsevier Ltd.

Hydrothermal Method

Hydrothermal synthesis is extensively employed for producing nanoparticles in the ceramic industry. The method is performed in aqueous solution under selected temperatures and/or pressure conditions. The autoclave reactor consists of stainless steel pressure vessels with or without a Teflon liner (Figure 11). The temperature can be set to 300 °C by controlling the pressure. The morphology

for the prepared TiO_2 nanomaterials depends on the nature of solution, pH value, temperature, and the reaction time (*5*).

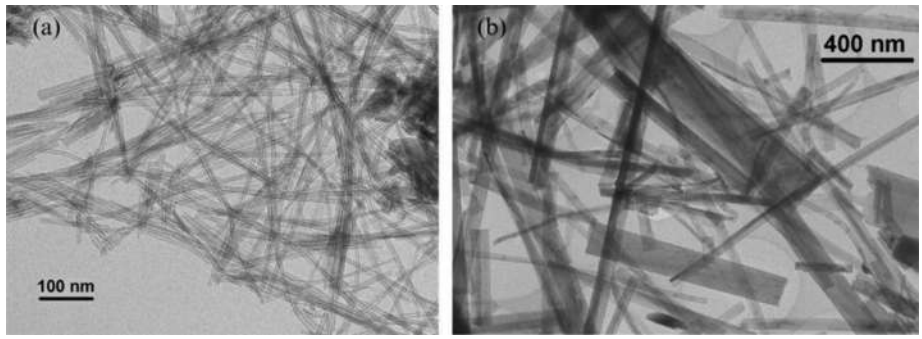

Figure 12. Q1D TiO_2 nanostructure transmission electron microscopy (TEM) images (a) TiO_2 nanotubes produced using 10 M NaOH aqueous solution at 140 °C, and (b) anatase TiO_2 nanowire produced using 10 M NaOH aqueous solution at 190 °C (38). Reproduced with permission from ref (38). Copyright 2004 Royal Society of Chemistry.

Q1D TiO_2 nanomaterials have also been produced using the hydrothermal method (Figure 12). This widely used method employs treating TiO_2 particles in a 5–15 M NaOH aqueous solution at 110–200 °C for 24–120 h (*38–44*). The transformation of TiO_2 powder into nanotubes involves cutting, exfoliation, or delamination of TiO_2 lamellar nanosheets from a crystalline precursor (*39*). The lamellar nanosheets edges have many atoms with dangling bonds that are unstable (*39*). Next, the lamellar nanosheets are bent and scrolled into Q1D nanotubes or nanowire to saturate the dangling bonds (Figure 12) (*39*).

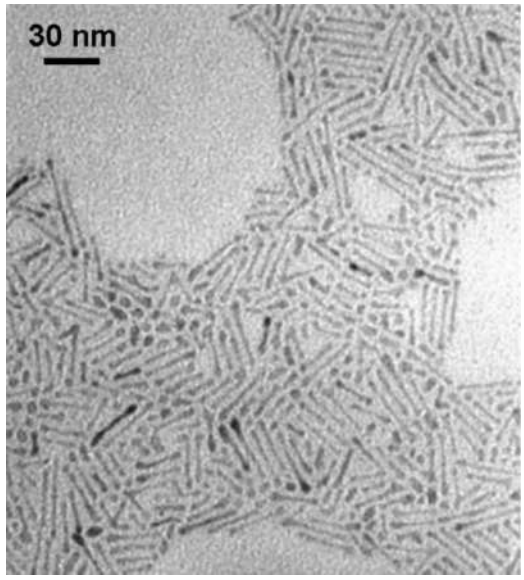

Figure 13. Nanorods TEM image synthesized using a solvothermal method (40). Note: TiO_2 nanorods were synthesized by mixing titanium isopropoxide, anhydrous toluene, and oleic acid at 250 °C for 20 h. Reproduced with permission from ref (40). Copyright 2003 Elsevier.

Solvothermal Method

The solvothermal method is identical to the hydrothermal process in that it uses only a nonaqueous solvent (e.g., toluene). The solvothermal process has better control of the reaction temperature, particle size, morphology, and crystallinity of TiO_2 products (*32*). The temperature can be significantly raised by employing organic solvents with high boiling points. Different solvents with different physical and chemical properties can affect the diffusion behavior, solubility, and reactivity of the reactants, which in turn influences the crystallization and the crystal morphology of the final products (*32*). Kim et al. reported that TiO_2 nanorods were produced by mixing titanium isopropoxide with anhydrous toluene and oleic acid at 250 °C for 20 h (Figure 13) (*40*).

Chemical/Physical Vapor Deposition Method

Vapor deposition involves producing a vapor that is subsequently condensed onto a heated solid surface. The process is usually executed in a vacuum chamber. If the final product does not involve a chemical reaction, the method is designated as PVD; otherwise, the process is designated as a CVD.

Producing TiO_2 nanowires using a simple PVD method is illustrated in the SEM image shown in Figure 14 (*41*). In a typical synthesis process, 1.5 g of precursor material (i.e., pure Ti metal powder) and a Si(100) substrate are separately placed on 2 graphite boats in a tube furnace. In this system, the precursor Ti powder is placed in a high-temperature zone (1050 °C) and the Si(100) substrate is positioned in a low-temperature zone (850 °C). The PVD process is initiated when an Ar/O_2 mixture gas flowing at a pressure of 40,000 Pa (300 Torr) is used to convert Ti into a layer of TiO_2 nanowires (*41*).

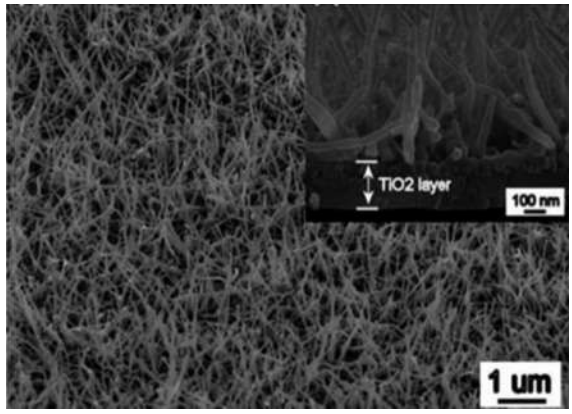

Figure 14. SEM images of TiO_2 nanowires SEM images grown on a Si(100) substrate using the PVD method (41). Reproduced with permission from ref (41). Copyright 2005 Elsevier.

Figure 15 shows evidence of producing TiO_2 anatase nanorods by growing them on silica substrates using the CVD method (*42*). By using a N_2/O_2 mixture gas, Wu and Yu demonstrated the vapors of the titanium acetylacetonate ($Ti(C_5H_7O_2)_4$) precursor were used to produce nanorods at a relative low temperature ranging between 200–230 °C (*42*). The precursor reacts and is grown at a relatively high temperature (500–700 °C) on a silica substrate surface. The phase and morphology of the TiO_2 products are tunable by adjusting the substrate temperature and pressure (*42*). For example, anatase and rutile TiO_2 nanorods were produced at 560 °C and 630 °C with the pressure set at 667 Pa

(5 Torr), respectively. In comparison, TiO_2 nanowalls were produced with the different conditions of 535 °C and under 480 Pa (3.6 Torr).

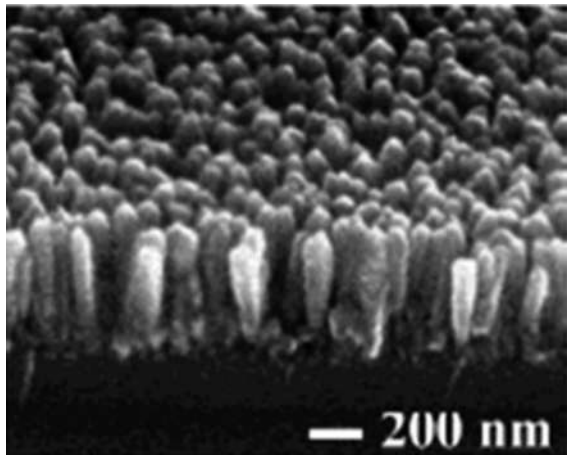

Figure 15. TiO_2 anatase nanorods SEM image (42). Note: CVD conditions were 560 °C and 667 Pa (5 Torr) (42). Reproduced with permission from ref (42). Copyright 2004 American Chemical Society

Electrochemical Method

Synthesis using the electrochemical method includes electrodeposition and electrochemical etching/anodization. Electrodeposition is frequently used to grow TiO_2 nanocoating on a substrate by reducing titanium ions in an electrolyte at the cathode surface. TiO_2 nanowires coatings are synthesized using a template such as an alumina membrane on an Al substrate. Typically, titanium deposits into the pores of the template utilizing 0.2 M $TiCl_3$ solution as the electrolyte (*43*). Anatase TiO_2 nanowires are produced after heating the Ti infused alumina membrane coating at 500 °C for 4 h in an open furnace (Figure 16). Next, the alumina membranes are partly removed by chemical etching in a 3 M NaOH for 5 min.

Besides the electrodeposition method, electrochemical etching/anodization is a versatile process that allows the production of a dense and well-defined TiO_2 nanomaterial onto a titanium surface (*1*, *32*, *44*, *45*). Electrochemical oxidation produces Ti^{4+} ($Ti \rightarrow Ti^{4+} + 4e^-$) when titanium metal is exposed to a sufficiently high anodic voltage in a cell. Next, the Ti^{4+} ions react with O^{2-} in the electrolyte (Eq. 2) to produce a solid TiO_2 layer (*29*, *45*, *46*).

$$Ti + 2H_2O - TiO_2 + 4H^+ + 4e^- \quad (2)$$

Direct Oxidation Method

Oxidizing titanium metal can be employed to produce TiO_2 nanomaterials. For example, TiO_2 nanorods on a titanium plate were produced by oxidation using a 30% H_2O_2 aqueous solution at 78 °C for 72 h (*47*). The TiO_2 nanorods phase structure is controllable by adding inorganic salts (e.g., NaF, NaCl or $NaSO_4$) (*47*). Pure anatase nanorods are produced by adding NaF or $NaSO_4$, while pure rutile nanorods are produced by adding NaCl.

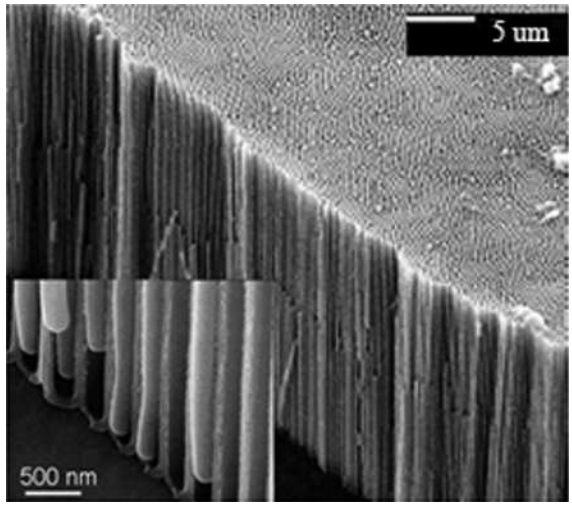

Figure 16. SEM image of TiO_2 nanowires produced using a electrodeposition method (43). Reproduced with permission from ref (43). Copyright 2005 AIP Publishing.

Surfactant Controlled Method

With the assistance of surfactants, the isotropic growth of TiO_2 nanostructures is accomplished by the hydrolysis of titanium alkoxides. Surfactants have the ability to select the crystal facet and manipulate the final structure of TiO_2 nanomaterials, since they modify the surface energy of desired facets (*32*). For example, Cozzoli et al. reported growing anatase nanorods by employing the hydrolysis of titanium tetraisopropoxide and using oleic acid as the surfactant (*48*).

Plasma-Assisted Method

Employing TiO_2 powders has many disadvantages, including the need for separation or filtration (*4*), problematic use in continuous flow systems, and particle agglomeration. Overcoming these disadvantages has been accomplished by employing TiO_2 thin films (Figure 17). In thin film systems, the TiO_2 photocatalyst is coated onto the wall of a solar parabolic reactor. Plasma-assisted deposition (PAD) processes (*49*) have been widely applied to prepare thin films (*50*). The PAD processes generally include plasma-enhanced chemical vapor deposition (PECVD) and magnetron sputter deposition. PAD processes have increased significant interests in industrial use, mainly due to the following: (1) Low temperature deposition when compared to conventional PVD and CVD processes. For example, silicon nitride a coating can be deposited by PECVD at 300 °C. Whereas, the conventional CVD process is conducted at 900 °C (*49*); (2) A broad range of experimental parameters (e.g., pressure, gas flow, excitation frequency, and power) can be adjusted to optimize composition and microstructure of the film (*51*); (3) High deposition rates (1 $nm \cdot s^{-1}$ – 40 $\mu m \cdot s^{-1}$)permit low-cost fabrication (*51*); (4) PAD allows for uniform coating on substrates with different shapes such as flat, hemispherical, long fibers, cylindrical shapes, and the interior of tubes (*51*); (5) PAD films show better mechanical properties (e.g., adhesion, stress compensation, abrasion, and wear resistance) when compared to their PVD counterparts (*51*); (6) PAD allows for doping to optimize the photocatalytic activities of the thin film (*51*).

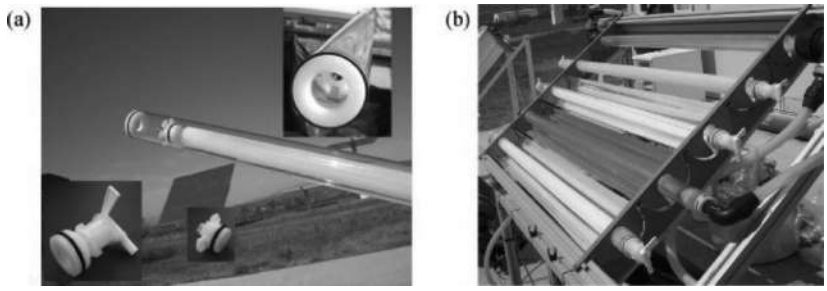

Figure 17. (a) TiO_2 coated glass cylinders using sol–gel method and annealed at 500 °C, and (b) a plug flow system for water purification (52). *Reproduced with permission from ref* (52). *Copyright 2014 Royal Society of Chemistry.*

PECVD is a method employed for film preparation using gas phase precursors activated in a glow discharge environment (*51*). Using a plasma as a reactive medium allows the CVD process to take place at a much lower temperature. Fragmentation of the precursor is accomplished by collisions with electrons produced in the plasma.

The PECVD process can be conducted under both low and atmospheric pressure conditions. In particular, the atmospheric-pressure plasma jet (APPJ) process (Figure 18) (*53*, *54*) and the dielectric barrier discharges (DBD) plasma (*55*) are promising candidates to replace the thermal CVD or sol–gel processes, which are employed for depositing functional coatings (*53*, *54*). Using these replacement technologies is due to low cost, high deposition rates, low operational temperatures, one step process, easy implementation, and in-line process capabilities. Careful control of the plasma parameters (i.e., plasma source, the titanium precursor, and precursor carrier gas) allows the formation of well-adherent and solid TiO_2 coatings with tunable properties at low temperature conditions (*56*). Utilizing low temperature conditions allows employing a wide selection of substrates without inflicting damage to the optical fiber glass, nickel film, and carbon-polymer composite (*56*, *57*).

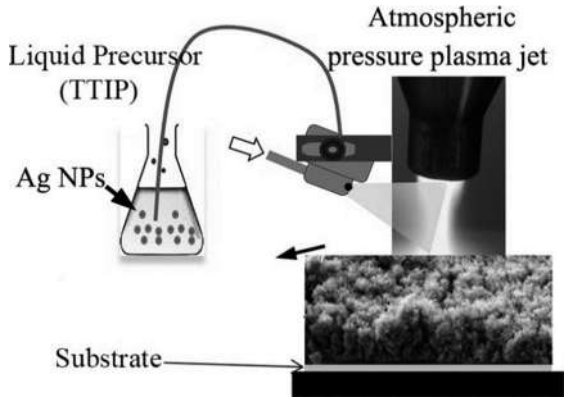

Figure 18. Illustration of an open-air APPJ setup for depositing TiO_2 coating on a flat substrate (53). *Reproduced with permission from ref* (53). *Copyright 2019 John Wiley and Sons.*

Fakhouri et al. (*54*) employed an open-air APPJ and titanium isopropoxide as precursor (Figure 18a) to deposit photocatalytic TiO_2 coatings with high porosity and high SSA at a high deposition rate (20–40 $\mu m \cdot s^{-1}$). In an open-air APPJ system, the porosity and crystallinity of the TiO_2 coating

was controlled by varying deposition parameters such as pulse frequency, gas flowrate, and the post-annealing temperature (*54*). A APPJ TiO_2 coating deposited at 23 kHz and 2400 $L{\cdot}s^{-1}$ was characterized with a high SSA porous structure (Figure 18b) and a significant enhancement in the photocatalytic efficiency for degrading RhB when compared to an N-doped TiO_2 coating, which was generated by radio frequency (RF) magnetron sputtering (*54*, *58*).

Using $TiCl_4$ and O_2 as precursors, Nie et al. employed an atmospheric cold DBD plasma for synthesizing nanocrystalline anatase TiO_2 (Figure 19a) (*55*). The size of the TiO_2 nanocrystal attained was 10–15 nm (Figure 19b) when the plasma energy density was set at 5.9 $kJ{\cdot}L^{-1}$. Peng et al. observed decreasing particles size with increasing the plasma energy density (*53*). The DBD plasma process is promising because it is a single-step process, low cost, easy to control, and utilizes simple equipment for the discharge.

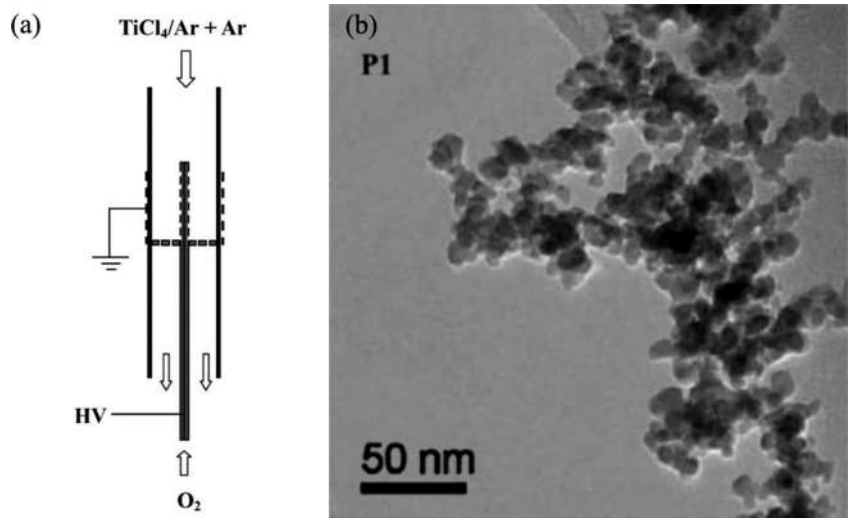

Figure 19. (a) Schematic of DBD reactor for synthesizing anatase TiO_2, and (b) TEM image of DBD TiO_2 nanocrystal (*55*). *Reproduced with permission from ref* (*55*). *Copyright 2007 John Wiley and Sons.*

Magnetron sputter deposition is mainly utilized for industrial application to deposit metals, oxides, nitrides, and alloys (*49*). In the case of physical magnetron sputtering (*49*), the bombarding ions (i.e., argon ions at 500–1000 V) physically sputter the target metallic atoms that are transferred to and deposited onto a substrate. When employing reactive magnetron sputtering, a reactive gas (O_2 and N_2) with dissociation products that chemically react with the target titanium is supplied in addition to the bombarding ions. For example, the physical magnetron sputtering of a Ti target with argon as the bombarding gas results in the formation of Ti thin film. A TiO_2 thin film can be synthesized if O_2 is supplied as reactive gas (*58*). Fakhouri et al. (*58*) synthesized N-doped TiO_2 thin films on silicon substrates (Figure 20) by reactive RF magnetron sputtering using a dual reactive gas mixture of N_2 and O_2.

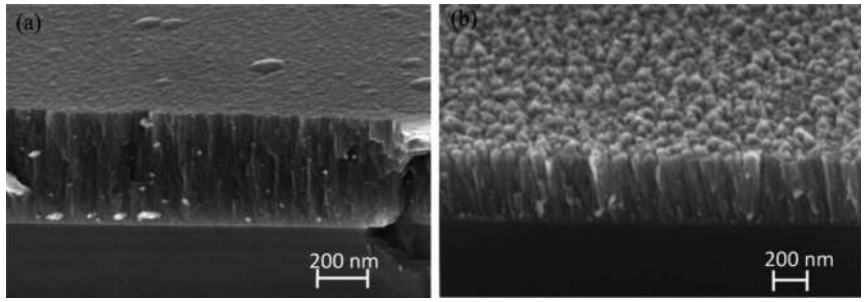

Figure 20. Scanning electron microscope (SEM) images of TiO_2 coatings synthesized by reactive RF magnetron sputtering at different pressures (a) 3 mTorr, and (b) 14 mTorr (58). Note: 1 mTorr represents 0.13 Pa. Reproduced with permission from ref (58). Copyright 2014 Elsevier.

Other Methods

Sonication has been employed to produce TiO_2 nanostructures (5). In addition, microwaves have been used to prepare TiO_2 nanomaterials (5). The main advantages of using microwaves are rapid volumetric and selective heating.

Modifications of TiO_2 Nanomaterials

A majority of pure semiconductors are characterized as low quantum yield, low optical response, and limited utilization rate of visible light. Low photocatalytic efficiency has become a challenge on designing and developing photocatalysts for practical applications. Fortunately, the modification of pure semiconductors is a facile strategy to enhance their overall efficiency. The mechanisms for modification include the following (*4*, *6*, *59–61*): (1) modifying the crystal structure and morphology; (2) narrowing bandgap; (3) suppressing charge recombination; (4) introducing cocatalysts; and (5) enhancing charge transfer.

Modifying TiO_2 Crystal Structure and Morphology

Modifying Crystal Structure

TiO_2 photocatalytic properties are significantly affected by the crystal structure and morphology (*62*). Pure anatase is more active than rutile. The poor photocatalytic activities of rutile are due to the intrinsic defects in the rutile structure where the electrons are trapped. The photocatalytic activity of biphasic anatase–rutile photocatalysts increases significantly when compared to pure phases of TiO_2 (*63*). When the two crystal phases are combined, electron migration across the anatase–rutile phase interface facilitates the charge separation that causes a subsequent increase in photocatalytic activity (Figure 21) (*63*, *64*).

Modifying Morphology and Nanostructure

Particle size and morphology can strongly affect the dynamics of e^--h^+ recombination (bulk and surface recombination) (*65–68*). Generally, bulk charge recombination is significant in a well-crystallized semiconductor with a large particle size (*65*). Decreasing the particle size closely correlates to a significant decrease in the bulk charge recombination, an increase of the SSA, and

improved photocatalytic activities (*65*). However, according to Okura and Kaneko, increasing the SSA beyond a threshold value could lead to enhancing surface defects and surface charge recombination with a subsequent negative effect on photocatalysis (*69*). Hence, a trade-off between bulk charge recombination and surface charge combination must be evaluated before designing a photocatalyst (*5*).

TiO_2 two-dimensional (2D) nanostructures (i.e., nanosheets and nanoplates) and Q1D nanostructures (i.e., nanowire, nanotube, nanoribbon, nanorod) also facilitate the charge transfer inside the crystals to the surface, and subsequently enhance the charge separation. Atomic scale thickness, smaller diameter, and large surface area shorten charge transfer distance and lower time; hence, the bulk charge recombination is impeded (*5*, *7*, *70*, *71*).

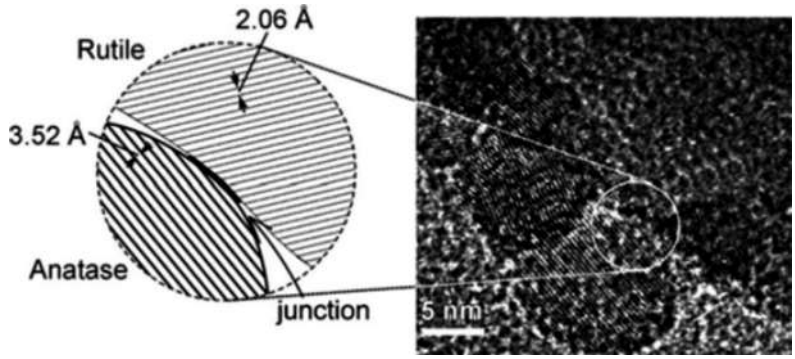

Figure 21. Anatase–rutile phase junction structure (*72*). *Reproduced with permission from ref* (*72*). *Copyright 2008 John Wiley and Sons.*

Doped-TiO_2

One effective solution to enhance the photocatalytic efficiency is to generate an impurity in the forbidden band via metal and nonmetal doping (*4*, *6*, *61*). Doping decreases the TiO_2 bandgap and expands the TiO_2 optical response into the visible region.

Metal Doped-TiO_2

Many researchers have reported that metal doping with Sn, Fe, Ru, Mo, Os, Re, V, and Rh can significantly increase photocatalytic activity under visible light conditions (*11*, *63*). The mechanism of visible light photocatalysts using metal doping is illustrated in Figure 22 (*62*). An appropriate doping element creates either a donor level or an acceptor level (*62*). These new levels narrow the original band to expand the optical response of the photocatalyst into the visible region (*62*). Additionally, by promoting charge separation, the doping ions serve as a recombination inhibitor by trapping charge carriers (*62*).

Nonmetal Doped-TiO_2

Unlike metal ion dopants, nonmetal doping elements are able to upshift the VB edge without the formation of any donor or acceptor levels in the forbidden band. The up-shifting valence of the band edge results in a narrowed band gap (Figure 23) (*62*). Various nonmetal chemicals such as C, N, and S have been used to dope TiO_2 (*62*, *73*). To date, N-doping is most efficient and most widely

investigated (*74*, *75*). In N-doped TiO_2, the substitution of N for O results in the mixing of the N 2p level with the O 2p level and the narrowing of the bandgap (*62*). The narrowed bandgap is closely linked to much higher photocatalytic activities in the visible range when compared to pure TiO_2.

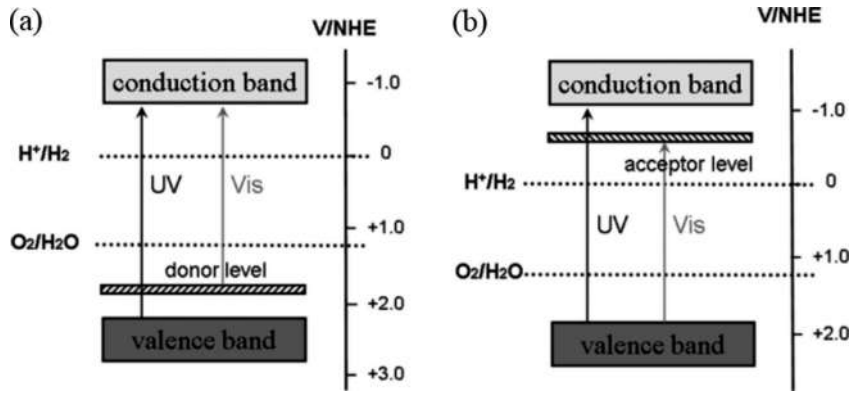

Figure 22. Donor level and acceptor level generated in forbidden band (a) without doping, and (b) with doping metal ion (*62*). *Reproduced with permission from ref* (*62*). *Copyright 2010 American Chemical Society.*

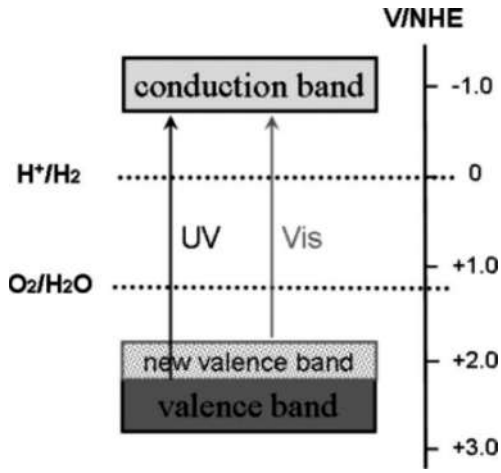

Figure 23. VB shifting by doping nonmetal ions (*62*). *Reproduced with permission from ref* (*62*). *Copyright 2010 American Chemical Society.*

Carbon-Based TiO_2 Composites

Introducing carbon nanomaterials into TiO_2 significantly increases the photocatalytic activity of TiO_2 (*76*, *77*). The main focus of this chapter is the utilization of graphene, carbon nanotubes (CNT), and carbon quantum dots (*78*, *79*). Carbon materials function by improving the TiO_2 photocatalytic activities through the following (*15*, *80–82*): (1) Enhancing the photocatalytic activity by increasing adsorption of organic molecules (e.g., graphene and CNTs has a high SSA and adsorbs organic pollutant molecules efficiently via π–π conjugation system (*78*). Phenol has the same aromaticity as graphene. As a result, the π–π conjugation facilitates the adsorption of chemicals such as phenol on graphene. (2) Extending the light absorption region utilizing carbon materials is able to generate a red shift in the photo-responding range and improve the utilization of visible light (*15*,

80–82). (3) Suppressing charge recombination (*15*, *80–82*) using carbon based materials serves as an electron scavenger by accepting electrons from the TiO_2 and providing a fast electron transfer route because of its high charge carrier mobility (*15*, *80–82*). The photogenerated electrons in TiO_2 are transported to carbon materials with holes remaining in TiO_2 (*15*, *80–82*).

CNT Based TiO_2

CNTs, cylindrical nanostructures with single or multiple walls (Figure 24), have been employed as electron acceptors to increase the photocatalytic activity. This enhancement is due to their chemical stability, unique structures, excellent electron mobility, adsorption, mechanical, and thermal properties (*83*). In a composite with TiO_2, CNTs enable charge separation and increase the SSA (*83*, *84*). CNT–TiO_2 hybrids have been synthesized by various methods such as mixing of TiO_2 with CNTs, sol–gel and hydrothermal synthesis of TiO_2 in the presence of CNTs, CVD, PVD, electrochemical as well as plasma-assisted methods (*83–85*).

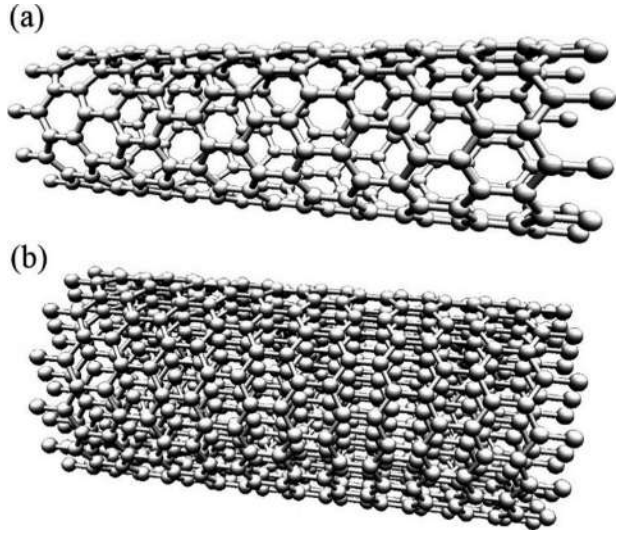

Figure 24. (a) Single-walled carbon nanotube and (b) multiwalled carbon nanotube.

Graphene Based TiO_2

Increasing interest in using graphene in recent years (Figure 25) is primarily due to its exceptional physical and chemical properties. Graphene, a 2D carbon atoms sheet, is characterized with a high charge carrier mobility (15,000 $cm^2 \cdot V^{-1} \cdot s^{-1}$), high SSA (up to 2630 $m^2 \cdot g^{-1}$), high thermal conductivity (approximately 5000 $W \cdot m^{-1} \cdot °C^{-1}$), and a tunable bandgap by chemical doping (*86–88*). These properties are leading reasons why graphene modified TiO_2 photocatalysts are able to find promising applications for air and water purification (*15*, *89*, *90*). Figure 26 shows a general morphology of graphene-modified TiO_2 nanotube composites (*78*). TiO_2 nanotubes dispersed on the graphene sheets maintain direct contact with the graphene sheets. Graphene has a high SSA and adsorbs organic pollutant molecules efficiently through a π–π conjugation system (*78*). In addition, graphene serves as an electron scavenger by accepting electrons from the TiO_2 and provides a fast electron transfer route because of its high charge carrier mobility (*15*, *80–82*). The photogenerated

electrons in TiO_2 are transported to the graphene nanosheet with holes remaining in TiO_2 (*15*, *80–82*). The electrons on graphene are transferred to electron acceptors and the remaining holes in TiO_2 are transferred to electron donors.

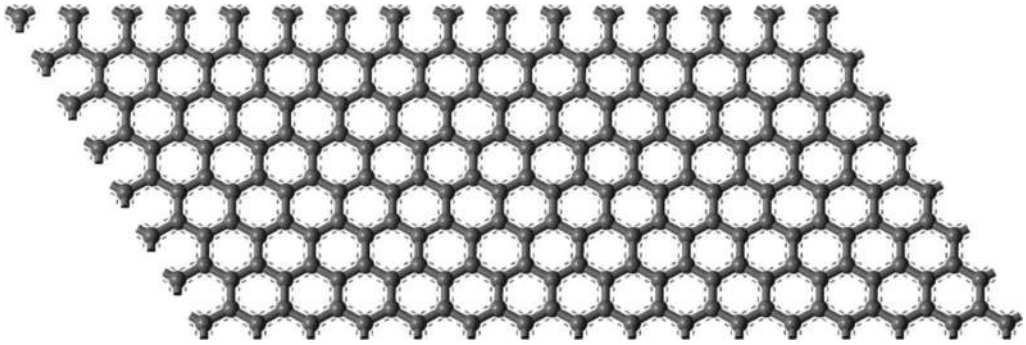

Figure 25. Graphene nanosheet composed of one atomic carbon layer.

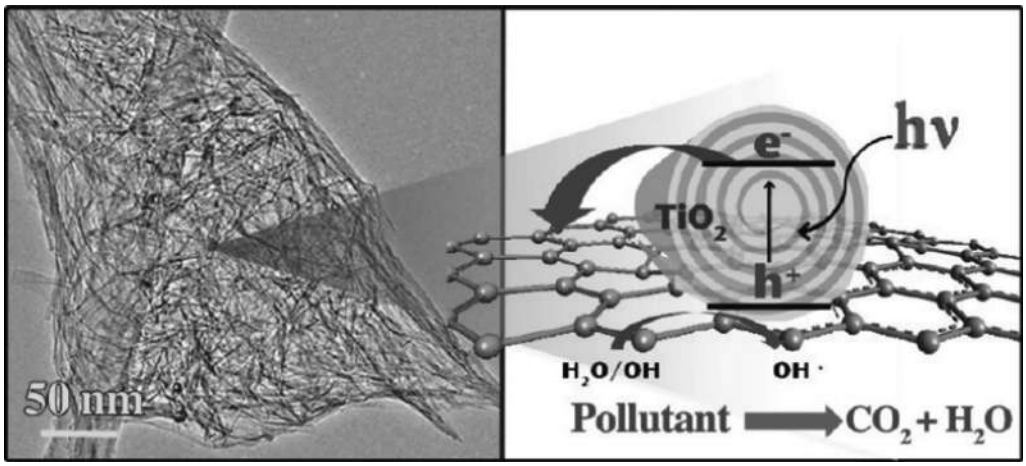

Figure 26. TEM image of graphene modified TiO_2 nanotubes (left) and its schematic figure for mechanism of charge transfer and separation (right) (78). Reproduced with permission from ref (78). Copyright 2012 American Chemical Society.

Noncarbon-Based TiO_2 Composites

The TiO_2 can be enhanced by incorporating noncarbonaceous materials including noble metals, semiconductors, and noncarbonaceous 2D materials.

Depositing Metal Nanoparticles

Depositing transition metals (Ag, Pt, Au, Cu, and Pd) on TiO_2 nanostructures can significantly improve photocatalytic activities (*18*, *91*, *92*). Transition metals serve as cocatalysts and as electron traps to delay the charge recombination (*19*, *93*). Figure 27 shows the electron trapping phenomenon at the Schottky barrier between the metal particle and a semiconductor (*19*, *94*). Due to the Schottky barrier, excited electrons migrate and are trapped in the transition metal during photocatalysis, while the holes in TiO_2 are free to transfer to the semiconductor's surface and subsequently, react with

reactants (*19*, *94*). For example, the Pt–TiO_2 system is notably efficient in producing H_2 gas because of the catalytic effect of Pt and electron trapping (*19*, *95*).

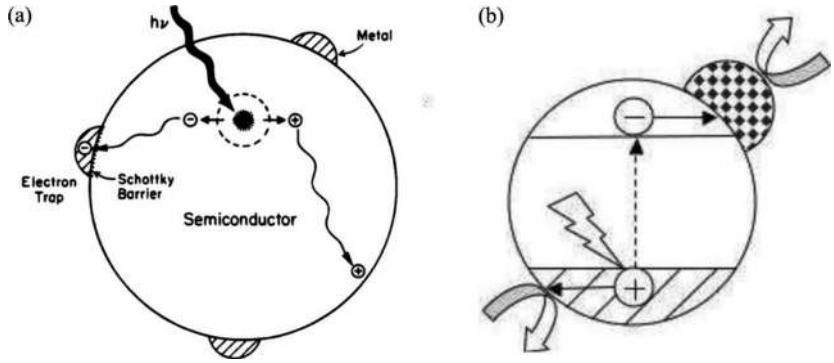

Figure 27. Metal modified semiconductor (a) charge transfer and (b) bandgap (*19*). *Reproduced with permission from ref* (*19*). *Copyright 1995 American Chemical Society.*

Semiconductor Coupling

Semiconductor coupling is another effective approach to improve the photocatalytic activity because of enhanced charge separation by forming a heterojunction structure (*19*, *96*). Coupling TiO_2 and CdS with a narrow bandgap of 2.5 eV improves its photocatalytic activity in the visible region (*14*). A charge separation diagram is shown in Figure 28. The photogenerated electrons in CdS are transported to the TiO_2 conductive band, whereas the holes remain in the CdS VB. This charge transfer facilitates the charge separation. In addition to CdS, other semiconductors such as CdSe, Fe_2O_3, and Cu_2O that possess a smaller bandgap and coupled with a proper band edge position are characterized with a negative potential to reduce reactants or a more positive potential to oxidize reactants (Figure 29) (*97*, *98*). These semiconductors can couple with TiO_2 and improve the photocatalytic efficiency (*97*, *98*).

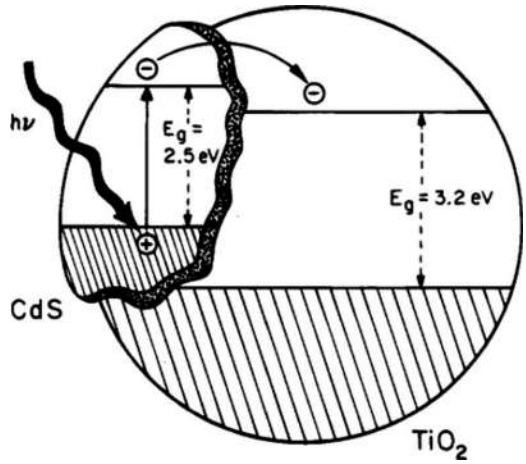

Figure 28. Electron transfer in the CdS/TiO_2 system (*19*). *Reproduced with permission from ref* (*19*). *Copyright 1995 American Chemical Society.*

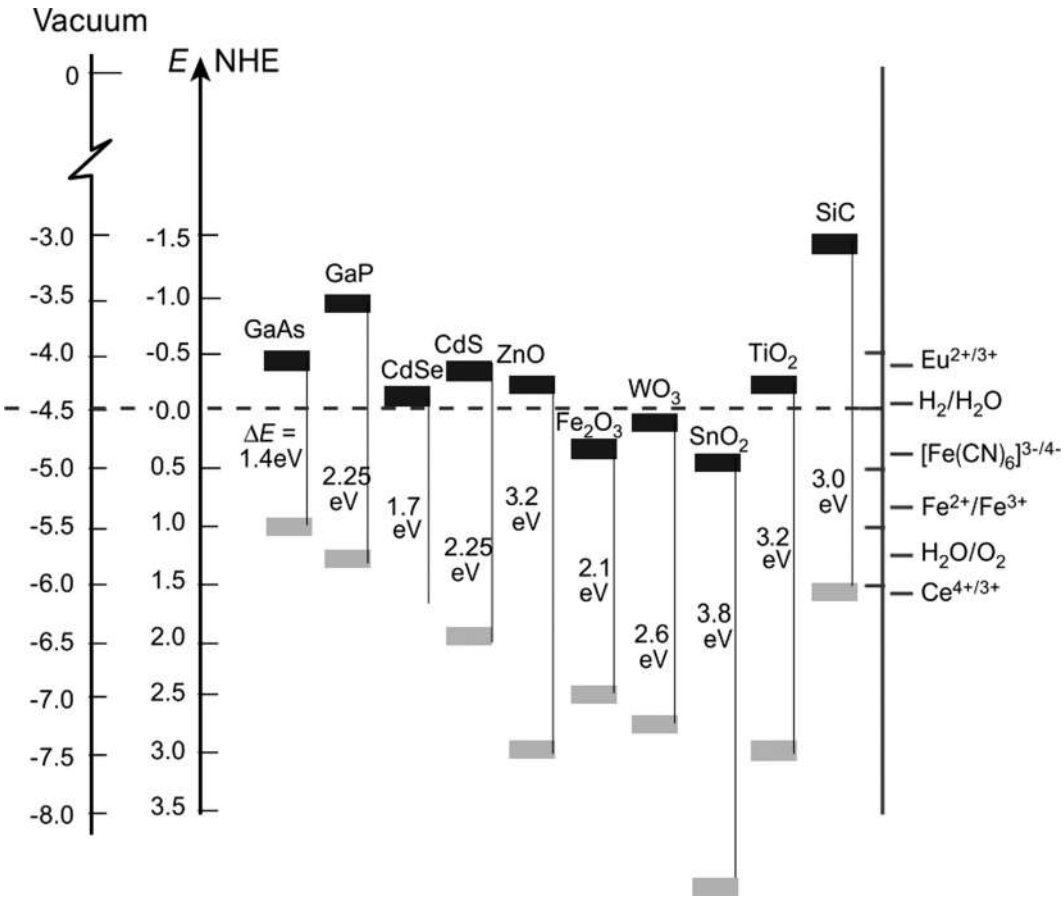

Figure 29. Bandgap edge position for different semiconductors in aqueous solution at pH = 1 (99). Reproduced with permission from ref (99). Copyright 2001 Springer Nature.

Dye Sensitized TiO_2

Increasing the TiO_2 visible light photocatalytic activity has been observed by adsorbing organic and inorganic dyes onto the TiO_2 surface (*96*, *100*). This increase is due to the electron transport from the excited dye to the TiO_2 CB when dye molecules are excited by visible light (*96*, *101*). The electrons in the titanium dioxide CB react with dissolved dioxygen to generate superoxide and hydrogen peroxide radicals that react with organic pollutants (*96*). Dye sensitized TiO_2 has been observed with increasing hydrogen production rate under visible light conditions. Dhanalakshmi et al. (*102*) reported increasing H_2 production rate using TiO_2 enhanced with Pt nanoparticles and $[Ru(dcpy)_2(dpq)]^{2+}$ dye. This observation indicated an effective electron transfer from dye molecules to TiO_2 under visible light (*102*).

Noncarbonaceous 2D Materials

Noncarbonaceous 2D materials, similar to graphene, can be used to enhance the photocatalytic properties of TiO_2 due to their large SSA, high charge mobility, tunable electronic properties, ultra-light weight, and high mechanical flexibility (*103*). The noncarbonaceous 2D materials used to

enhance TiO_2 include MoS_2, borophene (*104*), germanene (*105*), silicene (*106*), phosphorene (*107*), and bismuthene (*108*). Using a hydrothermal method, Zhou et al. (*109*) reported the synthesis of TiO_2 produced the nanobelt coated with a few layers of MoS_2 nanosheets (TiO_2@MoS_2). The TiO_2@MoS_2 composites exhibited efficient visible light absorption and a large increase in the H_2 production rate under visible light when compared to pure TiO_2 with a negligible photocatalytic H_2 production rate (*109*). The increasing H_2 production rate is due to the increasing charge separation provided by 2D MoS_2 nanosheets (*109*). In addition, the TiO_2@MoS_2 hybrids exhibited increased adsorption and photocatalytic decomposition of organic dyes when compared to pure TiO_2 (*109*).

Outlook

This chapter briefly introduced the electronic properties and structure of TiO_2, the principles of photocatalysis, the synthesis of TiO_2, and modifications of TiO_2 photocatalyst. Although significant progress has been made in TiO_2 photocatalytic research, the following issues need to be addressed:

(1) TiO_2 nanopowder needs to be recovered before discharging treated water. Using TiO_2 nanopowder is an effective solution for increasing its photocatalytic activities due to increasing the SSA; however, separating TiO_2 nanopowder from the treated water is difficult (*4*) and is considered as a contaminant (*96*). Residual TiO_2 nanoparticles in water bodies could cause an ecological risk to aquatic ecosystems (*96*). TiO_2 thin films coated on transparent substrate (i.e., glass and fiber) (*56*) is a promising strategy to overcome this problem.

(2) Regeneration and reuse of TiO_2-based photocatalysts is an important aspect. Regeneration and reuse will lead to decreasing production cost and conserve the use of TiO_2 and other materials. The stability and efficiency of a photocatalyst can be significantly reduced after several recycles and should be addressed (*4*) based on the process economics.

(3) TiO_2 catalysis can be enhanced by employing other 2D materials to modify its structure. Synthetic 2D materials with unique characteristics (i.e., borophene) have been examined in recent years (*104*, *110*, *111*). For instance, borophene provides increased tunability, due to its anisotropy and polymorphism within a family of chemically similar structures (*104*). Borophene is the lightest 2D metal with electrical properties, mechanical properties, and a large specific surface (*104*, *112–115*). These properties indicate borophene can function as an electron acceptor as well as a promising material to enhance photocatalysts, such as TiO_2.

(4) The production rate of H_2 can be enhanced by using electron donors such as ethanol, methanol, formic acid, and 1,2,3-propanetriol (*116*). Wang et al. (*117*) reported increasing H_2 production rate using organic pollutants as electron donors (i.e., methylene blue, methyl orange, rhodamine B, and 4-chlorophenol). This observation indicates the possibility of producing H_2 from pollutants.

Summary

This chapter presents an overview of the principle of photocatalysis for H_2 production, degradation of pollutants, CO_2 reduction, and N_2 reduction. TiO_2 is an extensively studied semiconductor. The development of a highly active TiO_2 photocatalyst is a challenge when employing solar energy to remediate polluted water and for producing green fuels, such as H_2 and ethanol. Modifying the morphological and crystallographic structures TiO_2 can significantly affect and improve the photocatalytic property under UV light. Other modification methods include doping and incorporating carbonaceous and noncarbonaceous materials. Future research should focus on recycling the photocatalysts, decreasing the impact of TiO_2 nanopowder discharge into the environment, and modifying TiO_2 with emerging materials.

Acknowledgments

The authors acknowledge funding from the Natural Sciences and Engineering Research Council (NSERC) of Canada (Grant No. 261797–2009), the University of Windsor (Grant No. 13320), as well as the Ontario Trillium scholarship, and the MITACS scholarship programs.

References

1. Roy, P.; Berger, S.; Schmuki, P. TiO_2 Nanotubes: Synthesis and Applications. *Angew. Chem., Int. Ed.* **2011**, *50*, 2904–2939.
2. Fujishima, A.; Honda, K. Electrochemical Photolysis of Water at a Semiconductor Electrode. *Nature* **1972**, *238*, 37–38.
3. Hashimoto, K.; Irie, H.; Fujishima, A. TiO_2 Photocatalysis: A Historical Overview and Future Prospects. *Jpn. J. Appl. Phys.* **2005**, *44*, 8269–8285.
4. Han, F.; Kambala, V. S. R.; Srinivasan, M.; Rajarathnam, D.; Naidu, R. Tailored Titanium Dioxide Photocatalysts for the Degradation of Organic Dyes in Wastewater Treatment: A Review. *Appl. Catal., A: Appl.* **2009**, *359*, 25–40.
5. Chen, X.; Mao, S. S. Titanium Dioxide Nanomaterials: Synthesis, Properties, Modifications, and Applications. *Chem. Rev.* **2007**, *107*, 2891–2959.
6. Sajan, C. P.; Wageh, S.; Al Ghamdi, A. A.; Yu, J.; Cao, S. TiO_2 Nanosheets with Exposed {001} Facets for Photocatalytic Applications. *Nano Res.* **2016**, *9*, 3–27.
7. Roy, N.; Sohn, Y.; Pradhan, D. Synergy of Low-Energy {101} and High-Energy {001} TiO_2 Crystal Facets for Enhanced Photocatalysis. *ACS Nano* **2013**, *7*, 2532–2540.
8. Zhao, Z.; Zhao, H.; Sun, Z.; Zhao, H.; Du, P.; Zheng, M.; Zhao, J.; Fan, H.; Zhao, J.; Fan, H. Phase Control of Hierarchically Structured Mesoporous Anatase TiO_2 Microspheres Covered with {001} Facets. *J. Mater. Chem.* **2012**, *22*, 21965.
9. Yang, S.; Yang, B. X.; Wu, L.; Li, Y. H.; Liu, P.; Zhao, H.; Yu, Y. Y.; Gong, X. Q.; Yang, H. G. Titania Single Crystals with a Curved Surface. *Nat. Commun.* **2014**, *5*, 5355.
10. Morgan, D. L. *Alkaline Hydrothermal Treatment of Titanate Nanostructures*; 2010.
11. George, S.; Pokhrel, S.; Ji, Z.; Henderson, B. L.; Xia, T.; Li, L.; Zink, J. I.; Nel, A. E.; Mädler, L. Role of Fe Doping in Tuning the Band Gap of TiO_2 for the Photo-Oxidation-Induced Cytotoxicity Paradigm. *J. Am. Chem. Soc.* **2011**, *133*, 11270–11278.

12. Batzill, M.; Morales, E. H.; Diebold, U. Influence of Nitrogen Doping on the Defect Formation and Surface Properties of TiO_2 Rutile and Anatase. *Phys. Rev. Lett.* **2006**, *96*, 026103–026104.
13. Linic, S.; Christopher, P.; Ingram, D. B. Plasmonic-Metal Nanostructures for Efficient Conversion of Solar to Chemical Energy. *Nat. Mater.* **2011**, *10*, 911–921.
14. Qin, N.; Liu, Y.; Wu, W.; Shen, L.; Chen, X.; Li, Z.; Wu, L. One-Dimensional CdS/TiO_2 Nanofiber Composites as Efficient Visible-Light-Driven Photocatalysts for Selective Organic Transformation: Synthesis, Characterization, and Performance. *Langmuir* **2015**, *31*, 1203–1209.
15. Li, X.; Yu, J.; Wageh, S.; Al Ghamdi, A. A.; Xie, J. Graphene in Photocatalysis: A Review. *Small* **2016**, *12*, 6640–6696.
16. Chen, C.; Cai, W.; Long, M.; Zhou, B.; Wu, Y.; Wu, D.; Feng, Y. Synthesis of Visible-Light Responsive Graphene Oxide/TiO_2 Composites with P/N Heterojunction. *ACS Nano* **2010**, *4*, 6425–6432.
17. Ismail, A. A.; Bahnemann, D. W. Photochemical Splitting of Water for Hydrogen Production by Photocatalysis: A Review. *Sol. Energy Mater. Sol. Cells* **2014**, *128*, 85–101.
18. Murdoch, M.; Waterhouse, G. I. N.; Nadeem, M. A.; Metson, J. B.; Keane, M. A.; Howe, R. F.; Llorca, J.; Idriss, H. The Effect of Gold Loading and Particle Size on Photocatalytic Hydrogen Production from Ethanol over Au/TiO_2 Nanoparticles. *Nat. Chem.* **2011**, *3*, 489–492.
19. Linsebigler, A. L.; Lu, G.; Yates, J. T. Photocatalysis on TiO_2 Surfaces: Principles, Mechanisms, and Selected Results. *Chem. Rev.* **1995**, *95*, 735–758.
20. Mott, N. F. Conduction in Non-Crystalline Materials. *Philos. Mag.* **1969**, *19*, 835–852.
21. Pelaez, M.; Nolan, N. T.; Pillai, S. C.; Seery, M. K.; Falaras, P.; Kontos, A. G.; Dunlop, P. S. M.; Hamilton, J. W. J.; Byrne, J. A.; O'Shea, K.; Entezari, M. H.; Dionysiou, D. D. A Review on the Visible-Light Active Titanium Dioxide Photocatalysts for Environmental Applications. *Appl. Catal., B: Environ.* **2012**, *125*, 331–349.
22. Ma, Y.; Wang, Z.; Xu, X.; Wang, J. Review on Porous Nanomaterials for Adsorption and Photocatalytic Conversion of CO_2. *Chin. J. Catal.* **2017**, *38*, 1956–1969.
23. Ran, J.; Jaroniec, M.; Qiao, S. Z. Cocatalysts in Semiconductor-Based Photocatalytic CO_2 Reduction: Achievements, Challenges, and Opportunities. *Adv. Mater.* **2018**, 30.
24. Guo, C.; Ran, J.; Vasileff, A.; Qiao, S.-Z. Rational Design of Electrocatalysts and Photo(electro)catalysts for Nitrogen Reduction to Ammonia (NH_3) under Ambient Conditions. *Energy Environ. Sci.* **2018**, *11*, 45–56.
25. Olsen, R. E. *Synthesis, Characterization, and Application of High Surface Area, Mesoporous, Stabilized Anatase TiO_2 Catalyst Supports*; 2013.
26. Swamy, V.; Gale, J. D.; Dubrovinsky, L. S. Atomistic Simulation of the Crystal Structures and Bulk Moduli of TiO_2 Polymorphs. *J. Phys. Chem. Solids* **2001**, *62*, 887–895.
27. Zhu, H. Y.; Lan, Y.; Gao, X. P.; Ringer, S. P.; Zheng, Z. F.; Song, D. Y.; Zhao, J. C. Phase Transition between Nanostructures of Titanate and Titanium Dioxides Via Simple Wet-Chemical Reactions. *J. Am. Chem. Soc.* **2005**, *127*, 6730–6736.
28. Damodaran, V. B.; Bhatnagar, D.; Leszczak, V.; Popat, K. C. Titania Nanostructures: A Biomedical Perspective. *RSC Adv.* **2015**, *5*, 37149–37171.

29. Kugel, K. I.; Khomskii, D. I. The Jahn-Teller Effect and Magnetism: Transition Metal Compounds. *Sov. Phys. Uspekhi* **1982**, *25*, 231.
30. Reyes-Coronado, D.; Rodriguez-Gattorno, G.; Espinosa-Pesqueira, M. E.; Cab, C.; de Coss, R.; Oskam, G. Phase-Pure TiO_2 Nanoparticles: Anatase, Brookite and Rutile. *Nanotechnology* **2008**, *19*, 145605.
31. Yang, D.; Liu, H.; Zheng, Z.; Yuan, Y.; Zhao, J.-c.; Waclawik, E. R.; Ke, X.; Zhu, H. An Efficient Photocatalyst Structure: TiO_2(B) Nanofibers with a Shell of Anatase Nanocrystals. *J. Am. Chem. Soc.* **2009**, *131*, 17885–17893.
32. Wang, X.; Li, Z.; Shi, J.; Yu, Y. One-Dimensional Titanium Dioxide Nanomaterials: Nanowires, Nanorods, and Nanobelts. *Chem. Rev.* **2014**, *114*, 9346–9384.
33. Armstrong, A. R.; Armstrong, G.; Canales, J.; Bruce, P. G. TiO_2-B Nanowires. *Angew. Chem.* **2004**, *116*, 2336–2338.
34. Kuo, H.-L.; Kuo, C.-Y.; Liu, C.-H.; Chao, J.-H.; Lin, C.-H. A Highly Active Bi-Crystalline Photocatalyst Consisting of TiO_2 (B) Nanotube and Anatase Particle for Producing H_2 Gas from Neat Ethanol. *Catal. Lett.* **2007**, *113*, 7.
35. Liu, S. M.; Gan, L. M.; Liu, L. H.; Zhang, W. D.; Zeng, H. C. Synthesis of Single-Crystalline TiO_2 Nanotubes. *Chem. Mater.* **2002**, *14*, 1391.
36. Zhu, J.; Wang, J.; Lv, F.; Xiao, S.; Nuckolls, C.; Li, H. Synthesis and Self-Assembly of Photonic Materials from Nanocrystalline Titania Sheets. *J. Am. Chem. Soc.* **2013**, *135*, 4719.
37. Byrappa, K.; Byrappa, K.; Adschiri, T.; Adschiri, T. Hydrothermal Technology for Nanotechnology. *Prog. Cryst. Growth Charact. Mater.* **2007**, *53*, 117–166.
38. Bavykin, D. V.; Parmon, V. N.; Lapkin, A. A.; Walsh, F. C. The Effect of Hydrothermal Conditions on the Mesoporous Structure of TiO_2 Nanotubes. *J. Mater. Chem.* **2004**, *14*, 3370–3378.
39. Wang, Y. Q.; Hu, G. Q.; Duan, X. F.; Sun, H. L.; Xue, Q. K. Microstructure and Formation Mechanism of Titanium Dioxide Nanotubes. *Chem. Phys. Lett.* **2002**, *365*, 427–431.
40. Kim, C.-S.; Moon, B. K.; Park, J.-H.; Choi, B.-C.; Seo, H.-J. Solvothermal Synthesis of Nanocrystalline TiO_2 in Toluene with Surfactant. *J. Cryst. Growth* **2003**, *257*, 309–315.
41. Wu, J.-M.; Shih, H. C.; Wu, W.-T. Electron Field Emission from Single Crystalline TiO_2 Nanowires Prepared by Thermal Evaporation. *Chem. Phys. Lett.* **2005**, *413*, 490–494.
42. Wu, J.-J.; Yu, C.-C. Aligned TiO_2 Nanorods and Nanowalls. *J. Phys. Chem. B* **2004**, *108*, 3377–3379.
43. Liu, S.; Huang, K. Straightforward Fabrication of Highly Ordered TiO_2 Nanowire Arrays in Aam on Aluminum Substrate. *Sol. Energy Mater. Sol. Cells* **2005**, 85.
44. Lee, H.; Park, T.-H.; Jang, D.-J. Preparation of Anatase TiO_2 Nanotube Arrays Dominated by Highly Reactive Facets Via Anodization for High Photocatalytic Performances. *New J. Chem.* **2016**, *40*, 8737–8744.
45. Tang, Y.; Zhang, Y.; Deng, J.; Wei, J.; Tam, H. L.; Chandran, B. K.; Dong, Z.; Chen, Z.; Chen, X. Mechanical Force-Driven Growth of Elongated Bending TiO_2-Based Nanotubular Materials for Ultrafast Rechargeable Lithium Ion Batteries. *Adv. Mater.* **2014**, *26*, 6111–6118.
46. Kasuga, T.; Hiramatsu, M.; Hoson, A.; Sekino, T.; Niihara, K. Formation of Titanium Oxide Nanotube. *Langmuir* **1998**, *14*, 3160–3163.

47. Wu, J.-M.; Hayakawa, S.; Tsuru, K.; Osaka, A. Porous Titania Films Prepared from Interactions of Titanium with Hydrogen Peroxide Solution. *Scr. Mater.* **2002**, *46*, 101–106.
48. Cozzoli, P. D.; Kornowski, A.; Weller, H. Low-Temperature Synthesis of Soluble and Processable Organic-Capped Anatase TiO_2 Nanorods. *J. Am. Chem. Soc.* **2003**, *125*, 14539–14548.
49. Lieberman, M. A.; Lichtenberg, A. J. *Principles of Plasma Discharges and Materials Processing*; John Wiley & Sons, 2005.
50. Essakhi, A.; Löfberg, A.; Supiot, P.; Mutel, B.; Paul, S.; Le Courtois, V.; Bordes-Richard, E. *Coating Metallic Foams and Structured Reactors by VO_x/TiO_2 Oxidation Catalyst: Application of Rpecvd*; Elsevier, 2010.
51. Martinu, L.; Poitras, D. Plasma Deposition of Optical Films and Coatings: A Review. *J. Vac. Sci. Technol. A* **2000**, *18*, 2619–2645.
52. Keane, D. A.; McGuigan, K. G.; Ibáñez, P. F.; Polo-López, M. I.; Byrne, J. A.; Dunlop, P. S. M.; O'Shea, K.; Dionysiou, D. D.; Pillai, S. C. Solar Photocatalysis for Water Disinfection: Materials and Reactor Design. *Catal. Sci. Technol.* **2014**, *4*, 1211–1216.
53. Peng, T.; Pulpytel, J.; Horovitz, I.; Jaiswal, A. K.; Avisar, D.; Mamane, H.; Lalman, J. A.; Arefi-Khonsari, F. One-Step Deposition of Nano-Ag-TiO_2 Coatings by Appj for Water Treatment: Application to Trace Pharmaceutical Removal by Solar Photocatalysis, Plasma Process. *Polymer* **2019**, e1800213.
54. Fakhouri, H.; Salem, D. B.; Carton, O.; Pulpytel, J.; Arefi-Khonsari, F. Highly Efficient Photocatalytic TiO_2 Coatings Deposited by Open Air Atmospheric Pressure Plasma Jet with Aerosolized Ttip Precursor. *J. Phys. D: Appl. Phys.* **2014**, *47*, 265301–265311.
55. Nie, L.-H.; Shi, C.; Xu, Y.; Wu, Q.-H.; Zhu, A.-M. Atmospheric Cold Plasmas for Synthesizing Nanocrystalline Anatase TiO_2 Using Dielectric Barrier Discharges. *Plasma Process. Polym.* **2007**, *4*, 574–582.
56. Baba, K.; Bulou, S.; Choquet, P.; Boscher, N. D. Photocatalytic Anatase TiO_2 Thin Films on Polymer Optical Fiber Using Atmospheric-Pressure Plasma. *ACS Appl. Mater. Interfaces* **2017**, *9*, 13733–13741.
57. Robotti, M.; Dosta, S.; Gardon, M.; Cano, I. G.; Guilemany, J. M.; Kourasi, M.; Mellor, B.; Wills, R. Enhancing the Performance of Common Electrode Materials by Means of Atmospheric Plasma Spray Coatings. *J. Energy Storage* **2016**, *5*, 127–133.
58. Fakhouri, H.; Pulpytel, J.; Smith, W.; Zolfaghari, A.; Mortaheb, H. R.; Meshkini, F.; Jafari, R.; Sutter, E.; Arefi-Khonsari, F. Control of the Visible and UV Light Water Splitting and Photocatalysis of Nitrogen Doped TiO_2 Thin Films Deposited by Reactive Magnetron Sputtering. *Appl. Catal., B: Environ.* **2014**, *144*, 12–21.
59. Wen, J.; Li, X.; Liu, W.; Fang, Y.; Xie, J.; Xu, Y. Photocatalysis Fundamentals and Surface Modification of TiO_2 Nanomaterials. *Chin. J. Catal.* **2015**, *36*, 2049–2070.
60. Ullattil, S. G.; Narendranath, S. B.; Pillai, S. C.; Periyat, P. Black TiO_2 Nanomaterials: A Review of Recent Advances. *Chem. Eng. J.* **2018**, *343*, 708–736.
61. Malato, S.; Fernández-Ibáñez, P.; Maldonado, M. I.; Blanco, J.; Gernjak, W. Decontamination and Disinfection of Water by Solar Photocatalysis: Recent Overview and Trends. *Catal. Today* **2009**, *147*, 1–59.

62. Chen, X.; Shen, S.; Guo, L.; Mao, S. S. Semiconductor-Based Photocatalytic Hydrogen Generation. *Chem. Rev.* **2010**, *110*, 6503–6570.
63. Tian, G.; Fu, H.; Jing, L.; Xin, B.; Pan, K. Preparation and Characterization of Stable Biphase TiO_2 Photocatalyst with High Crystallinity, Large Surface Area, and Enhanced Photoactivity. *J. Phys. Chem. C* **2008**, *112*, 3083–3089.
64. Hurum, D. C.; Agrios, A. G.; Gray, K. A.; Rajh, T.; Thurnauer, M. C. Explaining the Enhanced Photocatalytic Activity of Degussa P25 Mixed-Phase Tio_2 Using Epr. *J. Phys. Chem. B* **2003**, *107*, 4545–4549.
65. Zhang, Z.; Wang, C.-C.; Zakaria, R.; Ying, J. Y. Role of Particle Size in Nanocrystalline TiO_2-Based Photocatalysts. *J. Phys. Chem. B* **1998**, *102*, 10871–10878.
66. Kong, M.; Li, Y.; Chen, X.; Tian, T.; Fang, P.; Zheng, F.; Zhao, X. Tuning the Relative Concentration Ratio of Bulk Defects to Surface Defects in TiO_2 Nanocrystals Leads to High Photocatalytic Efficiency. *J. Am. Chem. Soc.* **2011**, *133*, 16414–16417.
67. Choi, W.; Termin, A.; Hoffmann, M. R. The Role of Metal Ion Dopants in Quantum-Sized TiO_2: Correlation between Photoreactivity and Charge Carrier Recombination Dynamics. *J. Phys. Chem.* **1994**, *98*, 13669–13679.
68. Serpone, N.; Lawless, D.; Khairutdinov, R.; Pelizzetti, E. Subnanosecond Relaxation Dynamics in TiO_2 Colloidal Sols (Particle Sizes Rp = 1.0–13.4 nm). Relevance to Heterogeneous Photocatalysis. *J. Phys. Chem.* **1995**, *99*, 16655–16661.
69. Okura, I.; Kaneko, M. *Photocatalysis Science and Technology*; Springer and Kodansha: Japan, 2002.
70. Tachikawa, T.; Yamashita, S.; Majima, T. Evidence for Crystal-Face-Dependent TiO_2 Photocatalysis from Single-Molecule Imaging and Kinetic Analysis. *J. Am. Chem. Soc.* **2011**, *133*, 7197–7204.
71. Giocondi, J. L.; Salvador, P. A.; Rohrer, G. S. The Origin of Photochemical Anisotropy in $Srtio_3$. *Top. Catal.* **2007**, *44*, 529–533.
72. Zhang, J.; Xu, Q.; Feng, Z.; Li, M.; Li, C. Importance of the Relationship between Surface Phases and Photocatalytic Activity of TiO_2. *Angew. Chem., Int. Ed.* **2008**, *47*, 1766–1769.
73. Zaleska, A. Doped-TiO_2: A Review. *Recent Pat. Eng.* **2008**, *2*, 157–164.
74. Asahi, R.; Morikawa, T.; Ohwaki, T.; Aoki, K.; Taga, Y. Visible-Light Photocatalysis in Nitrogen-Doped Titanium Oxides. *Science* **2001**, *293*, 269–271.
75. Modugno, G. Efficient Photochemical Water Splitting by a Chemically Modified N-TiO_2. *Science* **2002**, *297*, 2240–2243.
76. Di Paola, A.; Garcia-Lopez, E.; Marci, G.; Palmisano, L. A Survey of Photocatalytic Materials for Environmental Remediation. *J. Hazard. Mater.* **2012**, *211–212*, 3–29.
77. Leary, R.; Westwood, A. Carbonaceous Nanomaterials for the Enhancement of TiO_2 Photocatalysis. *Carbon* **2011**, *49*, 741–772.
78. Perera, S. D.; Mariano, R. G.; Vu, K.; Nour, N.; Seitz, O.; Chabal, Y.; Balkus, K. J., Jr. Hydrothermal Synthesis of Graphene-TiO_2 Nanotube Composites with Enhanced Photocatalytic Activity. *ACS Catal.* **2012**, *2*, 949–956.
79. Zhang, Z.; Zhang, J.; Chen, N.; Qu, L. Graphene Quantum Dots: An Emerging Material for Energy-Related Applications and Beyond. *Energy Environ. Sci.* **2012**, *5*, 8869–8890.

80. Zhang, H.; Lv, X.; Li, Y.; Wang, Y.; Li, J. P25-Graphene Composite as a High Performance Photocatalyst. *ACS Nano* **2010**, *4*, 380–386.
81. Kim, Y.-K.; Min, D.-H. Uv Protection of Reduced Graphene Oxide Films by TiO_2 Nanoparticle Incorporation. *Nanoscale* **2013**, *5*, 3638–3635.
82. Fan, Z.; Yan, J.; Zhi, L.; Zhang, Q.; Wei, T.; Feng, J.; Zhang, M.; Qian, W.; Wei, F. A Three-Dimensional Carbon Nanotube/Graphene Sandwich and Its Application as Electrode in Supercapacitors. *Adv. Mater.* **2010**, *22*, 3723–3728.
83. Djokić, V. R.; Marinković, A. D.; Ersen, O.; Uskoković, P. S.; Petrović, R. D.; Radmilović, V. R.; Janaćković, D. T. The Dependence of the Photocatalytic Activity of TiO_2/Carbon Nanotubes Nanocomposites on the Modification of the Carbon Nanotubes. *Ceram. Int.* **2014**, *40*, 4009–4018.
84. Bouazza, N.; Ouzzine, M.; Lillo-Ródenas, M. A.; Eder, D.; Linares-Solano, A. TiO_2 Nanotubes and CNT–TiO_2 Hybrid Materials for the Photocatalytic Oxidation of Propene at Low Concentration. *Appl. Catal., B: Environ.* **2009**, *92*, 377–383.
85. Chen, M.-l.; Zhang, F.-J.; Oh, W.-C. Synthesis, Characterization, and Photocatalytic Analysis of CNT/TiO_2 Composites Derived from MWCNTs and Titanium Sources. *New Carbon Mater.* **2009**, *24*, 159–166.
86. Novoselov, K. S.; Fal'ko, V. I.; Colombo, L.; Gellert, P. R.; Schwab, M. G.; Kim, K. A Roadmap for Graphene. *Nature* **2012**, *490*, 192–200.
87. Chen, Z.; Ren, W.; Gao, L.; Liu, B.; Pei, S.; Cheng, H. M. Three-Dimensional Flexible and Conductive Interconnected Graphene Networks Grown by Chemical Vapour Deposition. *Nat. Mater.* **2011**, *10*, 424–428.
88. Zhu, Y.; Murali, S.; Stoller, M. D.; Ganesh, K. J.; Cai, W.; Ferreira, P. J.; Pirkle, A.; Wallace, R. M.; Cychosz, K. A.; Thommes, M.; Su, D.; Stach, E. A.; Ruoff, R. S. Carbon-Based Supercapacitors Produced by Activation of Graphene. *Science* **2011**, *332*, 1537–1541.
89. Yu, J.; Wang, S.; Low, J.; Xiao, W. Enhanced Photocatalytic Performance of Direct Z-Scheme G-C_3N_4–TiO_2 Photocatalysts for the Decomposition of Formaldehyde in Air. *Phys. Chem. Chem. Phys.* **2013**, *15*, 16883–16890.
90. Lv, T.; Pan, L.; Liu, X.; Lu, T.; Zhu, G.; Sun, Z.; Sun, C. Q. One-Step Synthesis of CdS–TiO_2–Chemically Reduced Graphene Oxide Composites Via Microwave-Assisted Reaction for Visible-Light Photocatalytic Degradation of Methyl Orange. *Catal. Sci. Technol.* **2012**, *2*, 754–758.
91. Subramanian, V.; Wolf, E. E.; Kamat, P. V. Catalysis with TiO_2/Gold Level Nanocomposites. Effect of Metal Particle Size on the Fermi Equilibration. *J. Am. Chem. Soc.* **2004**, *126*, 4943–4950.
92. Liang, Y.-C.; Wang, C.-C.; Kei, C.-C.; Hsueh, Y.-C.; Cho, W.-H.; Perng, T.-P. Photocatalysis of Ag-Loaded TiO_2 Nanotube Arrays Formed by Atomic Layer Deposition. *J. Phys. Chem. C* **2011**, *115*, 9498–9502.
93. Bahnemann, D. W.; Hilgendorff, M.; Memming, R. Charge Carrier Dynamics at TiO_2 Particles: Reactivity of Free and Trapped Holes. *J. Phys. Chem. B* **1997**, *101*, 4265–4275.

94. Chinnamuthu, P.; Dhar, J. C.; Mondal, A.; Bhattacharyya, A.; Singh, N. K. Ultraviolet Detection Using TiO_2 Nanowire Array with Ag Schottky Contact. *J. Phys. D: Appl. Phys.* **2012**, *45*, 135102–135106.
95. Yu, J.; Qi, L.; Jaroniec, M. Hydrogen Production by Photocatalytic Water Splitting over Pt/TiO_2 Nanosheets with Exposed (001) Facets. *J. Phys. Chem. C* **2010**, *114*, 13118–13125.
96. Daghrir, R.; Drogui, P.; Robert, D. Modified TiO_2 for Environmental Photocatalytic Applications: A Review. *Ind. Eng. Chem. Res.* **2013**, *52*, 3581–3599.
97. Zhou, P.; Yu, J.; Jaroniec, M. All-Solid-State Z-Scheme Photocatalytic Systems. *Adv. Mater.* **2014**, *26*, 4920–4935.
98. Iwashina, K.; Iwase, A.; Ng, Y. H.; Amal, R.; Kudo, A. Z-Schematic Water Splitting into H_2 and O_2 Using Metal Sulfide as a Hydrogen-Evolving Photocatalyst and Reduced Graphene Oxide as a Solid-State Electron Mediator. *J. Am. Chem. Soc.* **2015**, *137*, 604–607.
99. Gratzel, M. Photoelectrochemical Cells. *Nature* **2001**, *414*, 338–344.
100. Ni, M.; Leung, M. K. H.; Leung, D. Y. C.; Sumathy, K. A Review and Recent Developments in Photocatalytic Water-Splitting Using TiO_2 for Hydrogen Production. *Renewable Sustainable Energy Rev.* **2007**, *11*, 401–425.
101. Abe, R. Recent Progress on Photocatalytic and Photoelectrochemical Water Splitting under Visible-Light Irradiation. *J. Photochem. Photobiol., C: Photochem. Rev.* **2010**, *11*, 179–209.
102. Dhanalakshmi, K. B.; Latha, S.; Anandan, S.; Maruthamuthu, P. Dye Sensitized Hydrogen Evolution from Water. *Int. J. Hydrogen Energy* **2001**, *26*, 669–674.
103. Di, J.; Yan, C.; Handoko, A. D.; Seh, Z. W.; Li, H.; Liu, Z. Ultrathin Two-Dimensional Materials for Photo- and Electrocatalytic Hydrogen Evolution. *Mater. Today* **2018**, *21*, 749–770.
104. Mannix, A. J.; Zhang, Z.; Guisinger, N. P.; Yakobson, B. I.; Hersam, M. C. Borophene as a Prototype for Synthetic 2D Materials Development. *Nat. Nanotechnol.* **2018**, *13*, 444–450.
105. Bampoulis, P.; Zhang, L.; Safaei, A.; Gastel, R. v.; Poelsema, B.; Zandvliet, H J W. Germanene Termination of Ge_2pt Crystals on Ge(110). *J. Phys.: Condens. Matter* **2014**, *26*, 442001.
106. Lalmi, B.; Oughaddou, H.; Enriquez, H.; Kara, A.; Vizzini, S.; Ealet, B.; Aufray, B. Epitaxial Growth of a Silicene Sheet. *Appl. Phys. Lett.* **2010**, *97*, 223109.
107. Zhou, L.; Zhang, J.; Zhuo, Z.; Kou, L.; Ma, W.; Shao, B.; Du, A.; Meng, S.; Frauenheim, T. Novel Excitonic Solar Cells in Phosphorene-TiO_2 Heterostructures with Extraordinary Charge Separation Efficiency. *J. Phys. Chem. Lett.* **2016**, *7*, 1880–1887.
108. Aktürk, E.; Aktürk, O. Ü.; Ciraci, S. Single and Bilayer Bismuthene: Stability at High Temperature and Mechanical and Electronic Properties. *Phys. Rev. B* **2016**, *94*, 014115.
109. Zhou, W.; Yin, Z.; Du, Y.; Huang, X.; Zeng, Z.; Fan, Z.; Liu, H.; Wang, J.; Zhang, H. Synthesis of Few-Layer MoS_2 Nanosheet-Coated TiO_2 Nanobelt Heterostructures for Enhanced Photocatalytic Activities. *Small* **2013**, *9*, 140–147.
110. Feng, B.; Zhang, J.; Zhong, Q.; Li, W.; Li, S.; Li, H.; Cheng, P.; Meng, S.; Chen, L.; Wu, K. Experimental Realization of Two-Dimensional Boron Sheets. *Nat. Chem.* **2016**, *8*, 563–568.
111. Gao, N.; Wu, X.; Jiang, X.; Bai, Y.; Zhao, J. Structure and Stability of Bilayer Borophene: The Roles of Hexagonal Holes and Interlayer Bonding. *FlatChem* **2018**, *7*, 48–54.

112. Padilha, J. E.; Miwa, R. H.; Fazzio, A. Directional Dependence of the Electronic and Transport Properties of 2D Borophene and Borophane. *Phys. Chem. Chem. Phys.* **2016**, *18*, 25491–25496.
113. Mortazavi, B.; Rahaman, O.; Dianat, A.; Rabczuk, T. Mechanical Responses of Borophene Sheets: a First-Principles Study. *Phys. Chem. Chem. Phys.* **2016**, *18*, 27405–27413.
114. Wang, H. F.; Li, Q. F.; Gao, Y.; Miao, F.; Zhou, X. F.; Wan, X. G. Strain Effects on Borophene: Ideal Strength, Negative Possion's Ratio and Phonon Instability. *New J. Phys.* **2016**, *18*, 073016.
115. Liu, Y. X.; Dong, Y. J.; Tang, Z. Y.; Wang, X. F.; Wang, L.; Hou, T. J.; Lin, H. P.; Li, Y. Y. Stable and Metallic Borophene Nanoribbons from First-Principles Calculations. *J. Mater. Chem. C* **2016**, *4*, 6380–6385J..
116. Peng, T.; Zhang, J.; Ray, S.; Ghareh Bagh, F. S.; Fakhouri, H.; Arefi-Khonsari, F.; Lalman, J. A. Optimizing One-Dimensional TiO_2 for Photocatalytic Hydrogen Production from a Water-Ethanol Mixture and Other Electron Donors. *J. Environ. Chem. Eng.* **2019**, *7*, 102868.
117. Wang, J.; Zhang, P.; Li, X.; Zhu, J.; Li, H. Synchronical Pollutant Degradation and H_2 Production on a Ti^{3+}-Doped TiO_2 Visible Photocatalyst with Dominant (001) Facets. *Appl. Catal., B: Environ.* **2013**, *134–135*, 198–204.

Chapter 8

A Collection of Recent Examples of Catalysis Using Carboxylate-Based Metal–Organic Frameworks

Allison M. Rabon, Jared G. Doremus, and Michael C. Young*

Department of Chemistry and Biochemistry, School of Green Chemistry and Engineering, The University of Toledo, Toledo, Ohio 43606, United States

***E-mail: michael.young8@utoledo.edu**

Metal–organic frameworks (MOFs) are a broadly-defined class of self-assembled structures prepared by combining organic linkers with metal-based secondary building units. Although these structures have been used for many applications, being the site for many interesting modes of catalysis is one of the more exciting utilities. In this chapter we review works in the field over the last three years and explore newer approaches to performing catalysis with these carboxylate-based metal–organic frameworks at the secondary building unit (SBU). This includes catalysis using the SBU or node, catalysis using post-synthetically introduced moieties at the SBU (metal or organic), and bifunctional MOFs, using both the node and ligand for catalysis.

Introduction

Metal–organic frameworks (MOFs) are an increasingly important class of supramolecular compounds that are formed via the self-assembly of organic linkers with metals or metal-containing secondary building units (SBUs) (*1*, *2*). The linkers, or struts, are typically di- or polytopic ligands based on carboxylates, although heterocycle-based ligands are also frequently used, along with nitriles, or combinations of multiple of these Lewis basic sites (Figure 1) (*3*–*7*).

A key factor of the use of and interest in these structures is their potential to exhibit permanent porosity and, therefore, high internal surface area (*8*). As a result, many applications have been explored that exploit these properties including use for gas storage (*8*–*10*), gas separation (*11*, *12*), solid-phase microextraction (*13*, *14*), water purification (*15*, *16*), toxic chemical (*17*–*19*) and heavy metal remediation (*20*, *21*), chemical sensing (*22*, *23*), drug delivery (*24*, *25*), water splitting (*26*–*28*), and photovoltaics (*29*, *30*), just to scratch the surface. Zeolites, a class of inorganic compounds that are themselves revered for their many uses, have similar applications (*31*). MOFs are similar to zeolites; however, the ability to modify both the SBU as well as the organic ligand gives MOFs extensive tailorability, affording a wider array of structures. As a result, MOFs have largely overtaken zeolites for many applications (*32*, *33*).

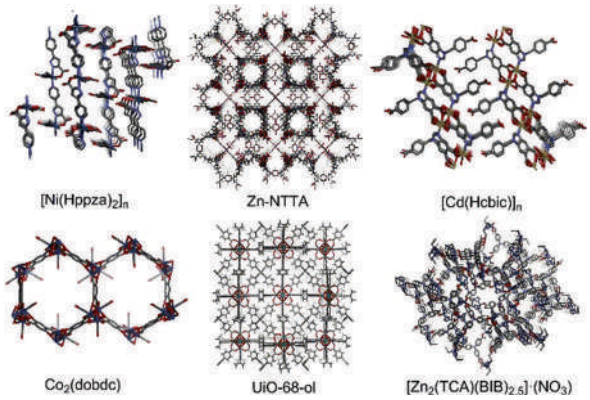

Figure 1. Six examples of different MOF motifs displaying porosity and periodicity.

In principle, the term metal–organic framework is meant to refer to a three-dimensional (3D) structure with pores, making them a specific subclass of coordination polymer (*34*). Robson et al. reported the first intentionally designed 3D coordination polymers using cyanide decorated struts (Figure 2, **1**). The $[Cu[C(C_6H_4\text{-}CN)_4]BF_4{\cdot}xC_6H_5NO_2]_n$ coordination network **1** exhibited an adamantane-like framework with solvent-filled cavities. This diamondoid framework initially demonstrated the possibility of a stable 3D porous coordination scaffold (*35*).

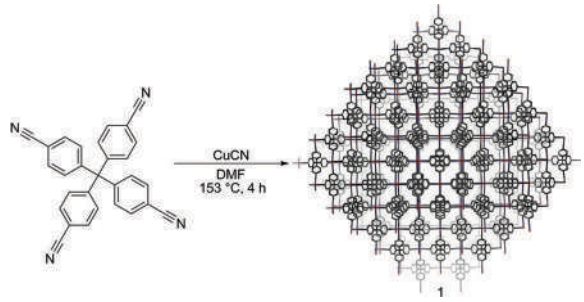

*Figure 2. Robson network containing a T-symmetry tetranitrile and Cu^I (**1**).*

The first robust metal–organic framework followed a few years later from Omar Yaghi's lab, the now infamous metal–organic framework 5, or MOF-5 (**2**) (Figure 3) (*36*). Yaghi exploited zinc acetate's ability to form a 3D node of the formula $[Zn_4(\mu_4\text{-}O)(\mu_2,\kappa O{:}\kappa O'\text{-}OAc)_6]$, but replaced the acetate with ditopic terephthalic acids (H_2BDC) that could bridge each of the tetrahedral zinc SBUs. As a consequence, a viable 3D coordination polymer was obtained that could retain its shape even after evacuation of solvent within the pores. This advance cannot be overstated, as it allowed the MOF to be emptied for subsequent gas absorption. As a heterogeneous system, it is worth noting that framework **2** has been prepared using various procedures, each giving slightly different properties (*37–41*).

Since the disclosure of MOF-5, thousands of new porous coordination polymers have been described and reported in the literature. One of the biggest challenges in preparing MOFs for different applications has been synthesizing frameworks that are stable to water (*42–44*) and moderately strong Lewis bases. Since MOFs are prepared via self-assembly, it makes sense that they can also be disassembled through similar processes. Zinc-based MOFs were originally quite popular, but it was soon realized that the weak bonds formed between late transition metals and

carboxylates were not conducive to overly stable structures (*45*). As a result, recent approaches often target more robust self-assemblages. Frameworks with increased stability can be accessed using larger transition metals (generally these are more resistant to ligand substitution) (*46*, *47*), and in the case of carboxylate ligands earlier transition metals are also known to form more robust complexes. With more stable MOFs in hand, their utility in catalysis has also improved dramatically. There have been many overarching reviews on MOF catalysis that are already written and readily available (*48*–*56*). More specifically, well-refined reviews have been published on MOF catalysis as well, including: using defect sites on MOFs (*57*, *58*), post-synthetically modified MOFs (*59*–*64*), use of encapsulated nanoparticles in MOFs (*65*–*67*), incorporated molecular catalysts (*68*), integrated porphyrin MOFs (*69*), and biomimetic MOFs (*70*, *71*), among other categories. This chapter will not try to reproduce these other reports, but instead provide a brief introduction to recent examples of catalysis using carboxylate-based MOFs between 2015–2018. For non-MOF chemists, this chapter's goal is to introduce the approaches to both synthesis and catalysis with these porous structures. This chapter will not be an exhaustive resource, but will highlight largely ignored references in contemporary review articles, as well as particularly noteworthy examples that have been well referenced.

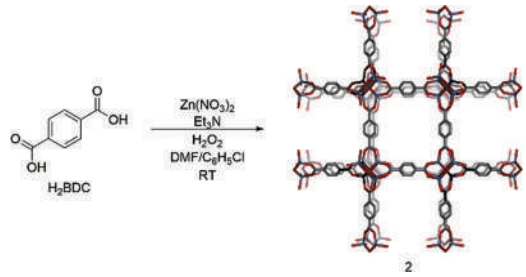

*Figure 3. Initial synthesis of MOF-5 (***2***), the first stable 3D porous MOF.*

Metal–Organic Framework Nodes as Catalysts

One of the simplest approaches to using metal–organic frameworks in catalysis is to bring two reactive components together to accelerate a reaction. This strategy is fairly common place in other types of supramolecular hosts; self-assembled metal–organic polyhedra (*72*, *73*), cavitands (*74*, *75*), and hydrogen-bonded assemblies (*76*, *77*) are well-precedented as catalysts for a variety of cycloaddition and electrophilic aromatic substitution reactions. In these small-volume hosts, transformations are often achieved by forcing the reactive components into close proximity, thereby facilitating their reactivity. In contrast, MOFs have much larger cavities that make it more challenging to achieve such reactions merely by coencapsulation. As a result, different strategies are needed to use MOFs as catalysts. Unlike metal–organic polyhdera, MOFs have multiple porous sites for guest encapsulation, including pores and secondary channels. Furthermore, unlike metal–organic polyhedral, MOFs can often contain defect sites, providing either Lewis acid or Lewis base sites for reversible bond formation or electrostatic interactions with substrates. One of the most appealing catalytic roles of MOFs is to use the nodes as catalysts. Many of the SBUs used in the self-assembly of MOFs involve Lewis acidic metals, including zinc, copper, titanium, zirconium, and hafnium. Manipulating the Lewis acidity of the structural metals, MOFs metal clusters can be exploited in order to bind various gases and small molecules and achieve catalysis.

Paddlewheels as Catalytically Active Sites

One unique class of MOFs are prepared by making binuclear paddlewheels, where two metals are bridged by four carboxylates. These are most commonly made with late transition metals, such as Zn, Cu, or Rh, and the metals are usually in either the +2 or +3 oxidation state. The benefit of these paddlewheels is their ability to provide an axial coordination site that can be exploited for chemistry. Alternatively, many frameworks will contain what are known as defect sites – locations where either a metal node or one or more ligand is absent. Both strategies can be effective in promoting catalysis. The most conspicuous type of catalysis to perform is to simply use these metals as Lewis acids. Although not typically as acidic as early transition metals, numerous examples have been published of these late transition metals catalyzing reactions. Paddlewheel complexes have been shown to exhibit Lewis acidity favorable for cycloaddition and silylcyanation chemistry, while defective paddlewheel complexes can provide redox active sites useful for hydrogenation with endogeneous or exogeneous bases, and even some photocatalyzed transformations. This section will focus on using paddlewheels to promoting CO_2 cycloaddition and photocatalysis featuring subsections on porphyrin-based and 1,1′-bi-2-naphthol (BINOL)-based MOFs.

Lewis Acid Catalytic Sites for CO_2 Cycloaddition

Sustainable chemistry toward reducing, capture, and conversion of CO_2 emissions has driven recent accounts of Lewis acid sites at paddlewheel SBUs in MOFs. In general, MOFs are very advantageous for this type of reaction because they are porous and have been found to have, in some cases, the ability to uptake enormous quantities of gases (*78*). In the case of CO_2 cycloaddition, CO_2 gas adsorbed within the MOF is used to promote cycloaddition of epoxides. Although typically high CO_2 pressure is required for this transformation (*79*), the MOF essentially provides a high localized amount of CO_2 through gas sorption. The planar geometry of the paddlewheel SBU provides open metal sites in which the unobstructed axial face(s) of each metal center are free to bind molecules and catalyze reactions. For the CO_2 cycloaddition of epoxides, the epoxide binds to the open coordination site while a cocatalyst, such as tetrabutylammonium bromide (TBAB), opens the epoxide (Figure 4). The resulting alkoxide is partially stabilized by the transition metal, preventing rapid closing to reform the epoxide. In the presence of CO_2, the alkoxide can attack, generating a carbonate anion which is also stabilized by the transition metal. Eventually this anion will undergo S_N2 displacement of the bromide, generating the desired cyclic carbonate and regenerating the halide cocatalyst.

Zhao et al. provide one example of this transformation catalyzed by an MOF. Using a C_{2v} symmetric, tritopic ligand, they were able to assemble a framework with both a characteristic binodal Zn_2 paddlewheel and a secondary Zn_4O tetrahedral SBU to form a cubic 3D coordination network called 1-Zn (Figure 5a, **3(Zn)**), which was isolated as a colorless material (*80*). The framework was stable up to 400 °C, and by single crystal to single crystal transformation through metal exchange could be converted into a bimetallic framework containing both Zn^{II} and either Cu^{II} or Co^{II} cations. The Cu^{II} mixed framework, **3(Cu)**, was observed as green crystals while the Co^{II}-containing **3(Co)** was observed as pink crystals. Both the Cu^{II} and Co^{II}-incorporating frameworks showed a slight increase in CO_2 uptake as compared to pristine **3(Zn)**. However, when the authors investigated the frameworks for catalyzing the cycloaddition of CO_2 with propylene epoxide to form propylene

carbonate (Figure 5b), **3(Zn)** exhibited a turn over frequency two times greater than **3(Co)** and three times more than **3(Cu)**. Using the Lewis acidity of the $[Zn_2(COO)_4]$ nodes (the tetrahedral nodes are coordinatively saturated, and therefore not useful for catalysis), the epoxide is activated such that the addition of Bu_4NBr can open the epoxide, which then attacks carbon dioxide bound to another metal center (in line with the generic mechanism in Figure 4). This system allows transformation to proceed at a relatively mild 12 bar of CO_2 pressure.

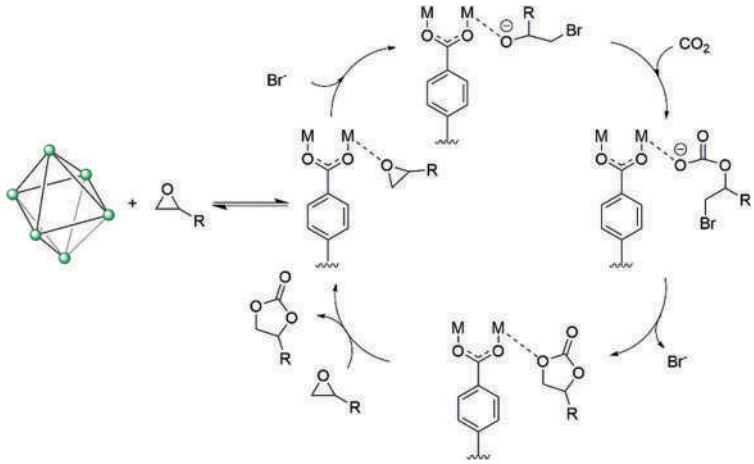

Figure 4. Generic cycle for CO_2 and epoxide cycloaddition.

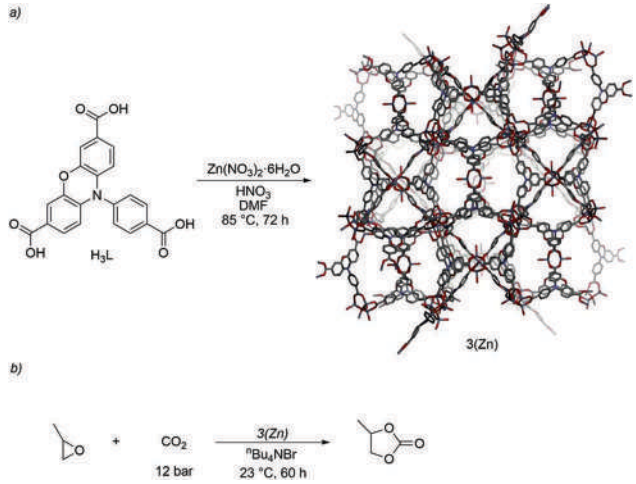

*Figure 5. A Zn-MOF (**3(Zn)**) for cyclization of epoxides with carbon dioxide. (a) Synthesis and X-ray structure of **3(Zn)**. (b) Application of **3(Zn)** for the cycloaddition of CO_2 and propylene oxide.*

Another example comes from Jian-Fang Ma et al., who used a porphyrin-based MOF $[Mn_5L(H_2O)_6{\cdot}(DMA)_2]{\cdot}5DMA{\cdot}4C_2H_5OH$ (**4**) built from manganese and an octacarboxylic acid ligand, 5,10,15,20-tetra(4-(3,5-dicarboxylphenoxy)- phenyl)porphyrin ($H_{10}L$) and coordinated DMA (*N*,*N*-dimethylacetamide) (Figure 6) (*81*). This porphyrin-based MOF stacks together into rutile-like nets and its SBUs form a paddlewheel configuration that have open axial coordination sites to promote catalysis. In addition to the axial coordination sites on the Mn^{II} paddlewheels, the porphyrin moiety of **4** incorporates an additional Mn^{II}, promoting high Mn^{II} density and additional

Lewis acid sites. Unsurprisingly, **4** displayed great activity for the cyclization of CO_2 with epoxides in the presence of Bu_4NBr as a cocatalyst, and the heterogeneous catalyst was displayed to have good reusability along with being easy to separate from the reaction mixture. Several epoxides could be used in the reaction, including epichlorohydrin.

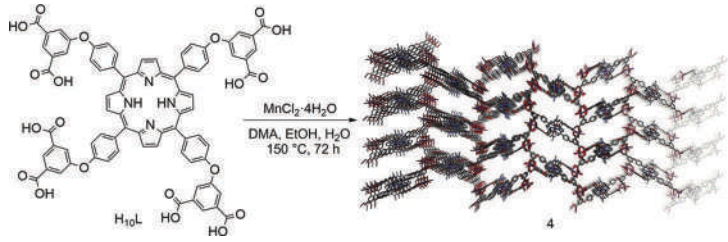

Figure 6. Synthesis of Mn porphyrin MOF ***4****.*

While carbonates are a common target for CO_2-incorporation, Shengqian Ma et al. targeted the less common cyclization of aziridines with CO_2 using the Cu^{II}-based framework **5** (*82*). Their metalloporphyrin framework, named MMPF-10, was obtained as dark red crystals by using a solvothermal synthesis between tetrakis-3,5-bis[(4-carboxy)phenyl]phenyl porphine and $Cu(NO_3)_2{\cdot}2.5H_2O$ (Figure 7a). Access to the Cu^{II} centers allows for Lewis acidic behavior. Compared with the nonporphyrin-containing Cu^{II} paddlewheel complex HKUST-1 (*83*), the authors were able to catalyze the synthesis of 3-methyl-5-phenyloxazolidin-2-one in greater yield using **5**, suggesting that both the Lewis acidic copper paddlewheels and the copper-metallated porphyrin play an important role during the transformation. The reaction could be carried out with 0.625 mol% of catalyst and CO_2 pressures as low as 0.1 MPa (1 bar), nearly complete conversion was achieved at approximately 2 bar (Figure 7b).

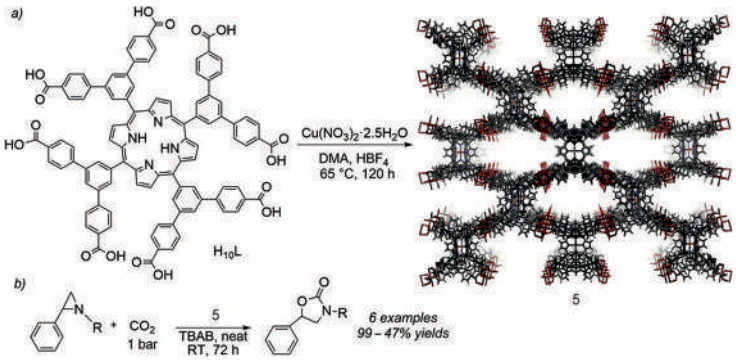

Figure 7. Cu porphyrin paddlewheel MOF ***5****. (a) Synthesis of* ***5****. (b) Cycloaddition reaction of substituted aziridines with CO_2 catalyzed by* ***5****.*

Photocatalysis

MOFs can also be prepared with photosensitive moieties and have therefore garnered attention for a variety of photocatalysis applications (*84–86*). The large surface area of MOFs, as well as the use of ligands with large π-systems, enhance their potential for photocatalysis as they have a large number of easily accessible and high-density sites inside the structure, while also able to absorb light from across the UV–vis spectrum. Highly crystalline MOFs with few defect sites have reduced

centers for recombination, while some MOFs can utilize their defect sites to promote photocatalysis. The paddlewheel SBU promotes photocatalytic activity much in the same way it did for CO_2 cycloaddition. Open metal sites on the axial faces are unobstructed and provide opportunity for high-density binding across the MOF infrastructure. In addition, porphyrin-based MOFs have recently become popular for photocatalytic applications, as they can absorb light from almost the entire range of the visible spectrum.

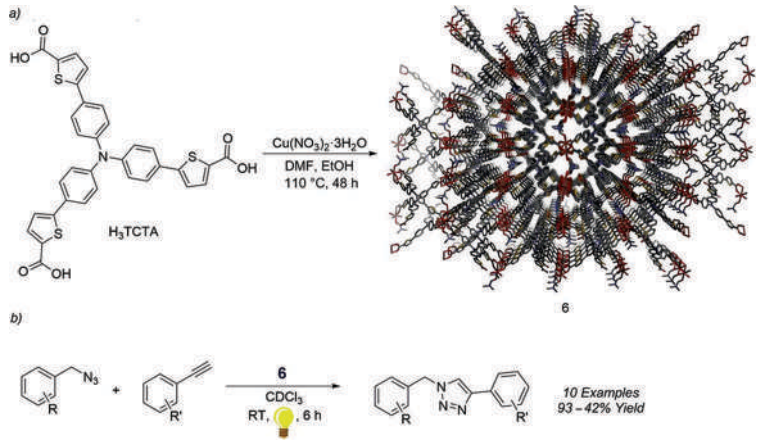

*Figure 8. An intercalated two-dimensional (2D) Cu^{II} framework (**6**). (a) Synthesis of **6** from H_3TCTA and Cu^{II} precursor. (b) Photocatalyzed CuAAC reactions using **6**.*

MOFs based on Cu^{II}-paddlewheels are common, but one of the most important reactions currently catalyzed by copper, Sharpless' Cu-assisted azide–alkyne cyclization (also known as the "click" reaction or CuAAC), requires Cu^{I} (*87*). However, recent work from Duan et al. has demonstrated a method to perform these reactions with a Cu^{II}-framework under photoirradiation (*88*). First the group prepared the 2D framework **6** by self-assembly of the H_3TCTA ligand (5,5′,5″-(nitrilotris(benzene-4,1-diyl))-tris(thiophene-2-carboxylic acid) with Cu^{II} (Figure 8a). The 2D framework **6** became intercalated during the assembly process to generate a 3D structure with sufficiently-sized pores to allow reagents to diffuse into the framework. The addition of thiophenes into the linker proved critical for the photoactivity of the catalysts, shifting the maximum absorption wavelength to 450 nm (compared to 390 nm for the shorter 4,4',4''-tricarboxytriphenylamine variant). Screening with the catalysts in hand showed that use of chloroform-*d* was satisfactory to achieve photocatalytic CuAAC reactions on a variety of substrates in moderate to great yields (Figure 8b). It is worth mentioning that while in principle MOF refers to 3D porous structures, in practice many formally lower- dimensional structures can still lead to 3D porous structures upon packing, leaving the use of the term metal–organic framework open for discussion (*89*, *90*).

Another example of a 2D layered framework that can interchelate and which could be used for photocatalysis was shown by Zheng et al. (*91*). In their report, the authors prepared a novel Co^{II} paddlewheel with both bridging carboxylate as well as pyridine groups to give **7**. The $[Co(bpba)(bdc)_{1/2}]_n$ framework **7** was synthesized via thermosolvolysis between 3,5-bis(pyridin-4-ylmethoxy)benzoic acid (bpba), terephthalic acid, and $Co(NO_3)_2$ in DMF to form purple prismatic crystals of the space group $P\bar{1}$ (Figure 9). Upon photoirradiation, **7** was able to photodegrade dyes in solution, with overall yields of 56% for methyl orange, 95% for methyl blue, 41% for neutral

red, 84% for methylene blue, while safranine T was fully degraded. Another notable feature of the photodegradation catalyst **7** was the ability to be recycled at least three times without affecting the overall degradation rates, and the crystallinity was unperturbed as evidenced by powder X-ray diffraction.

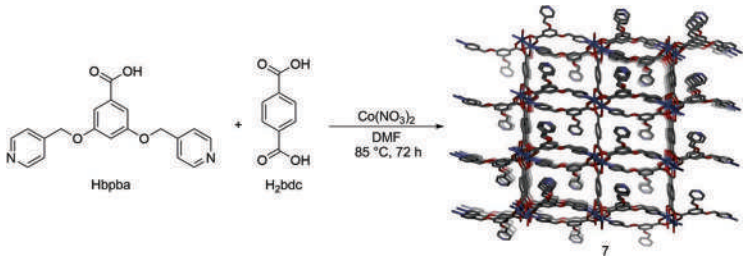

*Figure 9. Co paddlewheel **7**.*

Lin et al. designed a Zn-porphyrin Ru paddlewheel framework (**8**) that was also an efficient photocatalyst (92). The solvothermal synthesis between ruthenium chloride and 5,10,15,20-tetra(p-benzoic acid)porphyrinatozinc (H_4TBP-Zn) in DMF afforded a purple precipitate of the stoichiometry $[Ru_2(TBP\text{-}Zn)(H_2O)_2]Cl_2$ (Figure 10).

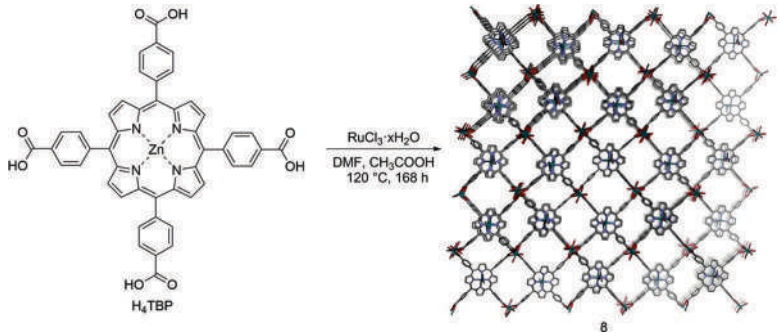

*Figure 10. Synthesis of Zn^{II} porphyrin Ru paddlewheel framework **8**.*

Although a Zn^{II}-deficient version of the framework was only able to catalyze hydrogen evolution reactions in neutral water at a rate of 0.13 $mmol \cdot h^{-1} \cdot g^{-1}$, framework **8** had considerably better activity at 0.24 $mmol \cdot h^{-1} \cdot g^{-1}$. The authors attributed the improved activity of **8** to the increased photosensitization ability of the TBP-Zn ligand compared with the free porphyrin. After 72 h irradiation Ru-TBP gave a TON 21.2, while **8** gave a TON of 39.4, compared to a lowly TON of 1.4 for the homogeneous equivalent.

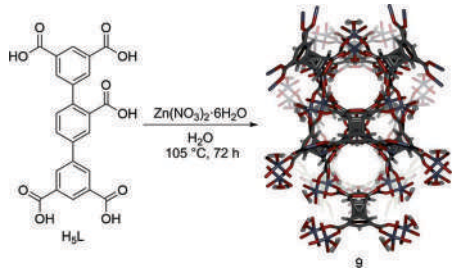

*Figure 11. Synthesis of Zn^{II} paddlewheel framework **9**.*

Another example of an MOF photocatalyst for degrading organic dyes was prepared from a low symmetry pentacarboxylate ligand and Zn^{II} (*93*). The 3D coordination network $[[Zn_2(HL)(H_2O)_2]\cdot H_2O]_n$ (**9**) was prepared under green thermosolvolysis in only water as solvent to give a colorless framework (Figure 11). Photocatalyst **9** was able to degrade methyl violet up to 77.8% after 100 m under UV irradiation, while rhodamine B could be degraded up to 53.2% in the same time frame. Control experiments without the catalyst showed that this represented an increase of 740% for methyl violet degradation, and 780% for rhodamine B. The authors further demonstrated that **9** may be reused up to five times without noticeable reduction of degradation potential.

Based on a 2D Zn porphyrin paddlewheel framework originally developed by Choe et. al. (*94*), Kawamoto et al. (*95*) demonstrated photoactivity by assembling a similar framework using rhodium instead of Zn^{II}, as the structural metal for the paddlewheel SBUs. The framework was synthesized via solvothermal reaction of $[Rh_2(O_2CCH_3)_4(H_2O)_2]$ and zinc tetra(4-carboxyphenyl)porphyrin (Zn-TCPP) to afford a purple hygroscopic powder with the stoichiometry $[Rh_2(Zn\text{-}TCPP)(H_2O)_{7.5}]$. A Langmuir surface area of 689.8 m^2g^{-1} and a pore volume of 0.22 cm^3g^{-1} were calculated after obtaining N_2 adsorption isotherms. Pore size was then estimated from the crystal structures to assess the similarity of the Rh paddlewheel, 4.7 Å, to the Zn paddlewheel homologue, 4.4 Å, finding only a 0.3 Å difference between the twin frameworks. The framework notably exhibits permanent porosity and noticeable photoinduced charge and/or energy transfer from the Zn porphyrin to the dirhodium center paving the way for applications for this framework as a potential photocatalyst.

*Figure 12. Zn paddlewheel porphyrin / 1,4-diazabicyclo[2.2.2]octane framework **11**.*

The same year Hasobe and team members synthesized two different Zn porphyrin paddlewheel frameworks by combination of [5,10,15,20-tetrakis(4-carboxyphenyl)-porphyrinato-zinc^{II} and 1,4-diazabicyclo[2.2.2]octane (DABCO) ligands (*96*). Two different synthesis methods, solvothermal and colloidal, were chosen to demonstrate other regioselectivities of assembly and subsequently afforded two different crystal structures. The solvothermal method produced an unusual arrangement with the ZnTCPP forming a 2D network with DABCO with one side of the azine coordinated to the open site of the Zn^{II} paddlewheel, while the other azine coordinated to the open site of the ZnTCPP ligand, giving a 3D structure (**10**). Meanwhile, colloidal synthesis gave a more traditional structure with the 2D ZnTCPP paddlewheels, bridged by the DABCO ligands, to give **11** (Figure 12). **10** was judged to be less efficient for photoinduced electron transfer than **11** considering **10** was so closely packed together and exhibited significantly shorter excited state lifetimes.

Paddlewheel Frameworks for Other Transition Metal-Catalyzed Transformations

In addition to catalyzing the cycloaddition between various strained substrates and gases, paddlewheel frameworks have also been used to catalyze transformations of nongaseous substrates. In this capacity, the frameworks can perform standard Lewis acid catalysis or redox chemistry, to facilitate a variety of transformations. Although privileged homogeneous catalysts such as Pd and Pt are rarely used to support self-assembly of MOFs, metals such as Rh and Cu are widely used and have seen numerous modes of catalytic activity.

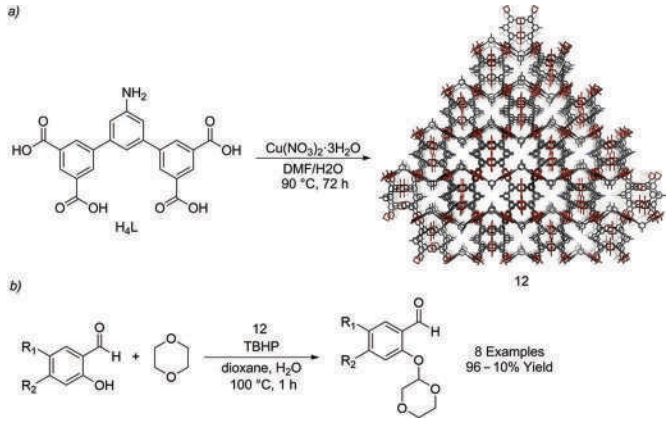

Figure 13. Cu paddlewheel ***12*** *for C–H activation. (a) Synthesis of* ***12****. (b) Use of* ***12*** *to catalyze the C–H oxidation reaction between salicylaldehydes and 1,4-dioxane.*

A Cu^{II} paddlewheel MOF synthesized by Bharadwaj et al. (Figure 13a, **12**) (*97*) was recently investigated for its application in catalyzing C–heteroatom coupling reactions (Figure 13b) (*98*). Traditionally, C–H bond functionalization is challenging due to the inertness of these bonds. This paper displays facile C–H bond activation in cleaner, greener, and faster coupling reactions. Their catalyst performs a cross-dehydrogenative coupling reaction of 2-hydroxybenzaldehydes with 1,4-dioxane with much higher efficiency than homogeneous Cu catalysts.

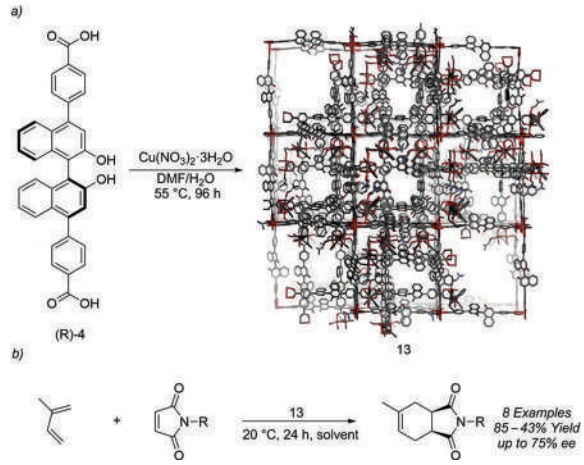

Figure 14. Chiral Cu-MOF ***13****. (a) Synthesis of* ***13*** *from a BINOL ligand and* Cu^{II}*. (b) Use of* ***13*** *to catalyze the asymmetric Diels–Alder reaction between isoprene and maleimides.*

Another Cu-based paddlewheel where the Lewis acidic paddlewheel is integral for catalysis is the [Cu_2(5,5′-BDA)$_2$] MOF (5,5′-H_2BDA is 2,2′-dihydroxy-1,1′-binaphthalene-5,5′-dicarboxylic acid) (*99*). The corresponding framework was able to affect asymmetric amination of epoxides by adding a chiral BINOL core to the linker. However, the presence of protonated BINOL led to some question if this system was truly promoted by Cu, or potentially only by hydrogen bonding with the BINOL hydroxyl group. Though the initial report was from 2010, it was only recently that quantum mechanical and molecular mechanical methods were applied to this system, which show that the activation of the epoxide does occur at a Cu^{II} center (*100*). What is noteworthy about this conclusion is that the computational methods point to an intermediate Cu^{II}-alkoxide bond that causes one of the carboxylate ligands to be displaced. This particular framework has also been used in the past for kinetic resolution of epoxides (*99*), and more recently as a stationary phase for chiral high-performance liquid chromatography separation (*101*).

These chiral paddlewheels are also capable of promoting other cycloaddition reactions. Extending the 5,5′-H_2BDA ligand by insertion of phenyl groups between the BINOL and carboxylic acid moieties gave rise to a ligand that forms larger analogues. Using what they have called (*R*)-CuMOF-2 (**13**) in a separate paper (Figure 14a), Tanaka et al. prepared an interpenetrated structure using this larger chiral BINOL ligand (*102*). They then demonstrated that this Cu^{II} paddlewheel can also affect the asymmetric Diels–Alder reaction between isoprene and maleimides (Figure 14b). The reaction exhibited significant solvent effects, with ethyl acetate serving as the best solvent in terms of the observed enantiomeric excess. Although the reason for this is not clear at present, less polar solvents such as *n*-hexane and toluene, or more polar solvents such as methanol or ethanol, gave lower enantioselectivities.

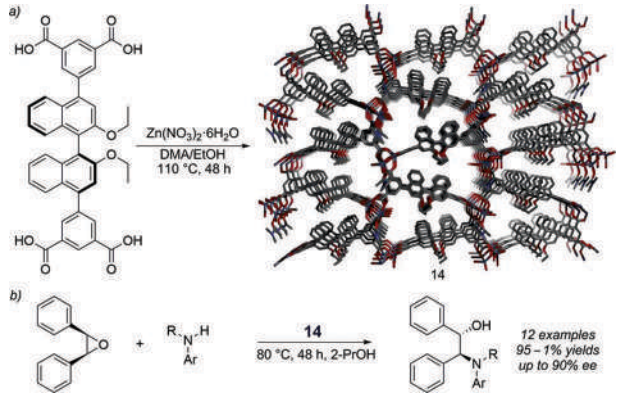

Figure 15. Chiral Zn-MOF ***14****. (a) Synthesis and X-ray structure of* ***14****. (b) Application of* ***14*** *for the enantioselective ring-opening of cis-stilbene oxide by aromatic amines.*

Extending the 5,5′-H_2BDA ligand by insertion of phenyl groups between the BINOL and increasing to tetratopic carboxylic acid moieties gave rise to a ligand that forms larger analogues, although the overall structure is retained in what the authors call (*R*)-CuMOF-2 (*99*). Alternatively, instead of using a benzoic acid group to self-assemble with Cu^{II}, the authors also prepared a 3,5-dibenzoate variant that was self-assembled with Zn^{II} to form what they called (*R*)-ZnMOF-4 (Figure 15a, **14**) (*103*). Unlike the previous MOFs that Tanaka studied with BINOL-based ligands, this tetracarboxylate forms a tricarboxylate-dizinc node, with a fourth carboxylate failing to bridge between both zinc centers. Using this framework, the efficiency and observed enantiomeric excess

of the epoxide amination was increased (possibly due to the lower coordination number of the zinc center without four coordinated carboxylates), giving enantiomeric excess values >90% (Figure 15b).

Metal–Oxo Clusters as Catalytic Sites

A major challenge with late transition metal-based MOFs is that they are not very tolerant of polar substrates or solvents. This prevents the use of strong acids or bases in reactions and, in many cases, even water exposure is a problem. Scientists have turned toward early transition-metal-based MOFs to obviate these challenges. Although simple paddlewheels are uncommon in this area, a number of metal–oxo SBUs have been developed show much greater stability. One of the most popular of these is the UiO (University of Oslo) family, which consists of linear diacid linkers combined with Zr^{IV} to give $[Zr_6(\mu_3\text{-}OH)_4(\mu_3\text{-}O)_4(COO)_{12}]_n$ nodes (*104*). These frameworks are at the forefront of many catalytic applications because of the stronger metal–ligand bonds, leading to their characteristic stability. These structures are often riddled with defect sites as a consequence of the decreased reversibility of bond formation. The method of synthesis therefore becomes critical to determining the number of defect sites, although the ability to control the number of defect sites does mean that it is possible to tune the relative concentration of active metal centers. This section will delve into utilization of metal oxide clusters as sites for catalytic transformations.

Lewis Acid Catalysis at Metal–Oxo Nodes

As detailed previously, the Lewis acidity of the structural metals used to self-assemble MOFs is a key factor why MOFs are a great choice for heterogeneous catalysts. MOFs assembled from metal–oxo clusters have an increased local concentration of metal ions, and thus the strength of the cluster of Lewis acidic sites can be significantly greater than a single Lewis acidic site. The increased strength allows the MOFs to activate substrates bearing more weakly Lewis acidic functional groups, such as esters and phosphonates. Unlike paddlewheel complexes, the metal–oxo SBUs are more likely to have defect sites and these can be tailored to facilitate both Lewis acidic and Lewis basic catalysis.

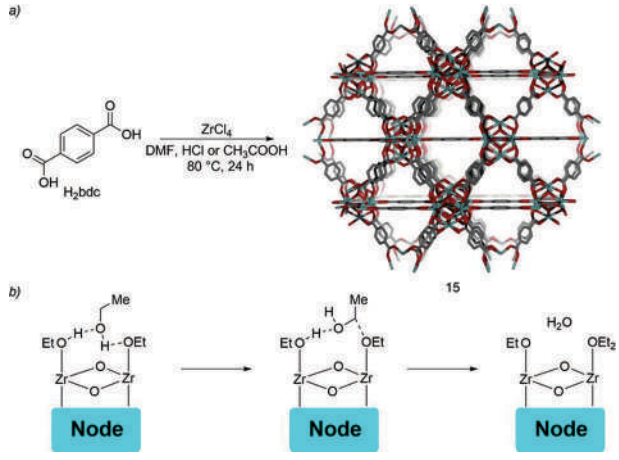

*Figure 16. The Zr^{IV}–oxo framework **15**. (a) Synthesis of **15** from 1,4-benzene dicarboxylic acid and $ZrCl_4$. (b) Proposed mechanism of ethanol dehydration catalyzed by **15**.*

A recent paper from the Gates lab has demonstrated how UiO-66 (*105*) (Figure 16a, **15**), which is prepared from $ZrCl_4$ and terephthalic acid, can be used to promote the dehydration of ethanol (*106*). Using **15**, the authors report that at 250 °C, ethanol can be converted to diethyl ether at the rate of 2.43 x 10^6 mols (g of catalyst)$^{-1}s^{-1}$. Performing this reaction would be problematic using a late transition-metal-based framework since both ethanol and the water produced would likely degrade the MOF under the reaction conditions. With the help of computational expertise from the Cramer and Gagliardi groups, it was determined that this transformation most likely occurs at a double defect site, meaning that two adjacent metals are coordinatively unsaturated (Figure 16b). This would occur when an organic strut is completely missing, as opposed to having the strut coordinated in a *κO,κO'*-fashion to a single Zr^{IV} metal center. This suggests, at least in some cases, that more defects can be better in terms of the overall catalytic ability of these frameworks.

In another example using **15**, Speybroeck et al. explored the Fischer esterification of levulinic acid with ethanol (Figure 17a) (*107*). Although such reactions had previously been explored using **15** (*108*), these authors also looked at the effect of hydrated versus dehydrated solvent on the reaction rate. Similar to the work of Gates, Cramer, and Gagliardi, theoretical treatment of the system suggested that a double defect site was the most energetically favorable pathway in both cases. The fully dehydrated MOF model began by deprotonation of the alcohol by the dehydrated node. Meanwhile, the hydrated pathway began by Lewis acid-assisted activation of the carboxylic acid, as well as proton-assisted stabilization of the carboxyl oxygen, facilitating the attack of the carbonyl by the alcohol (Figure 17b). The alcohol is simultaneously activated by a pendant hydroxyl group on an adjacent Zr^{IV} center.

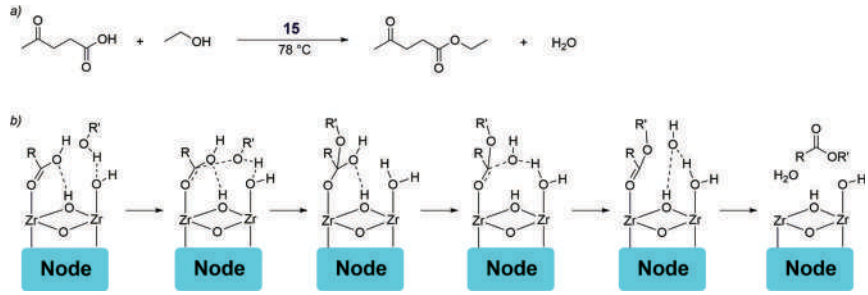

*Figure 17. Use of **15** for Fischer esterification. (a) Net transformation of levulinc acid to ethyl levulinate with **15** as catalyst. (b) Proposed mechanism for Fischer esterification using **15**.*

Although the UiO's $[Zr_6(\mu_3\text{-}OH)_4(\mu_3\text{-}O)_4(COO)_{12}]$ node is robust, Lin et al. has recently disclosed an alternative node that can be prepared from the same reagents, now giving rise to a $[Zr_{12}(\mu_3\text{-}OH)_8(\mu_3\text{-}O)_8(COO)_{18}]$ species (Figure 18a, **16**) (*109*). While this species has not been used for catalysis without further modifications, Momeni and Cramer predict that it could produce much greater catalytic activity for the hydrolysis of the nerve gas sarin compared to other MOFs (**15** (UiO-66), and members of the related NU family) (*110*). Similar to the previous mechanisms, coordination to a vacant Zr center brings the phosphonyl species in close proximity to an adjacent Zr–OH, which brings a water molecule in via hydrogen bonding (Figure 18b). The activated phosphonyl is attacked by this water, while the adjacent OH stabilizes the extra proton. Ultimately the P^V undergoes HF elimination to produce the less toxic phosphonate species.

Metal–oxo complexes do not have to be as large as the Zr_6 or Zr_{12} node. Relatively simple SBUs can also be used, such as in $[In_3(O)(btb)_2(HCOO)(solvent)]_n$ (H_3btb = 1,3,5-tris(4-carboxyphenyl)benzene acid), where the solvent is either water, methanol, or ethanol (*111*). Although indium is just past group 12 on the periodic table, it generally forms stronger complexes with oxygen ligands than zinc does (the same can be said of the smaller metallic congeners of group 13, gallium and aluminum), and thus it can still be useful for catalysis under harsher conditions. In this case, the $[In_3(O)(btb)_2(HCOO)(solvent)]$, or InPF-110 (Figure 19a, **17**), was found to be useful in catalyzing the Strecker multicomponent reaction. This reaction usually gives poor yields when the electrophile is a ketone rather than an aldehyde; however, using **17**, the authors were able to show a reasonable substrate scope for the transformation with a variety of aryl and aliphatic ketones, as well as using an assortment of electron rich anilines (Figure 19b). Interestingly, the solvent used to wash or activate **17** prior to the reactions made a difference, and in general using methanol gave rise to superior catalytic activity compared to ethanol, although the authors did not elaborate (nor is it clear) why this might be.

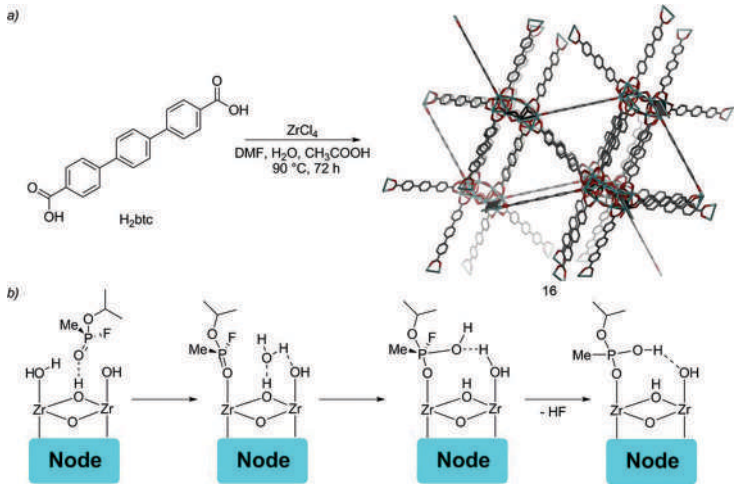

*Figure 18. An expanded node Zr^{IV}–Oxo-based MOF. (a) Synthesis of **16** using $ZrCl_4$ and 4,4"-terphenylene dicarboxylic acid. (b) Proposed application/mechanism of sarin hydrolysis promoted by **16**.*

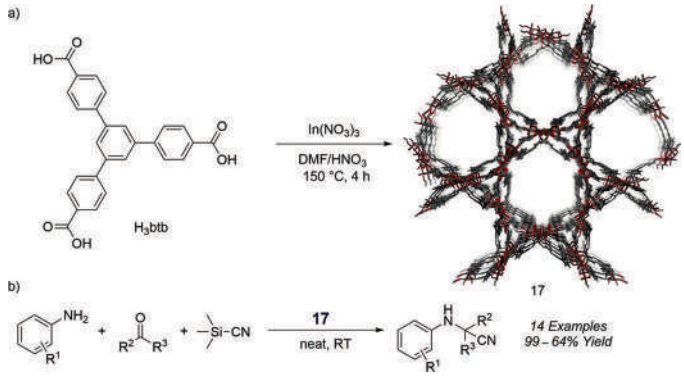

*Figure 19. In-MOF **17**. (a) Synthesis of **17** from a tritopic ligand and In^{III} precursor. (b) A multicomponent reaction catalyzed by **17**.*

Redox Active Metal–Oxo Frameworks

As previously mentioned, MOFs have the potential to be redox active due to their ability to accommodate a diverse range of metal clusters, organic ligands, and even guest molecules. When higher order polynuclear metal–oxos are used, there are multiple redox active metals in close proximity. While many of these MOFs are based on metals like Ti^{IV}, Zr^{IV}, Hf^{IV}, and even various lanthanides that generally have negligible redox chemistry, reduced forms can be stabilized and readily accessible under mild conditions inside of these clusters' single-electron.

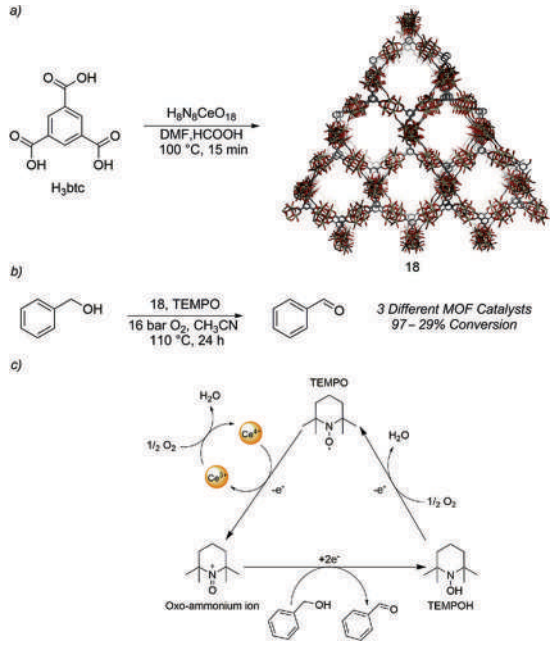

*Figure 20. Cerium Framework **18**. (a) Synthesis of **18** from trimesic acid and ceric ammonium nitrate. (b) Oxidation of benzyl alcohol to benzaldehyde catalyzed by **18** and TEMPO. (c) Proposed mechanism of the **18**/TEMPO-catalyzed oxidation of benzyl alcohol.*

A popular class of redox active MOFs are prepared from Ce^{IV} salts. Interestingly, the combination of Ce^{IV} with linear diacids provides access to the Ce-UiO family, which are isostructural with the Zr-based UiOs except with slightly expanded bond distances owing to the larger size of Ce^{IV} compared with Zr^{IV}. The structure of the Ce-UiO-66 species had to be deduced through Rietveld refinement of X-ray powder diffraction data, owing to the irreversibility and subsequent stability of the self-assembly which made growing X-ray diffraction quality crystals challenging. Due to the use of Ce^{IV} in ceric ammonium nitrate (CAN) as an oxidant in organic synthesis, Stock et al. explored the use of Ce-UiO-66 for the oxidation of benzyl alcohol to benzaldehyde. The authors found that by activating the framework at 220 °C and by including a catalytic amount of (2,2,6,6-tetramethylpiperidin-1-yl)oxyl (TEMPO), the transformation could be achieved in up to 29% yield (*112*). Later work by the same group demonstrated that this could be dramatically improved by switching to the Ce MOF-808 framework **18** (Figure 20a) (*113*). The catalytic cycle proposed involves a $Ce^{IV} \rightarrow Ce^{III}$ cycle that oxidizes TEMPO to generate the active oxidant. The Ce^{III} is then reoxidized by molecular oxygen to render the transformation catalytic. Unlike Lin's hydroboration work with **18**, in which all of the Ce^{IV} centers were reduced to Ce^{III}, X-ray absorption

spectroscopy suggested that only 16.7% (1/6th) of the Ce was reduced after a 7 h period, suggesting only one Ce in each node undergoes the redox chemistry.

Another recent example, this time from the Lin group, involves preparing **18** from $(NH_4)_2Ce(NO_3)_6$ and H_3btc in a mixture of N,N-dimethylformamide and water (*114*). The SBU of **18** prepared in this manner was remarkably stable and could be treated with excess of the organolithium $LiCH_2SiMe_3$ to deprotonate all of the coordinated water (**18-OH**). The resulting hydroxide SBU could then be treated with pinacolborane (HBpin) to ostensibly generate the Ce-dihydrides, which gave off H_2 via a putative bimetallic reductive elimination that led to a net one electron reduction of all of the Ce^{IV} to Ce^{III} to give the new framework **18-H**, with the formula $[Ce^{III}_6(\mu_3\text{-}O)_4(\mu_3\text{-}OLi)_4(H)_6(THF)_6Li_6(COO)_6]$, where THF is the solvent tetrahydrofuran. The authors then exploited the ease of this reduction by preparing **18-OH** as a precatalyst, and performed hydroboration of pyridines simply by combining pyridine substrates with the activated **18-OH** and HBpin (Figure 21a).

In addition, they also demonstrated that **18-OH** could be used to catalyze the hydroboration of both terminal and 1,1-disubstituted alkenes (Figure 21b). By switching to their prereduced catalyst **18-H**, the authors were even able to extend the use of this system to the hydrophosphination of terminal, 1,1-disubstituted, and even internal disubstituted alkenes (Figure 21c).

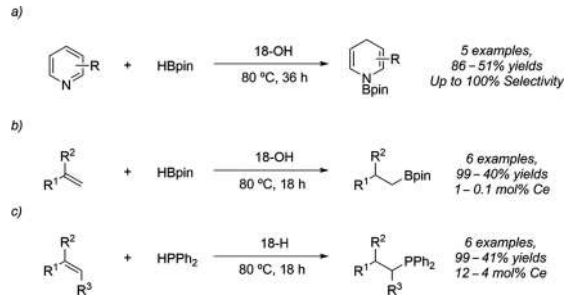

*Figure 21. Reactions catalyzed by Ce-Based MOFs. (a) Hydroboration of pyridine using **18-OH**. (b) Hydroboration of 1,1-disubstituted alkenes using **18-OH**. (c) Hydrophosphination of alkenes using **18-H**.*

Another example of a 2D layered MOF was shown to be a valuable photocatalyst for the H_2 evolution reaction by Zhao et al. (*115*). The 2D framework is made using a top-down approach from UiO-67(Hf) (**19**) (*116*), similar to the UiO-67(Hf) 2D nanosheets synthesized by Grey et. al. (*117*). After synthesizing **19** (Figure 22a), it can be rearranged under ambient conditions before ultrasonification to generate 2D nanosheets of **19-NS** (*118*), which exhibit an 84-fold increase in photocatalytic efficiency in hydrogen evolution as compared to parent **19**. A further increase to thirteen times, or up to 393 μmol g^{-1} h^{-1}, more H_2 evolution, can be seen for **19-NS(Ti)**, in which postsynthetic modification by exchanging Hf^{IV} for Ti^{IV} has occured. To probe the improved surface area and metal access, the Lewis acidity of **19-NS** was also used to catalyze the cyanosilylation of various aromatic aldehydes (Figure 22b), and was generally found to be more active than parent **19**.

Catalysts Derived from Postsynthetic Modification of the SBU

Although the majority of catalysis at metal–oxo-based MOFs has focused on the metal at the node; another strategy, previewed in the example above, is to use the SBU to serve as a foundation to

attach other metals instead. The improved structural integrity of early transition-metal-based MOFs can be used to support a more conventionally reactive late transition metal. This can allow late transition metals to be added to SBUs that are normally impossible and expands the scope of redox chemistry that can be performed at these sites.

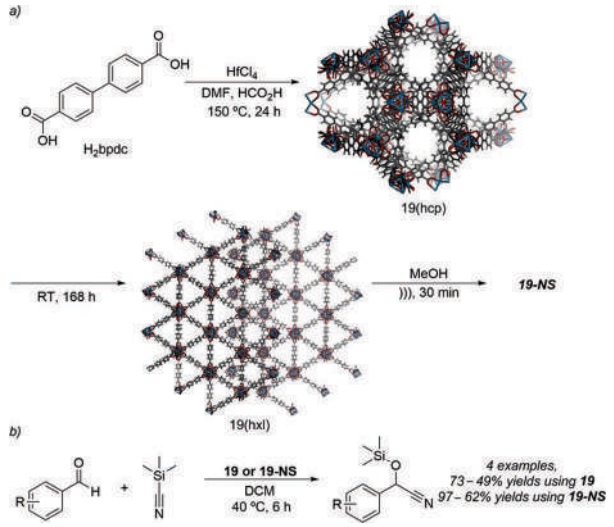

*Figure 22. A top-down approach to catalytically active 2D frameworks from 3D precursors. (a) Synthesis of the 2D nanosheet **19-NS** from **19**. (b) Cyanosilylation of aldehydes catalyzed by **19-NS** and **19**.*

Catalytically Active Metals Immobilized on the SBU

NU-1000 (Figure 23a, **20**), a popular framework for supporting metals at the node, utilizes the same Zr–oxo nodes as UiO-66 and tetratopic ligands (*119*). In a recent example from Farha and Hupp, **20** could be used to immobilize copper utilizing atomic layer deposition with a final copper concentration of ~10 wt % (*120*). The authors estimated that this meant that approximately four Cu atoms were incorporated for every node. Based on significant experiments and density functional theory-optimization, the authors propose a trinuclear Cu–oxo trimer that could bridge two of the Zr nodes (Figure 23b) as a potential manifestation of the Cu-inclusion. With the modified **20-Cu** in hand, the authors next explored the catalytic activity of their new MOF in the oxidation of methane. Their most productive conditions involved activating the framework with O_2 at 200 °C (3 h), followed by loading the framework with methane at 150 °C (3 h), and then using a steam/e mixture to desorb the products at 135 °C (2 h), ultimately giving a mixture of methanol, dimethylether, and carbon dioxide. Other activation procedures led to increased selectivity for carbon dioxide. Using the same framework (**20**), the group has also immobilized other catalysts, such as Co and demonstrated the utility for propane oxidative dehydration (*121*).

MIL-125 **(21)** was initially synthesized by Sanchez and Serre et al. via solvothermal synthesis using Ti^{IV} and terephthalic acid, giving a structure that is similar to **15**, but with an expanded Ti node (Figure 24a) (*122*). Lin et al. has shown how this can be used as a support for redox active Co, while simultaneously exploiting the redox activity of the Ti in the node (*123*). In this particular report, the authors demonstrated that after treating **21** with $LiCH_2SiMe_3$, to ensure complete deprotonation of all the oxo/hydroxo ligands, $CoCl_2$ could be added to generate ostensibly Ti_8-bdc-CoCl (**21-CoCl**). Using one equivalent of Co, approximately 70% incorporation of Co per node was observed

(determined by inductively coupled plasma mass spectrometry). Interestingly, when **21-CoCl** was treated with $NaBEt_3H$ as a reductant, reduction was observed to have occurred at two Ti^{IV} centers, rather than at the Co^{II} center (Figure 24b). The final product was determined to be $[Ti^{III}_2Ti^{IV}_6(\mu_3\text{-}O)_8(\mu_3\text{-}OLi)_2(COO)_{12}CoH]$ (**21-CoH(thf)**). This unique structure was active for hydrogenation of a number of arene (Figure 24c) and heteroarene (Figure 24d) substrates with low catalyst loadings, providing good selectivity across a fair range of substrates.

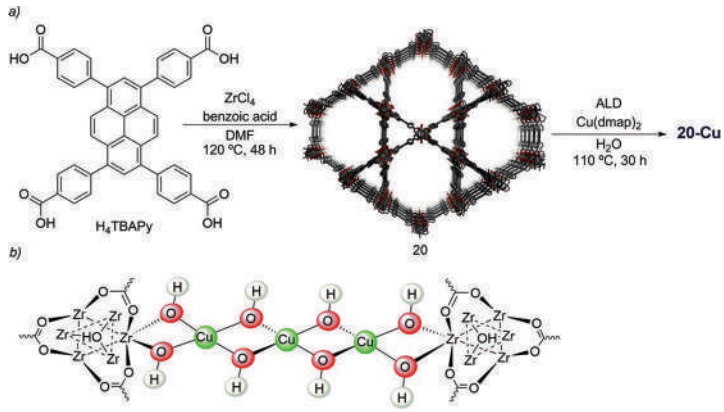

Figure 23. Zr-based framework for supporting transition metal catalysts. (a) Synthesis of ***20*** *and* ***20-Cu****. (b) Computational-optimized structure for supported copper atoms in* ***20-Cu****.*

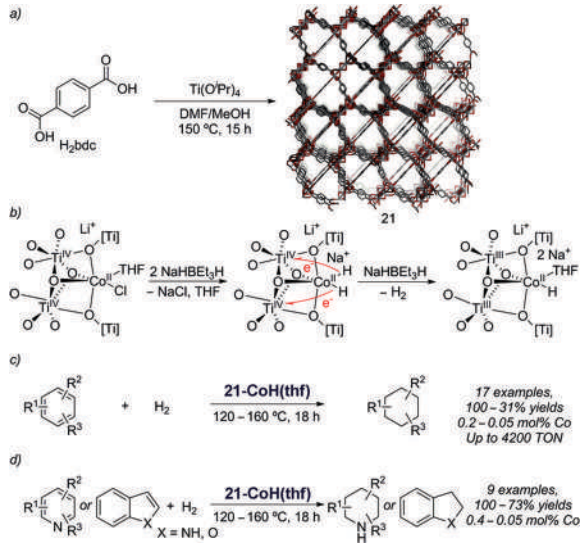

Figure 24. A Ti-based framework as a support for cocatalysis. (a) Synthesis of ***21****. (b) Reduction sequence to access* ***21-CoH(thf)****. (c) Use of* ***21-CoH(thf)*** *for the hydrogenation of arenes. (d) Use of* ***21-CoH(thf)*** *for the hydrogenation of heteroarenes.*

Oveisi et al. and Ghaffari-Moghaddam et al. developed a different approach and synthesized Fe@PCN-222(Fe) (**22**), a bioinspired iron porphyrin MOF with post-synthetically introduced iron chloride anchored to the Zr_6 cluster SBU (*124*). Uniquely, the node accommodated metalation using anhydrous $FeCl_3$ without the use of exogeneous acid or base. The authors tested the synthesized MOF as a cooperative photocatalysis and Lewis acid catalysis for one-pot tandem synthesis of

quinazolin-4(3H)-ones from reaction of alcohols and 2-amonibenzamide under visible light irradiation using air or O_2. Using O_2 as an oxidant the green catalyst performed slightly better than the combined **15**, $FeCl_3$, and 21% greater yield than Fe-porphyrin alone. **15** and $FeCl_3$ alone afforded only trace amount of product, respectively, while $ZrCl_4$ alone was inactive in the tandem reaction. Overall, the synthesis utilizes an earth-abundant, cheap, and nontoxic precursor to produce a novel, recyclable, and highly active photocatalytic mesoporous bimetallic porphyrin network.

Bifunctional MOFs for Catalysis

In addition to modifying the nodes to incorporate catalytically active metals, another approach to achieve bifunctional catalysis has been to install organic groups at the node or on an adjacent ligand. The main use of these kinds of bifunctional structures have been for absorption purposes, CO_2 cycloaddition of epoxides, or the cyanosilyation of aldehydes. The addition of the Lewis basic sites to the framework are key for activating some substrates; they can either act as a stabilizer to counteract the high Lewis acidic strength of the metal clusters or help activate a substrate such as CO_2. Additionally, they are great catalysts for one-pot tandem reactions since the Lewis acidic metal–oxo cluster can catalyze the one reaction while the Lewis basic sites on the ligand can catalyze the other simultaneously within a structurally robust MOF.

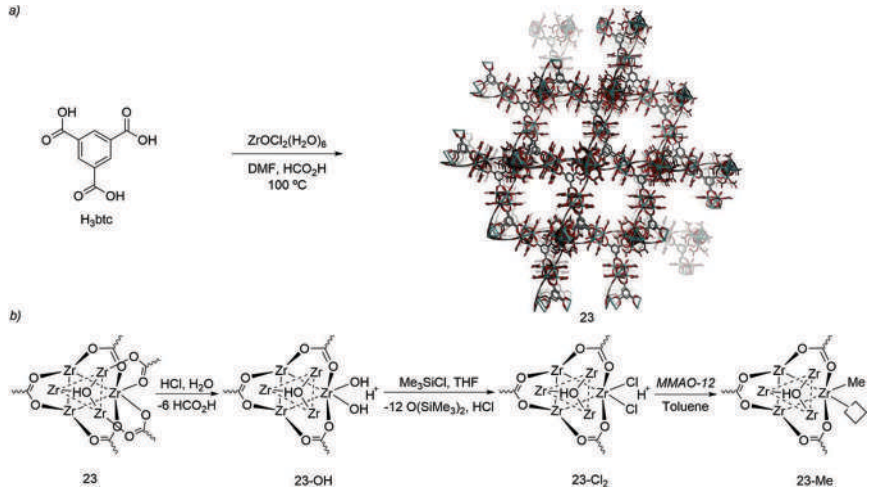

Figure 25. Synthesis of ***23*** *and conversion to* ***23-Me****. (a) Synthesis of* ***23*** *from H_3btc and a Zr–oxide precursor. (b) Conversion of* ***23*** *to* ***23-OH****,* ***23-Cl$_2$****, and ultimately to* ***23-Me****.*

One such example from Lin et al. entails preparing ZrMe-BTC (**23-Me**) consisting of methylated Zr nodes, $[Zr_6(\mu^3\text{-}O)_4(\mu^3\text{-}OLi)_4Me_{12}]^{6-}$, and woven together via tritopic trimesic acid linkers (*125*). To achieve this methylated MOF, the authors initially synthesized Zr MOF-808 (Figure 25a, **23**) (*126*). Protonation of the as-synthesized MOF allowed defect sites filled with formate to be replaced with water that was subsequently changed for chloride by treatment with Me_3SiCl, and finally activation using methylaluminoxane, also known as MMAO-12 (Figure 25b). This methylated Zr MOF analogue exhibits noteworthy electronic and steric properties when compared to similar homogeneous Zr MOF cognates. The new coordination network contains multiple active sites enhancing its ability to produce high molecular weight linear polyethylene after

employing activation using cocatalyst methylaluminoxane. The presence of the Zr–Me allows the MOF to become reactive for ethylene polymerization, although additional MMAO-12 was required for this. Increasing the pressure of ethylene unsurprisingly led to increased activity and subsequently product yield, with up to ~6.6 g of polyethylene produced at 800 psi with only 5 μmols of Zr used.

As mentioned above, these bifunctional systems prove to be good catalysts for CO_2 cycloaddition. The Kim and Park labs used **15** along with TBAB or tetrabutylammonium iodide salts as a cocatalyst to convert epoxides into cyclic carbonates (*127*). When they added functional groups to **15** they found that addition of a single hydroxyl group increased the conversion of the reagents to product. The authors credited this to the ability of the hydroxyl group to help stabilize the negative charge on the carboxylate oxygen through hydrogen bonding with the hydroxyl.

The Hou lab synthesized the Ba^{II}-based MOF **24** (Figure 26) from $Ba(NO_3)_2$ and N,N′-bis(isophthalic acid)-oxalamide (H_4BDPO) and demonstrated its utility for the cycloaddition of CO_2 (*128*). This MOF has a characteristic honeycomb structure with Ba-carboxylate rod SBUs is structurally unique. Due to the CO_2-philic Lewis basic oxalamide groups and unsaturated Lewis acid Ba^{II} sites in the large, tubular, hexagonal channels, this MOF showed great reusability and conversion of smaller epoxides into cyclic carbonates under ambient conditions while using TBAB as a cocatalyst. The authors note that larger epoxides are more difficult to convert based on their increased steric hindrance.

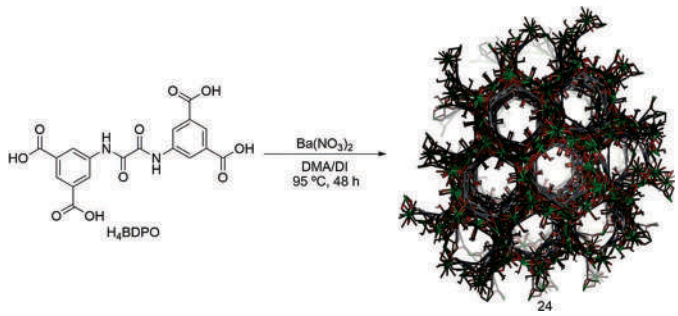

Figure 26. Synthesis of Ba-based MOF ***24****.*

Sun and He labs offer another example of a bifunctional MOF proven useful for selective gas adsorption, cooperative catalysis, and luminescent sensing (*129*). MOF **25** was assembled from $Zn(NO_3)_2{\cdot}6H_2O$, 2M nitric acid, and 2,4-bis(3,5-dicarboxyphenylamino)-6-ol triazine (also abbreviated H_4BDPO, the same as N,N′-bis(isophthalic acid)-oxalamide) ligands, and gave a structure with the formula $[Zn_{24}(BDPO)_{12}(DMF)_{12}]{\cdot}6DMF{\cdot}52H_2O$ (Figure 27a). Structurally, it formed 3D paddlewheel that featured abundant nitrogen functional groups to serve as a Lewis base alongside unsaturated metal sites that can act as Lewis acids. This MOF proved to be an efficient catalyst for a one-pot deacetalization and Knoevenagel condensation reaction of dimethoxymethylbenzene with malononitrile giving the desired product in ~99% yield, while numerous other heterogeneous or homongeneous catalysts could effectively convert the dimethoxymethylbenzene into benzaldehyde, but failed to simultaneously promote the Knoevenagel condensation (Figure 27b).

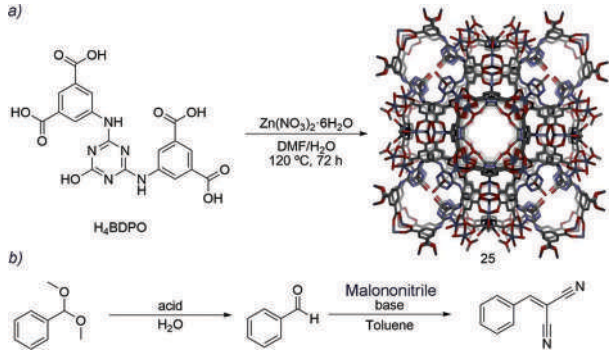

Figure 27. Zn-based MOF ***25****. (a) Synthesis of* ***25*** *from a triazine ligand and* Zn^{II} *salt. (b) Two-step acetal deprotection and knoevenagel catalyzed by* ***25****.*

Zhao et. al. synthesized a related triazine-based MOF with high stability (**26**) with the formula $[Eu(TATMA)(H_2O)\cdot 2H_2O]_n$ (Figure 28a) through solvothermal synthesis using $Eu(NO_3)_3\cdot 6H_2O$ and 4,4,4-s-triazine-1,3,5-triyltri-m-aminobenzoic acid ligands (H_3TATMA) (*130*). This MOF proved to be a highly active catalyst for the Knoevenagel condensation reaction, again owing to the high concentration of both Lewis basic and Lewis acidic sites within the framework. Zhao et al. demonstrated that neutral, electron rich, and electron poor aromatic aldehydes could all be condensed with malononitrile at 80 °C (Figure 28b), with the reactions generally being complete within 3 h.

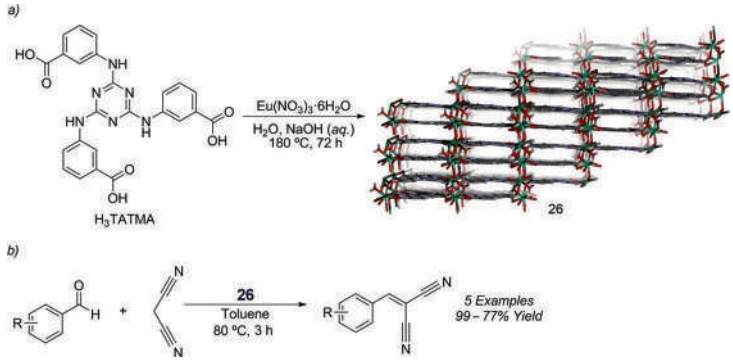

Figure 28. Triazine-Eu MOF ***26****. (a) Synthesis of* ***26*** *from* H_3TATMA *and* Eu^{III} *precursor. (b) General Knoevenagel condensation between aromatic aldehydes and malononitrile catalyzed by* ***26****.*

Considering a greener synthesis and reaction, the Wen lab produced an MOF that could catalyze both CO_2 cycloadditions and Knoevenagel condensations under solvent-free conditions at ambient conditions (*131*). By combining $Zn(NO_3)_2\cdot 6H_2O$, tricarboxytriphenyl amine (H_3TCA), and 1,3-bis(imidazol-1-ylmethyl)benzene (BIB) ligands in N,N′-dimethylacetamide (DMA) and ethanol at 100 °C, framework **27** could be prepared (Figure 29). Unlike most, this MOF has very unique and nonsymmetrical geometry due to its ligands. For example, it has orthorhombic space groups with asymmetric units where the Zn^{II} ions have tetrahedral coordination spheres; but different coordination environments and the 2D framework is cross-linked via π–π interactions between the benzene rings of the BIB ligands that causes a trinodal net. Using **27** and Bu_4NBr as a cocatalyst at 1 atm and 80 °C, the cycloaddition of CO_2 with a variety of aliphatic epoxides was achieved in nearly

100% conversion while aromatic epoxides gave conversion rates of only 50–60%. However, when the pressure was increased to 10 atm even the aromatic epoxides gave conversion rates over 90%. **27** could also be used as a Knoevenagel condensation catalyst. Adding the MOF with substrates at 60 °C gave a product with percent yields ranging from 60% to 99%, representing a reasonable substrate scope that included long aliphatic chains, chains with double bonds, aromatics, and aromatics with electron-donating and withdrawing groups. This success can be attributed to the unsaturated Zn^{II} Lewis acid sites in the MOF and the rich abundance of Lewis basic sites from the ligands that create a net around the epoxide or aldehyde.

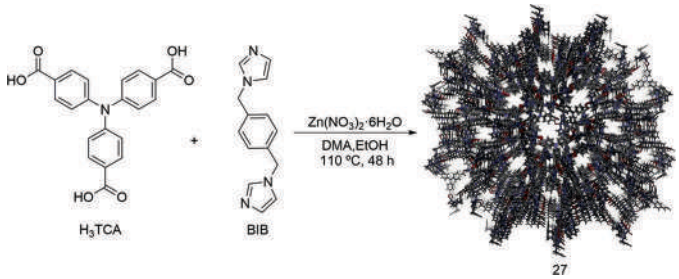

Figure 29. Synthesis of MOF ***27****, a versatile catalyst for CO_2-epoxide cycloaddition and knoevenagel condensation of aldehydes and malononitrile.*

A final example for catalyzing the cycloaddition of CO_2 with epoxides is documented by Du et al. with a dual wall 3D–3D interpenetrated MOF **28**, $[Zn_6(TATAB)_4(DABCO)_3(H_2O)_3]\cdot 12DMF\cdot 9H_2O$ (Figure 30) (*132*). This framework features two identical 3D interpenetrated networks with cubic Zn^{II} paddlewheel SBUs, extended triazine ligands, and DABCO. A uniquely defining feature for this network is a cage in one net is completely encircled by eight cages of the other network exhibiting a rare example of 3D polycatenanes by mechanically linking coordination cages. The pore's diameter is 32 Å with 42 Zn^{2+} catalytic Lewis acid sites and 48 Lewis basic sites able to interact with CO_2. **28** was reported to catalyze the cycloaddition between CO_2 and propylene oxide under neat conditions to produce propylene carbonate. The framework was easily recycled up to six cycles without appreciable loss of catalytic performance.

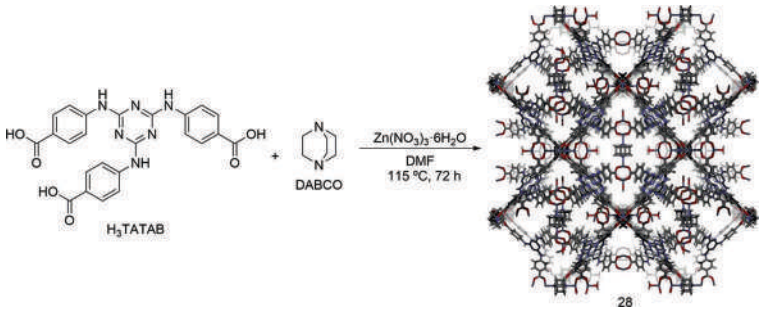

Figure 30. Synthesis of interpenetrated MOF ***28****.*

Summary and Future Applications

Catalysis using structurally vital metals within the SBU, catalysis using post synthetically modified nodes, and bifunctional MOFs are just a few of the ways MOFs can be used for catalytic

transformations. The versatility of structural composition of MOFs drive structural and operational innovation, reinforcing a fast-growing field. Additional approaches not covered in this chapter include ligand-based organocatalysis, using Lewis basic sites on the linkers as ligands for incorporating transition metal catalysts, and using photoactive ligands to promote photocatalysis.

Metal–organic frameworks have proven to be a valuable class of heterogeneous scaffolds. Their tunability can be exploited to likely achieve any imaginable application. Performing catalysis in MOFs can achieve selectivity and activity unparalleled by related homogeneous catalysts, while offering more options for performing reactions under neat conditions, mitigating challenges with catalyst recovery and decomposition, and even allowing synthesis of heterogeneous variants of inaccessible homogeneous species. In addition to the direct applications to the synthetic community, MOFs capable of catalysis, especially water splitting and oxygen reduction, have the potential to revolutionize many aspects of the current fossil fuel-based economy. Whether by providing new avenues for generating energy, or new ways to store and process energy, the idea of MOF-based fuel cells is a prominent area of research providing some valuable results. A more sustainable future will most likely include MOFs for toxic chemical remediation, energy applications, and to improve the efficiency of catalysis in organic synthesis, while opening the possibility of new modes of reactivity.

References

1. Lee, J.; Farha, O. K.; Roberts, J.; Scheidt, K. A.; Nguyen, S. T.; Hupp, J. T. Metal–organic framework materials as catalysts. *Chem. Soc. Rev.* **2009**, *38*, 1450–1459.
2. Yuan, S.; Feng, L.; Wang, K.; Pang, J.; Bosch, M.; Lollar, C.; Sun, Y.; Qin, J.; Yang, X.; Zhang, P.; Wang, Q.; Zou, L.; Zhang, Y.; Zhang, L.; Fang, Y.; Li, J.; Zhou, H.-C. Stable Metal–Organic Frameworks: Design, Synthesis, and Applications. *Adv. Mater.* **2018**, *30*, 1704303.
3. Feng, C.; Lv, C.-P.; Li, Z.-Q.; Zhao, H.; Huang, H.-H. A porous 2D Ni-MOF material with a high supercapacitive performance. *J. Solid State Chem.* **2018**, *265*, 244–247.
4. Guo, X.; Zhou, Z.; Chen, C.; Bai, J.; He, C.; Duan, C. New rht-Type Metal–Organic Frameworks Decorated with Acylamide Groups for Efficient Carbon Dioxide Capture and Chemical Fixation from Raw Power Plant Flue Gas. *ACS Appl. Mater. Interfaces* **2016**, *8*, 31746–31756.
5. Li, F.-F.; Zhu, M.-L.; Lu, L.-P. A luminescent Cd(II)-based metal−organic framework for detection of Fe(III) ions in aqueous solution. *J. Solid State Chem.* **2018**, *261*, 31–36.
6. Gonzalez, M. I.; Mason, J. A.; Bloch, E. D.; Teat, S. J.; Gagnon, K. J.; Morrison, G. Y.; Queen, W. L.; Long, J. R. Structural characterization of framework–gas interactions in the metal–organic framework Co2(dobdc) by in situ single-crystal X-ray diffraction. *Chem. Sci.* **2017**, *8*, 4387–4398.
7. Li, Y.-A.; Yang, S.; Li, Q.-Y.; Ma, J.-P.; Zhang, S.; Dong, Y.-B. UiO-68-ol NMOF-Based Fluorescent Sensor for Selective Detection of HClO and Its Application in Bioimaging. *Inorg. Chem.* **2017**, *56*, 13241–13248.
8. Kazemi, S.; Safarifard, V. Carbon dioxide capture in MOFs: The effect of ligand functionalization. *Polyhedron* **2018**, *154*, 236–251.
9. Jiang, J.; Furukawa, H.; Zhang, Y.-B.; Yaghi, O. M. High Methane Storage Working Capacity in Metal–Organic Frameworks with Acrylate Links. *J. Am. Chem. Soc.* **2016**, *138*, 10244–10251.
10. Li, H.; Wang, K.; Sun, Y.; Lollar, C. T.; Li, J.; Zhou, H.-C. Recent advances in gas storage and separation using metal–organic frameworks. *Mater. Today* **2018**, *21*, 108–121.

11. Adhikari, A. K.; Lin, K.-S. Improving CO2 adsorption capacities and CO2/N2 separation efficiencies of MOF-74(Ni, Co) by doping palladium-containing activated carbon. *Chem. Eng. J.* **2016**, *284*, 1348–1360.
12. Liu, X.; Li, X.; Li, J.; Li, G.; Guo, S.; Zhu, H.; Zhao, L.; Hao, C.; Guo, W. Anionic NbO-type copper organic framework decorated with carboxylate groups for light hydrocarbons separation under ambient conditions. *J. Mater. Sci.* **2018**, *53*, 8866–8877.
13. Jia, Y.; Su, H.; Wang, Z.; Wong, Y. L. E.; Chen, X.; Wang, M.; Chan, T. W. D. Metal–Organic Framework@Microporous Organic Network as Adsorbent for Solid-Phase Microextraction. *Anal. Chem.* **2016**, *88*, 9364–9367.
14. Zhang, N.; Huang, C.; Feng, Z.; Chen, H.; Tong, P.; Wu, X.; Zhang, L. Metal-organic framework-coated stainless steel fiber for solid-phase microextraction of polychlorinated biphenyl. *J. Chromatogr., A* **2018**, *1570*, 10–18.
15. Meng, A.-N.; Chaihu, L.-X.; Chen, H.-H.; Gu, Z.-Y. Ultrahigh adsorption and singlet-oxygen mediated degradation for efficient synergetic removal of bisphenol A by a stable zirconium-porphyrin metal-organic framework. *Sci. Rep.* **2017**, *7*, 6297.
16. Li, J.; Gong, J.-L.; Zeng, G.-M.; Zhang, P.; Song, B.; Cao, W.-C.; Liu, H.-Y.; Huan, S.-Y. Zirconium-based metal organic frameworks loaded on polyurethane foam membrane for simultaneous removal of dyes with different charges. *J. Colloid Interface Sci.* **2018**, *527*, 267–279.
17. Ouyang, H.; Chen, N.; Chang, G.; Zhao, X.; Sun, Y.; Chen, S.; Zhang, H.; Yang, D. Selective Capture of Toxic Selenite Anions by Bismuth-based Metal–Organic Frameworks. *Angew. Chem., Int. Ed.* **2018**, *57*, 13197–13201.
18. Dwyer, D. B.; Dugan, N.; Hoffman, N.; Cooke, D. J.; Hall, M. G.; Tovar, T. M.; Bernier, W. E.; DeCoste, J.; Pomerantz, N. L.; Jones, W. E. Chemical Protective Textiles of UiO-66-Integrated PVDF Composite Fibers with Rapid Heterogeneous Decontamination of Toxic Organophosphates. *ACS Appl. Mater. Interfaces* **2018**, *10*, 34585–34591.
19. de Koning, M. C.; van Grol, M.; Breijaert, T. Degradation of Paraoxon and the Chemical Warfare Agents VX, Tabun, and Soman by the Metal–Organic Frameworks UiO-66-NH2, MOF-808, NU-1000, and PCN-777. *Inorg. Chem.* **2017**, *56*, 11804–11809.
20. Mon, M.; Lloret, F.; Ferrando-Soria, J.; Martí-Gastaldo, C.; Armentano, D.; Pardo, E. Selective and Efficient Removal of Mercury from Aqueous Media with the Highly Flexible Arms of a BioMOF. *Angew. Chem., Int. Ed.* **2016**, *55*, 11167–11172.
21. Nozohour Yazdi, M.; Yamini, Y.; Asiabi, H.; Alizadeh, A. A metal organic framework prepared from benzene-1,3,5-tricarboxylic acid and copper(II), and functionalized with various polysulfides as a sorbent for selective sorption of trace amounts of heavy metal ions. *Microchim. Acta* **2018**, *185*, 525.
22. Chen, L.; Ye, J.-W.; Wang, H.-P.; Pan, M.; Yin, S.-Y.; Wei, Z.-W.; Zhang, L.-Y.; Wu, K.; Fan, Y.-N.; Su, C.-Y. Ultrafast water sensing and thermal imaging by a metal-organic framework with switchable luminescence. *Nat. Commun.* **2017**, *8*, 15985.
23. Yi, F.-Y.; Gu, M.; Wang, S.-C.; Zheng, J.-Q.; Pan, L.; Han, L. A Dual-Functional Luminescent MOF Sensor for Phenylmethanol Molecule and Tb3+ Cation. *Inorg. Chem.* **2018**, *57*, 2654–2662.
24. Wu, M.-X.; Yang, Y.-W. Metal–Organic Framework (MOF)-Based Drug/Cargo Delivery and Cancer Therapy. *Adv. Mater.* **2017**, *29*, 1606134.

25. Chen, X.; Tong, R.; Shi, Z.; Yang, B.; Liu, H.; Ding, S.; Wang, X.; Lei, Q.; Wu, J.; Fang, W. MOF Nanoparticles with Encapsulated Autophagy Inhibitor in Controlled Drug Delivery System for Antitumor. *ACS Appl. Mater. Interfaces* **2018**, *10*, 2328–2337.
26. Ming, F.; Liang, H.; Shi, H.; Xu, X.; Mei, G.; Wang, Z. MOF-derived Co-doped nickel selenide/C electrocatalysts supported on Ni foam for overall water splitting. *J. Mater. Chem. A* **2016**, *4*, 15148–15155.
27. Yang, F.; Zhao, P.; Hua, X.; Luo, W.; Cheng, G.; Xing, W.; Chen, S. A cobalt-based hybrid electrocatalyst derived from a carbon nanotube inserted metal–organic framework for efficient water-splitting. *J. Mater. Chem. A* **2016**, *4*, 16057–16063.
28. Anandhababu, G.; Huang, Y.; Babu, D. D.; Wu, M.; Wang, Y. Oriented Growth of ZIF-67 to Derive 2D Porous CoPO Nanosheets for Electrochemical-/Photovoltage-Driven Overall Water Splitting. *Adv. Funct. Mater.* **2018**, *28*, 1706120.
29. Zheng, X.; Chen, W.; Chen, L.; Wang, Y.; Guo, X.; Wang, J.; Wang, E. A Strategy for Breaking Polyoxometalate-based MOFs To Obtain High Loading Amounts of Nanosized Polyoxometalate Clusters to Improve the Performance of Dye-sensitized Solar Cells. *Chem.—Eur. J.* **2017**, *23*, 8871–8878.
30. Li, M.; Xia, D.; Yang, Y.; Du, X.; Dong, G.; Jiang, A.; Fan, R. Doping of [In2(phen)3Cl6]·CH3CN·2H2O Indium-Based Metal–Organic Framework into Hole Transport Layer for Enhancing Perovskite Solar Cell Efficiencies. *Adv. Energy Mater.* **2018**, *8*, 1800552.
31. Weckhuysen, B. M.; Yu, J. Recent advances in zeolite chemistry and catalysis. *Chem. Soc. Rev.* **2015**, *44*, 7022–7024.
32. Liang, J.; Liang, Z.; Zou, R.; Zhao, Y. Heterogeneous Catalysis in Zeolites, Mesoporous Silica, and Metal–Organic Frameworks. *Adv. Mater.* **2017**, *29*, 1701139.
33. Ogawa, T.; Iyoki, K.; Fukushima, T.; Kajikawa, Y. Landscape of Research Areas for Zeolites and Metal-Organic Frameworks Using Computational Classification Based on Citation Networks. *Adv. Mater. Res. (Durnten-Zurich, Switz.)* **2017**, *10*, 1428.
34. Biradha, K.; Ramanan, A.; Vittal, J. J. Coordination Polymers Versus Metal−Organic Frameworks. *Cryst. Growth Des.* **2009**, *9*, 2969–2970.
35. Hoskins, B. F.; Robson, R. Infinite polymeric frameworks consisting of three dimensionally linked rod-like segments. *J. Am. Chem. Soc.* **1989**, *111*, 5962–5964.
36. Li, H.; Eddaoudi, M.; O'Keeffe, M.; Yaghi, O. M. Design and synthesis of an exceptionally stable and highly porous metal-organic framework. *Nature* **1999**, *402*, 276.
37. Huang, L.; Wang, H.; Chen, J.; Wang, Z.; Sun, J.; Zhao, D.; Yan, Y. Synthesis, Morphology Control, and Properties of Porous Metal-Organic Coordination Polymers. *Microporous Mesoporous Mater.* **2003**, *58*, 105–114.
38. Choi, J.-S.; Son, W.-J.; Kim, J.; Ahn, W.-S. Metal–organic framework MOF-5 prepared by microwave heating: Factors to be considered. *Microporous Mesoporous Mater.* **2008**, *116*, 727–731.
39. Saha, D.; Deng, S. Synthesis, characterization and hydrogen adsorption in mixed crystals of MOF-5 and MOF-177. *Int. J. Hydrogen Energy* **2009**, *34*, 2670–2678.
40. Saha, D.; Deng, S.; Yang, Z. Hydrogen adsorption on metal-organic framework (MOF-5) synthesized by DMF approach. *J. Porous Mater.* **2009**, *16*, 141–149.

41. Chaemchuen, S.; Luo, Z.; Zhou, K.; Mousavi, B.; Phatanasri, S.; Jaroniec, M.; Verpoort, F. Defect formation in metal–organic frameworks initiated by the crystal growth-rate and effect on catalytic performance. *J. Catal.* **2017**, *354*, 84–91.
42. An, Y.; Liu, Y.; Wang, Z.; Wang, P.; Zheng, Z.; Dai, Y.; Qin, X.; Zhang, X.; Whangbo, M.-H.; Huang, B. Stabilizing the titanium-based metal organic frameworks in water by metal cations with empty or partially-filled d orbitals. *J. Colloid Interface Sci.* **2019**, *533*, 9–12.
43. DeCoste, J. B.; Peterson, G. W.; Jasuja, H.; Glover, T. G.; Huang, Y.-G.; Walton, K. S. Stability and degradation mechanisms of metal–organic frameworks containing the Zr6O4(OH)4 secondary building unit. *J. Mater. Chem. A* **2013**, *1*, 5642–5650.
44. Burtch, N. C.; Jasuja, H.; Walton, K. S. Water Stability and Adsorption in Metal–Organic Frameworks. *Chem. Rev.* **2014**, *114*, 10575–10612.
45. Brozek, C. K.; Dincă, M. Cation exchange at the secondary building units of metal–organic frameworks. *Chem. Soc. Rev.* **2014**, *43*, 5456–5467.
46. Beyzavi, M. H.; Vermeulen, N. A.; Howarth, A. J.; Tussupbayev, S.; League, A. B.; Schweitzer, N. M.; Gallagher, J. R.; Platero-Prats, A. E.; Hafezi, N.; Sarjeant, A. A.; Miller, J. T.; Chapman, K. W.; Stoddart, J. F.; Cramer, C. J.; Hupp, J. T.; Farha, O. K. A Hafnium-Based Metal–Organic Framework as a Nature-Inspired Tandem Reaction Catalyst. *J. Am. Chem. Soc.* **2015**, *137*, 13624–13631.
47. Ji, P.; Feng, X.; Veroneau, S. S.; Song, Y.; Lin, W. Trivalent Zirconium and Hafnium Metal–Organic Frameworks for Catalytic 1,4-Dearomative Additions of Pyridines and Quinolines. *J. Am. Chem. Soc.* **2017**, *139*, 15600–15603.
48. Jiao, L.; Wang, Y.; Jiang, H.-L.; Xu, Q. Metal–Organic Frameworks as Platforms for Catalytic Applications. *Adv. Mater.* **2017**, *30*, 1703663.
49. Fang, Y.; Ma, Y.; Zheng, M.; Yang, P.; Asiri, A. M.; Wang, X. Metal–organic frameworks for solar energy conversion by photoredox catalysis. *Coord. Chem. Rev.* **2018**, *373*, 83–115.
50. Freire, C.; Fernandes, D. M.; Nunes, M.; Abdelkader, V. K. POM & MOF-based Electrocatalysts for Energy-related Reactions. *ChemCatChem* **2018**, *10*, 1703–1730.
51. Tu, W.; Xu, Y.; Yin, S.; Xu, R. Rational Design of Catalytic Centers in Crystalline Frameworks. *Adv. Mater.* **2018**, *30*, 1707582.
52. Yang, S.; Peng, L.; Bulut, S.; Queen, W. L. Recent Advances of MOFs and MOF-Derived Materials in Thermally Driven Organic Transformations. *Chem.—Eur. J.* **2018**, *24*, 1–19.
53. Kalmutzki, M. J.; Hanikel, N.; Yaghi, O. M. Secondary building units as the turning point in the development of the reticular chemistry of MOFs. *Sci. Adv.* **2018**, *4*, eaat9180.
54. Yang, H.; Wang, X. Secondary-Component Incorporated Hollow MOFs and Derivatives for Catalytic and Energy-Related Applications. *Adv. Mater.* **2018**, 1800743.
55. Drake, T.; Ji, P.; Lin, W. Site Isolation in Metal–Organic Frameworks Enables Novel Transition Metal Catalysis. *Acc. Chem. Res.* **2018**, *51*, 2129–2138.
56. Bhattacharjee, S.; Lee, Y.-R.; Puthiaraj, P.; Cho, S.-M.; Ahn, W.-S. Metal–Organic Frameworks for Catalysis. *Catal. Surv. Asia* **2015**, *19*, 203–222.
57. Dissegna, S.; Epp, K.; Heinz, W. R.; Kieslich, G.; Fischer, R. A. Defective Metal-Organic Frameworks. *Adv. Mater.* **2018**, *30*, 1704501.
58. Canivet, J.; Vandichel, M.; Farrusseng, D. Origin of highly active metal–organic framework catalysts: defects? Defects! *Dalton Trans.* **2016**, *45*, 4090–4099.

59. Islamoglu, T.; Goswami, S.; Li, Z.; Howarth, A. J.; Farha, O. K.; Hupp, J. T. Postsynthetic Tuning of Metal–Organic Frameworks for Targeted Applications. *Acc. Chem. Res.* **2017**, *50*, 805–813.
60. Lollar, C. T.; Qin, J.-S.; Pang, J.; Yuan, S.; Becker, B.; Zhou, H.-C. Interior Decoration of Stable Metal–Organic Frameworks. *Langmuir* **2018**, *34*, 13795–13807.
61. Huang, Y.-B.; Liang, J.; Wang, X.-S.; Cao, R. Multifunctional metal–organic framework catalysts: synergistic catalysis and tandem reactions. *Chem. Soc. Rev.* **2017**, *46*, 126–157.
62. Ma, D.; Li, B.; Shi, Z. Multi-functional sites catalysts based on post-synthetic modification of metal-organic frameworks. *Chin. Chem. Lett.* **2018**, *29*, 827–830.
63. Zhang, Y.; Yang, X.; Zhou, H.-C. Synthesis of MOFs for heterogeneous catalysis via linker design. *Polyhedron* **2018**, *154*, 189–201.
64. Xiong, Y. Y.; Wu, H. Q.; Luo, F. The MOF+ Technique: A Potential Multifunctional Platform. *Chem.—Eur. J.* **2018**, *24*, 13701–13705.
65. Li, G.; Zhao, S.; Zhang, Y.; Tang, Z. Metal–Organic Frameworks Encapsulating Active Nanoparticles as Emerging Composites for Catalysis: Recent Progress and Perspectives. *Adv. Mater.* **2018**, 1800702.
66. Dhakshinamoorthy, A.; Asiri, A. M.; Garcia, H. Metal Organic Frameworks as Versatile Hosts of Au Nanoparticles in Heterogeneous Catalysis. *ACS Catal.* **2017**, *7*, 2896–2919.
67. Yang, Q.; Xu, Q.; Jiang, H.-L. Metal–organic frameworks meet metal nanoparticles: synergistic effect for enhanced catalysis. *Chem. Soc. Rev.* **2017**, *46*, 4774–4808.
68. Wu, C.-D.; Zhao, M. Incorporation of Molecular Catalysts in Metal–Organic Frameworks for Highly Efficient Heterogeneous Catalysis. *Adv. Mater.* **2017**, *29*, 1605446.
69. Pereira, C.; Simões, M.; Tomé, J.; Almeida Paz, F. Porphyrin-Based Metal-Organic Frameworks as Heterogeneous Catalysts in Oxidation Reactions. *Molecules* **2016**, *21*, 1348.
70. Cohen, S. M.; Zhang, Z.; Boissonnault, J. A. Toward "metalloMOFzymes": Metal–Organic Frameworks with Single-Site Metal Catalysts for Small-Molecule Transformations. *Inorg. Chem.* **2016**, *55*, 7281–7290.
71. Chen, Y.; Ma, S. Biomimetic catalysis of metal–organic frameworks. *Datlton Trans.* **2016**, *45*, 9744–9753.
72. Hastings, C. J.; Pluth, M. D.; Bergman, R. G.; Raymond, K. N. Enzymelike Catalysis of the Nazarov Cyclization by Supramolecular Encapsulation. *J. Am. Chem. Soc.* **2010**, *132*, 6938–6940.
73. Brown, C. J.; Bergman, R. G.; Raymond, K. N. Enantioselective Catalysis of the Aza-Cope Rearrangement by a Chiral Supramolecular Assembly. *J. Am. Chem. Soc.* **2009**, *131*, 17530–17531.
74. Hooley, R. J.; Rebek, J., Jr. Chemistry and Catalysis in Functional Cavitands. *Chem. Biol.* **2009**, *16*, 255–264.
75. Wu, N.-W.; Rebek, J., Jr. Cavitands as Chaperones for Monofunctional and Ring-Forming Reactions in Water. *J. Am. Chem. Soc.* **2016**, *138*, 7512–7515.
76. Zhang, Q.; Tiefenbacher, K. Terpene cyclization catalysed inside a self-assembled cavity. *Nat. Chem.* **2015**, *7*, 197–202.
77. La Manna, P.; Talotta, C.; Floresta, G.; De Rosa, M.; Soriente, A.; Rescifina, A.; Gaeta, C.; Neri, P. Mild Friedel–Crafts Reactions inside a Hexameric Resorcinarene Capsule: C−Cl Bond

Activation through Hydrogen Bonding to Bridging Water Molecules. *Angew. Chem., Int. Ed.* **2018**, *57*, 5423–5428.

78. Olajire, A. A. Synthesis chemistry of metal-organic frameworks for CO2 capture and conversion for sustainable energy future. *Renewable Sustainable Energy Rev.* **2018**, *92*, 570–607.
79. Büttner, H.; Longwitz, L.; Steinbauer, J.; Wulf, C.; Werner, T. Recent Developments in the Synthesis of Cyclic Carbonates from Epoxides and CO2. *Top. Curr. Chem.* **2017**, *375*, 50.
80. Zou, R.; Li, P.-Z.; Zeng, Y.-F.; Liu, J.; Zhao, R.; Duan, H.; Luo, Z.; Wang, J.-G.; Zou, R.; Zhao, Y. Bimetallic Metal-Organic Frameworks: Probing the Lewis Acid Site for CO2 Conversion. *Small* **2016**, *12*, 2334–2343.
81. Jiang, W.; Yang, J.; Liu, Y.-Y.; Song, S.-Y.; Ma, J.-F. A Porphyrin-Based Porous rtl Metal–Organic Framework as an Efficient Catalyst for the Cycloaddition of CO2 to Epoxides. *Chem.—Eur. J.* **2016**, *22*, 16991–16997.
82. Wang, X.; Gao, W.-Y.; Niu, Z.; Wojtas, L.; Perman, J. A.; Chen, Y.-S.; Li, Z.; Aguila, B.; Ma, S. A metal–metalloporphyrin framework based on an octatopic porphyrin ligand for chemical fixation of CO2 with aziridines. *Chem. Commun.* **2018**, *54*, 1170–1173.
83. Chui, S. S. Y.; Lo, S. M. F.; Charmant, J. P. H.; Orpen, A. G.; Williams, I. D. A Chemically Functionalizable Nanoporous Material. *Science* **1999**, *283*, 1148–1150.
84. Celis-Salazar, P. J.; Epley, C. C.; Ahrenholtz, S. R.; Maza, W. A.; Usov, P. M.; Morris, A. J. Proton-Coupled Electron Transport in Anthraquinone-Based Zirconium Metal–Organic Frameworks. *Inorg. Chem.* **2017**, *56*, 13741–13747.
85. Zhu, J.; Maza, W. A.; Morris, A. J. Light-harvesting and energy transfer in ruthenium(II)-polypyridyl doped zirconium(IV) metal-organic frameworks: A look toward solar cell applications. *J. Photochem. Photobiol., A* **2017**, *344*, 64–77.
86. Rowe, J. M.; Zhu, J.; Soderstrom, E. M.; Xu, W.; Yakovenko, A.; Morris, A. J. Sensitized photon upconversion in anthracene-based zirconium metal–organic frameworks. *Chem. Commun.* **2018**, *54*, 7798–7801.
87. Heravi, M.; Tamimi, M.; Yahyavi, H.; Hosseinnejad, T. Huisgen's Cycloaddition Reactions: A Full Perspective. *Curr. Org. Chem.* **2016**, *20*, 1–57.
88. Guo, X.; Zeng, L.; Wang, Z.; Zhang, T.; He, C.; Duan, C. Photocatalytic copper-catalyzed azide–alkyne cycloaddition click reaction with Cu(II) coordination polymer. *RSC Adv.* **2017**, *7*, 52907–52913.
89. Batten, S. R.; Champness, N. R.; Chen, X.-M.; Garcia-Martinez, J.; Kitagawa, S.; Öhrström, L.; O'Keeffe, M.; Suh, M. P.; Reedijk, J. Coordination polymers, metal–organic frameworks and the need for terminology guidelines. *CrystEngComm* **2012**, *14*, 3001–3004.
90. Seth, S.; Matzger, A. J. Metal–Organic Frameworks: Examples, Counterexamples, and an Actionable Definition. *Cryst. Growth Des.* **2017**, *17*, 4043–4048.
91. Qin, L.; Chen, H.-Z.; Lei, J.; Wang, Y.-Q.; Ye, T.-Q.; Zheng, H.-G. Photodegradation of Some Organic Dyes over Two Metal–Organic Frameworks with Especially High Efficiency for Safranine T. *Cryst. Growth Des.* **2017**, *17*, 1293–1298.
92. Lan, G.; Zhu, Y.-Y.; Veroneau, S. S.; Xu, Z.; Micheroni, D.; Lin, W. Electron Injection from Photoexcited Metal–Organic Framework Ligands to Ru2 Secondary Building Units for Visible-Light-Driven Hydrogen Evolution. *J. Am. Chem. Soc.* **2018**, *140*, 5326–5329.

93. Liu, J.; Wu, J.; Luo, Z.; Li, B.; Singh, A.; Abhinav, K. A porous zinc(II) metal–organic framework exhibiting high sensing ability for ferric and nitroaromatics as well as photocatalytic degradation activities against organic dyes. *J. Coord. Chem.* **2017**, *70*, 3946–3958.
94. Choi, E.-Y.; Wray, C. A.; Hu, C.; Choe, W. Highly tunable metal–organic frameworks with open metal centers. *CrystEngComm* **2009**, *11*, 553–555.
95. Kataoka, Y.; Kataoka, K. S.; Murata, H.; Handa, M.; Mori, W.; Kawamoto, T. Synthesis and characterizations of a paddlewheel-type dirhodium-based photoactive porous metal-organic framework. *Inorg. Chem. Commun.* **2016**, *68*, 37–41.
96. Sakuma, T.; Sakai, H.; Araki, Y.; Wada, T.; Hasobe, T. Control of local structures and photophysical properties of zinc porphyrin-based supramolecular assemblies structurally organized by regioselective ligand coordination. *Phys. Chem. Chem. Phys.* **2016**, *18*, 5453–5463.
97. Sharma, V.; De, D.; Saha, R.; Das, R.; Chattaraj, P. K.; Bharadwaj, P. K. A Cu(II)-MOF capable of fixing CO2 from air and showing high capacity H2 and CO2 adsorption. *Chem. Commun.* **2017**, *53*, 13371–13374.
98. Sharma, V.; De, D.; Bharadwaj, P. K. A Multifunctional Metal–Organic Framework for Oxidative C–O Coupling Involving Direct C–H Activation and Synthesis of Quinolines. *Inorg. Chem.* **2018**, *57*, 8195–8199.
99. Tanaka, K.; Otani, K.-I. Asymmetric alcoholytic kinetic resolution of styrene oxide catalysed by chiral metal–organic framework crystals. *New J. Chem.* **2010**, *34*, 2389–2391.
100. Doitomi, K.; Xu, K.; Hirao, H. The mechanism of an asymmetric ring-opening reaction of epoxide with amine catalyzed by a metal–organic framework: insights from combined quantum mechanics and molecular mechanics calculations. *Dalton Trans.* **2017**, *46*, 3470–3481.
101. Tanaka, K.; Hotta, N.; Nagase, S.; Yoza, K. Efficient HPLC enantiomer separation using a pillared homochiral metal–organic framework as a novel chiral stationary phase. *New J. Chem.* **2016**, *40*, 4891–4894.
102. Tanaka, K.; Nagase, S.; Anami, T.; Wierzbicki, M.; Urbanczyk-Lipkowska, Z. Enantioselective Diels–Alder reaction in the confined space of homochiral metal–organic frameworks. *RSC Adv.* **2016**, *6*, 111436–111439.
103. Tanaka, K.; Kinoshita, M.; Kayahara, J.; Uebayashi, Y.; Nakaji, K.; Morawiak, M.; Urbanczyk-Lipkowska, Z. Asymmetric ring-opening reaction of meso-epoxides with aromatic amines using homochiral metal–organic frameworks as recyclable heterogeneous catalysts. *RSC Adv.* **2018**, *8*, 28139–28146.
104. Cavka, J. H.; Jakobsen, S.; Olsbye, U.; Guillou, N.; Lamberti, C.; Bordiga, S.; Lillerud, K. P. A New Zirconium Inorganic Building Brick Forming Metal Organic Frameworks with Exceptional Stability. *J. Am. Chem. Soc.* **2008**, *130*, 13850–13851.
105. Yang, Q.; Guillerm, V.; Ragon, F.; Wiersum, A. D.; Llewellyn, P. L.; Zhong, C.; Devic, T.; Serre, C.; Maurin, G. CH4 storage and CO2 capture in highly porous zirconium oxide based metal–organic frameworks. *Chem. Commun.* **2012**, *48*, 9831–9833.
106. Yang, D.; Ortuño, M. A.; Bernales, V.; Cramer, C. J.; Gagliardi, L.; Gates, B. C. Structure and Dynamics of Zr6O8 Metal–Organic Framework Node Surfaces Probed with Ethanol Dehydration as a Catalytic Test Reaction. *J. Am. Chem. Soc.* **2018**, *140*, 3751–3759.
107. Caratelli, C.; Hajek, J.; Cirujano, F. G.; Waroquier, M.; Llabrés i Xamena, F. X.; Van Speybroeck, V. Nature of active sites on UiO-66 and beneficial influence of water in the catalysis of Fischer esterification. *J. Catal.* **2017**, *352*, 401–414.

108. Cirujano, F. G.; Corma, A.; Llabrés i Xamena, F. X. Conversion of levulinic acid into chemicals: Synthesis of biomass derived levulinate esters over Zr-containing MOFs. *Chem. Eng. Sci.* **2015**, *124*, 52–60.
109. Ji, P.; Manna, K.; Lin, Z.; Feng, X.; Urban, A.; Song, Y.; Lin, W. Single-Site Cobalt Catalysts at New Zr12(μ3-O)8(μ3-OH)8(μ2-OH)6 Metal–Organic Framework Nodes for Highly Active Hydrogenation of Nitroarenes, Nitriles, and Isocyanides. *J. Am. Chem. Soc.* **2017**, *139*, 7004–7011.
110. Momeni, M. R.; Cramer, C. J. Dual Role of Water in Heterogeneous Catalytic Hydrolysis of Sarin by Zirconium-Based Metal–Organic Frameworks. *ACS Appl. Mater. Interfaces* **2018**, *10*, 18435–18439.
111. Reinares-Fisac, D.; Aguirre-Díaz, L. M.; Iglesias, M.; Snejko, N.; Gutiérrez-Puebla, E.; Monge, M. Á.; Gándara, F. A Mesoporous Indium Metal–Organic Framework: Remarkable Advances in Catalytic Activity for Strecker Reaction of Ketones. *J. Am. Chem. Soc.* **2016**, *138*, 9089–9092.
112. Lammert, M.; Wharmby, M. T.; Smolders, S.; Bueken, B.; Lieb, A.; Lomachenko, K. A.; Vos, D. D.; Stock, N. Cerium-based metal organic frameworks with UiO-66 architecture: synthesis, properties and redox catalytic activity. *Chem. Commun.* **2015**, *51*, 12578–12581.
113. Smolders, S.; Lomachenko, K. A.; Bueken, B.; Struyf, A.; Bugaev, A. L.; Atzori, C.; Stock, N.; Lamberti, C.; Roeffaers, M. B. J.; De Vos, D. E. Unravelling the Redox-catalytic Behavior of Ce4+ Metal–Organic Frameworks by X-ray Absorption Spectroscopy. *ChemPhysChem* **2018**, *19*, 373–378.
114. Ji, P.; Sawano, T.; Lin, Z.; Urban, A.; Boures, D.; Lin, W. Cerium-Hydride Secondary Building Units in a Porous Metal–Organic Framework for Catalytic Hydroboration and Hydrophosphination. *J. Am. Chem. Soc.* **2016**, *138*, 14860–14863.
115. Wang, J.; Zhang, J.; Peh, S. B.; Zhai, L.; Ying, Y.; Liu, G.; Cheng, Y.; Zhao, D. Dimensional Impact of Metal-Organic Frameworks in Catalyzing Photo-Induced Hydrogen Evolution and Cyanosilylation Reactions. *ACS Appl. Energy Mater.* **2019**, DOI:10.1021/acsaem.8b01303.
116. Katz, M. J.; Brown, Z. J.; Colón, Y. J.; Siu, P. W.; Scheidt, K. A.; Snurr, R. Q.; Hupp, J. T.; Farha, O. K. A facile synthesis of UiO-66, UiO-67 and their derivatives. *Chem. Commun.* **2013**, *49*, 9449–9451.
117. Cliffe, M. J.; Castillo-Martínez, E.; Wu, Y.; Lee, J.; Forse, A. C.; Firth, F. C. N.; Moghadam, P. Z.; Fairen-Jimenez, D.; Gaultois, M. W.; Hill, J. A.; Magdysyuk, O. V.; Slater, B.; Goodwin, A. L.; Grey, C. P. Metal–Organic Nanosheets Formed via Defect-Mediated Transformation of a Hafnium Metal–Organic Framework. *J. Am. Chem. Soc.* **2017**, *139*, 5397–5404.
118. Hu, Z.; Mahdi, E. M.; Peng, Y.; Qian, Y.; Zhang, B.; Yan, N.; Yuan, D.; Tan, J.-C.; Zhao, D. Kinetically controlled synthesis of two-dimensional Zr/Hf metal–organic framework nanosheets via a modulated hydrothermal approach. *J. Mater. Chem. A* **2017**, *5*, 8954–8963.
119. Mondloch, J. E.; Bury, W.; Fairen-Jimenez, D.; Kwon, S.; DeMarco, E. J.; Weston, M. H.; Sarjeant, A. A.; Nguyen, S. T.; Stair, P. C.; Snurr, R. Q.; Farha, O. K.; Hupp, J. T. Vapor-Phase Metalation by Atomic Layer Deposition in a Metal–Organic Framework. *J. Am. Chem. Soc.* **2013**, *135*, 10294–10297.
120. Ikuno, T.; Zheng, J.; Vjunov, A.; Sanchez-Sanchez, M.; Ortuño, M. A.; Pahls, D. R.; Fulton, J. L.; Camaioni, D. M.; Li, Z.; Ray, D.; Mehdi, B. L.; Browning, N. D.; Farha, O. K.; Hupp, J. T.; Cramer, C. J.; Gagliardi, L.; Lercher, J. A. Methane Oxidation to Methanol Catalyzed by Cu-

Oxo Clusters Stabilized in NU-1000 Metal–Organic Framework. *J. Am. Chem. Soc.* **2017**, *139*, 10294–10301.

121. Li, Z.; Peters, A. W.; Bernales, V.; Ortuño, M. A.; Schweitzer, N. M.; DeStefano, M. R.; Gallington, L. C.; Platero-Prats, A. E.; Chapman, K. W.; Cramer, C. J.; Gagliardi, L.; Hupp, J. T.; Farha, O. K. Metal–Organic Framework Supported Cobalt Catalysts for the Oxidative Dehydrogenation of Propane at Low Temperature. *ACS Cent. Sci.* **2017**, *3*, 31–38.
122. Dan-Hardi, M.; Serre, C.; Frot, T.; Rozes, L.; Maurin, G.; Sanchez, C.; Férey, G. A New Photoactive Crystalline Highly Porous Titanium(IV) Dicarboxylate. *J. Am. Chem. Soc.* **2009**, *131*, 10857–10859.
123. Ji, P.; Song, Y.; Drake, T.; Veroneau, S. S.; Lin, Z.; Pan, X.; Lin, W. Titanium(III)-Oxo Clusters in a Metal–Organic Framework Support Single-Site Co(II)-Hydride Catalysts for Arene Hydrogenation. *J. Am. Chem. Soc.* **2018**, *140*, 433–440.
124. Ghaleno, M. R.; Ghaffari-Moghaddam, M.; Khajeh, M.; Reza Oveisi, A.; Bohlooli, M. Iron species supported on a mesoporous zirconium metal-organic framework for visible light driven synthesis of quinazolin-4(3H)-ones through one-pot three-step tandem reaction. *J. Colloid Interface Sci.* **2019**, *535*, 214–226.
125. Ji, P.; Solomon, J. B.; Lin, Z.; Johnson, A.; Jordan, R. F.; Lin, W. Transformation of Metal–Organic Framework Secondary Building Units into Hexanuclear Zr-Alkyl Catalysts for Ethylene Polymerization. *J. Am. Chem. Soc.* **2017**, *139*, 11325–11328.
126. Furukawa, H.; Gándara, F.; Zhang, Y.-B.; Jiang, J.; Queen, W. L.; Hudson, M. R.; Yaghi, O. M. Water Adsorption in Porous Metal–Organic Frameworks and Related Materials. *J. Am. Chem. Soc.* **2014**, *136*, 4369–4381.
127. Noh, J.; Kim, Y.; Park, H.; Lee, J.; Yoon, M.; Park, M. H.; Kim, Y.; Kim, M. Functional group effects on a metal-organic framework catalyst for CO2 cycloaddition. *J. Ind. Eng. Chem.* **2018**, *64*, 478–483.
128. Li, X.-Y.; Ma, L.-N.; Liu, Y.; Hou, L.; Wang, Y.-Y.; Zhu, Z. Honeycomb Metal–Organic Framework with Lewis Acidic and Basic Bifunctional Sites: Selective Adsorption and CO2 Catalytic Fixation. *ACS Appl. Mater. Interfaces* **2018**, *10*, 10965–10973.
129. He, H.; Zhang, D.-Y.; Guo, F.; Sun, F. A Versatile Microporous Zinc(II) Metal-Organic Framework for Selective Gas Adsorption, Cooperative Catalysis, and Luminescent Sensing. *Inorg. Chem.* **2018**, *57*, 7314–7320.
130. Zhao, S. A novel 3D MOF with rich lewis basic sites as a base catalysis toward knoevenagel condensation reaction. *J. Mol. Struct.* **2018**, *1167*, 11–15.
131. Yao, C.; Zhou, S.; Kang, X.; Zhao, Y.; Yan, R.; Zhang, Y.; Wen, L. A Cationic Zinc–Organic Framework with Lewis Acidic and Basic Bifunctional Sites as an Efficient Solvent-Free Catalyst: CO 2 Fixation and Knoevenagel Condensation Reaction. *Inorg. Chem.* **2018**, *57*, 11157–11164.
132. Han, Y.-H.; Zhou, Z.-Y.; Tian, C.-B.; Du, S.-W. A dual-walled cage MOF as an efficient heterogeneous catalyst for the conversion of CO2 under mild and co-catalyst free conditions. *Green Chem.* **2016**, *18*, 4086–4091.

Editor's Biography

Meng Zhou

Meng Zhou was born in Chengdu, China, and received his Bachelor of Science from Purdue University in 2008. Meng studied the C–H functionalization reactions catalyzed by organometallic iridium complexes with Robert Crabtree at Yale University (Ph.D.) and later with Alan Goldman at Rutgers University (Postdoc). He then investigated the acetate-stabilized cobalt(II,III) oxide nanoparticles with Richard Finke at Colorado State University. Since 2016, he has been an assistant professor of inorganic chemistry at Lawrence Technological University in Michigan, where his research focuses on nanomaterials and catalysis. He supervises undergraduate students conducting research in a regular, collegewide curriculum supported by the Howard Hughes Medical Institute Inclusive Excellence initiative.

Author Index

Subject Index

ACS SYMPOSIUM SERIES

VOLUME 1317

CASE STUDIES OF CATALYST SYSTEMS

This book introduces readers to the fundamentals and applications of contemporary catalysts derived from transition metals. Case studies on the selected catalysts demonstrate the unique challenges and solutions in catalyst design and niche applications. Two sections on metal complexes and nanomaterials provide contemporary examples to illustrate the principles and mechanisms of catalysis. Active researchers in chemistry, chemical engineering, or nanomaterials will find this book useful.

PUBLISHED BY THE
American Chemical Society

ISBN 978-0-8412-3437-6